Performance of Low Cost Composites for Tidal Turbine Applications

Hassan Izadi Gonabadi

Thesis submitted in fulfilment of the requirements for the degree of

Doctor of Philosophy

School of Engineering

Faculty of Science, Agricultural and Engineering

Newcastle University

March, 2019

Declaration of authenticity and author's rights

This thesis is the result of the author's original research. It has been composed by the author and has not been previously submitted for examination which has led to the award of a degree. The copyright of this thesis belongs to the author under the terms of the United Kingdom Copyright Acts as qualified by Newcastle University Regulation.

Signed:

Date:

Acknowledgements

I would like to thank my supervisory team Professor Steve Bull and Dr. Adrian Oila for their support through this project and for giving me the freedom to follow the topics that I found interesting. I would also like to thank Neville Dickman for his advice during laboratory experiments, allowing this thesis to reach a greater depth in the field of tidal energy.

I would like to thank all my friends in the Sun Air research institute (Ferdowsi University of Mashhad-Iran) who have helped me with my work and kept me company throughout the duration of my PhD.

Finally, my greatest thanks go to my wife and my family at home who supported me emotionally and financially during my PhD program. Without your support, I would never had made it to where I am now.

ABSTRACT

Interest in tidal power is continuously increasing due to its huge potential for energy generation. This has led to the emergence of tidal turbine designs often inspired from earlier developments in the wind turbine industry. In comparison with land-based structures such as wind energy devices, development of marine energy conversion devices places more emphasis on material properties. Maintenance cost at sea is high and for marine energy supply to become economically viable, long term durability and reliability of these materials must be considered. Fluctuating loads due to the tidal flow are a common characteristic of marine energy conversion devices and they must withstand both extreme one-off and fatigue loads during their lifetimes in an aggressive environment, therefore it is expected that long term environmental fatigue performance will be a major consideration in their design. Fibre reinforced composites can provide the required hydrodynamic performance of tidal turbine blades and they are relatively low-cost and low-weight candidate materials for blade construction, however limited information is available to predict material properties and failure modes under coupled environmental conditions and oscillating loading. This study fills this gap by introducing a methodology for prediction of the fatigue behaviour of composite tidal turbine blades. The methodology combines: (a) a hydrodynamic model to calculate the distributions of tangential and axial forces on the blade; (b) a Finite Element structural model to predict the mechanical and fatigue behaviour of blade and (c) cyclic and quasi static tests at laboratory scale in sea water to generate realistic mechanical data for modelling. All tests have been performed in conjunction with the Digital Image Correlation technique in order to evaluate strain distribution and strain localization. Damage characterization and failure analysis based on this method was performed to identify damaged zones on the test coupon surface and to follow failure mode development during the fatigue life.

For simplicity, and regarding the typical loading on a tidal turbine blade, the three point bending fatigue test was selected from different types of standard tests to determine fatigue life and failure mechanisms of a FRP composite. A submerged fatigue test rig, capable of exerting cyclic loads of up to 15kN was designed and manufactured to enable fatigue tests to be carried out on multiple GFRP composite test coupons in sea water. The influence of the sea water environment on fatigue behaviour and failure mechanisms was characterized using failure analysis techniques such as Scanning Electron Microscopy and Energy-dispersive X-ray

spectroscopy. Microscopic techniques were used to reveal information about the multiple failure mechanisms on the specimen fracture surface.

The stiffness parameter was considered as an important index to monitor damage evolution during each fatigue test. Also for further verification of microscopic and DIC results, the X-ray Micro-computed tomography technique was used to characterize the internal damage and the geometry of flaws including delamination.

The Finite Element method was used to conduct stress analysis on composite test coupons and composite tidal turbine blades. This was done in order to interpret the experimental results and to examine the failure modes of the test specimens under static loads and also to predict failure of composite blades under both static and cyclic loads. Ply-by-ply stress analysis and the Tsai-Hill failure criterion were employed for the strength and failure prediction.

Fatigue properties of a GFRP composite in a form of strain-life diagrams showed that sea water can considerably reduce the fatigue life of GFRP composite and the main failure mechanisms associated with environmentally affected fatigue of GFRP composite are delamination, degraded fibre/matrix interface and fibre breakage. Furthermore, it was found that delamination and de-bonded fibre/matrix play an important part during the fatigue test, therefore using a composite resistant to delamination and de-bonding can significantly increase the life of composite components.

Finally, on the basis of experimentally generated fatigue data (Strain-Life diagram) and Finite Element structural analysis of blade, the fatigue life of the blade was estimated to be about between 4-5 years. This means that if replacing tidal turbine blades every 5 years is economically viable, this low cost composite (G10) can be a good candidate for tidal turbine systems.

NOMENCLATURE

A	Cross-sectional area
A_{ij}	Extensional stiffness matrix
B_{ij}	Bending-extensional coupling stiffness matrix
C_D	Drag coefficient
C_L	Lift coefficient
D_f	Maximum deflection at the centre of sample
D_{ij}	Bending stiffness matrix
D	Vertical deflection of loading roller
E	Young's modulus
E_{eff}	Effective flexural modulus of elasticity
E_f	Flexural modulus of elasticity
F	Force applied by the loading roller
F_A	Axial force
F_t	Tangential force
G	Shear Modulus
G_{ij}	Shear modulus
K	Plate curvature
L	Distance between two supports
M	Moment resultant
N	Resultant stress
P	Applied load in Iosipescu shear test
Q_{ij}	Plane stress reduced stiffness
R	Strain ratio
S_a	Stress amplitude
S_e	Equivalent fatigue strain
S_m	Mean Stress
S_u	Ultimate strength
T_g	Glass transition temperature
V_b	Rotational (tangential) velocity of a blade element

V_d	Axial velocity at the rotor disc
V_t	Net tangential velocity of fluid experienced by the blade element
V_T	Velocity of tidal currents
V_0	Free stream velocity of seawater current
W	Relative velocity experienced by the blade
a	Axial induction factors
b	Width
c	Chord length
h	Thickness
k	Slope of the tangent to the linear portion of the load-displacement curve
n	Number of counted cycles
r	Radius of local blade element
t	Time
w	Distance between two notches in Iosipescu shear test
z	Ply thickness
α	Angle between relative velocity and chord line
β	Pitch angle
γ	Shear Strain
γ_u	Maximum Allowable Shear Strain
δL	Lift force at each blade element
δD	Drag force at each blade element
ε	Normal Strain
ε_a	Strain Amplitude
ε_{cu}	Maximum Allowable Compressive Strain
ε_f	Failure strain
ε_m	Mean strain
ε_{max}	Maximum strain
ε_{tu}	Maximum Allowable Tensile Strain
ε_u	Ultimate strain
ε_V	Von Mises strain

ε^0	Mid-plane strain
ζ	Fraction of axial velocity remaining at the downstream exit of the stream tube
Θ	Angle between resultant relative velocity and the rotational plane of the rotor
ν	Poisson's Ratio
ρ	Density of seawater
σ	Normal Stress
σ_{cu}	Maximum Allowable Compressive Strength
σ_f	Flexural stress
σ_{tu}	Maximum Allowable Tensile Strength
σ_V	Equivalent Stress
σ_y	Yield Strength
τ	Shear Stress
τ_u	Maximum Allowable Shear Strength
ω	Angular velocity of blade
a'	Tangential induction factors
ΔS	Index of the irreversible composite degradation

Abbreviations

ACP	ANSYS Composite Pre-post
BEMT	Blade Element Momentum Theory
CFRP	Carbon Fibre Reinforced Polymer
C-GFRP	Carbon-Glass Fibre Reinforced Polymer
DIC	Digital Image Correlation
DOF	Degree of Freedom
DSC	Differential Scanning Calorimetry
DVC	Digital Volume Correlation
ESC	Environmental Stress Cracking
FEA	Finite Element Analysis
FRP	Fibre Reinforced polymer
GFRP	Glass Fibre Reinforced Polymer
KFRP	Kevlar Fibre Reinforced Polymer
MATLAB	Matrix Laboratory
NACA	National Advisory Committee for Aeronautics
RPM	Revolutions per minute
RTM	Resin Transfer Moulding
RVE	Representative Volume Element
SCC	Stress Corrosion Cracking
SEM /EDX	Scanning Electron Microscope/Energy Dispersive X-ray
S-N	Stress-Number of cycles
UD	Unidirectional
UFS	Ultimate Flexural Strength
UTS	Ultimate Tensile Strength
VARTM	Vacuum Assisted Resin Transfer Moulding
Ɛ-N	Strain-Number of cycles
µ-CT	Micro-Computed Tomography
3PBT	Three point bending test

List of Figures

List of Tables

Table of Contents

List of Publications

1. **H.I. Gonabadi**, A. Oila, S.J. Bull "Fatigue of Sandwich Composites in Air and Seawater" Journal of Bio and Tribo-Corrosion, June 2016

2. **H.I. Gonabadi**, A. Oila, S.J. Bull 'Wet Flexural Fatigue Behaviour of Tidal Turbine Blade Composite Materials' Proceeding of Wave and Tidal Energy conference, 11th EWTEC, Nantes, France- Sep 2015.

3. **H.I. Gonabadi**, A. Oila, S.J. Bull 'Flexural Characteristics of Tidal Turbine Blades Made of Composite Materials' Proceeding of Wave and Tidal Energy conference, 11th EWTEC, Nantes, France- Sep 2015.

4. **H.I. Gonabadi**, A. Oila, S.J. Bull "Comparative Study of Flexural Versus Tensile Behaviour of composite Materials Using Finite Element Analysis (ANSYS)".Paper presented at Composite Structure conference, ICCS18, Lisbon, Portugal, June 2015

Chapter 1
Introduction

1. Introduction

1.1 Background

Nowadays there is a great interest in extracting renewable energy from oceans using tidal and wave energy devices (Pelc and Fujita, 2002; Bahaj, 2011). These devices experience aggressive environmental conditions and complex loading due to tidal currents and waves. Therefore, in material selection and design, the interaction with sea water must be taken into account.

A typical tidal turbine is designed to operate without major interruptions for over 20 years (Davies *et al.*, 2013b) . Therefore tidal turbine manufacturers must consider the long-term behaviour of construction materials. Information and experience gained from the past in similar industries (e.g. wind turbine data) may serve as a guideline but data regarding tidal turbine applications are in considerable demand, in particular for Fibre Reinforced Polymer (FRP) composites manufactured by low-cost, large-volume processing methods such as vacuum assisted resin infusion.

Composite materials are extensively used in marine structures (Smith, 1990; Shenoi and Wellicome, 1993), and the influence of sea water on composite materials has been investigated for many years and is well understood (Springer, 1988; Weitsman, 1991; Martin, 2008). In comparison to conventional construction materials, FRP composites offer higher stiffness-to-weight and strength-to-weight ratios as well as the advantages of good corrosion and fatigue resistance, however, there is little information regarding composite behaviour under long term cyclic loading during sea water immersion.

Composites are ideal candidate materials for tidal turbine blades. It is, therefore, important to understand the performance and durability of such materials under harsh environmental conditions. A typical tidal turbine experiences approximately 5 million revolutions per year, consequently fatigue failure is a major consideration in the design of these blades.

One of the major challenges in the marine energy industry is the ability to predict fatigue failure of composite structures. Fatigue failure occurs in marine energy conversion devices, in particular tidal turbine blades are subjected to environmentally affected fatigue loads, and therefore the fatigue is a lifetime-limiting factor. Glass fibre reinforced epoxies are frequently used in the design of tidal turbine blades and the primary fatigue failure modes reported are delamination and fibre breakage (Kennedy *et al.*, 2012; Boisseau *et al.*, 2013; Davies *et al.*,

2013a). Although a gel-coat layer protects the GFRP surface, under certain circumstances, due to high static and cyclic loads the gel-coat can fail, leaving the GFRP material exposed to the sea water. Therefore it is important to understand the effect of sea water on the failure mechanisms of these materials.

Determining the resistance of reinforced polymer-based composites to a complex state of fluctuating stress is an important problem in many engineering applications. Composite materials show complex and multiple damage mechanisms. This is due to the presence of interfaces causing stress redistribution and also the anisotropy of stiffness and strength of FRP laminates. Unlike isotropic materials where the predominant failure mechanism is the beginning and growth of a single crack, fatigue failure in FRP composites is due to the general degradation throughout the specimen volume. Fatigue failure modes in FRP composites are resin cracking, interfacial de-bonding between fibres and polymer matrix, delamination and fibre breakage. The different damage mechanisms coupled with complex strain fields and non-linear behaviour of FRP composites significantly limit understanding of the true nature of fatigue failure of FRP composites.

It has been shown (Kotsikos *et al.*, 2000; Karbhari and Zhang, 2003; Cauich-Cupul *et al.*, 2011) that the degradation under humid conditions is a complex phenomenon as the harsh environment could cause degradation in mechanical properties of the composite (Miyano and Nakada, 2006) and fibre /matrix interface strength. Moisture lowers the composite fatigue life by affecting mechanical properties of the resin since moisture may act as a plasticizer (moisture reduces the glass transition temperature of the resin). Moisture may adversely affect the composite by dimensional changes or swelling. The most important feature of the response of composite materials in an environment such as sea water is the stress corrosion cracking mechanism (SCC), which leads to the unexpected (early) failure of composite materials exposed to a stress in an aggressive environment (Renaud and Greenwood, 2005).

The full field measurement method is a well-established experimental technique for the measurement of mechanical displacement and strain. The Digital Image Correlation (DIC) method has been employed in numerous investigations (Chu *et al.*, 1985; Sun *et al.*, 1997; Clocksin *et al.*, 2002; Zhang *et al.*, 2006; Godara and Raabe, 2007; Canal *et al.*, 2012; He *et al.*, 2012; Laurin *et al.*, 2012; Crupi *et al.*, 2013). In terms of failure analysis, inter-laminar shear and tensile properties of GFRP composites have been investigated using the DIC method to obtain full field strain maps that showed inhomogeneity of strain distribution and the areas

on the sample surface where delamination occurs (Chu *et al.*, 1985; Godara and Raabe, 2007; Brynk *et al.*, 2012; Canal *et al.*, 2012; He *et al.*, 2012; Laurin *et al.*, 2012; Crupi *et al.*, 2013). In general, the DIC method allows for accurate measurement of the surface displacements of the deforming materials, however little knowledge is available about DIC damage development analysis under environmentally assisted fatigue loads.

Investigations of the fatigue behaviour of GFRP composites generally focuses on the tensile and/or compressive configuration of the fatigue test, with less consideration being given to the fatigue behaviour under bending modes particularly when the composite material is subjected to fluctuating loads while immersed in sea water. Environmental affected fatigue performance of GFRP under bending loads is not sufficiently investigated.

1.2 Aims and objectives

The main aim of this work was to estimate the lifetime of tidal turbine blades manufactured from low cost composite materials. For this purpose, long term environmentally affected fatigue properties of woven GFRP composites is evaluated, so that the performance limiting issues can be understood and confidence can be acquired in the extensive use of GFRP for application in marine energy conversion devices.

The objective is obtained by developing a methodology to predict the fatigue life for composite tidal turbine blades. The method incorporates: (a) a hydrodynamic model to evaluate the distributions of cyclic loads on the blade which is due to the velocity fluctuations of tidal currents; (b) a Finite Element (FE) model to predict the mechanical and fatigue performance of the blade and (c) performing cyclic and quasi static mechanical tests at the material scale in both sea water and air environments to generate realistic mechanical data for modelling.

1. Mechanical properties of GFRP (Stress-strain response)
   In order to provide mechanical properties for Finite Element (FE) analysis of a GFRP composite turbine blade, quasi-static mechanical tests including Tensile, Iosipescu shear and Three Point bending (3PB) tests have been performed in conjunction with a full field strain measurement technique via a Digital Image Correlation (DIC) system. Therefore stress-strain curves in each of these mechanical tests were built on the basis of DIC strain maps. In addition DIC strain localization maps help to characterize and analyse failure mechanisms and therefore damaged zones can be identified on the test coupon surface. Experimentally generated strain fields by the DIC method were

compared with FE-calculated strain maps to verify the correctness of material properties for subsequent modelling.

2. Fatigue testing and Strain-Life curve

   In order to provide fatigue properties (i.e. Strain-Life diagrams) for fatigue life prediction of composite blade on the basis of FE analysis, a large number of coupons were subjected to 3PB fatigue load configuration at various constant displacements in both sea water and air. This is done by designing and manufacturing a 3PB fatigue test rig in order to approximate the blade performance and replicate the associated stresses and failure modes of composite tidal turbine blades.

3. Microscopic and Damage development analysis:

   During the fatigue testing of GFRP composite, DIC technique was also employed to determine the evolution of elastic modulus associated with fatigue damage. Modulus decay gives clear evidence about damage evolution and gradual deterioration of mechanical properties of composites during the fatigue test. A specific characteristic parameter is proposed for damage evaluation which is a function of the modulus decay parameter. Environmentally affected fatigue failure mechanisms of GFRP test coupons were characterized using different techniques. Initially, electron and light microscopes were used to identify the specific types of failure mode. Secondly, Energy Dispersive X-ray spectroscopy was used to reveal information about the degraded fibre-matrix interface region and lastly X-ray 3D micro-computed tomography was employed to identify and measure the geometry and dimensions of delamination.

4. Hydrodynamic analysis

   In order to define the boundary conditions and mode of loading for FE model of turbine blade, a hydrodynamic model based on BEMT was used and therefore the amount and distribution of fluid forces (i.e. tangential and axial) from tidal current velocities were predicted. Finally, the hydrodynamic loads predicted by this method were applied in an FE model of a tidal turbine blade for stress/strain analysis.

5. FE analysis

   By incorporating experimentally determined mechanical properties with FE model of turbine blade, structural analysis is performed for determining maximum stress/strain at the critical elements/hot spots of the blade.

6. Fatigue life prediction

   In the final stage, fatigue life of composite tidal turbine blade is predicted by FE strain/stress analysis and recording the cyclic strains that the blade experiences at the hot spot. This is obtained using Fatigue model (Miner damage rule) based on strain-life approach.

In this study in order to develop an FE model of either mechanical testing samples or a composite blade, micro-computed tomography (μ-CT) was initially used to obtain geometrical information about the internal microstructure of the GFRP composite. This includes the geometry and orientation of fibre bundles and thickness of each ply. The data for fabric structure (i.e. yarn specifications) can then be used for FE models of composite components.

1.3 Thesis structure

Chapter 2 looks at the overview of composite tidal turbine blades and marine experience of FRP composites. Both static and fatigue failure mechanisms and the effect of internal and external factors on fatigue behaviour of composites are discussed in detail. Much attention was paid to the effect of the sea water environment on individual properties of each constituent in FRP composites (i.e. fibres, matrix and fibre-matrix interface region). Characteristics of fatigue tests in FRP composites including the effect of frequency and stress concentrators are discussed. In addition, regarding the typical cyclic loadings on tidal turbine blades, causes of fatigue loads in tidal turbine blades are discussed briefly in this chapter. Moreover, microstructural aspects of damage mechanisms are assessed and typical failure modes and failure criteria in composite materials are explained. Finally manufacturing processes of composite wind/tidal turbine blades are explained briefly.

In the subsequent chapter, the process by which the project was carried out is explained in detail. Firstly, the method for performing all quasi-static mechanical testing and fatigue tests is explained. This includes conducting strain mapping in tensile, shear and three point bending fatigue tests via the Digital Image Correlation technique. Finally fundamentals of failure analysis techniques such as SEM/EDX, X-ray micro computed tomography and DIC are detailed thoroughly. These techniques were used for damage development analysis of GFRP composite test specimens for both static and fatigue tests. In this chapter a brief overview of constitutive equations that govern the load-deflection behaviour of laminated composite using composite laminate plate theory is discussed as well.

In chapter 4, the process through which the computer simulation was carried out is explained in detail (Finite Element Simulation and model generation). It includes using different modules in the Finite Element software (ANSYS code) to generate an FE model on the basis of fibre structures (ANSYS Composite Pre-post).

In chapter 5, a hydrodynamic model based on Blade Element Momentum (BEM) and stream tube momentum theory was developed using a MATLAB code. This was done in order to determine the magnitude of tangential and axial loads acting on the blade surface. Output from the hydrodynamic model was used in the FE model of a turbine blade for fatigue life assessment.

Chapter 6 discusses the results obtained from the quasi-static mechanical testing, in terms of experimental techniques. Effect of fibre orientation on bending, tensile and shear properties of GFRP material were investigated thoroughly. Light and electron microscopy techniques were used to determine failure modes under static mechanical testing of GFRP. The main input parameters for Finite Element analysis of the blade was obtained from these mechanical tests in terms of tensile and shear elastic modulus. In addition, mechanical tests including three point bending, tension and shear tests were simulated using ANSYS. This was done in order to interpret the stress distribution and failure modes on GFRP samples under mechanical testing.

In chapter 7, the Digital Image Correlation strain mapping technique was applied on a wide range of mechanical testing of GFRP sample. This was done in order to identify strain localization and strain distribution on samples during deformation. Results of FE simulations of the mechanical test (i.e. FE calculated strain fields) were compared with DIC/experimentally generated strain fields for GFRP composite samples with 0/90 fibre configuration.

Chapter 8 discusses the results obtained from fatigue testing. Initially damage evolution during fatigue test was explained through strain-life diagrams and multiple failure mechanisms were observed. Then the stiffness degradation method (by applying the DIC system) was used in order to analyse damage development during the fatigue testing of GFRP composite. In addition fatigue failure modes were analysed using characterization techniques.

In chapter 9, it is shown that a non-destructive technique (X-ray 3D micro-computed tomography) can be used to obtain information about the geometry and dimension of defects and microstructure of FRP composites. Therefore information about fibre orientation which is required for FE analysis of composite is obtained by this method.

In chapter 10, Finite Element results of tidal turbine blade are discussed. Evaluation of stress/strain distribution on the blade surface and identifying critical elements on the blade was the main objective of this chapter. ANSYS results show clearly the critical zones on the blade surface where potential damage can initiate. Finally ANSYS n Code Design Life is used in order to predict the fatigue life of turbine blade. In addition another approach for fatigue damage/life assessment of turbine blade is discussed in this chapter.

In chapter 11, the conclusions of the thesis and detailed discussion of the results are presented.

In chapter 12, potential future work and suggested further research are described.

Chapter 2

Literature Review

2 Literature Review

2.1 Ocean Energy

Nowadays due to environmental concerns and limited reserves of fossil fuels, there is a considerable investment in the exploitation of renewable energy sources. Oceans offer a renewable energy source which can be used to generate sustainable and predictable power. One form of this energy is the kinetic energy contained within the currents and tides.

Tidal energy is derived from the movement of the ocean tides and the associated kinetic energy can be converted into other forms of energy such as electricity. This kinetic energy is related to the energy of water motion. Tidal movement can generate electricity in areas where there is a considerable difference between low and high tides.

Tidal energy can be harnessed when the moving water rotates turbine blades similar to air movement in wind turbines. The rotating motion of the turbine blades can generate electricity. In tidal energy generators, turbines are anchored in tidal currents. A tidal current is a flowing body of sea water and a turbine is a device that extracts energy from a fluid flow (air or water). Since the density of water (1000 kg/m^3) is significantly higher than the density of air (1.225 kg/m^3), tidal turbines require shorter blades than wind turbines in order to convert the same amount of energy without serious deflection and damage.

In comparison to other sources of energy, tidal energy has many advantages, including:

- ✓ Renewable; predictable and sustainable resource.
- ✓ Pollution-free; tidal power creates no greenhouse gas emissions, no liquid or solid pollution.
- ✓ Efficiency; based on the state of maximum power output as per Betz limit (i.e. maximum hydrodynamic efficiency) approximately 60% of the kinetic energy of tidal power can be converted to electricity, however in coal and oil this efficiency is only about 30%.
- ✓ Using tidal energy the dependence upon fossil fuels is significantly reduced
- ✓ Tidal energy has little visual impact

There are also challenges in using this form of energy, which include;

- ✓ Devices used to extract tidal energy are in contact with seawater, consequently the cost of maintenance is high
- ✓ Harnessing tidal energy is expensive compared to wind energy
- ✓ Marine life can be affected
- ✓ Device failure; corrosion and storms can damage the equipment, therefore the cost of construction will be increased by design for higher durability.

In comparison to wind energy, tidal energy is more expensive. This is related to the corrosive sea water environment where tidal turbine blades operate. Also higher density of water compared to air (almost 800 times greater), results in higher flap-wise bending moment and therefore tidal turbine blades experience higher bending moment compared to wind turbine blades. As a result maintenance cost increases significantly.

Because tidal turbine blades are intended to operate in a harsh environment for at least 20 years, choosing an appropriate material as a blade is crucial. The blade in a tidal turbine is designed according to hydrodynamic science in order to extract the maximum energy from the tidal currents. In recent years blades of horizontal axis systems are made of composite materials. Composite materials have low weight and adequate stiffness and can provide good resistance to the sea water corrosion and cyclic loading.

A typical turbine blade in cross section is shown in Figure 2-1.

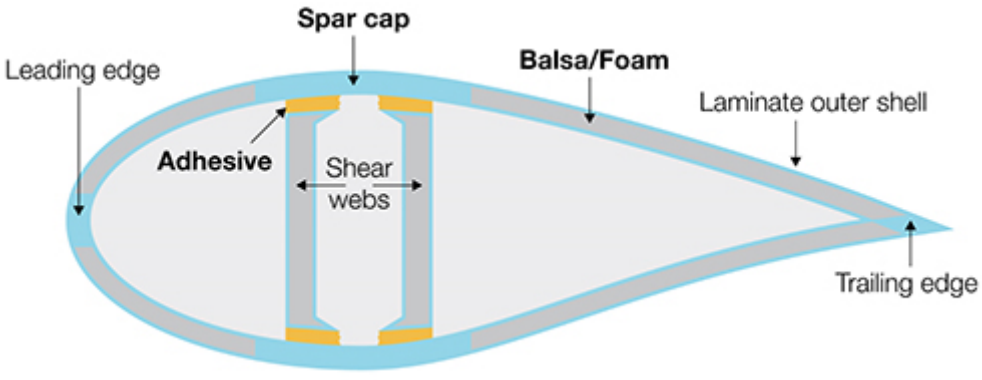

Figure 2-1. Cross section of a typical turbine blade (Lee *et al.*, 2012).

As shown in Figure 2-1 a typical turbine blade is composed of different components (i.e. skin, spar caps and shear webs). The materials used for fabrication of the skin, shear webs and spar caps of the blades are chosen according to the characteristics listed below.

- ✓ Stiffness
- ✓ Strength
- ✓ Corrosion and buckling resistance
- ✓ Shear modulus
- ✓ Water non permeability

According to the above evaluation criteria carbon fibre/epoxy, S-2 glass/epoxy and E-glass/epoxy could be suitable candidate materials for manufacturing the skin and the web. Considering the high strength and stiffness to weight ratio, good corrosion resistance, relatively long fatigue life and good wear resistance of composite materials, they are recommended for applications in the sea environment.

Tidal turbine blades are susceptible to fatigue and the design of their blades are dictated by fatigue concerns. Marine turbine blades are subjected to the corrosion-fatigue phenomenon due to several factors summarized as below (Khan *et al.*, 2009; Davies *et al.*, 2013b);

- Unpredictability in the loading spectra due to the origin of tidal currents and waves
- Continuous operation under an aggressive environment such as sea water
- Velocity fluctuation of tidal currents. During the each day, there are two high and two low tides. As a result, during each movement of tide, velocity of tidal current slowly increases and decreases. This velocity fluctuation is transformed to the loading fluctuation on the blade (time-series of axial and tangential loading). Therefore the blade experiences cyclic stress/strain which is the main cause of fatigue failure. In addition, as the tidal turbine blades are exposed to the corrosive sea water environment, a mechanism similar to the stress-corrosion usually affects the durability and fatigue life of the blades.
- Relatively long and bendable structures. (Although the long and bendable structures of tidal turbine blades are susceptible to fatigue, it must be noted in comparison with wind turbine blades where the length of blade is up to 85 meters, the length of tidal turbine blade rarely exceeds 12 meters, and therefore they are much shorter than wind turbine blades. Also wind turbine blade, are more bendable compared with tidal turbine blade)

A tidal turbine blade is expected to operate for approximately 20-25 years. The aforementioned reasons and the relatively long expected lifetime impose design limitations for tidal turbines that fall into either extreme load or fatigue classifications. For the case of extreme load design, the maximum load level that the tidal turbine structure has to withstand is difficult to predict.

Generally tidal turbine blades are subjected to bending loads and flexural cyclic loads from sea water currents. Currently very limited information is available regarding flexural fatigue performance of composite materials in sea water, consequently conducting flexural fatigue tests in the environment of sea water on specimens of composite which potentially can be used for tidal turbine blades can substantially contribute to identify future problems in the marine current turbine industry.

2.2 Tidal Energy

In tidal turbines the kinetic energy of the tidal currents is converted into electricity via a rotor. In terms of design, the lifetime of tidal turbine is 20 years (Harper and Hallett, 2015) but there is greater motivation for low repair requirements due to the corrosive seawater in which they work and the cost and difficulty of access for repair.

A typical structure of tidal turbine is shown in Figure 2-2(a). The blade consists of a spar caps and shear webs, surrounded by a shell profile (Figure 2-2(b)). Figure 2-2(c) shows composite ply drops and typical failure mode.

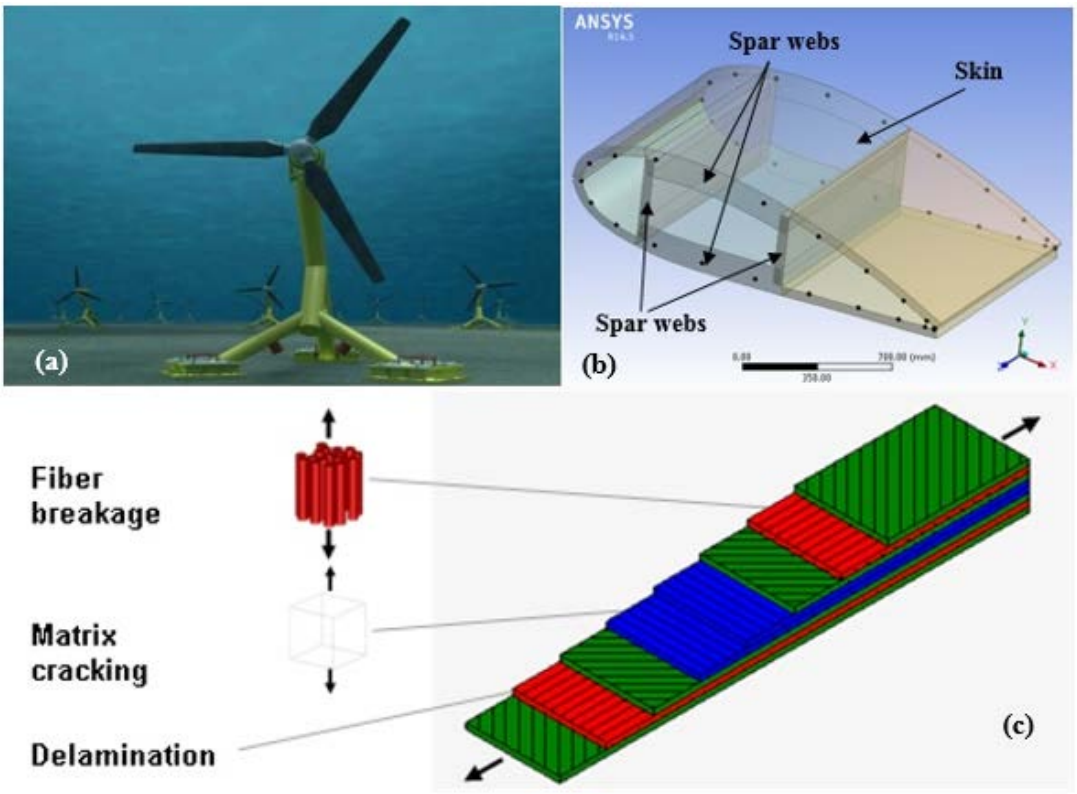

Figure 2-2. (a) Typical structure of marine turbine, (b) cross-section of blade showing shear webs and spar caps, (c) composite ply drop and potential failure modes (Harper and Hallett, 2015).

2.3 Materials Evaluation Criteria for Tidal Turbine Blades

The most important evaluation criteria for selecting appropriate material for tidal turbine blades are:

- Corrosion and fatigue resistance
- Flexural stiffness and strength
- Shear modulus and strength
- Water im-permeability
- Buckling resistance

One of the main benefits of using FRP composite materials for turbine blades is the ability to reinforce the blade structures in highly stressed directions by selecting suitable fibre orientations and positioning. The structural properties of FRP composite materials are dependent on the fibre orientation, fibre/polymer volume fraction, stacking sequences, fibre/polymer types and fibre/matrix interface. From the materials analysed according to above

criteria Carbon and Glass fibre epoxy resin are suitable materials to use for fabrication of tidal turbine blades.

2.4 Material Selection

Recently there is great curiosity in capturing energy from the ocean environments using tidal turbine blades (Bahaj, 2011). These devices are subjected to harsh environments and hydrodynamic loading due to the tidal currents, and interactions with seawater must be reflected during material selection and designing process. Fibre reinforced polymer composite materials have been used in tidal turbine blades and effect of aging on quasi-static and cyclic behaviour has been well documented (Kong *et al.*, 2006; Kennedy *et al.*, 2011; Boisseau *et al.*, 2012; Kennedy *et al.*, 2012; Boisseau *et al.*, 2013).

In order to guarantee the long term durability of FRP composites used for tidal turbine structures four conditions must be fulfilled. First, the reinforcements (fibres and sizings) must be selected properly. Second, an appropriate matrix resin system must be chosen. Third, the engineering manufacturing process and quality must be suited to the application. Finally, the structure must be considered and designed to resist the loading conditions. These conditions are mutually dependent, but the designer can use a large available database to help in developing a consistent FRP composite structure.

2.4.1 Fibres and Sizing

There is a wide range of fibres available. For cost reasons it is usual to examine Glass fibres, however, Carbon fibres can be suitable if higher stiffness is required. Usually carbon fibre spars are used in stiffening glass composite turbine blades (Fraenkel, 2006), but the glass composite envelope can resist long term loading in a marine environment.

Table 2-1. Fibre properties ('CES EduPack 2017,').

Types of Fibres	**Density (kg/m^3)**	**Tensile modulus (GPa)**	**Tensile strength (MPa)**
E-glass	2.56	72-85	1950-2050
S-glass	2.5	86-93	4700-4800
Advantex	2.62	80-84	2200-2600
Hiper-Tex	2.55	89-91	3000-3400
Carbon high modulus	1.8-1.85	370-390	2400
Carbon high strength	1.8-1.84	225-245	4500-4800

Table 2-2. Mechanical and fatigue properties of epoxy resin based composites, fibre weight fraction: 60% ('CES EduPack 2017,').

Types of fibre	Stacking sequence	Young's modulus	Tensile Strength	Fatigue strength at 10^7 cycles
GFRP (E-glass)	Unidirectional prepreg UD lay up	45GPa	1100MPa	400MPa
CFRP	Unidirectional prepreg UD lay up	120GPa	1700 MPa	950MPa

In addition to their basic mechanical properties (Table 2-1) the durability of glass fibres in a wet environment varies considerably. The standard E-glass fibres are sensitive to water due to the existence of boron in their chemical composition. Prolonged exposure to water environment in combination with mechanical stresses results in a stress corrosion phenomenon and early failure due to the crack development at the fibre surface (Charles, 1958a; Renaud and Greenwood, 2005). Therefore, the Advantex and HiPer-tex glass fibre types are to be favored for ocean energy applications, as they are boron free.

In comparison with GFRP, CFRP has superior fatigue performance. This is due to the higher modulus of carbon fibres compared with glass (Table 2-1). In general, CFRP exhibits a flatter S-N curve than GFRP and therefore they can execute longer fatigue life at a certain level of stress/strain (Table 2-2). This is also due to the less constraining effect of glass fibres in straining of the matrix. The use of stiff carbon fibres limits the strain in the composite and therefore prevents large deformation in the matrix.

Fibre stiffness is the most important factor in determining fatigue properties. Generally, composites containing fibres with low modulus have a steeper S-N curve than those containing fibres with high modulus. From the early 1970's, a large number of investigations into the fatigue behaviour of carbon fibre-reinforced polyester and epoxy matrix composites were carried out by Owen et al (Owen, 1974), Curtis et al (Curtis and Dorey, 1986; Curtis, 1987), Harris et al (Beaumont and Harris, 1971), Dharan (Dharan, 1975) and other groups (Favre and Vidal, 1983; Lorenzo and Hahn, 1986). It was found that high modulus carbon fibre composites exhibited a superior fatigue performance, better than that of E-glass and S-glass reinforced composites. Curtis and Dorey (Curtis and Dorey, 1986) Jones et al (Jones *et al.*, 1984b) studied

KFRP composites and found that they had a fatigue behaviour intermediate between carbon and glass fibre composites.

2.4.2 Matrix Resin System

For most marine applications the resin choice is between polyesters, vinyl esters and epoxies. The former are cheaper but they are sensitive to hydrolysis when they are in direct contact with a sea water environment over long periods. A preliminary investigations about in-plane shear properties of these four matrix systems with the same E-glass fibres showed that significant changes in composite properties were noted after 18 months in seawater, particularly for the polyester resins (Gellert and Turley, 1999).

2.4.3 Manufacturing and Quality

It is attractive to use wind turbine blades as a model for tidal turbines. Wind turbine blades can be made in lengths up to 85 meters, and the resin infusion process has become the most widespread manufacturing method. This provides high fibre content and is well-suited to manufacture of long wind blades. However, the higher density of seawater compared to air means that tidal turbines need to be shorter, the prototypes being tested at present are about 11 meters long, so other manufacturing methods may be more popular. The choice of manufacturing technique necessitates a careful analysis of the economics of the process, particularly mold costs and production time.

2.5 Marine Experience of Composites

In recent years many industrial fields including marine equipment have employed composite materials for load bearing components. In the ocean environment, composite materials are a good candidate for structures given their high specific strength and stiffness, good corrosion, wear and fatigue resistance, and environmental stability. However structural optimization needs to be considered; for example, the number of plies of a certain material, laminate orientation and consequently the design can be customized. For designing turbine blades with composite materials a reliable data base of material properties and static structural analysis, simulation and modelling techniques are required. The multiple potential stacking sequences and ply orientation make the design of composite structures complex. For example in anisotropic materials there are 21 independent elastic constants in the stress-strain relationship, in orthotropic materials, there are nine independent elastic constants in the stiffness matrix and there are five independent elastic constants for transversely isotropic materials, however, for

isotropic materials just two independent elastic constants are needed. Fibre-reinforced composites, in general, contain the three orthogonal planes of material property symmetry and are classified as orthotropic materials. In an anisotropic material, a combination of extensional and shear deformation is produced by a normal stress acting in any direction. This phenomenon of creating both extensional and shear deformations by the application of either normal or shear stresses is termed as extension-shear coupling and is not observed in isotropic materials.

The mechanical properties of FRP composites depend on the fibre orientation, polymer type and fibre/polymer volume fraction. Using fibre reinforced composite materials enables engineers to align the stiff fibres with the main loading axis and consequently use the composite to its optimum advantage. In some situations such as marine energy conversion devices where the loading and pressure acting on blades are complicated and multi-directional in nature, cross woven glass fibre reinforced laminates can be required.

The high reliability and durability required for tidal turbine systems to be economical makes composite materials a normal choice in terms of corrosion and fatigue resistance. The latter is important to reduce installation costs, and simplify repair if needed. However, the consequences of the marine environment combined with cyclic load for design have not been fully investigated (Davies *et al.*, 2013b).

2.6 Fatigue of Fibre Reinforced Composite Materials

Extensive use of composites in weight critical applications is due to their high specific strength and stiffness. Examples of engineering applications where composite materials are commonly used are in the areas of aerospace, automotive and marine. Composite components in many of these applications are subjected to the cyclic loading and therefore fatigue is a major consideration in composite components. This means that cyclic loads of a magnitude less than the ultimate strength of the composite materials can cause fatigue failure in composite structures. Indeed determining the resistance of reinforced polymer-based composites to the state of cyclic stress is a major factor in their engineering applications. However, current knowledge on fatigue behaviour and fatigue life prediction of FRP composite materials is still developing.

The basic tactic to assess fatigue is to establish curves of stress or strain versus the number of cycles to failure. These curves are recognized as S-N curves.

The fatigue behaviour of composites in an air environment is generally good, the wind energy industry has performed a large number of investigations to prove this, but few published data

are available from tests in a seawater environment. The standard E-glass fibres are known to be susceptible to stress corrosion in aqueous environments under sustained loading but improved fibres are now available to limit this phenomenon.

Boller (KH, 1970) followed by Owen (Owen and Howe, 1972) and his collaborators were laying down the foundations that explain the fatigue behaviour of fibre reinforced composites almost fifty years ago. Much of this work was focused on the phenomenological effects of fatigue. Researchers such as Reifsnider and Talreja (Talreja, 1981a; Reifsnider and Gao, 1991) are associated with developments in the field of microstructural aspects of damage mechanisms of FRP composites responsible for failure under fluctuating loads.

In order to investigate effectively the fatigue characteristics of glass fibre reinforced polymer blades, this section provides a brief review of the relevant literature. The review covers mainly the fatigue of composite materials and structures, including FRP composite structures. Only the most common reinforcing fibres i.e. glass, carbon and Kevlar incorporated in epoxy resin matrices are discussed. More extensive and detailed reviews of this subject have been carried out by Konur and Matthews (Konur and Matthews, 1989) and Curtis (Curtis, 1989).

Initially, the fatigue characteristics of general composite materials are discussed. This includes fatigue mechanisms and the effect of various material, structural and loading parameters. First of all, some basic concepts of fatigue are described.

2.6.1 Basic Concepts of Fatigue in FRP laminates

Fatigue is a gradual process which causes damage in structures under cyclic loads of a magnitude less than the ultimate strength of the constituent materials (Benham *et al.*, 1996). The accumulated damage may lead to a gradual and substantial reduction in mechanical properties such as strength and stiffness leading to crack growth and finally total failure. The speed of the fatigue process is regulated by the magnitude of the cyclic loads or displacement cycles, usually defined as the stress or strain range. The main concepts associated with fatigue are fatigue life, fatigue strength and fatigue limit.

- ✓ Fatigue life is the total number of cycles of a given stress or strain range which can be withstood by the component before fatigue failure occurs. Fatigue failure can be defined either as total collapse or as a given reduction of strength or stiffness (Dowling, 2012).
- ✓ Fatigue strength is the maximum cyclic stress range that a material or structure can tolerate for a certain fatigue life (Dowling, 2012).

- ✓ Fatigue limit is the maximum cyclic stress that can be resisted indefinitely without failure (Dowling, 2012).

The most important part in fatigue analysis is the relationship between fatigue stresses/strains and the number of cycles that material or structure can survive before it fails (Benham *et al.*, 1996). The relationship between the fatigue strength and the fatigue life is most commonly presented in the form of Stress-Life (S-N curves) for constant amplitude loading and Strain-Life diagrams for a constant amplitude deflection, as shown in Figure 2-3 (Reifsnider, 2012). The abscissa represents the number of cycles N, and is normally presented on a logarithmic scale. The ordinate represents the fatigue strength and may be plotted on a logarithmic or a linear scale. The fatigue strength is usually presented in the form of a stress range. However, sometimes the fatigue strength is represented by the load amplitude or even by the maximum of the load cycle (Hertzberg *et al.*, 1996).

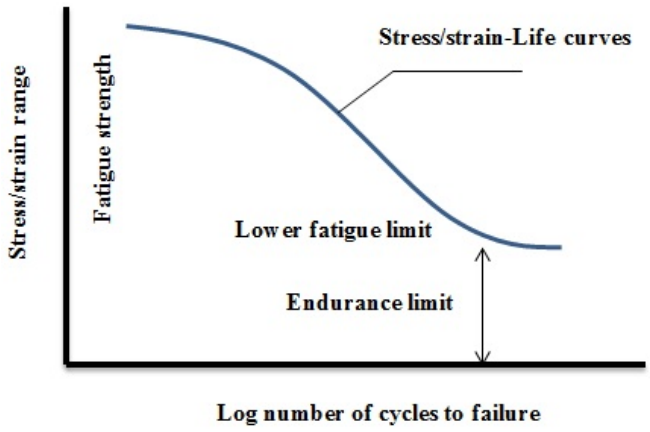

Figure 2-3. Fatigue life curve (Reifsnider, 2012).

A simplistic definition of fatigue phenomenon is that the load-bearing capacity of materials under a fluctuating loading condition falls with time and this leads to failure at stress level much below the normal strength of that material (Benham *et al.*, 1996). The mechanisms by which this degradation occurs in FRP composites are entirely different from the fatigue failure mechanisms of metals (Stephens *et al.*, 2000). The challenge for design engineers is to select the suitable material for a particular structural application so as to prevent failure of material within the design lifetime. Therefore it is important to know the fatigue failure mechanisms to be able to envisage the life of a given composite structure under specific design conditions (Reifsnider and Jamison, 1982; Schaff and Davidson, 1997).

Composite materials show complex and multiple damage mechanisms. This is due to the presence of interfaces causing stress redistribution and also anisotropic characteristics in mechanical stiffness and strength of FRP laminates (Dharan, 1975) . Fatigue failure in FRP composites is due to general degradation throughout the specimen volume. Basically fatigue failure modes in FRP composites are matrix cracking, interfacial de-bonding between fibre and matrix, delamination and fibre breakage (Lorenzo and Hahn, 1986). The different damage mechanisms coupled with complex strain fields and non-linear behaviour of FRP composites significantly limit prediction of the true nature of fatigue failure of FRP materials.

Many aspects of fatigue behaviour of FRP, such as the effects of frequency, moisture, defects, heat, etc. have been studied (Jones *et al.*, 1984b; Demchik *et al.*, 1973; Curtis and Moore, 1983; Talreja, 1980). Due to many variables such as fibre orientation, stacking sequences, etc., different possibilities are available for the impact of the above factors on composites, which makes each composite behave differently in practice (Hinton *et al.*, 2004).

In the literature extensive investigations have been performed to establish suitable failure criteria for the fatigue failure of FRP composites. In order to define fatigue failure criteria, degradation of stiffness or strength during the fatigue tests can be considered (Hinton *et al.*, 2004). Therefore constant strain amplitude cycling until a given strength degradation and stiffness degradation is achieved are two methodologies for determining the fatigue lives of FRP composites (Hwang and Han, 1986). Depending on the design requirements, each of these approaches can be adopted. Generally stiffness degradation is a suitable failure criterion for many components which incorporate FRP composite laminates (Ellyin and El-Kadi, 1990). Variation in stiffness which can be easily measured and interpreted is a good index of damage development during fatigue. Indeed there is a direct relation between stiffness degradation and microscopic damage in FRP composites (Hahn, 1979; Hashin, 1980; Hinton *et al.*, 2004).

Regarding constant strain amplitude cycling until a given stiffness reduction, the deterioration rate is associated with the stress within the composite coupon. Initially a high stress level is needed to deflect the test coupon. As the cyclic loading continues, a lower stress level is required for deflection corresponding to the stiffness reduction of the composite sample. The reduced stress within the specimen means that the degradation rate decreases. Therefore in the process of damage evolution in a constant strain amplitude fatigue test, at the beginning of life (first stage), damage initiation and propagation start causing a drop in the composite stiffness properties; in the second stage a gradual material degradation is observed and finally the third

stage follows with a catastrophic reduction of material properties and a huge loss in stiffness in the damaged zones is predicted (Shokrieh and Lessard, 1997; Giancane *et al.*, 2010a).

The mechanisms of fatigue failure in fibre reinforced composites are entirely different from those which are responsible for fatigue occurrences in metals. Fatigue in metals occurs by the initiation of an individual crack, which grows until disastrous failure occurs. Cracks are initiated by localised plastic deformation, as a result of dislocation movement. Surface defects may be created during fluctuating loads or deformation, as, for example the formation of intrusions and extrusions or PSBs (persistent slip bands) in metals (Forrest, 2013). But in fibre reinforced composites, there are several different damage accumulation mechanisms as was discussed previously. These failure mechanisms can occur interactively or autonomously depending on the material properties and testing conditions (Harris, 1977).

Generally the fatigue life of polymer composite materials is affected by a number of external and internal variables as depicted in Figure 2-4.

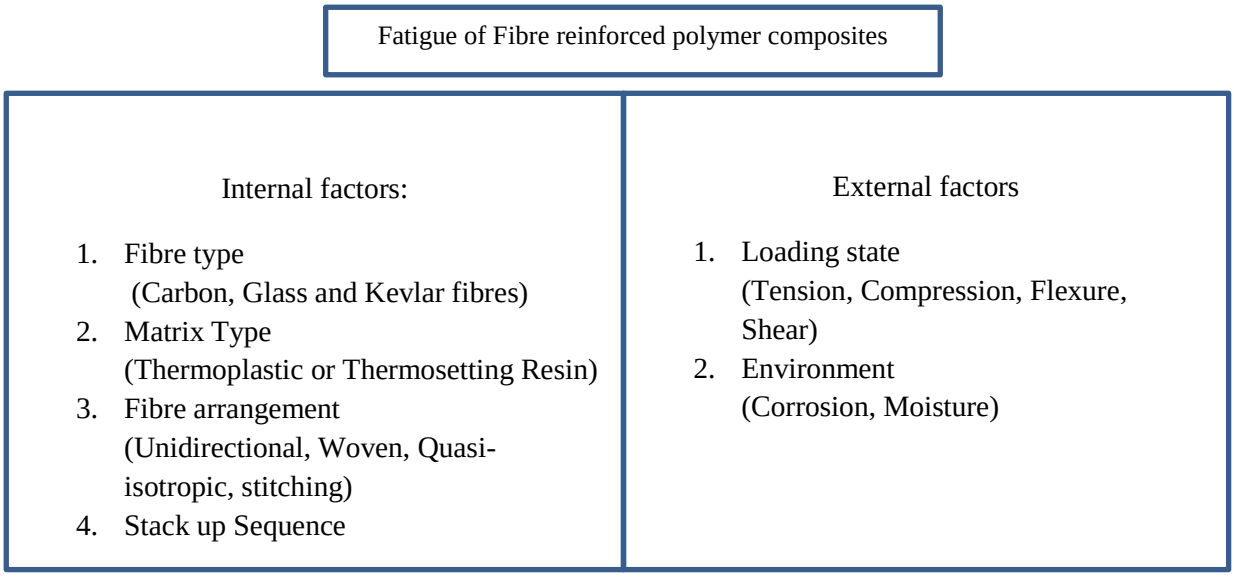

Figure 2-4. Factors influencing the fatigue properties of FRP composites.

2.6.2 Effect of Fibre

- ***Effect of fibre type***

As the key load carrying member in laminated composites, the type of fibre used will influence the composite fatigue performance. From investigation of the S-N curves of three common fibre reinforced composites, Carbon, Glass and Kevlar fibres with the same thermoplastic matrix, it has been shown that the S-N curve of GFRP shows a more substantial drop in its

fatigue strength than that of CFRP (Wicaksono and Chai, 2013). This is due to the less constraining effect of glass fibres in straining of the matrix. The use of stiff carbon fibres confines the strain in the composite and therefore prevents large deformation in the matrix (Figure 2-5) (Curtis, 1989).

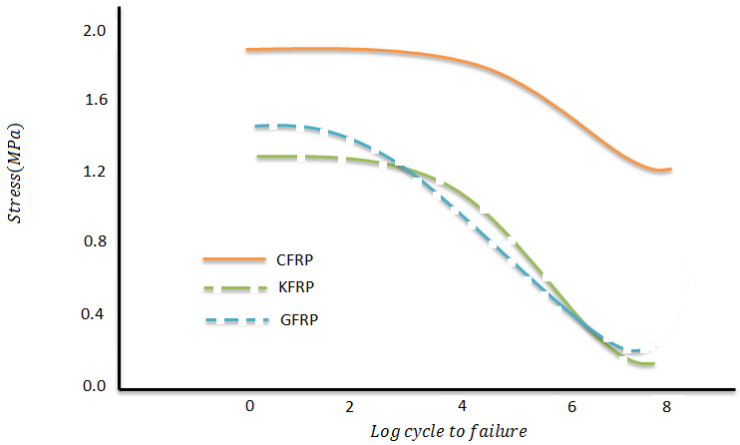

Figure 2-5. Representative S-N fatigue curves for FRP composite materials (Reifsnider, 2012).

Fibre stiffness and failure strain are the most important factors in determining fatigue properties. Generally, composites having fibres with low modulus have a steeper S-N curve than those having fibres with high modulus. From tests by various investigators it is suggested that a ranking of fibre materials from best to worst would be (Konur and Matthews, 1989; Scholte, 1994b):

- High modulus carbon fibre
- High strength and low modulus carbon
- Aramid/carbon hybrid
- Aramid
- Glass/aramid hybrid
- S-glass
- E-glass

- ***Effect of Fibre Fraction***

The effect of fibre fraction on the longitudinal and transverse properties of composites can be described by the rule of mixtures. This states that a composite property is equal to the volume fraction weighted-average of the contributions from the fibre and matrix: The longitudinal and transverse modulus of composite materials can be calculated by the rule of mixtures (Christensen, 2012). Experimental results (Tanimoto and Amijima, 1975) confirm that an

increase in fibre content results in an improvement of fatigue properties in GFRP laminates. The matrix properties are used to estimate the transverse and shear properties of the composite.

- ***Effect of Anisotropy***

For FRP composite specimens with fibres aligned at a specific angle to the main loading axis, the fatigue properties are found to decrease as the fibre orientation angle increases. Specimens with an aligned angle of 0° (when the fibres are oriented in a longitudinal direction with respect to main loading axis) provide the highest fatigue strength and other properties in the load direction, whereas an angle of 90° (when the fibres are oriented in a transverse direction with respect to the main loading axis) gives the lowest fatigue properties.

- ***Effect of Fibre Length***

Short fibre reinforced composites have much lower fatigue strengths than those reinforced with long fibres. GFRP containing short fibres (0.25 mm) has approximately 30% of the ultimate strength of continuous GFRP. The reason for this is that in short fibre composites the load must be transferred from one fibre to another by the matrix between them. This results in a higher induced stress in the polymer matrix and an increased shear stress at the fibre/matrix interface of the composite with short fibres.

- ***Effect of Fibre Arrangement***

Many experiments have been performed to study the effect of fibre configuration and fabric on mechanical properties of FRP composites (Boller, 1964; Curtis, 1989; Bernasconi *et al.*, 2007; Godara and Raabe, 2007; Mortazavian and Fatemi, 2015). Fibre configurations and construction play a pivotal role in fatigue properties of composites. Generally, the more fibres are aligned with the main loading axis, the higher fatigue strengths for a given number of cycles and therefore the S-N curves are flatter. The fatigue properties of an FRP composite decreases in the following order:

  - Laminates with UD reinforcement in the loading direction,
  - Non-woven reinforcement,
  - Woven fabrics
  - Random short fibre mats (Greene, 1999).

This ordering can be explained by the discrepancies in the fraction of reinforcements orientated parallel to the loading direction. Other factors which affect the stiffness of the laminate and thus the fatigue performance are the continuity of the fibres and the amount of stretching. Unidirectional fibres are continuous and capable of relatively good stretching, resulting in higher stiffness. The same applies for the non-woven fabrics, although not all fibres are oriented parallel to the loading direction, resulting in a smaller load carrying fibre-volume fraction and thus a lower fatigue strength.

Woven composites have important advantages in handling and fabrication compared with non-woven materials. However, their mechanical properties, in particular fatigue strength (Curtis, 1989), is poorer than the equivalent non-woven material, not only because of the distortion of the fibres, but also because of the difficulties associated with obtaining high fibre volume fractions in woven composites.

2.6.3 Effect of Fibre/Matrix Interface

An "interface" exists from some areas in the reinforcement where the local properties start to change from the fibre's bulk properties, through the boundary into the matrix. Interface thickness varies from a few hundred of nano-meters (nm) to a few micro-meters (μm). The fatigue damage process in composites starts with the onset of de-bonding between fibres and matrix. Differences between the elastic properties of fibres and matrix in FRP laminates must be offset by the interface. Indeed forces and stresses applying on the matrix can only be transferred to the reinforcement through the interface, therefore the characteristics of the fibre-matrix interface have a significant effect on the mechanical properties of composite materials (Shih and Ebert, 1987).

Depending on the selected coupling agent, the bond strength of the matrix to fibres may increase by a factor of 4 or 5 (Dew-Hughes and Way, 1973). It can be expected that this will also affect the fatigue life at both high and low cycles. The effect of the interface on fatigue performance of fibre reinforced composites has been studied by Shih and Ebert (Shih and Ebert, 1987), Harris (Harris, 1977) and other researchers. Depending on the bonding strength of the fibre/matrix interface and the fibre orientation, the interface has an appreciable effect on crack initiation and crack propagation. On one hand, as a stress concentration site, the fibre/matrix interface can cause crack initiation and thus considerably reduce the fatigue life of the composite. On the other hand, the presence of interfaces may decelerate the crack propagation rate by effectively obstructing and shifting the orientation of the crack propagation path.

Furthermore, the energy required for crack propagation can be consumed by friction developed between the fibre and the matrix.

Failure mechanisms such as de-bonding and fibre pull out from the matrix during the process of crack propagation play an important role on the mechanical properties of the interface. As a result of these failure modes, composites with weak interfaces tend to have a low stiffness and strength performance but are resistant to fracture (ductile material), however, composite materials with strong interfaces demonstrate high stiffness and strength but are brittle (Hull, 1981)

2.6.4 Effect of Manufacturing Process

During the process of composite production, hardening and curing affect the properties of fibres, matrix and interface. Entrapped air bubbles in the composite which are not removed during the manufacturing process can lead to void formation in the cured composite and may result in a fatigue strength reduction factor of up to 1.5 for the onset of matrix cracking (Owen and Griffiths, 1978). The laminating process determines matrix distribution, reinforcement saturation and thus fatigue strength may be locally or globally affected by inhomogeneous matrix distribution and poorly impregnated fibres.

2.6.5 Types of Matrix

In a typical composite material, the matrix plays an important role to transfer the load to the fibres and it is also considered as a protection for the reinforcement against the harsh environment. It has been shown that the fatigue behaviour of fibre reinforced composites is strongly contingent upon the properties of the matrix (KH, 1970; Owen and Howe, 1972), however some believe that the fatigue behaviour of composites using various matrix systems is not very different, the major effect is in the different reinforcement configuration (Harper, 2000).

The early work on the impact of matrix properties on the fatigue performance of polymer based composites was conducted out by Boller (Boller, 1964) and Davis et al (Davis *et al.*, 1964). They investigated the comparative fatigue behaviour of laminates of epoxy, silicone, polyester and phenolic matrices reinforced with E-glass fabric, and concluded that the epoxy matrix composites exhibited the best results (Figure 2-6). Further investigations have been subsequently carried out by Harris (Mandell *et al.*, 1980), Curtis (Curtis, 1987), Newaz (Newaz, 1985) and other groups.

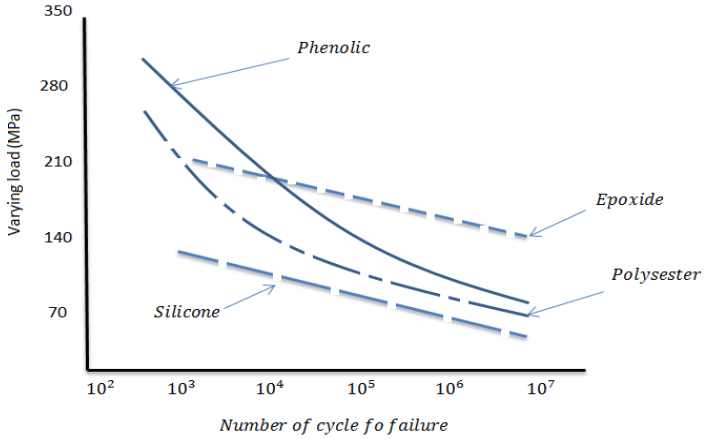

Figure 2-6. S-N data points (plots) for E-glass fibre composites with different polymeric matrices (Sauer and Richardson, 1980).

In terms of toughness and ductility, there are lots of advantages in using thermoplastic resins instead of thermosetting resins in FRP composites, due to the substantially longer fatigue life of thermoplastic resins (Bathias, 1991; Caprino and D'Amore, 1998; Bureau and Denault, 2000). Increased fatigue resistance of a tougher resin against the delamination failure mode is due to higher inter-laminar fracture toughness. The fibre/matrix interface in fibre reinforced composites has a direct impact on fracture toughness of these composites as well (Zhuang, 1995; Hojo *et al.*, 2006).

The resins most commonly used as matrices for GFRP are polyester, epoxy and vinyl ester resins. The fatigue performance of epoxy resins is slightly superior to polyester, vinyl ester, phenolic and silicone resins particularly at low stress level. The better performance of epoxy resins is associated with their higher strength, better bonding to fibres, and high strain without cracking (Thompson, July 1957). From bending fatigue tests of polyester and vinyl ester resins (Burrell *et al.*, 1986) it was concluded that vinyl ester type resins had a substantially better fatigue performance than polyester resin. Isophthalic polyester was found to be somewhat better than orthophthalic polyester resin whereas little difference was observed between the standard vinyl ester and pre-accelerated thixotropic vinyl esters. In spite of great chemical discrepancy, the effect of the resin on the fatigue strength of FRP is rather small when compared with the effect of the different reinforcements (Scholte, 1994b).

Usually Fatigue damage in the form of cracking occurs in the matrix region. Generally in composite materials due to differences in Poisson's ratio of fibres and matrix, there is always a possibility of matrix cracking or de-bonding.

2.6.6 Effect of Loading Type

- ***Mean stress***

Information on fatigue in the form of stress/strain-life diagram does not show clearly the influence of the mean stress on the fatigue performance. However, in design, this information may be crucial, in which case further Stress/life diagrams for different mean stresses are required. From these diagrams it is possible to produce a master diagram in which the stress amplitude is plotted versus to the mean stress. Using a linear relationship between the stress amplitude (S_a), the mean stress (S_m), the fatigue strength (S_e) at zero mean stress for a given life and the ultimate strength (S_u) of the material, an approximation of the diagram can be constructed as below:

$$\frac{S_a}{S_e} = 1 - \frac{S_m}{S_u} \qquad \textbf{2-1}$$

This equation is known as the Goodman law and is applicable to many materials including metals and alloys. Regarding FRP composites, the use of rupture strength for the time corresponding to the endurance limit may be preferred to the ultimate strength.

- ***Effect of Tensile and Compressive Loading***

Under compressive types of loading, the fibre buckling strength and shear strength of the fibre/matrix interface dominate the fatigue performance of FRP composites. As the principal load bearing elements, fibres supported by the matrix and the interface become locally unstable and undergo a micro-buckling (Purslow, 1981) therefore, the integrity of the matrix and the interface is more critical in a compressive fatigue test than in tension. Damage development in the matrix and fibre/matrix interface occurs for the same reasons as in tensile fatigue test, however due to greater demands on the matrix and the interface, compressive fatigue loading has a higher impact on the strength of composite materials than tensile loading (Rosenfeld and Gause, 1981). Generally, not too much information exists on the compressive fatigue of composites, as the compressive testing of these materials introduces many problems. These include the need to support the specimens from undergoing micro-buckling, and the limitations imposed on the sample geometry by the anisotropic nature of the materials.

Reversed axial fatigue, or tension - compression loading has a very adverse impact on fatigue behaviour compared to zero-compression or zero-tension loading. The poorer properties of composite materials in reversed axial fatigue loading compared with tensile or compressive loading is associated with the inter-ply damage development in the laminate plies with the absence of fibres in the test loading direction.

2.6.7 Environmental Conditions

In order to study the effect of environment on the fatigue performance of FRP composites, the sensitivity of the composite to the matrix and fibre/matrix interfacial properties needs to be considered, as the absorbed moisture usually affects the matrix or fibre/matrix interface properties. For example for some carbon and glass fibre laminates with a strong fibre/matrix interface properties moisture content has little effect on fatigue performance (Curtis and Moore, 1983). Moreover, loading modes such as compression or shear, which apply substantial stresses in the matrix, can cause degradation in properties when coupled with environmental exposure. The fatigue life of components in offshore structures may be substantially reduced because of harsh environmental conditions. This is due to the fact that the surrounding medium (sea water) can penetrate into the laminated composite along the cracks and de-bonded fibres. In this respect degradation of fatigue properties is considerable at high stress level, however it is negligible at low amplitude (Demchik *et al.*, 1973).

It is worth noting that under a random fatigue loading distribution, penetration of sea water into the cracks (resin cracking) may occur at an early stage of fatigue life and therefore affects the fatigue strength of composites during subsequent cycles more intensely than in the case of constant loading amplitude. This indicates the significance of a strong surface layer, for example protecting the surface of composite with a layer of gel-coating.

The influence of environmental conditions such as humidity and corrosion on fatigue properties of FRP composites properties is summarized in the following:

- ***Effect of Humidity and Sea water***

Fibre reinforced polymer laminates are used in marine application for the construction of ships and energy conversion devices and therefore they are in direct contact with corrosive fluids (Gellert and Turley, 1999; Kootsookos and Mouritz, 2004; Miyano *et al.*, 2005; Alawsi *et al.*, 2009). Recently they have been replacing conventional construction engineering materials because of the advantages they provide in terms of corrosion and fatigue resistance. In these applications although there is a layer of gel-coat to protect the GFRP material, under some

circumstances such as static and cyclic loads the gel-coat could fail, leaving the GFRP material unprotected to the harsh sea water environment. Therefore, it is important to understand the effect of degradation on the mechanical properties and mechanisms of failure of material caused by sea water exposure.

In the literature it is shown that the degradation that the humid conditions could cause on GFRP material is a complex problem as the humid environment can affect the modulus of elasticity, material strength (Miyano and Nakada, 2006), fibre /matrix interface degradation and variation in the matrix material in terms of glass transition temperature and plasticisation (Kotsikos *et al.*, 2000; Karbhari and Zhang, 2003; Cauich-Cupul *et al.*, 2011).

It has been shown that FRP composites are susceptible to an acidic corrosive environment (Alias and Brown, 1993; Myers *et al.*, 2007). In this environment the polymer matrix is degraded faster and the reinforcement fails at much lower loads than the design load. This is due to environmental stress corrosion cracking (ESCC) (Myers *et al.*, 2007). At higher acid concentration combined with loading, ESCC escalates.

Humidity is known to affect the properties of the matrix but not those of the reinforcement. Between polymer matrixes, thermoset resins are more sensitive towards humidity than thermoplastic resins. Humidity influences the resin properties by chemical degradation of the resin network or plasticization, consequently the composite fatigue life and maximum service temperature will be reduced. It is worth noting that moisture reduces the glass transition temperature of the polymer matrix. The most important factors for determining the effect of moisture is moisture diffusion rate (Jones, 2003).

- ***SCC Mechanisms in FRP Composites***

The most important feature of composite materials in a corrosive environment such as sea water is the stress corrosion cracking mechanism (SCC), which leads to the unexpected failure of composite materials exposed to a stress in an aggressive environment. The environment attacks reinforcements in fibre reinforced composite materials, which can cause premature failure, and thus in order to avoid this kind of failure where glass fibre reinforced composites are subjected to harsh environments for a long period of time, boron free glass fibres are recommended, which are more resistant to SCC (Renaud and Greenwood, 2005). In terms of the fatigue behaviour of composite materials in sea water it must be noted that environmental exposure and mechanical forces can combine together to speed up deterioration in the composite material

i.e. mechanical forces accelerate water penetration and water penetration accelerates damage induced by mechanical stresses (Suri and Perreux, 1995).

Results from fatigue tests in wet and dry unidirectional glass/epoxy samples shows lower fatigue life for wet samples at high stresses, however at low stresses the fatigue life of wet samples can be longer than dry samples (Kensche, 2006). In cyclic loading it has been shown that there is a huge impact of water absorption on the development of damage in glass/epoxy composites (Kotsikos *et al.*, 2000). Generally, durability of the GFRP composite materials in a wet environment can vary with exposure time. E-glass fibres are sensitive to water diffusion and long term exposure to a sea water environment in combination with mechanical stresses will result in premature failure due to crack propagation at the fibre interface (Doremus, 1974; Renaud and Greenwood, 2005).

Regarding the effect of sea water condition coupled with static/cyclic loads on the properties of fibre reinforced polymer composites with epoxy resins as the matrix system, more references can be found (Ellyin and Rohrbacher, 2003; Abdel-Magid *et al.*, 2005; Cauich-Cupul *et al.*, 2011) which show similar results.

- ***ESC Mechanisms on Polymers***

As was mentioned before environmental stress cracking (ESC) is one of the causes of failure in composites, particularly in polymer matrix composites. Various features such as liquid penetration, craze creation and crack development are the main reasons for such a complex phenomenon. Once the liquid penetrates into the polymer it becomes dissolved and thus stimulates cracking and crazing. Basically cracking is preceded by the crazing initiated at stress concentration sites. Actually crazes are voids that are linked together by drawn streaks of polymer, which bridges the void letting the craze transfer stress and hinder it from spreading (Arnold, 1996; Wright, 1996).

2.6.8 Corrosion Effect

Environmental fatigue behaviour of FRP is affected by all of its constituents, that is, the fibre, the matrix and the fibre/matrix interface (Romanenkov, 1967; Martin and Gardner, 1981; Garg and Pawar, 1982; Rege and Lakkad, 1983; Jones *et al.*, 1984b; Sekine *et al.*, 1988; Komai *et al.*, 1991; am E Grami *et al.*, 1995; Suri and Perreux, 1995; Renaud and Greenwood, 2005). Some investigations focusing on each of these components is discussed below:

- ***Fibre Effects***

It has been well studied that GFRP is degraded upon exposure to a harsh environment like sea water under cyclic loads (Charles, 1958a; Charles, 1958b; Schmitz and Metcalfe, 1966; Jones and Rock, 1983; Jones *et al.*, 1983). The exchange of metal ions (Na^+ and K^+) in the glass with hydrogens (H^+) of the attacking fluid is the mechanism of stress corrosion (Schmitz and Metcalfe, 1966; Metcalfe and Schmitz, 1972). Vauthier et al have shown that more broken fibres were found in environmentally aged GFRP specimens than those without aging indicating deteriorated fibre strength (Vauthier *et al.*, 1995). There is also evidence of fibre degradation during environmental fatigue where particles from glass fibres were found in the liquid media (Komai *et al.*, 1991).

- ***Matrix Effects***

Crack formation in the polymer matrix plays an important role in environmentally affected fatigue behaviour of composite materials. An investigation was conducted on the fatigue behaviour of FRP composite in both air and several liquid environments including water and acids. It has been shown that matrix cracks are created prior to failure for samples tested in air, however a few cracks were found in specimens tested in sea water, which indicates that the major damage followed immediately after the formation of the first cracks in sea water (Carswell and Roberts, 1980). In another study of fatigue behaviour of glass/epoxy composites it has been shown that moisture diffusing into the network of resin cracks influences the mechanical properties of the fibre/matrix interface region of the plies quickly beyond the last cracked ply. This causes acceleration of matrix cracking and reduces the fatigue life of the composites (Hofer *et al.*, 1987).

- ***Fibre/Matrix Interface***

The fibre/matrix interface effectively controls the environmental fatigue behaviour of composites. As an example, interfacial de-bonding between fibres and matrix can be found during environmental aging without externally applied loads (Pritchard and Taneja, 1973). The shear fatigue strength of GFRP composites exposed to a sea water environment was considerably reduced indicating the interface effect. Comparison between Woven and UD GFRP exposed to a sea water environment shows that the reduction rate of fatigue strength in woven GFRP is higher than in UD GFRP (Fried, 1967).

Comparing the microscopic features of several types of GFRP composites under cyclic loading in both air and water environment, it has been found that failure surfaces of the specimens in water environment was uneven, with many de-bonding areas (Watanabe and Tsai, 1979).

2.7 Fatigue Failure Mechanisms of Composite Materials

Fatigue failure mechanisms in FRP composite materials depend on the properties of both the matrix and the reinforcement as well as the interaction between the two (Dew-Hughes and Way, 1973; Harris, 1977; Reifsnider, 1980; Talreja, 1981b).

Figure 2-7 shows schematically fatigue failure modes for unidirectional fibre composites based on the strain-life diagram (Talreja, 1981b). This figure illustrates the relationship between fatigue failure and fatigue loading. For cycles with short life at high strain amplitudes, fibre fracture is prevailing and failure occurs within the scatter band of the static failure strain. For intermediate cycles, progressive failure mechanisms become predominant, while at low stress levels below the fatigue limit, only matrix micro cracking is observed and the fibre dominated strength does not reduce any further (Talreja, 2008b).

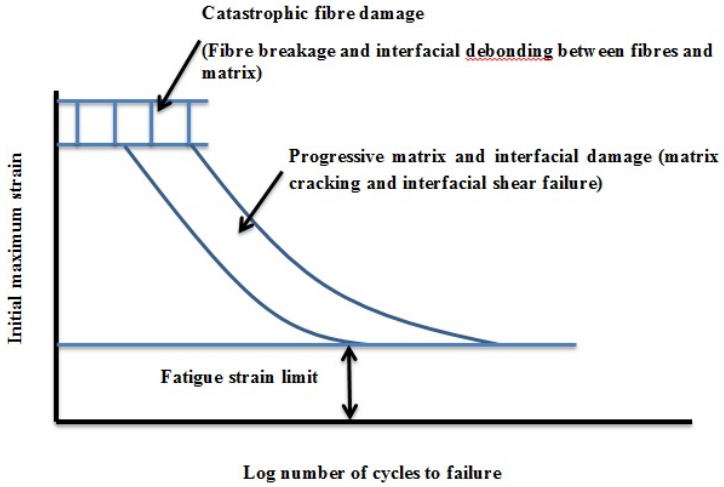

Figure 2-7. Strain-life diagram for UD fibre composites displaying the prevailing regions of fatigue failure modes, based on the fatigue-life diagram (Talreja, 1981b).

The progression of fatigue failure mechanisms in unidirectional FRP composites is in the following sequence;

- ✓ Interfacial de-bonding or de-bonding of the fibre /matrix interface which is regarded as crack initiation. Normally de-bonding happens first in fibres

perpendicular to the tensile axis and consequently needs a component of normal stress perpendicular to the interface (Figure 2-8) (Dew-Hughes and Way, 1973).

- ✓ Joining up of de-bonded regions which is considered as crack growth parallel to the interface.
- ✓ Crack growth through the matrix or resin cracking (Figure 2-9) (Dew-Hughes and Way, 1973).
- ✓ Tensile, compressive and shear fracture of fibres or fibre breakage (Figure 2-10)(Dew-Hughes and Way, 1973).

For multidirectional fibre reinforced composites, a fourth basic failure mechanism resulting from matrix cracking and interfacial de-bonding is called delamination. This causes de-bonding between adjacent layers of reinforcement.

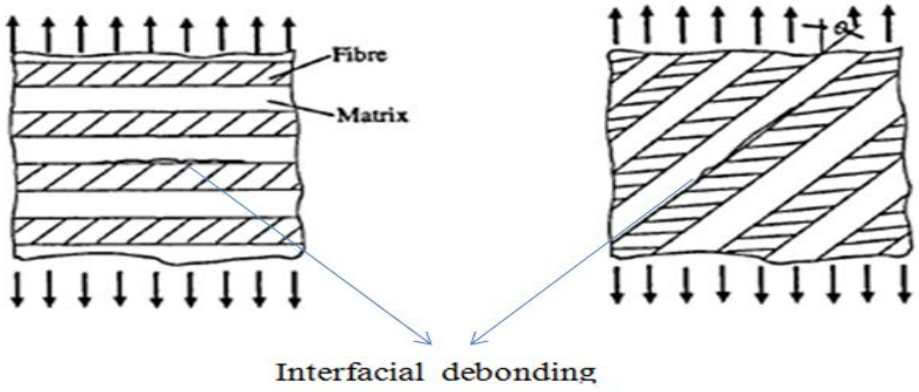

Figure 2-8. Interfacial de-bonding and crack propagation (Harris, 2003).

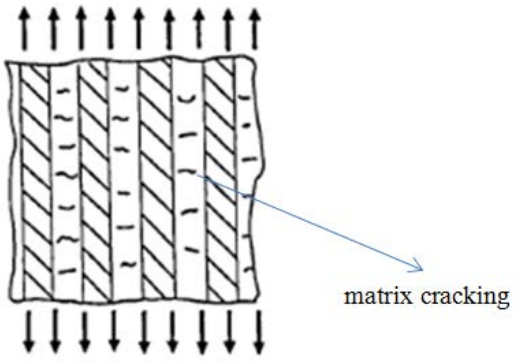

Figure 2-9. Crack propagation through resin cracking (Harris, 2003).

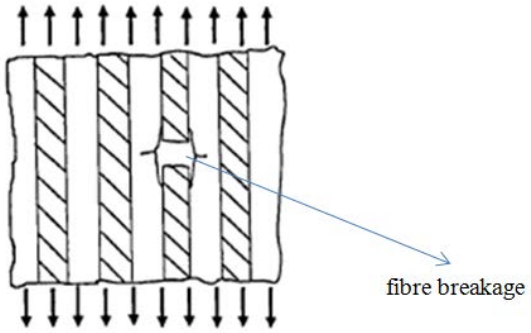

Figure 2-10. Tensile fracture of fibres or fibre breakage (Harris, 2003).

Regarding fibre deformation characteristics and matrix resin fatigue limit relations, failure mechanisms in unidirectional composites using various fibres are extensively discussed in the literature (Stinchcomb and Reifsnider, 1979; Curtis, 1989). Progressive fatigue failure has been investigated in experiments on glass and carbon fibre reinforced composites (Harris, 2003; Agarwal *et al.*, 2006). The observed failure mode is in the form of matrix cracking and longitudinal splitting, which initiates from interfacial de-bonding and early matrix cracking. It was found that more extensive damage took place in glass fibre composites than in carbon fibre composites.

Some experimental work has been performed on cross-ply laminates (Jones *et al.*, 1984b; Liao *et al.*, 1999b) and angle-ply laminates (Sturgeon, 1977). It was found that the failure mechanisms for cross-ply and angle-ply composites were different from those in unidirectional composites

Failure modes in angle-ply laminates are:

- Interfacial de-bonding started in the ply highly aligned to the main loading axis,
- Matrix cracking,
- Delamination,
- Fibre breakage.

Failure mechanisms in cross-ply laminates are developed in the following order:

- Transverse ply cracking
- Delamination,
- Longitudinal cracks,
- Fibre/matrix interfacial de-bonding and fibre breakage.

Although the above descriptions of progressive fatigue failure mechanisms are based on composites with unidirectional, cross-ply and angle-ply, these failure modes may be taken into account as applicable to all fibre reinforced polymer materials.

Since damage occurs progressively from de-bonded areas, matrix cracking and fibre breakage, fatigue test results for composite materials should preferably be shown as in Figure 2-11 (Owen and Howe, 1972; Dew-Hughes and Way, 1973). Interfacial de-bonding and matrix cracking occur at much lower load levels than that required for total failure. This de-bonding and matrix cracking may result in leakage and, if the penetrating environment be able to attack the fibre/matrix interface and thereby degrade the composite material, can cause premature failure.

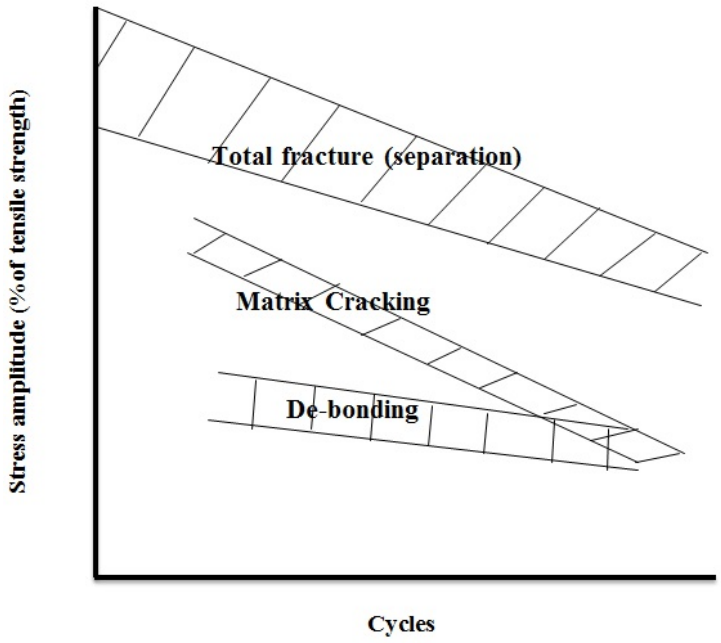

Figure 2-11. S-N diagrams showing the various stages of failure of glass fibre reinforced polyester under tension/ compression loading (Talreja, 1987).

For composite marine devices, the resin cracking strength and delamination resistance is of particular concern because of the problem of media diffusion caused by cracking.

It is suggested that fatigue degradation in composite materials can be categorized in three distinctive regions where failure modes are totally different (Talreja, 1981a). Region 1 corresponding to low cycles, where the stresses are sufficiently high to cause fibre breakage and accumulation of fibre breakages determines the number of cycles to failure at which this causes strength reduction of the composite below the applied stress and total fracture occurs. In region 2, as a result of cyclic loading and stress level, matrix fracture occurs, however, through a combination of mechanisms, crack propagation can be arrested by the

reinforcements. Finally crack accumulation causes fibre fracture and therefore damage reduces the composite strength below the applied stress and failure occurs. In region 3, the number of cycles that composite material can execute before failure is infinite as the stress is not enough to cause matrix cracking.

Generally speaking, in GFRP composites at low cycles, fatigue strength is attributed to the strength of glass fibres, however, at high cycles (low stress), polymer matrix properties are the determinant factor of fatigue life (Talreja, 2008a).

In GFRP composites, fatigue failure is preceded by substantial matrix cracking. Matrix cracking causes an initial reduction in stiffness followed by a lower stiffness slope during the fatigue life, finishing with a significant drop at failure (Mao and Mahadevan, 2002). During this process, reduction in stiffness and residual strength is of the order of 15-25% (Tong, 2002), consequently both phenomena can be used for modelling of composite damage (Kassapoglou, 2010). In fact, many models have been proposed for fatigue and mechanical performance of composite structures, however all need careful application. Quasi-static mechanical and fatigue testing of actual components under realistic loading/pressure is the best way to determine the mechanical and fatigue behaviour of composite laminates.

2.8 Characteristics of a Fatigue Test in FRP Composites

2.8.1 Frequency Effect

As a result of the hysteresis loop during fatigue testing of polymer composite samples, temperature increases above the ambient temperature, consequently hysteretic heating and corresponding thermal softening occurs leading to the fatigue strength reduction of composites. The degree of hysteretic heating and thermal softening is contingent upon the stress amplitude, frequency and viscoelastic properties of the materials.

During the fatigue testing of GFRP composites, the frequency of the fatigue loading substantially influences the properties. For other composites (CFRP and KFRP) tested, however, the effect is insignificant, as long as hysteresis heating is also insignificant (Jones *et al.*, 1984b). The reason for this is the environmental sensitivity of the glass fibres rather than any viscoelastic effect. Composites with less fibre in the testing direction, where the matrix has viscoelastic behaviour, will also often show an appreciable rate effect.

In FRP composites high-frequency cyclic loading (more than 10 Hz) has been shown to cause hysteresis heating and early failure; consequently in order to avoid heating of the composite

samples during the fatigue tests, the loading frequency should be set low enough, otherwise hysteresis heating will result in thermally induced failure (Makeev, 2013). The origins of hysteresis heating are the mechanical response of the thermosetting resin, the properties of fibre-resin interface and the effect of damage sites and stress concentration areas.

As a general rule for fatigue testing of composite materials, the fatigue test frequency should be selected so as to minimise the hysteresis heating of the materials, or at least to confine the temperature rise to no more than a few degree centigrade above ambient temperature. Generally for laminates or composites dominated by fibres in the test direction, frequencies of up to 10 Hz can be appropriate since they exhibit lower strains and low hysteresis heating, however, for resin dominated composites frequencies should be limited to less than 5 Hz due to this fact that they show larger strains and considerable hysteresis heating.

In GFRP materials, as well as with laminates showing substantial hysteresis heating, fatigue tests are performed at a constant rate of loading or at a constant rate of strain/displacement. High cycle fatigue tests can be carried out at relatively high frequencies and low cycle fatigue tests at low frequencies. This project aims to evaluate the degradation of mechanical properties of GFRP material during the fatigue test. The degradation can be assessed directly from the variation of load versus time. With the use of a data logger connected to a system of load cell and a computer attached to the fatigue rig, the variation of load with respect to time is a proxy for stiffness degradation. Therefore fatigue tests are conducted at a constant rate of strain. For all high cycle and low cycle fatigue tests, a frequency of 1 *Hz*, was chosen, therefore the effect of hysteresis heating and thermally induced failure can be minimized.

2.8.2 Structural Effect

Usually fatigue data points are collected from laboratory tests carried out on small test coupons however specific features in composite structures can cause them to be more prone to fatigue failure than the base composite materials (test specimens). Therefore actual fatigue life of composite structures may be underestimated. For example, bonded joints and composite ply drop-offs could have an adverse impact on fatigue behaviour. When such fatigue effects occur, their influence can be reduced by accurate design.

Fatigue behaviour of composite structures shows that fatigue failure, including matrix cracking and interfacial de-bonding at stress-concentrators such as holes, usually remains limited to a small area with a minor effect on total structural behaviour. However, fatigue is more likely to lead to severe complications at joined and bonded structural connections which are usually

used in offshore tidal turbine blades systems. For example some locations on the turbine systems such as the connection point between hub and composite blades are very susceptible to inter-laminar shear stress. The weakness is due to the lack of reinforcing fibres across the joined interfaces and by low inter-laminar shear strength in combination with the occurrence of stress concentrations associated with joint geometry and bond imperfections. Load events perpendicular to the plane of the composite laminate will intensify the problem. Therefore development of a new high-performance design must contain a detailed programme of experiments on all critical joints with the assessment of static and fatigue strength (Scholte, 1994a).

2.8.3 Effect of Stress Raisers

In composite materials there are numerous stress concentration features including holes, notches, scratches and other imperfections. Some researchers (Talreja, 1980) believe that these stress raisers have a negligible effect on fatigue strength due the huge number of de-bonding sites already existing in the material. On the contrary, the results presented by Owen indicated that holes have adverse impact on initiation of fatigue damage. It was found that a semi-circular hole acts as a stress raiser at the onset of damage, with the reduction of the fatigue strength by a factor of approximately 3 in most GFRP materials and up to 10 in unidirectional GFRP (Jones *et al.*, 1984a).

Generally stress raisers have less effect on fatigue strength than they do on static strength. At low cycles, stress concentrators may significantly cause fatigue strength reduction of the composite, but after a large number of load cycles the fatigue strength approaches that of the plain composite. Basically stress raisers influence the matrix cracking strength and have little effect on fibre breaking strength. Since one of the most important concern for GFRP blades is their matrix cracking strength, and since tidal turbine composite blades experience cycles of low stress, the stress raisers may greatly affect the fatigue strength of GFRP blades used for offshore applications.

2.8.4 Effect of Edge-Induced Stresses/strains

Edge-induced stresses in FRP laminates are a complex issue in many types of mechanical and fatigue testing. Development of shear and normal stresses at the FRP specimen edges, are associated with the mismatch of properties between the plies (Pagano and Pipes, 1971; Curtis, 1984; Curtis, 1989). The stacking sequence of plies is an important variable and the value of

edge stresses varies significantly with respect to the positions of the layers/plies. Indeed composites with thin and uniformly-distributed layers have the lowest edge stress.

The values of edge-induced stresses in composites are also affected by the temperature and moisture. This is due to the different expansion coefficients of layers and also due to the fact that the composite layers expand to different extents depending on the absorbed moisture (Curtis, 1980).

The type of external loading also affects the edge effects. For example, a laminated composite which shows no edge effects in tension, may develop serious edge-induced damage in compression. In fatigue, edge induced damage grows with increasing numbers of cycles. Once edge-induced damage increases, laminated composites can become delaminated, leading to environmental attack and to significant reduction in compressive properties.

The GFRP composite blade joints in offshore systems are submerged in sea water. The edge effects and sea water penetration may combine together and therefore, edge induced damage grows. This can significantly reduce the fatigue strength of composite blade joints.

2.9 Microstructural Aspects of Damage Mechanisms in FRP composites

For CFRP and GFRP materials three failure mechanisms are most significant: crack formation of the fibres in on-axis plies, resin cracking in off-axis plies, and development of delamination between plies (Reifsnider, 1990). Defects are created at the beginning of the fatigue life causing a rapid reduction in the composite strength properties and a certain stiffness reduction; a second stage of damage follows with a slow material degradation rate, a function of the fatigue load level and environmental conditions (Highsmith *et al.*, 1982; Reifsnider, 1990; Giancane *et al.*, 2010a). The last part of the fatigue life consists of accelerated stiffness decay in the damaged zones, causing visible defects and flaws to appear and leading to the final catastrophic failure (Reifsnider, 1990; Giancane *et al.*, 2010a).

The two main microstructural damage mechanisms observed in fibre reinforced composites are fibre and matrix failure (Talreja, 1981a; Thom, 1998). As a result of this damage, the failure process depends on the types of reinforcements and stack up sequences of plies in the composite.

2.9.1 Failure of Reinforcements

Static and fatigue fibre failure in composites are categorized into two failure modes: tensile and compressive fibre failure. Typical tensile fibre failure modes are fibre de-bonding, fibre

pull out and breakage (Miller and Wingert, 1979). Fibre pull out occurs where fibre and matrix are brittle (Thom, 1998). For composites in tension in the early loading stage, local fibre breakage occurs which is followed by stress redistribution. After this interfacial de-bonding between fibres and matrix occurs and this is followed by fibre fracture and fibre pull out leading to the final failure. The compressive fibre failure mode occurs in the form of fibre buckling/kinking (Figure 2-12)(Thom, 1998).

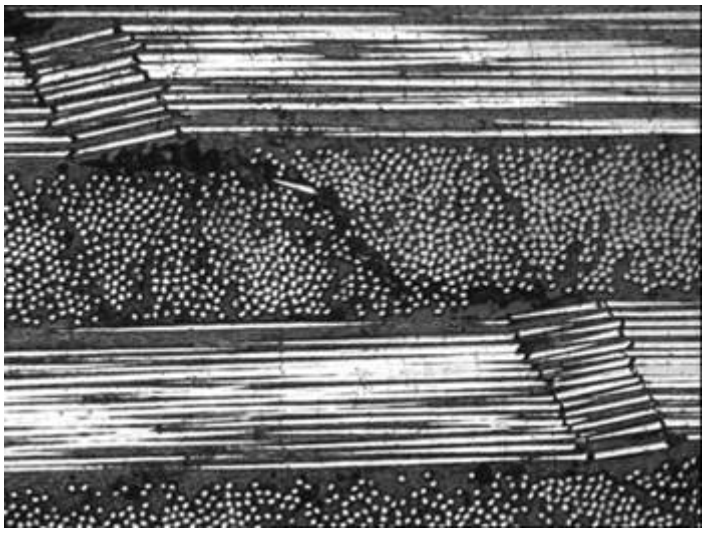

Figure 2-12. Fibre buckling failure mode (Sun *et al.*, 2017) .

2.9.2 Failure of the Matrix

Matrix failure can be divided into two modes of failure: matrix failure between plies known as delamination and matrix failure in a ply known as inter-fibre fracture (Franz, 1990). Delamination is created as a result of inter-laminar stress and is a direct impact of transverse or longitudinal micro-cracks in the matrix, however inter fibre fracture initiates at the fibre/matrix interface and then grows into the matrix (Thom, 1998). In multi directional laminates, free edges generate inter-laminar shear stress which initiates at micro-cracks.

2.9.3 Unidirectional Composites

In unidirectional composites fatigue behaviour is a function of fibre properties and the orientation of fibres with respect to main loading axis. In the early stages of fatigue response of composites with fibres oriented parallel to loading direction, longitudinal matrix cracks initiate along the fibres (Pagano and Pipes, 1971) As the fluctuating loads continue, the cracks propagate and accumulate at stress concentration sites. Once the residual strength of specific

composites is satisfied by maximum cyclic loads, fibre and matrix fracture causes final failure. It has been proposed that when the fibre orientation (ply angle) in unidirectional composites is less than 15° with respect main loading axis, the failure mechanism is the same as the failure mechanisms of unidirectional composites aligned at 0°, however once the fibres are aligned at ply angle bigger than 15° the failure is dominated by the properties of the matrix (Wicaksono, 2009)

2.9.4 Multi-Directional Composites

Multidirectional composites can be classified as cross-ply and angle-ply laminates. The progression of fatigue damage mechanisms in multidirectional composites are in the following order (Naik, 2003):

- Crack initiation in matrix
- Localized fibre breakage - crack coupling
- Delamination and interfacial de-bonding between fibres and matrix
- Fracture failure

Figure 2-13 illustrates potential failure modes in FRP composites.

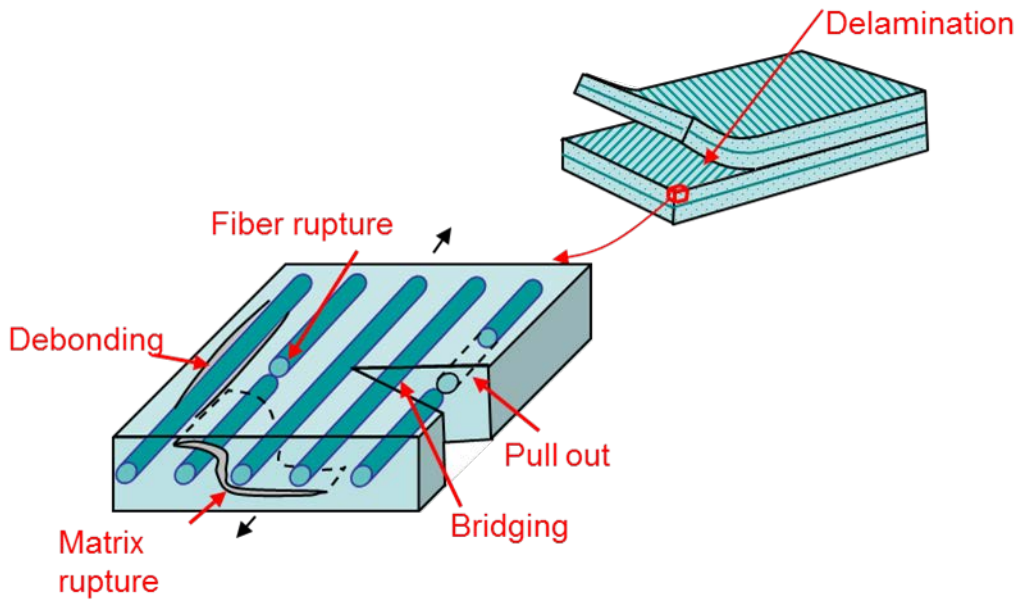

Figure 2-13. Potential failure modes in fibre reinforced composites (Altabey and Noori).

In cross-ply composite laminates, fatigue damage initiates as longitudinal matrix cracks. This is followed by cracks along the fibres in the transverse plies. As the cyclic load continues the density of matrix cracks increases followed by crack coupling and interfacial de-bonding

between fibres and matrix. As the composite is further stressed, delamination appears and sometimes micro-cracking in the matrix intersects with a delamination crack at the fibre/matrix interface (Figure 2-14). The last stage is fibre breakage in either fibre tension or compression depending on the loading conditions. The progression of fatigue failure modes leads to the graph of damage accumulation with respect to fatigue life (Figure 2-15).

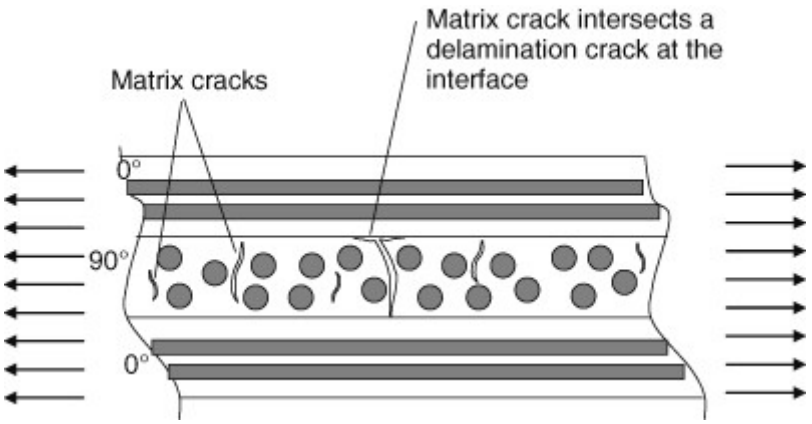

Figure 2-14. Micro-crack associated with delamination (Guedes and de Moura, 2012).

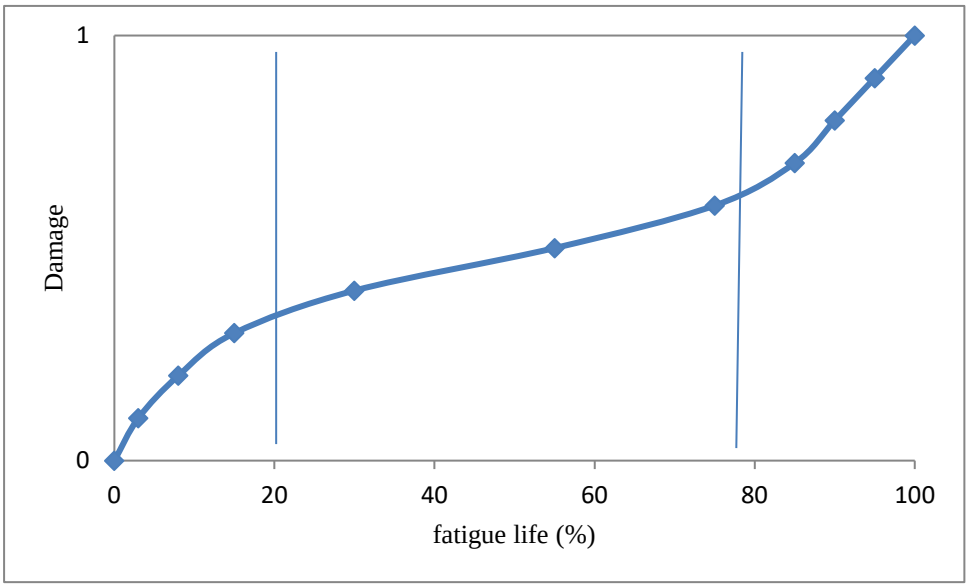

Figure 2-15. Growth of Fatigue damage in cross-ply composites during fatigue life (Naik, 2003).

In angle-ply composite laminates, fatigue damage mechanisms strongly depends on ply orientation. In chapter 6, it is shown that when the ply angle changes from 0° to 45°, matrix properties dominate the composite mechanical and fatigue behaviour and consequently the

matrix failure mode is the determinant factor. The relationship between fibre orientation and fatigue properties is discussed in chapter 8.

2.9.5 Woven Composites

Generally woven composites have lower in-plane properties compared with unidirectional and multi-directional composites, however in terms of impact resistance and damage tolerance they are superior to unidirectional and multi directional composites. The mechanical behaviour of woven composite depends on the fibre, matrix, weave pattern, fabric geometry, volume fraction of fibres and laminate orientation (Naik and Shembekar, 1992; Ganesh and Naik, 1996; Naik and Ganesh, 1996).

The usual microscopic damage which can be observed in woven laminates under fatigue loading is micro-cracking in the matrix, fibre breakage, interfacial de-bonding between fibre and matrix, crack coupling and delamination between adjacent plies.

The fatigue life of woven composites is usually divided into three stages. In the early stage of the fatigue response, microstructural damage and longitudinal inter-laminar cracks are found. Also inter-laminar transverse cracks (Figure 2-16) are observed to develop at this stage. There is a quick reduction in stiffness during this stage, which is mainly due to crack coupling and fibre-matrix interfacial de-bonding. In the middle stage of fatigue life, crack density in the resin increases and the main damage mechanism is delamination between adjacent plies. In the final stage, all failure mechanisms are activated and grow rapidly and finally the composite coupons fail with evidence of fibre breakage. Fibre breakage is in the form of fibre pull-out, fibre tension cracks or fibre buckling (Naik, 2003). The corresponding diagram of stiffness degradation versus fatigue life for a woven composite laminate is shown in Figure 2-17.

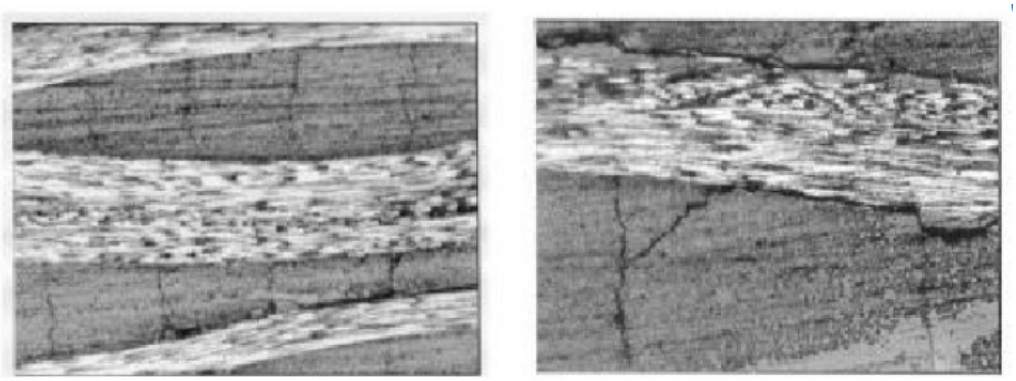

Figure 2-16. Transverse matrix cracking (Talreja, 2015) .

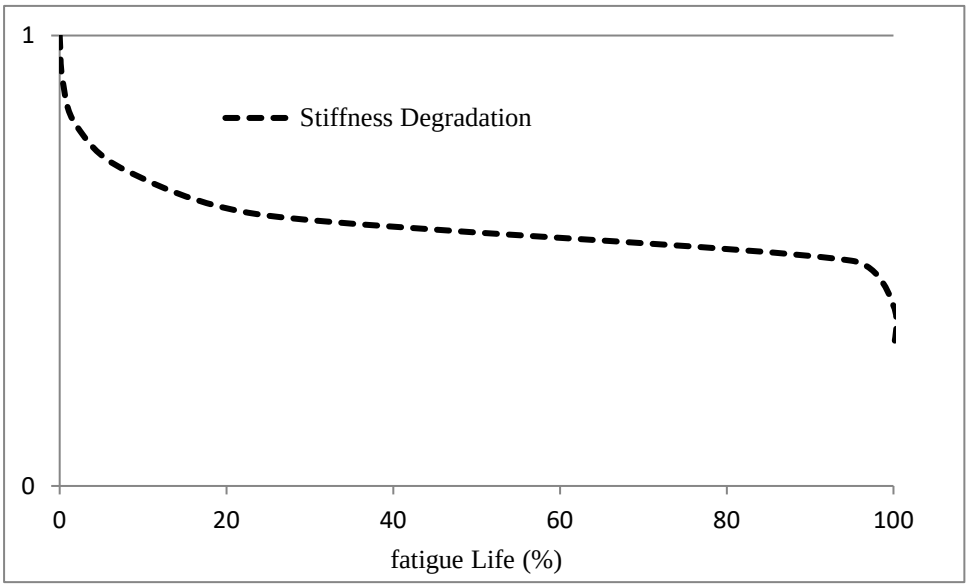

Figure 2-17. Stiffness degradation in woven composite laminates during fatigue life (Van Paepegem and Degrieck, 2002).

2.10 Composite Failure Criteria

Regarding static and fatigue performance of composite laminates under multi-axial loadings various failure criteria have been proposed and it is found that Tsai-Hill, Tsai-Wu, maximum stress and strain failure criteria are most promising (Quaresimin *et al.*, 2010).

Composite failure occurs through various individual failure modes as described earlier. One failure mode can interact with another failure mode therefore selecting a set of suitable failure criteria is required for prediction of the failure of composites under either static or cyclic loading. A data base of composite failure criteria was set by many researchers (Azzi and Tsai, 1965; Tsai and Wu, 1971; Hashin and Rotem, 1973; Soni, 1983). Failure criteria in fibre reinforced composites can be categorised into two main groups; mode-dependent and mode-independent (Echaabi *et al.*, 1996; Icardi *et al.*, 2007; Garnich and Akula, 2009). Regarding the discussion of failure criteria, in the following sections, some notations are used. Components of normal stresses (σ_{ij}) and shear stress (τ_{ij}) shown in Figure 2-18 indicate the general three dimensional state of stresses at the material point. The corresponding shear and normal strains are denoted by γ_{ij} and ε_{ij} respectively, and Poisson's ratios are defined by ν_{ij}.

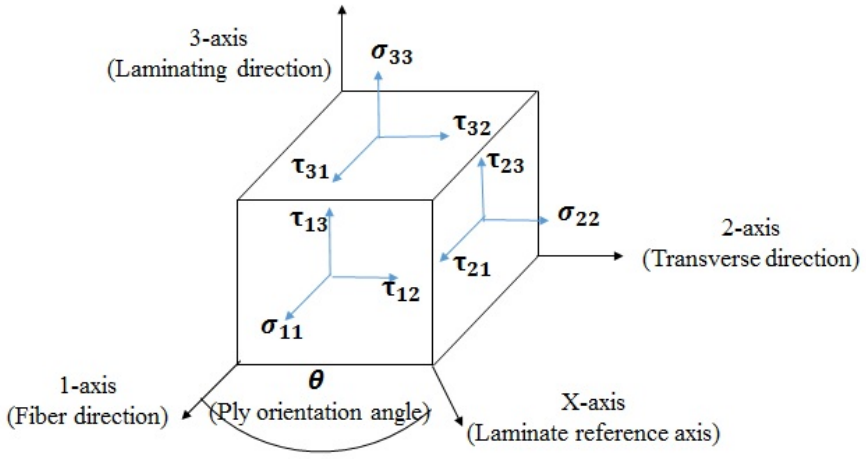

Figure 2-18. 3D state of stresses at material point.

2.10.1 Maximum Stress (Mode-dependent failure criterion)

Since composite materials are anisotropic, the most commonly used failure criterion is maximum stress. According to this failure criterion the material fails once the magnitude of stress in each direction goes beyond its corresponding acceptable level in that direction. The major advantage of this failure criterion is that it predicts the particular failure mode. According to the conditions in Table 2-3, failure of a composite material in any principal direction can be predicted.

The maximum stress failure criterion predicts that a material will fail once the stress in each direction overcomes its endurable level. The allowable stresses in the six directions (σ_{ij} and τ_{ij}) are compared to their corresponding ultimate strength (Table 2-3). In this table σ_{11tu} is the tensile strength in the longitudinal direction, $\sigma_{11cu}$is the compressive strength in the longitudinal direction, σ_{22tu} is the tensile strength in the transverse direction, σ_{22cu} is the compressive strength in the transverse direction, σ_{33tu} is the tensile strength in the third direction, σ_{33cu} is the compressive strength in the third direction, τ_{23u} is the shear strength in the 23-plane, τ_{13u} is the shear strength in the 13-plane and τ_{12u} is the shear strength in the 12-plane. In the stress and strain components subscript u indicates the ultimate strain or stress components and subscripts t and c represent tension and compression respectively.

Table 2-3. Conditions for failure and failure modes-Maximum Stress Failure Criterion.

Conditions	Failure mode
$\sigma_{11} > 0$ and $\sigma_{11} > \sigma_{11tu}$	Tension of fibres
$\sigma_{11} < 0$ and $\lvert\sigma_{11}\rvert > \sigma_{11cu}$	Compression of fibres
$\sigma_{22} > 0$ and $\sigma_{22} > \sigma_{22tu}$	Tension in the matrix
$\sigma_{22} < 0$ and $\lvert\sigma_{22}\rvert > \sigma_{22cu}$	Compression in the matrix
$\sigma_{33} > 0$ and $\sigma_{33} > \sigma_{33tu}$	Tension in the matrix
$\sigma_{33} < 0$ and $\lvert\sigma_{33}\rvert > \sigma_{33cu}$	Compression in the matrix
$\tau_{23}\rvert > \tau_{23u}$	Inter-laminar shear
$\tau_{13}\rvert > \tau_{13u}$	Inter-laminar shear
$\lvert\tau_{12}\rvert > \tau_{12u}$	In plane shear

2.10.2 Maximum Strain (Mode-dependent failure criterion)

The maximum strain failure criterion predicts that a material will fail once the strain in any direction overcomes its tolerable level. The mechanical strains in the six directions (ε_{ij} and γ_{ij}) are compared to their corresponding maximum allowable strain (Table 2-4) in the same manner as described for the maximum stress criterion.

Table 2-4. Conditions for failure and failure modes-Maximum Strain Failure Criterion.

Conditions	Failure mode
$\varepsilon_{11} > 0$ and $\varepsilon_{11} > \varepsilon_{11tu}$	Tension of fibres
$\varepsilon_{11} < 0$ and $\lvert\varepsilon_{11}\rvert > \varepsilon_{11cu}$	Compression of fibres
$\varepsilon_{22} > 0$ and $\varepsilon_{22} > \varepsilon_{22tu}$	Tension in the matrix
$\varepsilon_{22} < 0$ and $\lvert\varepsilon_{22}\rvert > \varepsilon_{22cu}$	Compression in the matrix
$\varepsilon_{33} > 0$ and $\varepsilon_{33} > \sigma_{33tu}$	Tension of matrix
$\varepsilon_{33} < 0$ and $\lvert\varepsilon_{33}\rvert > \sigma_{33cu}$	Compression of matrix
$\lvert\gamma_{23}\rvert > \gamma_{23u}$	Inter-laminar shear
$\lvert\gamma_{13}\rvert > \gamma_{13u}$	Inter-laminar shear
$\lvert\gamma_{12}\rvert > \gamma_{12u}$	In plane shear

2.10.3 Tsai-Wu Quadratic Interaction and Tsai-Hill criteria

Mode-independent failure criteria are sets of criteria which are employed to predict failure of composite materials. This type of failure criterion is unable to reveal specific information regarding the nature and type of failure mechanisms (Garnich and Akula, 2009). One of the most popular failure criteria is the Tsai-Wu criterion (Tsai and Wu, 1971). According to this failure criterion, failure of composite material can be predicted when the following equations are satisfied.

$$H_1(\sigma_{11}) + H_2(\sigma_{22}) + H_{11}({\sigma_{11}}^2) + H_{22}({\sigma_{22}}^2) + 2H_{12}(\sigma_{11})(\sigma_{22}) + H_{66}({\tau_{12}}^2) \geq 1$$

2-2

Where

$$H_1 = \frac{1}{\sigma_{11tu}} - \frac{1}{\sigma_{11cu}} \ , \ H_2 = \frac{1}{\sigma_{22tu}} - \frac{1}{\sigma_{22cu}} \ , \ H_{11} = \frac{1}{(\sigma_{11tu})(\sigma_{11cu})} , \ H_{22} = \frac{1}{(\sigma_{22tu})(\sigma_{22cu})}$$

$$H_{66} = \frac{1}{(\tau_{12u})^2} , \ H_{12} = -\frac{1}{2(\sigma_{11tu})(\sigma_{11cu})}$$

2-3

The other quadratic criterion is the Tsai-Hill criterion (Azzi and Tsai, 1965), which is a modified form of an earlier failure yield criterion of homogenous materials (Hill, 1998) for predicting FRP composite failure. According to this criterion, failure will occur once the following inequality is violated:

$$(\frac{\sigma_{11}}{\sigma_{11u}})^2 + (\frac{\sigma_{22}}{\sigma_{22u}})^2 + (\frac{\tau_{12}}{\tau_{12u}})^2 - (\frac{\sigma_{11}}{\sigma_{11u}})(\frac{\sigma_{22}}{\sigma_{22u}}) < 1$$

2-4

2.11 Full-field Measurement Technique for FRP Composite Laminates

The mechanical performance of composites strongly depends on the elastic-plastic interaction between fibres and matrix, fibre-matrix interfacial properties and the fibre orientation with respect to main loading axis (Bakir and Hashem; Godara and Raabe, 2007; Alam *et al.*, 2010; Mortazavian and Fatemi, 2015). The microscopic mechanical behaviour of composites is controlled by the inhomogeneous response upon straining. In other words once a FRP composite laminate is subjected to mechanical deformation, strain localization and heterogonous plastic flow pattern can be observed. This can cause failure of fibres, of the matrix or interfacial de-bonding between fibres and matrix, finally leading to catastrophic failure.

Experimental studies have been conducted to identify the strain localization mechanism inside composites. Matrix type and the fibre-matrix interfacial strength have a substantial effect on micro-mechanical causes of such a complex failure process (Kies, 1962; De Buhan and

Taliercio, 1991; Asp *et al.*, 1995; Briançon *et al.*, 1996). For example the effect of strain localization in the matrix on the transverse failure of fibre reinforced composites has been well documented (Christensen and Rinde, 1979; Joneja, 1984) and it has been found that reduced transverse failure strength of reinforced polymer-based laminates is due to the residual stresses developed in the matrix. Indeed reinforcing fibres are much stiffer than the polymer matrix, so strain concentration phenomena occur in the polymer matrix between the surrounding fibres.

One of the most important factors responsible for the failure of FRP composites is the plastic strain localization in the matrix which is constrained by neighbouring fibres, therefore, investigation about the effect of plastic micro-strain distribution/localization on the micro-mechanical behaviour of FRP composite laminates is crucial. A better understanding of microscopic mechanical performance of composites under deformation will make the use of these materials more reliable and increase the design safety of engineering parts manufactured by them. A detailed investigation of strain localization in heterogeneous materials such as FRP composite materials can be performed by mapping strain fields via the DIC technique.

2.11.1 Introduction to DIC

In experimental solid mechanics, measuring the surface displacement of materials subjected to mechanical loading is an important task. For this purpose different full-field non-contact optical techniques (Rastogi, 2003) including non-interferometry methods such as digital image correlation have been developed. DIC has been widely used as an effective tool for measuring surface deformation. It calculates full field strain and displacement measurements by comparing the grey scale distribution changes of the planer surface in the un-deformed (reference) and deformed states. Basically DIC is an optical measurement technology that works on the basis of digital image processing and numerical computing.

The approach for determining surface deformation using the DIC method was developed by researchers at the University of South Carolina in the 1980s (Peters and Ranson, 1982; Chu *et al.*, 1985; Sutton *et al.*, 1986; Sutton *et al.*, 2000) when numerical computation and processing of digital images were still in their early stages. In the literature the same method has been given various names such as texture correlation, photogrammetry, and computer-aided speckle interferometry, however in this study the technique is called DIC.

Recently the DIC technique has been extensively improved for an expanding range of applications. For instance, the DIC technique using a single camera is limited to in-plane

deformation measurement of the object surface, therefore for three dimensional deformation of test coupons after loading, the 2D DIC method is no longer useful. In order to address this disadvantage, 3D DIC and digital volume correlation (DVC) has been developed (Luo *et al.*, 1993; Helm *et al.*, 1996; Bay *et al.*, 1999; Garcia *et al.*, 2002; Smith *et al.*, 2002). The latter technique is used for measuring internal deformation of solid objects by tracking the volume unit movement within the digital image volumes of the object.

Using the DIC method has some advantages compared to interferometric optical techniques.

- Simplicity of sample preparation and experimental set up:

To prepare specimen, spray paints can be used on the sample surface in order to create a random grey intensity distribution. In some cases specimen preparation is not necessary as the natural texture of a specimen surface has this random grey intensity level. Also to record the images of the test coupon surface before and after deformation only a single camera is required.

- Low requirements in terms of measurement environment:

To illuminate the sample during deformation a white light source or natural light can be used.

- Wide range of measurement resolution:

Different images recorded by image acquisition apparatus can be processed by the DIC technique. For instance in order to achieve micro-scale to nano-scale deformation measurement, DIC can be coupled with scanning electron microscopy (SEM) (Kang *et al.*, 2005; Canal *et al.*, 2012) and light microscopy (Sun *et al.*, 1997; Zhang *et al.*, 2006).

Nevertheless, DIC technique has its own drawbacks, for example the surface of the object must have a random speckle pattern and also the quality of imaging systems heavily affects the measurements.

2.11.2 2D DIC Method for In-plane Movement

Engineering strain has been determined in a variety of methods, with varying results. One technique to calculate the strain is through the crosshead displacement of tensile test machine, however this method does not account for compliance in the test machine. Extensometers have been developed to address this. Initially there were contacting systems but now non-contact extensometers are available. The extensometer technique is useful for materials that show a necking behaviour as for this technique prior to the point of failure extensometer must be

removed to hinder damage of extensometer. In laminated composite materials which show linear elastic behaviour up to the point of failure when to remove the extensometer is not clear.

The best technique for strain measurement is a strain gauge that has been extensively used for local measurement however, it is not ideal for fibre reinforced composites because of inhomogeneous nature of the composite architecture. Due to the anisotropy effect of composites the displacement and strain on the surface of composite can differ depending on the location of the strain gauge.

The ideal technique for measuring strain and characterizing progression of failure in FRP composites is a non-contact strain measurements method. Regarding non-contact measurement tools two techniques, i.e. laser extensometer and Digital Image Correlation methods, have been developed. The latter one allows to characterize the progression of failure and measure strain similar to the use of strain gauges without making contact with the test coupon.

Digital image correlation has been extensively used as a tool for quantitatively and qualitatively measuring planer object surface deformation. Basically in the DIC measurement set up, comparing the digital images of a test specimen surface obtained before and after deformation results in full-field displacement/strain measurement. By combining the DIC technique with microscopes such as SEM and AFM, micro-scale measurement can also be achieved.

2.11.3 DIC through Photogrammetry

The Digital image correlation technique also known as photogrammetry has been implemented for determination of strain fields in materials with inhomogeneous microstructures (Sachtleber *et al.*, 2002; Godara and Raabe, 2007; Brynk *et al.*, 2012). The DIC technique is based on the recognition of geometrical changes in the grey intensity distribution of surface speckle patterns before and after deformation. The following consecutive steps should be performed for implementation of the DIC technique:

I. Sample and experimental preparation
II. Recording digital images of the planar test coupon surface before and after deformation
III. Processing the digital images via a computer program (such as a MATLAB code) to obtain full field displacement/strain measurement information.

After recording the digital images of the test object surface before and after deformation, DIC compares these images at different stages and then computes the motion of each image point. In the following, the basic principles of the 2D DIC technique are discussed.

2.11.4 Principle of DIC

In the 2D DIC method, displacements and strains are identified from digital images of an object surface. A typical DIC measurement set up using an optical imaging apparatus is schematically illustrated in Figure 2-19. The plane surface of the test specimen is observed by a camera with an imaging lens. The camera is positioned with its optical axis perpendicular to the surface of the specimen (object), imaging the planar object surface in different loading states. The digital images of the object surface, one before and another after deformation, are recorded and digitized in a computer. Displacements can be detected by comparing these images and searching for a matched point from one image to another. The matching process can be done by defining a target area (subset) with multiple pixel points such as 30×30 pixels. This subset has a unique grey level distribution. It is assumed that this grey level distribution does not change during loading of the test coupon. A part of the digital image before and after deformation is shown in Figure 2-20. The displacement of the subset on the reference image is found in the image after deformation by tracking the area of equal light grey level within the subset. In order to perform this process, the object surface must have a random speckle pattern. A random grey intensity distribution can be made artificially by spraying black/white paints onto the specimen surface. A typical example of random speckle pattern (grey intensity distribution) on the object surface is shown in Figure 2-21.

It should be noted that during the deformation the sensor of camera and specimen surface should be parallel and the surface of an object must be flat. Out-of-plane motion and geometric distortion of sample during deformation should be small enough to be neglected.

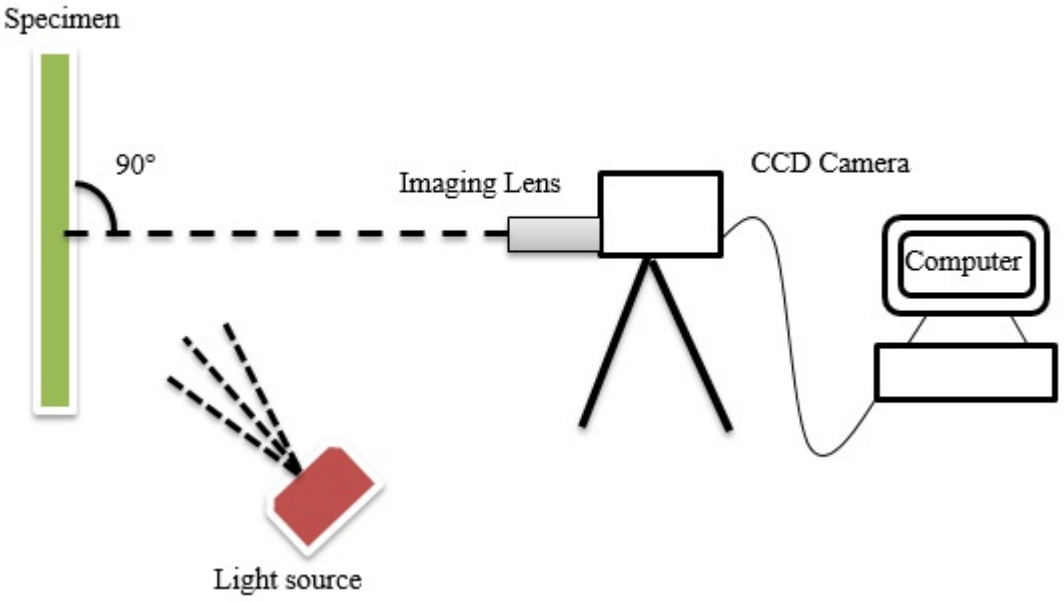

Figure 2-19. Set up for displacement/strain measurement using DIC method.

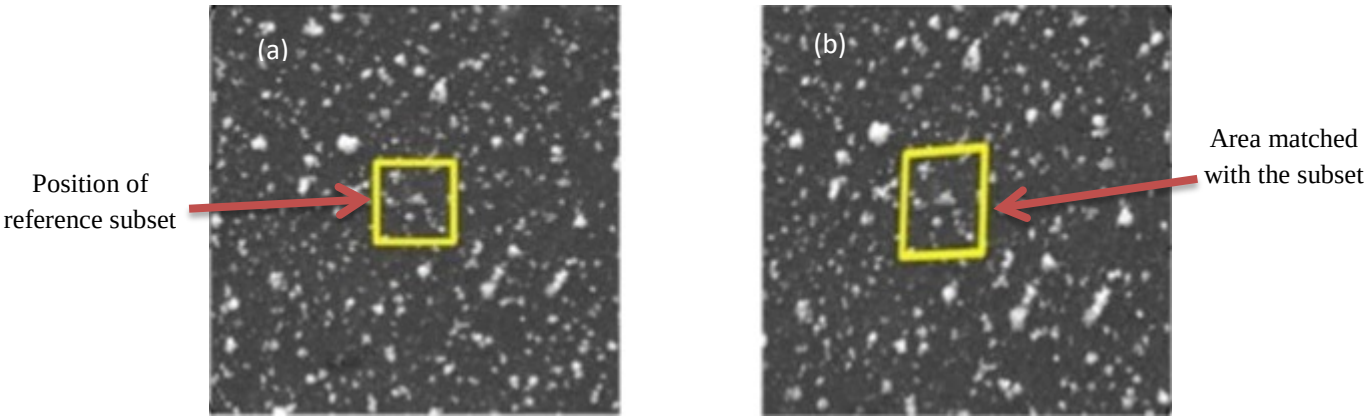

Figure 2-20. Tracking the subset before and after deformation, (a) Reference image, and reference subset before deformation, (b) deformed image, Target or deformed subset after deformation (Kammers and Daly, 2011).

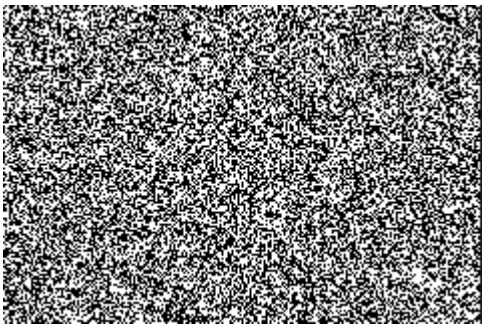

Figure 2-21. Typical example of speckle pattern on the test coupon surface.

Based on the above theory, a correlation criterion must be defined to assess the similarity degree between the un-deformed and the deformed subset before the correlation analysis. Several criteria are available in the literature (Giachetti, 2000; Tong, 2005) to match the subset from one image to another, one is the normalized cross-correlation as

$$F(x, y, x^*, y^*) = \frac{\sum P(x,y)Q(x^*,y^*)}{(\sum P(x,y)^2 \sum Q(x^*,y^*)^2)^{1/2}}$$

2-5

Where $P(x,y)$ and $Q(x^*,y^*)$ represents the gray intensity levels within the un-deformed and deformed subset images, in which (x,y) and (x^*,y^*) correspond to the point coordinates on the subset before and after deformation respectively. The relationship between coordinates (x^*,y^*) after deformation and coordinates (x,y) before deformation is determined by maximizing the above equation.

The most important parameters involved in the DIC analysis software are the interpolation type, facet (subset) size and the step size (calculation step). The initial digital image is mapped by a grid of square facets. The grey intensity distribution that characterizes the facets and their two-dimensional coordinates are assigned to the centre of the facets. The subset size is the dimension of one single square and the calculation step is the distance between the centres of adjacent facets. Spatial resolution will be optimized by setting the calculation step smaller than the subset size. In the above equation the coordinates of point $Q(x^*,y^*)$ in the deformed sub-set may locate between pixels. Before evaluating the similarity degree between un-deformed and deformed subsets using the cross-correlation criteria mentioned above, the grey intensity of these points with sub pixel locations must be determined by utilizing a sub-pixel interpolation scheme. Some of these sub-pixel interpolation schemes are bilinear, bi-cubic, bi-cubic B-spline and bi-cubic spline interpolation methods which have been mentioned in the literature. The detailed algorithms of these interpolation schemes are available in numerical computing references (Press, 2003).

2.12 Causes of fatigue in tidal turbine blades

2.12.1 Effect of Tidal Currents

Basically tides are created due to the variation in the Earth's gravitational field. This is because of the motions and gravitational attractions of the moon and the sun. As a result of gravitational

attraction of the moon as it revolves around the earth and also gravitational attraction of the earth as it revolves around the sun, tides are produced. This results in the rise and fall of ocean waters around the world. In fact, the moon and sun create a force which causes the movement of tides.

Usually tides behave in different manners, depending on the position of celestial bodies of the sun and the moon. This is due to the moon and sun gravitational forces. This means that, once there are unidirectional forces from the sun and the moon (i.e. when the sun and the moon are in alignment), gravitational forces support each other. This is known as “Spring tide” (highest tides)(Figure 2-22). This phenomenon takes place twice in each cycle.

When the position of the moon is at right angles to the Sun (i.e. when the moon is at 90° to the sun), the gravitational forces are independent of each other. This is known as “Neap tide” (lowest tides), (Figure 2-22). This phenomenon takes place twice in each cycle and therefore, Spring and Neap tides each have periods of about 14 days.

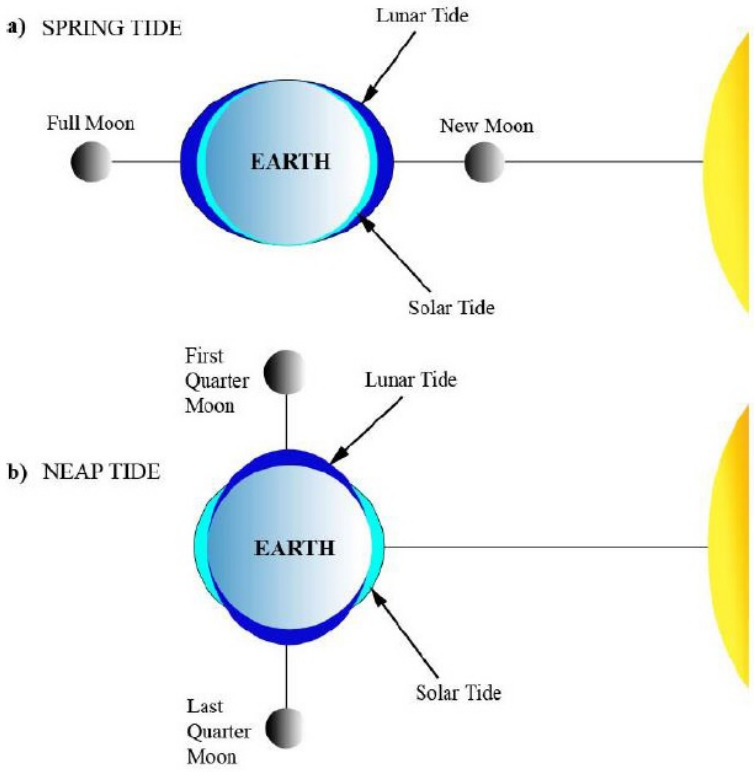

Figure 2-22. Schematic of spring and neap tides (Nicholls-Lee, 2011)

- ***Tide Height and Resultant Tidal Current Velocity***

Figure 2-23 shows a characteristic tide height-time series from the west of coast of Ireland. As can be seen in this figure, there are two low and high tides per day and the level of tides varies about 40% during each month (Kennedy *et al.*, 2012). The velocity of tidal currents at any time due to the variation in tide height can be estimated by approximation detailed in (Kennedy *et al.*, 2012). The water velocity-time series corresponding to the tide-height time series is shown in Figure 2-24.

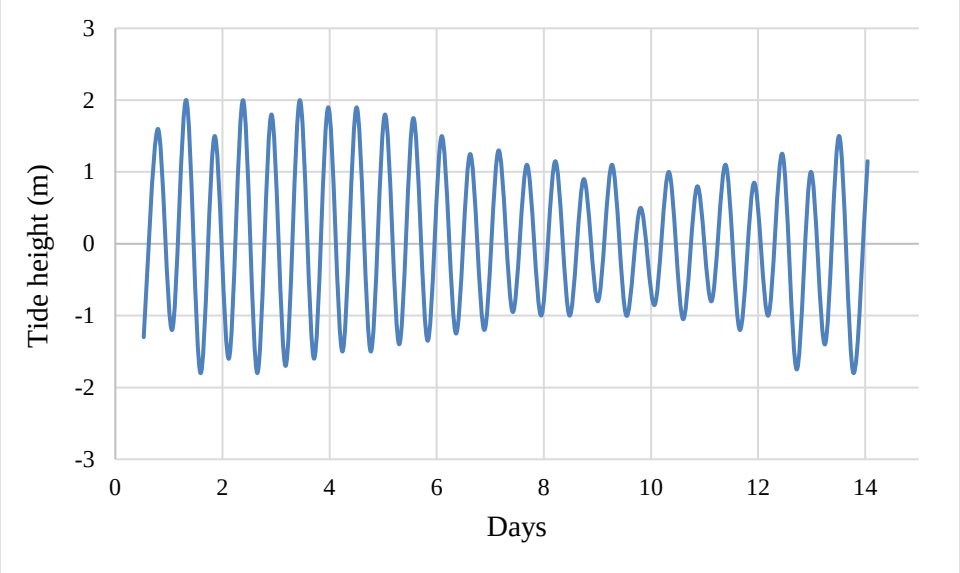

Figure 2-23. Typical pattern of tide around Ireland (Kennedy *et al.*, 2012)

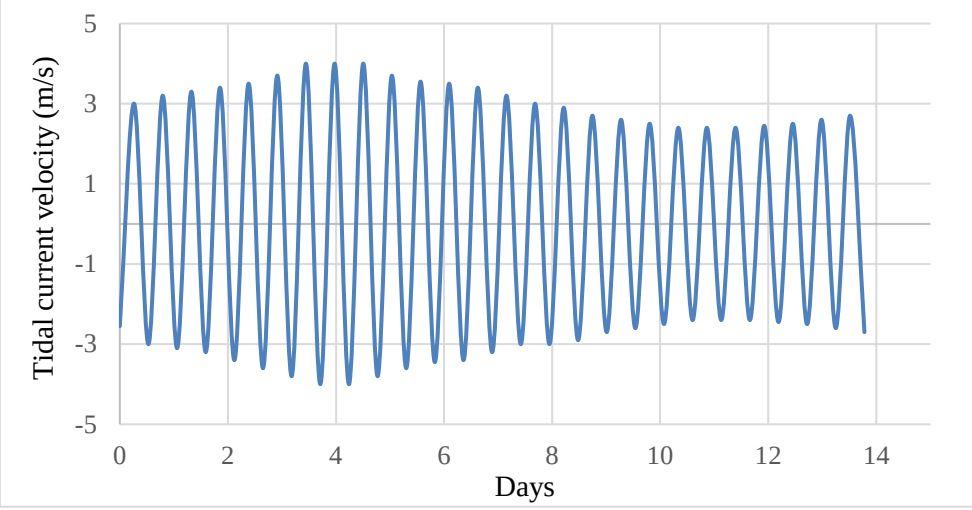

Figure 2-24. Tidal current velocity-time history corresponding to tide height pattern in Figure 2-23 (Kennedy *et al.*, 2012).

The tidal current flow over turbine blades, generates tangential and axial (thrust) forces which cause rotation of blade (powering the turbine) and flap-wise bending of turbine blade respectively. The tangential and axial forces can be calculated using BEMT or stream tube momentum methods. In chapter 5, it will be shown how tangential and axial forces acting on tidal turbine blades can be calculated using a hydrodynamic model. In addition in section 5.2, it will be shown how loading-time history can be estimated using tidal current velocity time-series.

In general, models for fatigue life prediction of tidal turbine blades focus on the maximum strain/stress, which is related to bending-induced strain/stress. This means that, corresponding to loading-time history calculated by hydrodynamic models, strain/stress-time series are developed over the fatigue critical elements (hot spot) on the blade. During each motion of tide, a rise and drop in the maximum stress/strain on a hot spot of the turbine blade occurs. In chapter 10 section 10.4, it will be shown how the loading-time series resulting from tidal current velocity-time series is applied in an FE model of a turbine blade to evaluate fatigue damage. This is done by using a methodology based on the strain-life approach and Miner's rule.

2.12.2 Waves, Shear Profile, Turbulence and Tower Shadow Effects

Tidal turbine blades are required to be able to survive hydrodynamic forces during their lifetime operation. These loads as shown in Figure 2-25, are due to the flow turbulence, shear current profile and surface waves (Milne *et al.*, 2010; Draycott *et al.*, 2017). These loads are contributors to fatigue loads of tidal turbine blades.

Tidal turbine blades are vulnerable to failure because of the cyclic stresses/strains brought on by the changes in inflow velocity. As mentioned above, the sources of these inflow changes, are waves, shear, turbulence and profile of velocity which exist in tidal currents. The variations in inflow velocity, induce thrust load on turbine blades which result in cyclic stress/strain on the blade.

The effects of wave motions, shear profile and inflow turbulence are not uniformly spread in the sea water column, therefore, the interaction between blade rotation and flow variations creates a non-uniform and varying axial load configuration across the rotor plane of the turbine blade. These axial loads on the blade can cause a flap-wise bending moment. Figure 2-26 shows schematically a tidal turbine blade operating in non-uniform marine flow environment and the scattering of axial loads along the span of the blade is pictured.

In fact, waves in the flow cause fatigue of turbine blade in a similar way to tidal currents, in that they result in velocity fluctuations in the incoming flow to the turbine that translate into loading fluctuations. The difference is the timescale of each, with tidal current varying over about 12 hour period, whereas waves in the field would have a period typically between 4-10 seconds.

The degree of wave loading that a turbine blade must resist is dependent on the location where turbine blade is installed in water column. Turbines that are installed on the seabed in a deep water column, are not subjected to substantial wave loading, however, turbines that are installed near the surface of sea water must resist considerable wave loading. Also other factors associated with waves which can affect the degree of wave loading that a turbine blade experiences, are; wave height, wavelength, wave orbital motion and wave vertical/horizontal velocity component.

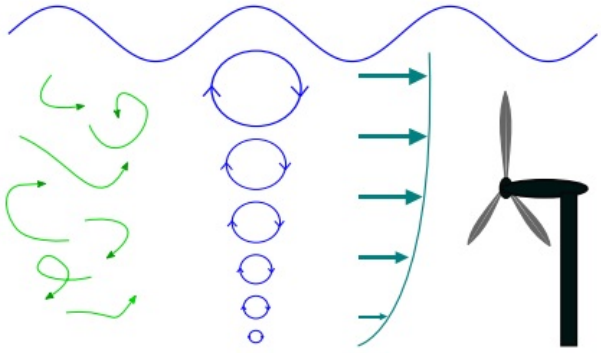

Figure 2-25. Schematic of the cause of unsteady hydrodynamic forces acting on a tidal turbine blade. the effect of turbulence (green arrows), wave (blue circles) and shear flow (dark green arrows) (Draycott *et al.*, 2017).

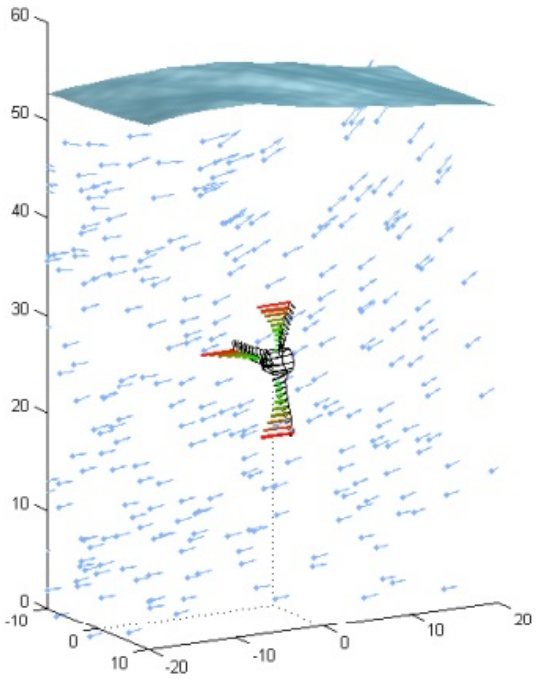

Figure 2-26. Distribution of axial (thrust) loads across the blade which is due to the inflow caused by the surface wave on the turbine blade, shown by red and green directions (Nevalainen, 2016).

Researchers around the world have used many simulation/numerical and experimental methods such as BEMT and small scale experiments, in order to characterize and predict the hydrodynamic loads caused by the surface waves and shear profile on tidal turbine blades (Faudot and Dahlhaug, 2012; Nevalainen, 2016; Draycott *et al.*, 2017).

Another source of fatigue is the tower shadow effect, which is due to the support structure. This happens when the turbine blades passes by the tower and therefore it causes a shadow effect in the water flow. In fact every time the turbine blades pass the support structure they will see a different load because the support structure affects the current velocity (Figure 2-27). This can disrupt the tidal flow experienced by the blade each time a blade passes the support structure. The support structure causes a periodic reduction in the tidal current velocity. This can lead to a reduction in forces and consequently a reduction on maximum bending stresses/strains on the turbine blade (Kennedy *et al.*, 2012).

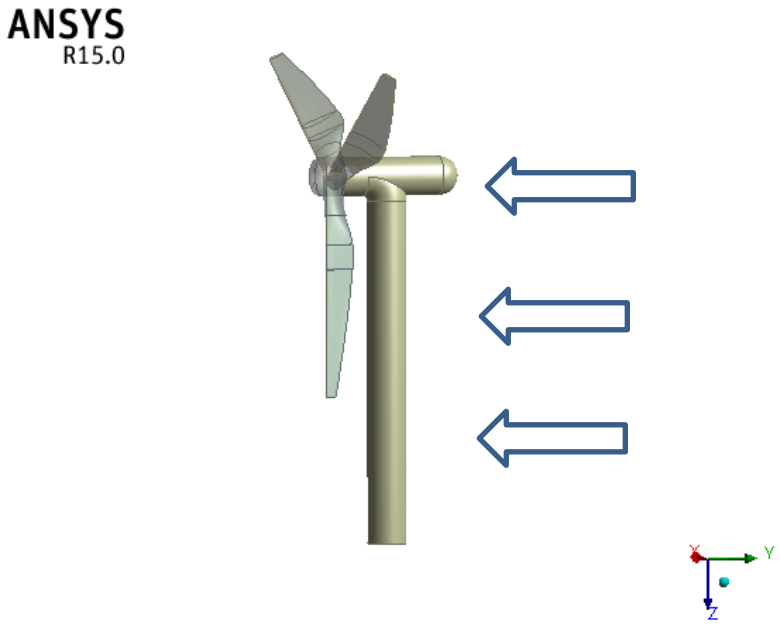

Figure 2-27. Effect of support structure (tower) shadow on turbine blade.

It is clear that marine flow environment has high levels of turbulence intensities, surface waves, and shear profile and these inflow variations will ultimately cause variations of loads on tidal turbine devices and they can cause fatigue of tidal turbine blades. However, this study will only investigate the effects of cyclic loads due to the variations in tidal current velocity, thus ignoring the additional variation brought on by the wave-current interaction, tower shadow effect, turbulence and shear profile.

2.13 Fabrication Processes of Composite Wind/Tidal Turbine Blades

In the early development of wind energy industry, the main manufacturing technology for wind turbine blades were wet hand lay-up (for small and medium blades) and filament winding (for larger blades). Nowadays resin infusion technology is the dominant manufacturing process.

In the wet lay-up process, layers of fabrics (e.g. woven, bonded, stitched) containing fibre reinforcement, are combined with resin to produce laminate. This process is usually done by manually placing reinforcement materials in the tool/mould and then the layers of reinforcement materials (glass or carbon) are impregnated with a resin. The resin system is applied by pouring and brushing/rolling. Layup is made by putting layers upon layers. This process continues until the desired thickness of laminate is obtained. In the next step curing is required in which, depending on the type of resin, curing can be done at room temperature or using heat. Using vacuum bagging systems are highly recommended for improving resin distribution and producing high quality laminated components. (Lind and Richards, 1984). In terms of turbine blades, the blade skins and spar were then bonded using paste adhesive.

In the filament winding technique, reinforcement materials (fabric) are wound around a mandrel. Before the winding process, the fabric is impregnated in a resin bath. The final products in this process are usually tube-shaped. For turbine blades, tubular spars are wound and then leading and trailing edge are included. The final mechanical properties of composite components made by this method is controlled by fibre orientation (Lind and Richards, 1984).

The introduction of prepreg, vacuum infusion, pultrusion and advanced fibre placement technologies have made positive contribution for improving the quality of manufacturing process of composite turbine blades (Araj *et al.*, 1991; Schaff and Davidson, 1997).

In the prepreg technology, semi-finished fabrics which are pre-impregnated with an uncured resin are produced. The resin is near-solid at room temperature. Layup of pre-impregnated materials (prepregs) is made by building layer upon layer into the mould surface. Vacuum bagging system and then heating is used to allow the resin to re-flow and cure (Daniel *et al.*, 1994).

Resin infusion technology is mainly used for manufacturing wind/tidal turbine blades. In the resin infusion technology, reinforcement materials are placed in a closed vacuum mould (i.e. between a mould and vacuum bag) and the resin system is injected into the mould. Once the volume between reinforcing fibres are filled by the resin, polymerization of resin occurs by

applying heat. The resin infusion technologies is classified into two categories: Resin Transfer Moulding (RTM) (resin is injected under pressure) and Vacuum Assisted Resin Transfer Moulding (VARTM) (resin injection under vacuum) (Beckwith, 2007).

Another commonly used method for manufacturing wind/tidal turbine blades is vacuum assisted resin transfer moulding. In VARTM method, layers of fabrics which are aligned in the direction along the span-wise of the blade, are placed on the mould along with polymer foam cores. To design a thick laminate at the blade root which becomes thin towards the blade tip, ply termination (ply-drop) is used meaning that most plies are terminated along the blade length at several positions. The fabrics are then enclosed by a vacuum bag (vacuum packed). By the application of vacuum, resin runs in and saturates the fibres. After infusion, curing of the resin and polymerization occur at room temperature.

In some tidal turbine applications other processes have been used, chiefly fibre placement and pultrusion techniqu. In the pultrusion process the reinforcement materials are impregnated with resin and pulled through a mould where the resin is subjected to polymerization. The impregnation is usually done by pulling the reinforcement materials through a resin bath (resin impregnator) where impregnation is conducted and then impregnated fibres (resin saturated fibres) enter into the mould.

In the advanced fibre placement method, pre-impregnated tows of fibres (i.e. bundles of resin-impregnated fibres with oval shaped cross-sectional appearance) are subjected to heating and compacting across a tool surface. In this method, a fibre placement machine places fibres on the tool surface in 0°, +45°, -45° and 90° orientation to produce a high quality laminate with good mechanical properties in all directions.

In this study commercial composites made by resin transfer moulding have been used throughout since this technology is commonly used in tidal turbine blades manufacturers.

Chapter 3

Experimental Methods

3 Experimental Methods

This project is concerned with the improvement of a methodology for fatigue life estimation of tidal turbine blades. A program of fatigue testing was employed to characterize the strain-life behaviour of composite material in air and sea water conditions. The test specimens are made up of biaxial woven GFRP. A Finite Element (FE) model of a turbine blade was established to predict the stresses/strains under typical hydrodynamic loading. The hydrodynamic loads were calculated using the stream tube momentum approach, based on tidal current velocities.

In order to predict the fatigue life of tidal turbine blades, a methodology is proposed which is depicted in Figure 3-1. The methodology incorporates: (a) a hydrodynamic model to calculate the tangential/axial forces on blade; (b) an FE structural model to predict the mechanical and fatigue behaviour of the blade; (c) cyclic and quasi static mechanical tests at the laboratory scale in sea water and air to provide data for lifetime prediction.

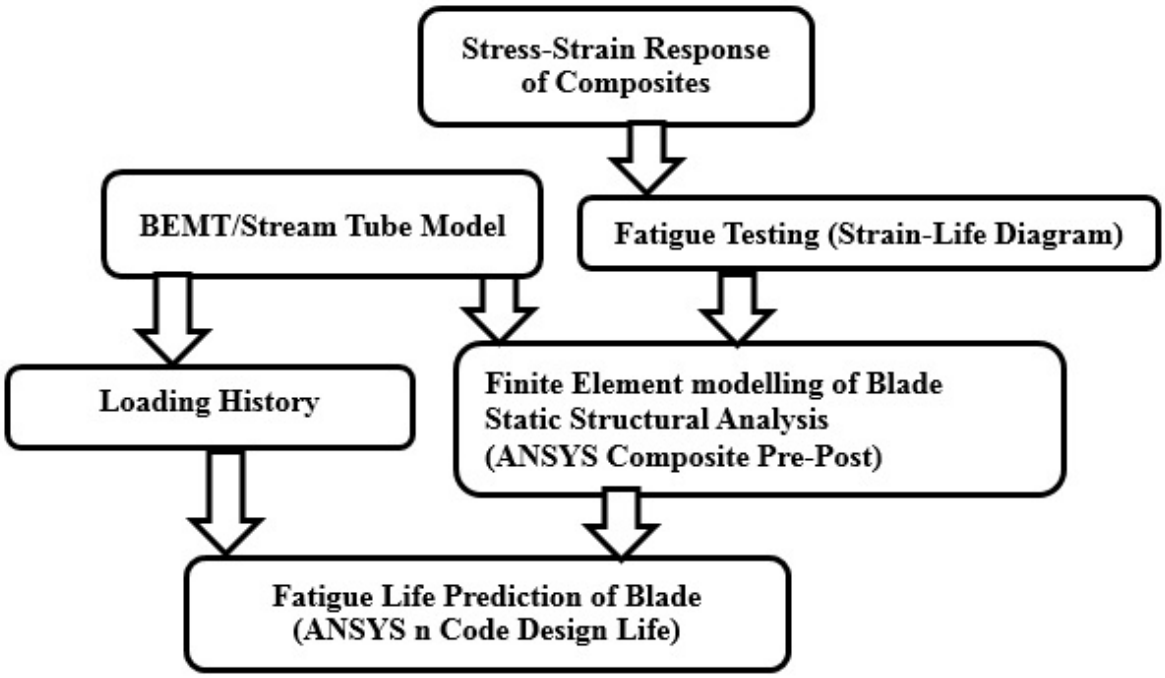

Figure 3-1. Flowchart of Life Prediction methodology.

In this work in order to estimate the fatigue behaviour of a composite blade, a full blade design was modelled using the FE software ANSYS and material properties determined from laboratory static and fatigue tests. Characterization techniques including Light Microscopy, SEM/EDX Full Field Measurement (DIC technique) and X-ray micro-computer tomography

were employed to investigate damage development and failure mechanisms occurring in test samples. The loads applied to the surface of FE model of blade were determined using a hydrodynamic model and the distribution of obtained forces were imported into a structural model of a representative blade design.

Microstructural analysis was used to observe fibre orientation and the stacking sequences of the plies which were then used in ANSYS Composite Pre-Post (ACP) to define the composite material properties. After importing experimental results such as the tensile and shear elastic modulus, Poisson's ratio, and S-N curves, the mechanical behaviour of the blade under predicted loads can be estimated. ANSYS n Code design life was then employed to predict the fatigue life of tidal turbine blade subjected to cyclic bending loads from the velocity fluctuations in sea water currents.

3.1 Hydrodynamics of a Tidal Turbine Blade

The tidal currents flow over the tidal turbine blades, producing lift and drag forces which are then translated to tangential (power producing) and thrust load (bending of blade). In order to transfer the tidal current flow velocity into lift and drag forces, a 2-D aerofoil is used to make up the blade. The foil series used in this study is NACA4415, for which the maximum camber height is 4% of chord length, maximum camber location is at 40% of the chord length from the leading edge and the ratio of thickness to chord length is 15. Figure 3-2 shows the aerofoil characteristics. Camber allows the foil to generate lift at a certain incidence angle. The NACA4415 aerofoil has been chosen because it is widely used in the wind turbine sector. Drag and lift coefficients for different sections along the blade can be found using the XFOIL code (Drela and Youngren, 2008).

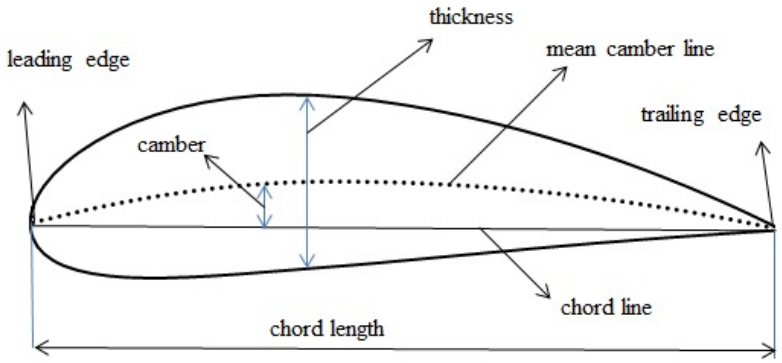

Figure 3-2. Aerofoil characteristics.

3.2 Materials

A large variety of alloys and metals have been efficiently substituted by composites in marine applications. This is due to the advantages of specific strength and stiffness of composites. In FRP composites the fibres are protected from abrasion, scratch, wear and environmental effects by the neighboring matrix. The reinforcing fibres are responsible for the high stiffness and strength. The polymer matrix has a great effect on inter-laminar shear strength which is vital for applications under flexural loads.

The composite material studied in this project is a multi-layered cross woven composite with an epoxy resin matrix reinforced with glass (commercially known as G10). This type of low cost composites is used in the construction of tidal turbine blades and are expected to withstand severe static and cyclic bending stresses in the marine environment where they operate. The as-received materials were 1.2m×1.2m×0.005m plates.

In terms of manufacturing process, resin transfer moulding (RTM) has been used to produce G10 composite. In this method, the plates are created by stacking multiple layers of glass fabric, then the layers are impregnated by injecting epoxy resin under pressure and finally the composite plates were cured at room temperature in air. In the RTM process multiple reinforcement layers are impregnated using pressure in a sealed and closed mould. In this method, reinforcement materials are placed in a closed vacuum mould (i.e. between a mould and vacuum bag) and the resin system is injected into the mould. The resin is driven into the mould under pressure, moving the air through openings. This continues until the mould is occupied completely by resin. Once the volume between reinforcing fibres are filled by the resin, polymerization of resin occurs.

The mechanical properties of G10 composite are reported in appendix 2. The chemical composition of fibre and matrix system, fibre volume fraction and weave style provided by the manufacturer are given in Table 3-1.

Table 3-1. Information of GFRP material commercially known as G10. The composite was provided by Attwater Group ('Attwater and Sons Ltd,').

Type of Fibre	E-glass
Chemical composition of fibre	$SiO_2$52-56%, $Al_2O_3$12-16%, CaO16-25%, MgO0-5% ($B_2O_3$5-10%) Na_2O+K_2O less than 2%
Type of matrix	Epoxy resin based on Bisphenol A cured and cross-linked with an amine hardener
Chemical composition of matrix	$(CH_3)_2C(C_6H_4OH)_2$
Fibre volume fraction	40%
Weave style	Plain woven fabric (Figure 3-3)
Manufacturing process	RTM

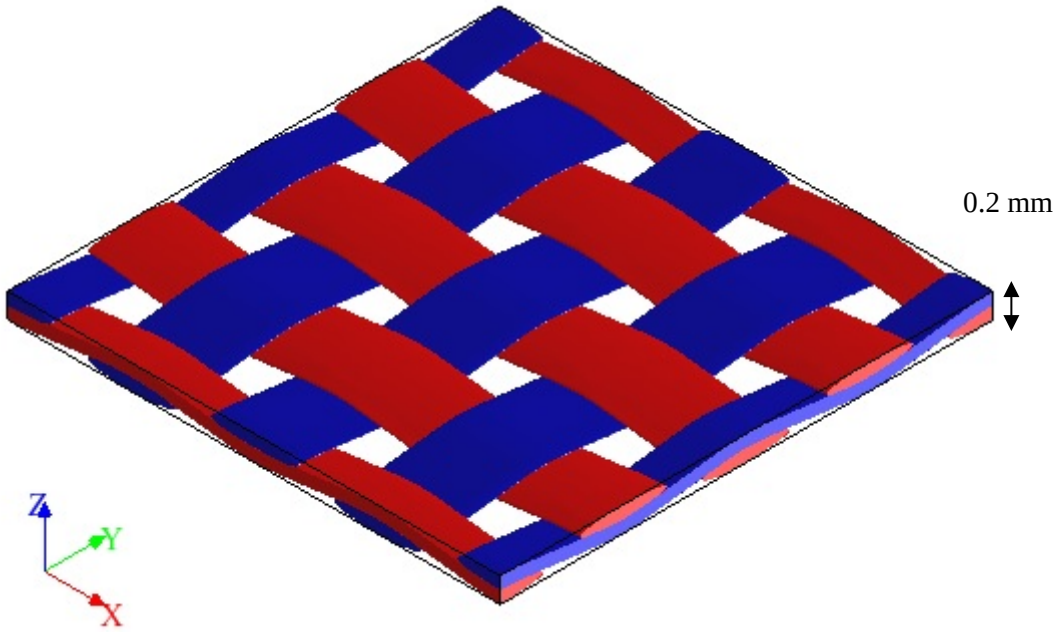

Figure 3-3. Schematic of plain woven fabric (G10 composite), (ply thickness: 0.21 mm).

3.2.1 Glass transition Temperature

The Glass Transition Temperature (T_g) is one of the most important properties of any epoxy resin systems. It is a temperature region where the thermosetting polymer changes from a hard and rigid state to a soft and rubbery state. In other words it is a temperature range over which the mobility of the polymer chains escalates. Therefore, epoxy resin experiences a softening (phase change) when heated above this temperature.

Humidity can affect the glass transition temperature of polymers. In particular moisture absorption reduces the glass transition temperature of polymeric materials. Therefore, the maximum operating temperature of polymeric materials should be lower than a certain fraction of the glass transition temperature, otherwise components and/or structures made up of polymeric materials will experience thermally induced failure. As a results, in both wind and tidal turbine blades made of FRP composite, the glass transition temperature of matrix system should be much higher than service conditions to avoid softening of polymer after humidity exposure. Typical composite tidal turbine blades are expected to operate in a sea water environment for at least 20-25 years and therefore FRP composite blades will be affected by moisture absorption so that the glass transition temperature of composite tidal turbine blades is critical. In this study, the glass transition temperature (T_g) of the epoxy resin which is the matrix component of GFRP was measured by the means of Differential Scanning Calorimetry (DSC) to be around 146℃ (Figure 3-4). The GFRP composite samples are subjected to fatigue loads in a tank of sea water at room temperature, so the maximum operating temperature of the composite samples is well below the T_g of the epoxy resin used here and softening after water exposure is not very likely to occur.

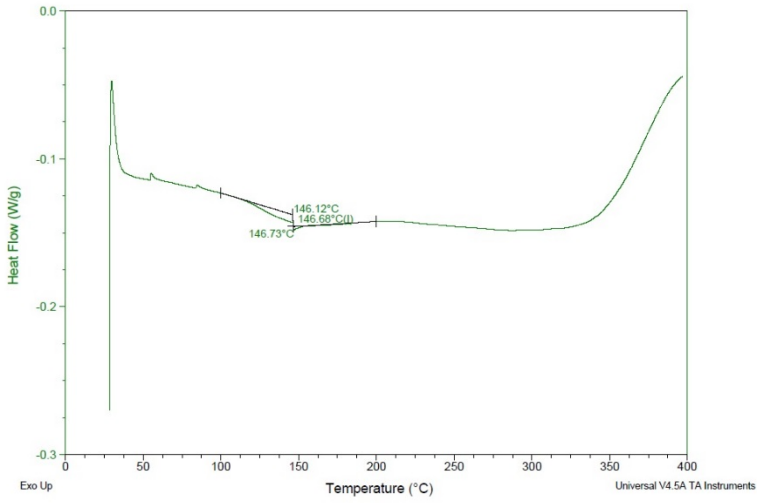

Figure 3-4. Heat flow versus temperature obtained by DSC method showing glass transition temperature.

3.3 Mechanical Tests

In order to investigate the effect of anisotropy and fibre orientation on GFRP composites mechanical behaviour, the composite specimens were cut at 0°/90°, 15°/75°, 30°/60° and ±45° fibre orientations (Figure 3-5).

A universal tensile test machine coupled with a DIC measurement set up were used for all tests. During the mechanical tests the camera was positioned perpendicular to the surface of the specimens to record the deformation and strain. The camera features a spatial resolution of 0.0055mm/pixel with the speed of 50fps and was equipped with lenses of 0.193 magnification and a working distance of 309 mm. In order to get enough light falling on the camera's sensor, the shutter speed and aperture size were adjusted accordingly. Although a longer shutter speed and a larger aperture size allows more light to pass through the lens and results in a brighter image, it is vital that none of the pixels within target are over exposed. The video gauge controller highlights any parts of the image that are overexposed in yellow. If the target areas were over exposed, the image brightness was reduced by lowering the shutter speed and reducing the aperture size. The ideal image brightness was achieved when the image was as bright as possible without any target areas containing over exposed pixels. Adjusting the aperture size also affects the depth of field. Reducing the aperture increases the depth of field while enlarging the aperture decreases it. During the deformation of the sample, digital grey scale images of the surface were taken every two seconds.

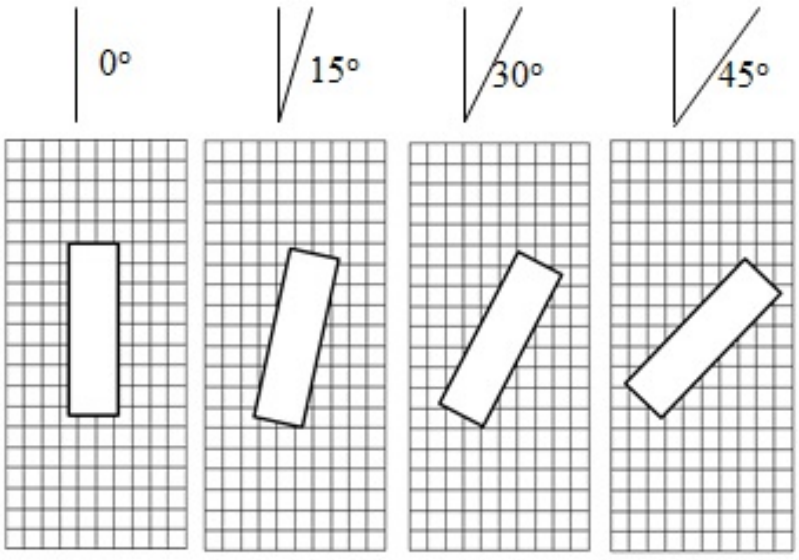

Figure 3-5. Four configurations were selected for the bending and tensile testing, namely the 0°, 15°, 30°, 45° orientation with respect to the main loading axis, Location and direction of specimens cut from composite plate.

3.3.1 Three Point Bending (3PB) tests

Three point bending (3PB) tests on composite specimens were carried out using a Tinius Olsen (25kN) test machine at a speed of 2mm/min, according to the BS EN 14125 (BSOL, 2011).

The machine was also equipped with a video gauge (DIC measurement set up) to record the deflection and strain during the test. Bar specimens of dimension 150mm×15mm×5mm were cut from the plate in accordance with the standard BS EN 14125 (BSOL, 2011) for static and fatigue tests with the 3PB configuration.

The test specimen is a flat rectangular beam with a constant cross-sectional area. The specimen geometry is shown in Figure 3-6. As shown in Figure 3-7 in the flexural test, one loading roller and two supporting rollers are employed and the specimens is tested with a span to thickness ratio of 20. The distance between the supports was 100 mm and the diameter of each support was 4 mm. The loading roller had a diameter of 10 mm and was adjusted to move at 2 mm/min. During the test, a load cell and the video gauge record the load-displacement data. Force-displacement data was converted to stress-strain curves for all samples by applying standard bending equations (3-1) from BS EN 14125 (BSOL, 2011), where *F* is the force applied by the loading roller, *L* is the distance between supports, *h* and *b* are thickness and width of the test coupon respectively, *D* is the vertical deflection of sample at centre (vertical deflection of loading roller) and *k* is the slope of the tangent to the linear portion of the load-displacement curve. According to beam theory (BSOL, 2011; Allen, 2012), the flexural applied stress, flexural modulus of elasticity, effective flexural elastic modulus and strain are given by the following equations:

$$\sigma_f = 3FL/2bh^2$$

$$\varepsilon_f = 6Dh/L^2$$

$$E_f = L^3k/4bh^3$$

$$E_{Effective} = FL^3 \Big/ 4bh^3D_f$$

3-1

Where $\boldsymbol{D_f}$ is the maximum deflection at the center of sample. At least five specimens were used for each test performed to obtain average results. In this test method, loads were measured by a load cell attached on the loading ram and displacement was recorded at mid span by using DIC measurement set up. The DIC technique is based on the recognition of geometrical changes in the grey intensity distribution of surface speckle patterns before and after deformation (Chu *et al.*, 1985; Sun *et al.*, 1997; Zhang *et al.*, 2006; Brynk *et al.*, 2012). Speckle patterns were applied by alternately spraying white and black paint at the test specimen surface prior to mechanical tests. An investigation of the fracture surface was carried out by the means

of scanning electron microscope (SEM). Prior to the SEM examination the fracture surface was sputter coated with gold to prevent charging.

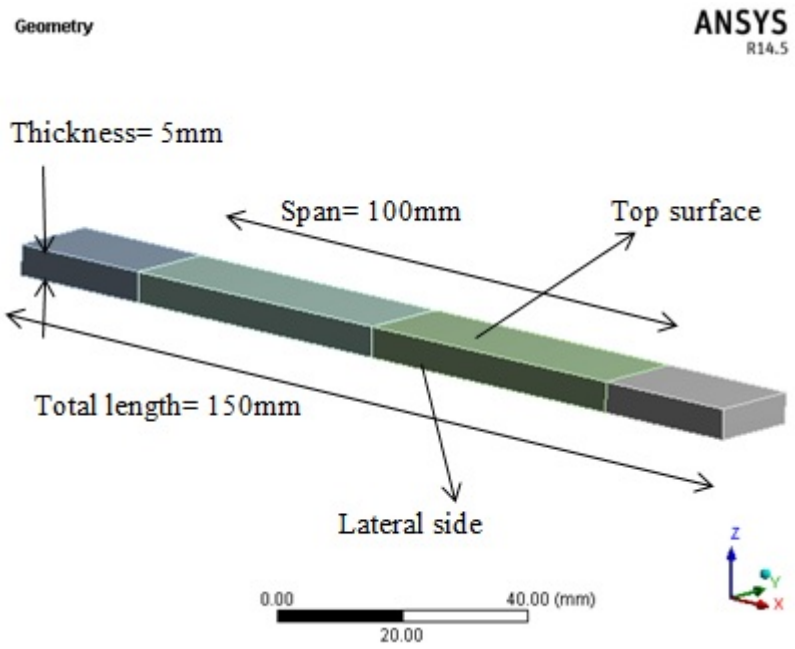

Figure 3-6. Specimen geometry used for 3PB tests.

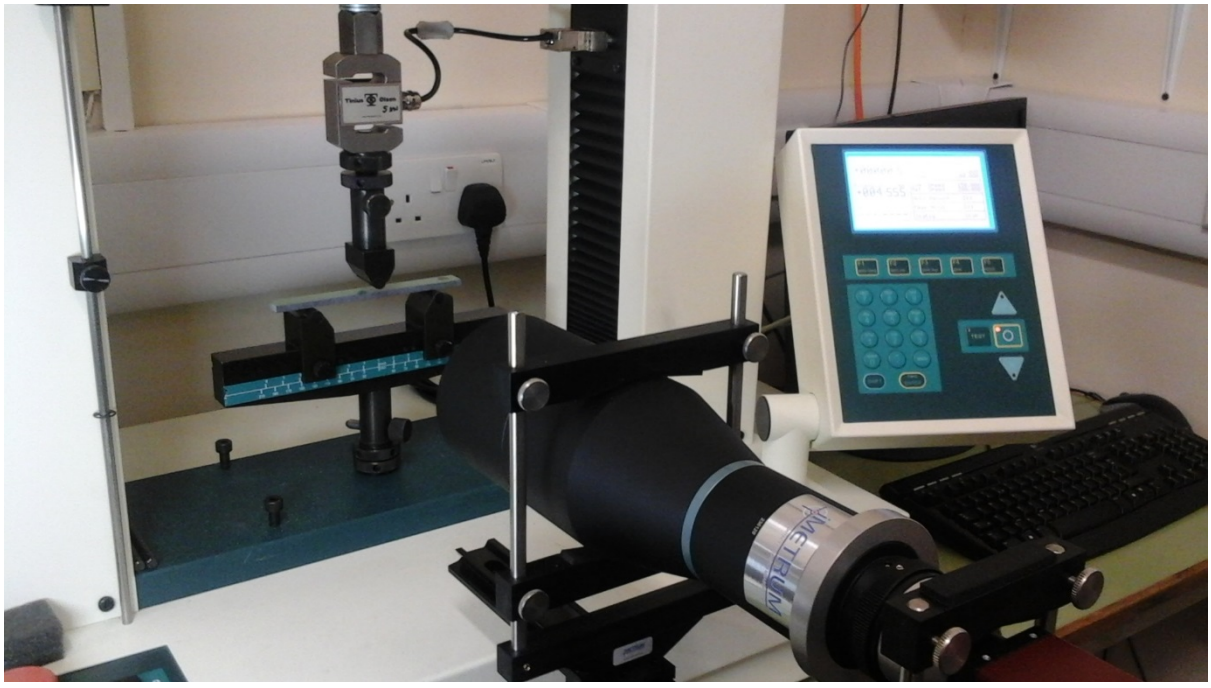

Figure 3-7. Experimental set up for a 3PB test including camera used for DIC set up.

3.3.2 Tensile Test

Bar specimens of dimension 150mm×20mm×5mm were machined from the initial plates. The specimen has a dog-bone shape and is shown in Figure 3-8. Rectangular end-tabs were bonded to the gripping area of each test specimen. The employment of end tabs during testing not only reduce stress concentration but also prevent slipping of the test specimen from the grip where the tooth of the grip indented the tab. The tensile properties were measured in accordance with the BS EN 2747 (BSOL, 2006). A Tinius Olsen 50kN testing machine (Figure 3-9) and a digital controller were used. Tensile test samples were loaded at 2 mm/min crosshead displacement rate and a video gauge (DIC measurement set up) was used to measure the strain. An investigation of the fracture surface was carried out by the means of SEM. Prior to the SEM examination fracture surface was sputter coated with gold to prevent charging.

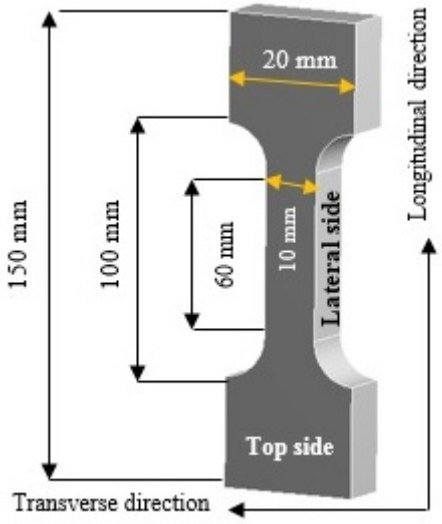

Figure 3-8. Specimen geometry used for tensile tests and defined nomenclature

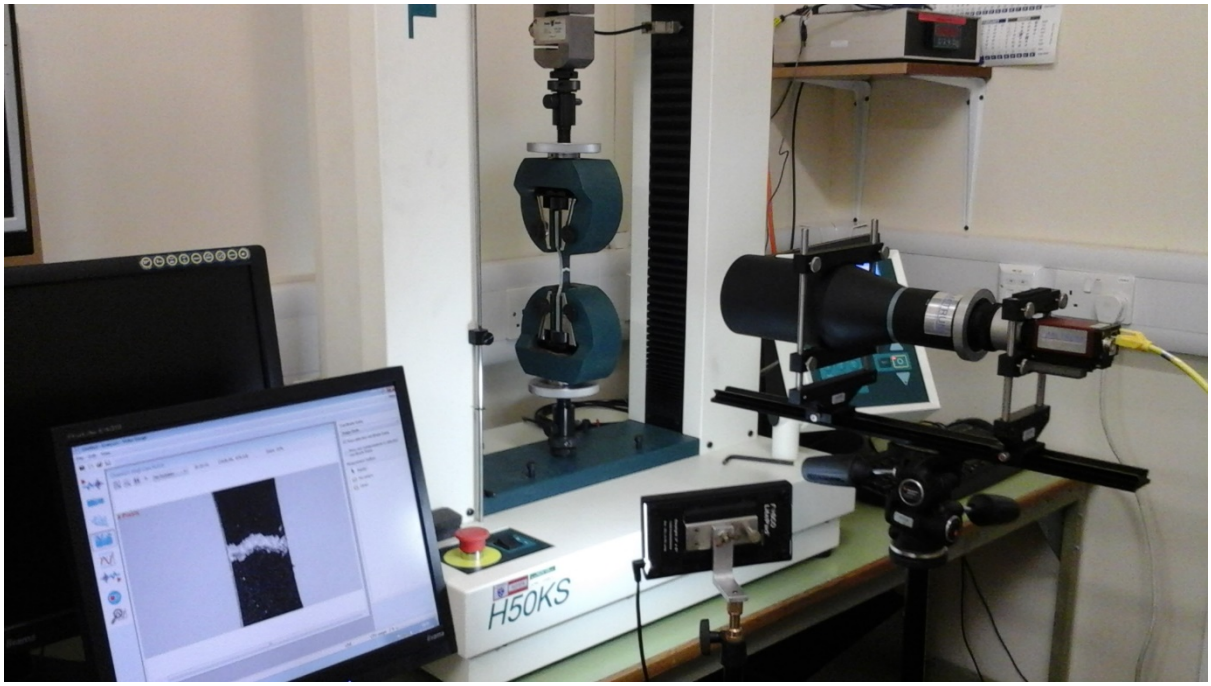

Figure 3-9. Experimental set up for tensile testing including DIC set up.

3.3.3 Shear Test (Iosipescu Test Method)

Due to the anisotropic nature of FRP composites, a specific test method is required to determine the shear properties of these materials. Many FRP composites fail due to shear stresses. Shear behaviour of FRP composite laminates is usually evaluated through either inter-laminar shear or in-plane shear testing. FRP composites have low shear modulus in comparison to their longitudinal elastic modulus (Jalali Mosallam, 1998). In order to measure the shear strength/modulus of composites various methods have been developed. These methods include 3PB mode with different span to thickness ratio (Jalali Mosallam, 1998), torsion test (Davalos *et al.*, 2002), $\pm$45 degree off-axis tension (Kumosa *et al.*, 2002) and asymmetrical four-point bending (AFPB) (Slepetz *et al.*, 1978), however all of these test methods have some disadvantages, making them less reliable. The Iosipescu (V-notch) shear test method is one of the most efficient techniques for determining shear properties of FRP composites as specimen preparation is much easier compared to other methods (Walrath and Adams, 1983; Morton *et al.*, 1992; Odegard and Kumosa, 1999). Also in this test method, over the test region a pure and uniform shear stress state can be produced, therefore the outcomes are more useful. In addition, in the field of mechanical properties of FRP composites this test method has been widely accepted among researchers. The in-plane shear properties of multidirectional glass fibre reinforced composites have been investigated using the Iosipecsu shear test method. The

results show that due to the stress concentration at the free edges of the V-notch, premature failure of the composite specimen occurred (He *et al.*, 2002). In terms of composite shear strength, some investigators have considered the stress value corresponding to the ultimate load as the in-plane shear strength while, the first load drop in the load-displacement curves was considered as the inter-laminar shear strength (Bhatnagar *et al.*, 1995). In addition, the in-plane shear strength has been also defined as the ratio of the load prior to the non-linear behaviour over the cross-sectional area between the two notches (Khashaba, 2004). In this study, in order to perform the Iosipescue in-plane and inter-laminar shear testing, GFRP composite coupons were cut with two different directions detailed in Figure 3-13 (a) and (b). Conducting shear testing on composite in Figure 3-13 (a) and Figure 3-13 (b) results in in-plane shear and inter-laminar properties.

An Iosipescu shear test fixture was manufactured in accordance with the specifications (ASTM D5379/D5379M) (Standard, 2005), Figure 3-10. The left half of fixture is immovable firmly attached to the baseplate. By applying a force from the loading member of the testing machine, displacement on the V-notch specimen was achieved, so in the central region of the specimen between the two V notches, a state of shear was created. In each test, the sample was positioned in the fixture with correct alignment, and was loaded to failure at a cross head speed of 1mm/min. During the test, the entire face of the test coupon remains visible and failure progression was monitored with the aid of the video gauge. The experimental set up is shown in (Figure 3-11). During the shear tests, the deformation was recorded by taking images using a camera adjusted perpendicular to the face of the specimen in the mid-length region between the two notches.

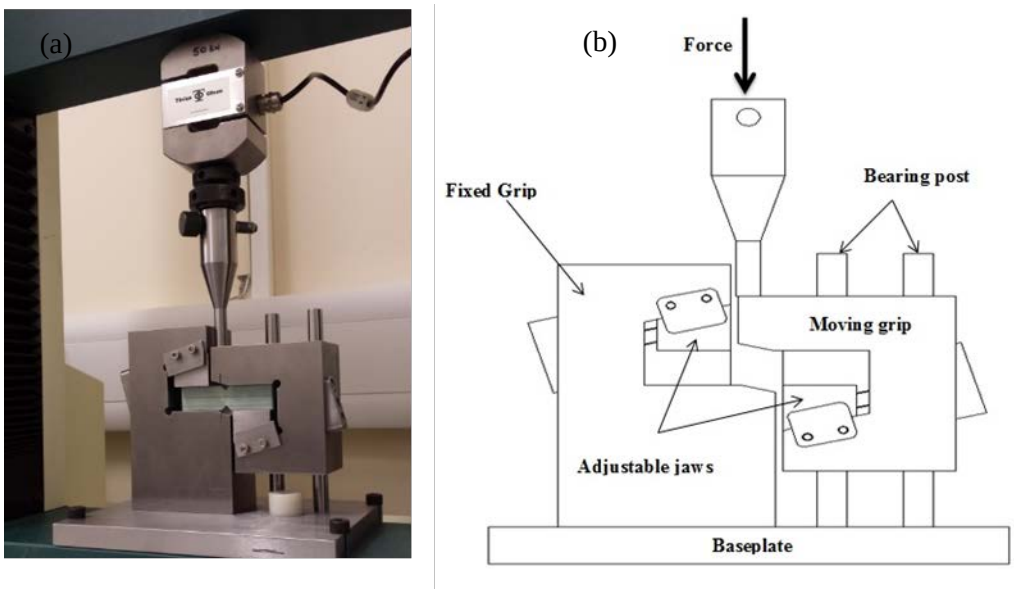

Figure 3-10. (a) Iosipescu shear test configuration, (b) Schematic of V-notched Beam Test Fixture.

Figure 3-11. Experimental set up for Iosipescu shear testing coupled with DIC system.

- ***Test Coupon Design***

The composite plates were cut to strips with dimension $76\times20mm^2$. The width of the specimen was then further machined to 19 mm. The final dimensions are shown in Figure 3-12. Two 90°

V-notches were machined on each side through the thickness of the shear test coupon with a depth of 3.8 mm. The radius of notch was 1.3mm in all specimens. In order to avoid buckling-induced failure the specimen thickness, *h*, was set to 5 mm, however the fixture shown in Figure 3-10 can accommodate a specimen up to 13 mm thick. By performing a shear test in any of the three directions, as defined in Figure 2-18 and proper machining the shear test specimen (shown in Figure 3-12), the in-plane and inter-laminar shear properties can be evaluated.

In-plane shear properties can be determined with the Iosipescu shear test by using laminated specimens as suggested in Figure 3-13(a). The inter-laminar shear properties are calculated using the specimen shown in Figure 3-13(b) and Figure 3-13(c). The shear strength of the specimens shown in Figure 3-13(c) is much lower than the specimens shown in Figure 3-13(b).

The composite plates were cut at two different ply orientation angles to give samples with two stacking sequences, (0°/90°,±45°). The composite coupons in the form of a rectangular flat strips with two V-notches, illustrated in Figure 3-12, were loaded in shear using the special fixture (Figure 3-10). The relative displacement between the two halves of the fixture loads the specimen in shear. By placing two virtual strain gauge elements provided by the DIC, oriented at ±45° to the loading axis in the middle of the sample, the shear strain and the shear modulus were determined.

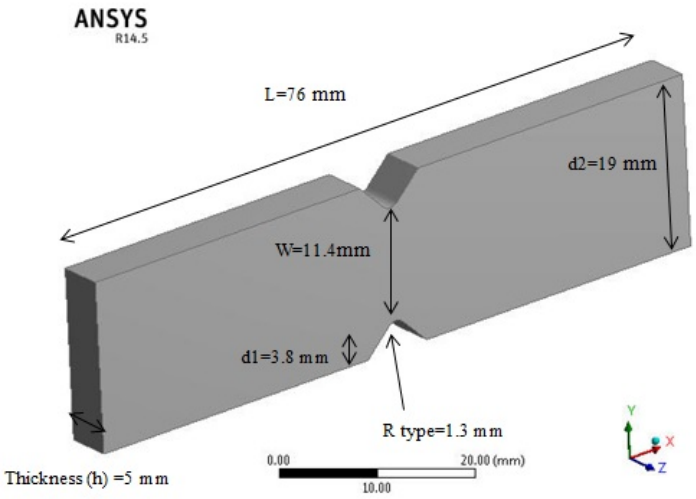

Figure 3-12. Schematic of the V-Notched Beam Test coupon.

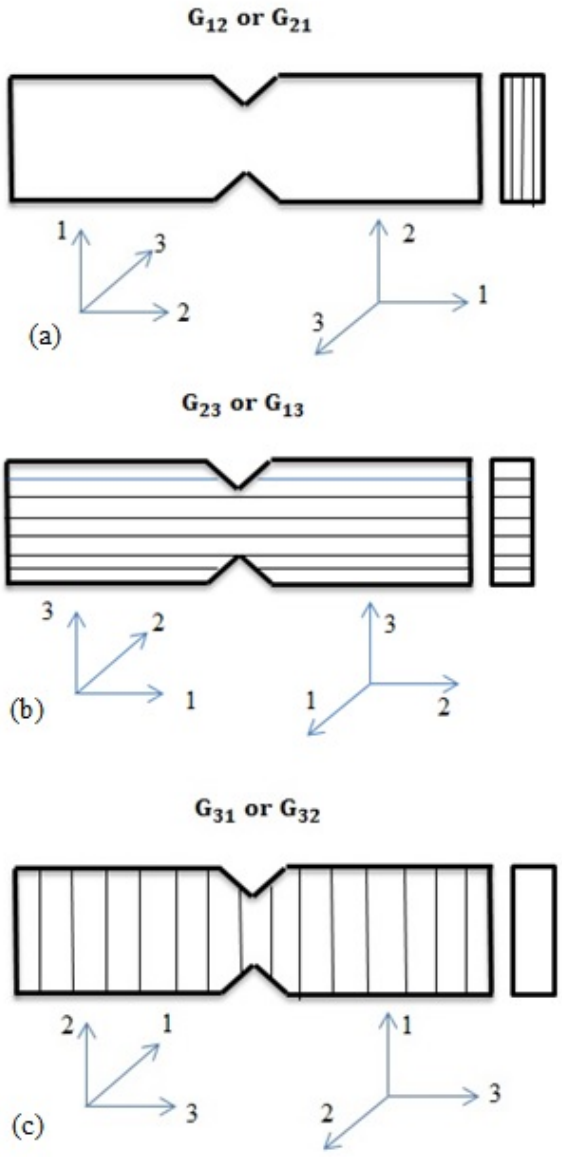

Figure 3-13. Possible fibre orientations for the shear test specimens. (a) In-plane shear testing, (b) inter-laminar shear testing, (c) out of plane shear testing

3.4 Digital Image Correlation (DIC) Measurements

In all mechanical testing, a camera was placed in front of the specimen. The image acquisition has been started as soon as the mechanical test began. The DIC method is based on the comparison of digital images before and after straining and tracking the displacement of a subset in a target area. The tracing process is viable when the object surface of the specimen has a random speckle pattern, which in this project was obtained by alternately spraying white and black paint. This artificial stochastic spot pattern on the specimen surface serves as the input pattern, however in most cases the natural characteristics of an unprepared specimen

surface is taken into account. By applying a random speckle pattern on the surface of the sample, each rectangle has a unique grey intensity distribution. The position of the subset after straining is calculated by minimizing the correlation criteria as below:

$$F(x, y, x^*, y^*) = \sum_{i,j=-t/2}^{t/2} (P(x+i, y+j) - P^*(x+x^*+i, y+y^*+j))^2$$

3-2

Where x, y = pixel coordinates, x^*, y^*=displacement vectors, t= subset size, $P(x+i, y+j)$= pixel intensity on the image before straining, $P^*(x+x^*+i, y+y^*+j)$= pixel intensity on the image after straining.

After coupling the mechanical test machine with the DIC and applying the deformation, the distorted grey scale pattern on the specimen surface is recognized based on the assumption that during the deformation, the grey intensity distribution around a pixel remains unchanged. 2D full field displacement/strain is determined at each facet centre from the change in the border coordinates containing the initial grey intensity distribution around the facet centre.

Digital images of the specimen surface were recorded with the frequency of 6 Hz. After the test, the series of digital images were processed using the DIC software, VIC-2D (Correlated Solutions). A field size or target area of (5×20mm) and (15×30mm) were defined on each initial image of the 3PB and tensile samples respectively (Figure 3-14).

In order to avoid the effects of micro-cracks created during the machining of the test coupons, 0.5 mm space was left unmasked at both lateral sides of tensile and bending specimens. The lateral side of the bending specimens was masked by spraying paint and for the tensile test specimen, the top surface was masked. The most important parameters related to calculations are facet size, t in equation (3-2), step size and interpolation type. The results were obtained with facet size of 30 pixels corresponding to 165**μ**m, step size of 10 pixels which is equal to a spatial resolution of 55**μ**m and bi-cubic interpolation.

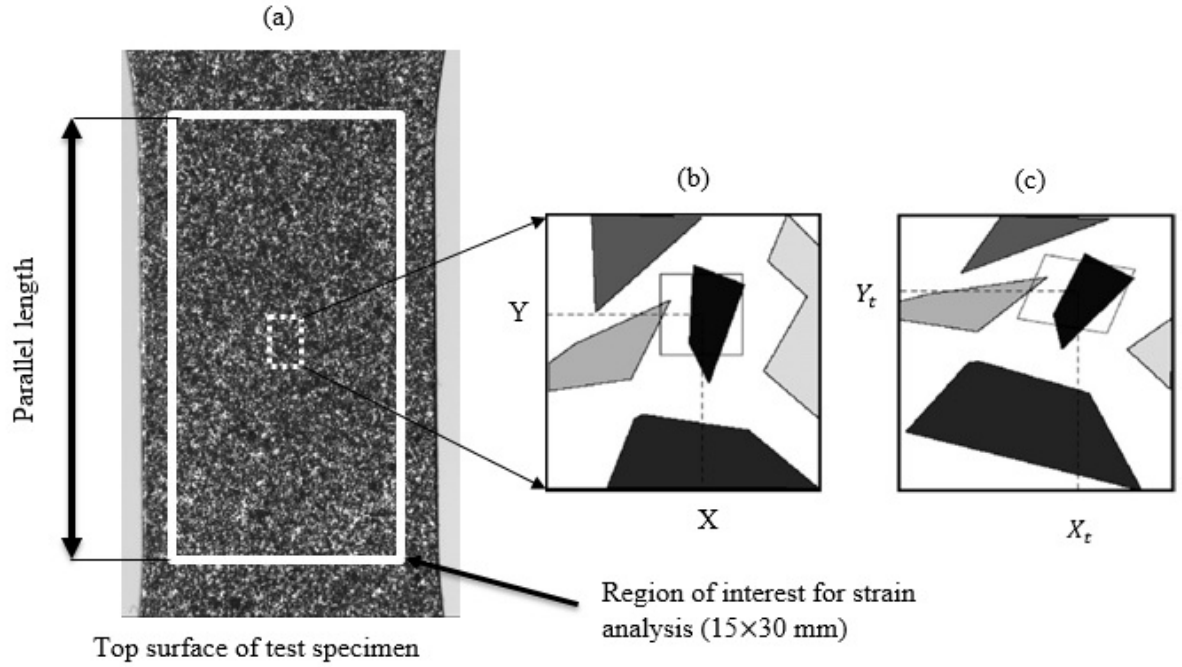

Figure 3-14. (a)The image of spray coated specimen showing stochastic speckle pattern and the region of concern for strain examinations, (b) initial image (before deformation), (c) distorted image (after deformation).

In order to get the strain maps, during the deformation, the displacement gradient tensor and the subsequent strain tensor were measured. A full field DIC measurement is determined by interpolating between pixel intensities. The longitudinal displacement and the strain measurement were correlated with the data recorded by the load cell and were used to provide stress-strain or load-displacement plots. The linear elastic portion of load-displacement curves was taken into consideration when determining elastic modulus. The optical extensometer function in the DIC technique, allows for fast calculation of all registered images of specimen surfaces since within this function the DIC software tracks only two facet positions and the distance between them. By applying this function both longitudinal/ transverse displacement and strain can be measured, therefore Poisson's ratio was also determined.

3.4.1 Specimen Preparation for Full Field Strain Mapping

In order to create stochastic white and black contrast patterns for DIC measurement, prior to mechanical testing the surface of the test coupons were sprayed with black and white spray paint using a technique that was found to produce an adequate speckle pattern after some trial and error. The quality of results obtained by the DIC technique strongly depends on the surface quality of original digital images (Clocksin *et al.*, 2002). The most crucial factors which need

to be considered before imaging are the effects of shadowing, over exposure of specimen surface and the size of the stochastic spot patterns. For example, if the size of the spray droplets is too big, the subset and the calculation step should be kept big and this can diminish the spatial resolution. Over-exposure or shadowing affects the grey intensity distribution in a subset, consequently the DIC procedure is unable to identify the same subset. This can lead to the loss of information.

3.5 Constitutive Relations in Non-isotropic Materials

3.5.1 Stress and Strain Relation

In isotropic materials, two elastic constant are needed to evaluate the stress-strain relation. However in orthotropic materials (e.g. composite materials), at least nine elastic constants are required to assess the stress-strain behaviour. In orthotropic materials, there are three mutually orthogonal planes of material property symmetry. Fibre-reinforced composites, in general, contain the three orthogonal planes of material property symmetry and are categorised as orthotropic materials. The material behaviour is called as especially orthotropic, when the normal stresses are applied in the principal material directions (either parallel or perpendicular to the fibre directions). Otherwise, it is called as generally orthotropic material which behaves similar to the anisotropic material. There are nine independent elastic constants in the stiffness matrix for an especially orthotropic material. With respect to the stress-strain behaviour when the normal stresses are applied in one of the principal material directions on an orthotropic material, elongation is created in the direction of the applied stresses and the contractions is created in the other two transverse directions. However, normal stresses applied in any directions other than the principal material directions cause both extensional and shear deformations.

In general, composite laminated plates experience stresses/strains in more than one direction within the plate and also Poisson's ratio can become involved in their stress-strain relationship (Reddy, 2004). Under the plane stress condition (stress through the thickness direction is ignored) for composite laminated plate assumed in this project, only the value of longitudinal modulus (E_1), in-plane transverse modulus (E_2), major Poisson's ratio (ν_{12}) and in-plane shear modulus (G_{12}) are required to define the orthotropic nature of the laminae (Grogan *et al.*, 2013), Therefore stress as a function of strain in the kth layer which is characterized as a specially

orthotropic lamina, by ignoring thermal and moisture effects, is evaluated by reduced stiffness (Q_{ij}) (Reddy, 2004).

$$\begin{bmatrix}\sigma_1\\ \sigma_2\\ \sigma_{12}\end{bmatrix}=\begin{bmatrix}Q_{11} & Q_{12} & 0\\ Q_{21} & Q_{22} & 0\\ 0 & 0 & Q_{66}\end{bmatrix}\begin{bmatrix}\varepsilon_1\\ \varepsilon_2\\ \gamma_{12}\end{bmatrix},\quad Q_{11}=\frac{E_1}{1-\nu_{12}\nu_{21}},\ Q_{22}=\frac{E_2}{1-\nu_{12}\nu_{21}},\ Q_{21}=\frac{\nu_{21}E_1}{1-\nu_{12}\nu_{21}}\ Q_{12}=\frac{\nu_{12}E_1}{1-\nu_{12}\nu_{21}}$$

$$Q_{66}=G_{12},\qquad \sigma_{33}=0$$

$$\begin{bmatrix}\sigma_{23}\\ \sigma_{13}\end{bmatrix}=\begin{bmatrix}Q_{44} & 0\\ 0 & Q_{55}\end{bmatrix}\begin{bmatrix}\varepsilon_{23}\\ \varepsilon_{13}\end{bmatrix},\ Q_{44}=G_{23},\ Q_{55}=G_{13}$$

3-3

For biaxial woven composite studied in this project $E_1=E_2=E$ and $\nu_{12}=\nu_{21}=\nu$

Therefore

$$Q_{11}=Q_{22}=\frac{E}{1-\nu^2}\qquad \text{and}\quad Q_{12}=Q_{21}=\frac{\nu E}{1-\nu^2}$$

3-4

For generally orthotropic lamina (i.e. when the loading direction does not correspond to the principal materials direction), the stress and strain components must be converted into coordinates that correspond to the principal materials direction and therefore, stiffness matrix is introduced by $\overline{Q_{ij}}$ (Reddy, 2004).

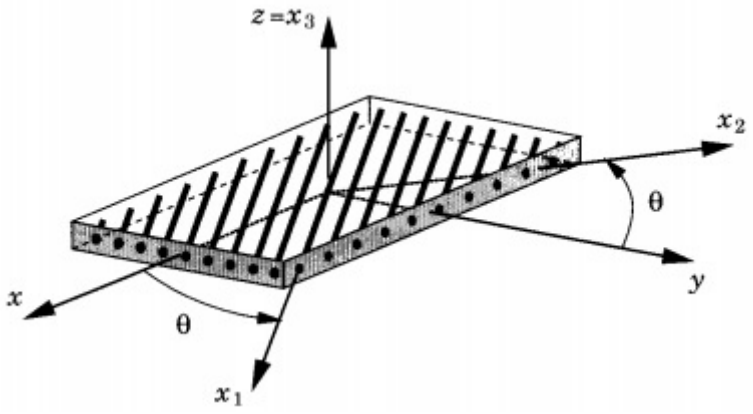

Figure 3-15, generally orthotropic lamina ((Reddy, 2004)

$$\begin{bmatrix} \overline{Q_{11}} & \overline{Q_{12}} & \overline{Q_{16}} \\ \overline{Q_{21}} & \overline{Q_{22}} & \overline{Q_{26}} \\ \overline{Q_{61}} & \overline{Q_{62}} & \overline{Q_{66}} \end{bmatrix}$$

$$\begin{bmatrix} \overline{Q_{44}} & \overline{Q_{45}} \\ \overline{Q_{45}} & \overline{Q_{55}} \end{bmatrix}$$

$\overline{Q_{11}} = Q_{11}m^4 + 2(Q_{12}+2Q_{66})m^2n^2+Q_{22}n^4$

$\overline{Q_{12}} = (Q_{11}+Q_{22} - 4Q_{66})\, m^2n^2 + Q_{12}(m^4+n^4)$

$\overline{Q_{22}} = Q_{11}n^4 + 2(Q_{12}+2Q_{66})m^2n^2+Q_{22}m^4$

$\overline{Q_{16}} = (Q_{11}-Q_{12} - 2Q_{66})\, m^3n + (Q_{12}-Q_{22} + 2Q_{66})\, mn^3$

$\overline{Q_{26}} = (Q_{11}-Q_{12} - 2Q_{66})\, mn^3 + (Q_{12}-Q_{22} + 2Q_{66})\, m^3n$

$\overline{Q_{66}} = (Q_{11}+Q_{22} - 2Q_{12} - 2Q_{66})\, m^2n^2 + Q_{66}(m^4+n^4)$

$\overline{Q_{45}} = (Q_{55} - Q_{44})\, mn$

$\overline{Q_{55}} = (Q_{55}m^2 - Q_{44}n^2)$

$m = cos\theta, n = sin\theta$

3-5

And therefore the stress-strain relation is;

$$\begin{bmatrix} \sigma_x \\ \sigma_y \\ \sigma_{xy} \end{bmatrix} = \begin{bmatrix} \overline{Q_{11}} & \overline{Q_{12}} & \overline{Q_{16}} \\ \overline{Q_{21}} & \overline{Q_{22}} & \overline{Q_{26}} \\ \overline{Q_{61}} & \overline{Q_{62}} & \overline{Q_{66}} \end{bmatrix} \begin{bmatrix} \varepsilon_x \\ \varepsilon_y \\ \gamma_{xy} \end{bmatrix}$$

$$\begin{bmatrix} \sigma_{yz} \\ \sigma_{xz} \end{bmatrix} = \begin{bmatrix} \overline{Q_{44}} & \overline{Q_{45}} \\ \overline{Q_{45}} & \overline{Q_{55}} \end{bmatrix} \begin{bmatrix} \varepsilon_{yz} \\ \varepsilon_{xz} \end{bmatrix}$$

3-6

3.5.2 Transformation of Stresses and Coordinate Transformations

The relationship between the components of stress in the problem (laminate) coordinates system *(x, y, z)* and material (Lamina) coordinate system (x_1, x_2, x_3) which can be obtained using the free body diagram (Reddy, 2004) is:

$$\begin{bmatrix}\sigma_1\\ \sigma_2\\ \sigma_{12}\end{bmatrix} = \begin{bmatrix} cos^2\theta & sin^2\theta & sin2\theta \\ sin^2\theta & cos^2\theta & -sin2\theta \\ -sin\theta cos\theta & sin\theta cos\theta & cos^2\theta - sin^2\theta \end{bmatrix} \begin{bmatrix}\sigma_{xx}\\ \sigma_{yy}\\ \sigma_{xy}\end{bmatrix}$$

or

$$\begin{bmatrix}\sigma_{xx}\\ \sigma_{yy}\\ \sigma_{xy}\end{bmatrix} = \begin{bmatrix} cos^2\theta & sin^2\theta & -sin2\theta \\ sin^2\theta & cos^2\theta & sin2\theta \\ sin\theta cos\theta & -sin\theta cos\theta & cos^2\theta - sin^2\theta \end{bmatrix} \begin{bmatrix}\sigma_1\\ \sigma_2\\ \sigma_{12}\end{bmatrix}$$

3-7 (Reddy, 2004)

3.5.3 Constitutive Equations for Laminates

Deriving the constitutive equations that relate the force and moment resultants to the strain in a laminate requires the use of classical laminate plate theory and equations of motion. Further details of above theory is discussed in (Reddy, 2004).

Through the thickness of a composite laminate (Figure 3-16), the stresses acting on the edge can be divided into increments and then integrated (Nettles, 1994). The resultant stress (N_x);

$$N_x = \int_{-h/2}^{h/2} \sigma_x (dz)$$

3-8

By assuming the same procedure for the y-direction and shear stress, three stress resultants are required in the form of matrix:

$$\begin{bmatrix}N_x\\ N_y\\ N_{xy}\end{bmatrix} = \int_{-h/2}^{h/2} \begin{bmatrix}\sigma_x\\ \sigma_y\\ \sigma_{xy}\end{bmatrix} dz$$

3-9

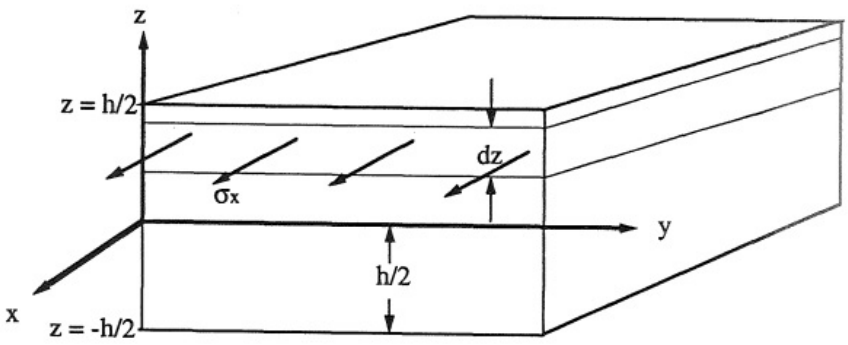

Figure 3-16. Force resultant on a plate element, total force in x direction = $\sum \boldsymbol{\sigma_x}\,(\mathbf{d_z})\mathbf{y}$ (Nettles, 1994).

From Figure 3-16, it is clear that the stress acting on an edge causes a moment about the mid-plane. Consequently by the same approach as for the stress resultant, the moment resultant in the form of matrix;

$$\begin{bmatrix} M_x \\ M_y \\ M_{xy} \end{bmatrix} = \int_{-h/2}^{h/2} \begin{bmatrix} \sigma_x \\ \sigma_y \\ \sigma_{xy} \end{bmatrix} z\, dz$$

3-10

With the reference to Figure 3-17 showing the numbering of plies used for the cross section of composite laminate plate , stress and moment resultant equations can be written;

$$\begin{bmatrix} N_x \\ N_y \\ N_{xy} \end{bmatrix} = \sum_{k=1}^{n} \int_{z_{k-1}}^{z_k} \begin{bmatrix} \sigma_x \\ \sigma_y \\ \sigma_{xy} \end{bmatrix} dz$$

$$\begin{bmatrix} M_x \\ M_y \\ M_{xy} \end{bmatrix} = \sum_{k=1}^{n} \int_{z_{k-1}}^{z_k} \begin{bmatrix} \sigma_x \\ \sigma_y \\ \sigma_{xy} \end{bmatrix} z\, dz$$

3-11

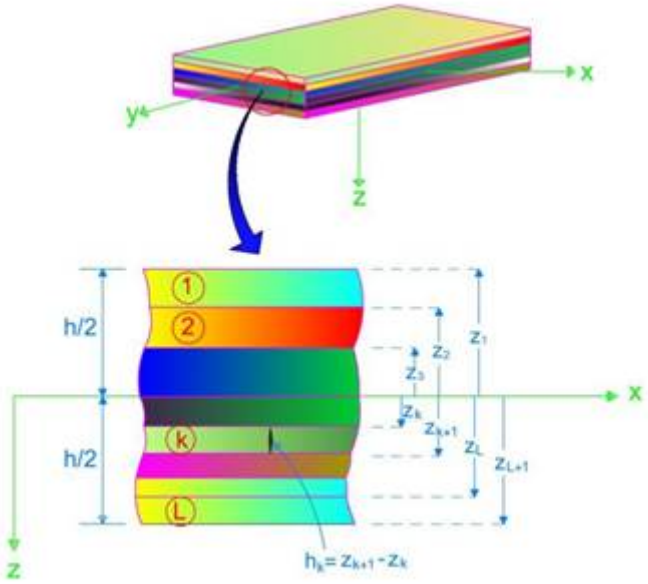

Figure 3-17. Numbering of plies used for cross section of composite laminate plate (Reddy, 2004)

Given the relation between strain and displacement (plate curvature and mid-plane strains) (Reddy, 2004) regarding the un-deformed and deformed geometries of the edge of a plate;

$$\begin{bmatrix} \varepsilon_x \\ \varepsilon_y \\ \varepsilon_{xy} \end{bmatrix} = \begin{bmatrix} \varepsilon_x^0 \\ \varepsilon_y^0 \\ \gamma_{xy}^0 \end{bmatrix} + z \begin{bmatrix} K_x \\ K_y \\ K_{xy} \end{bmatrix}$$

3-12

Where

ε_x^0, ε_y^0 and γ_{xy}^0 are mid-plane strain and K_x, K_y and K_{xy} are plate curvatures (Reddy, 2004).

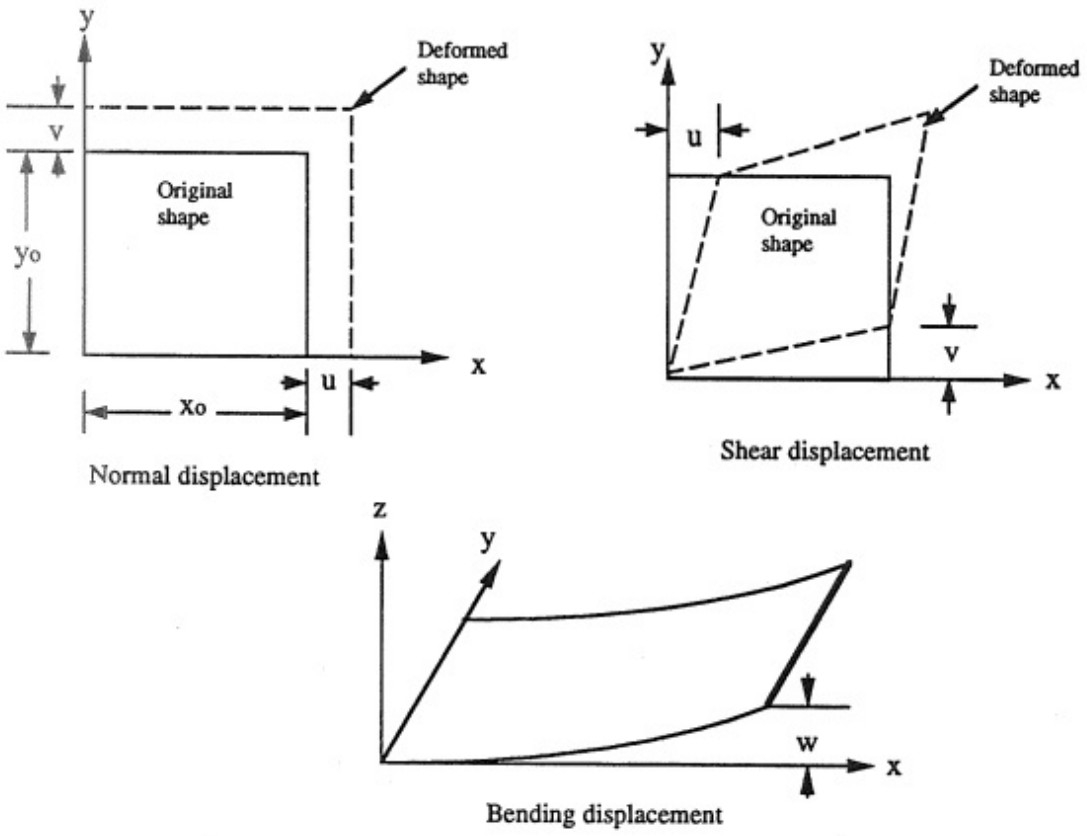

Figure 3-18, introducing normal, shear and bending displacements of a plate (Nettles, 1994)

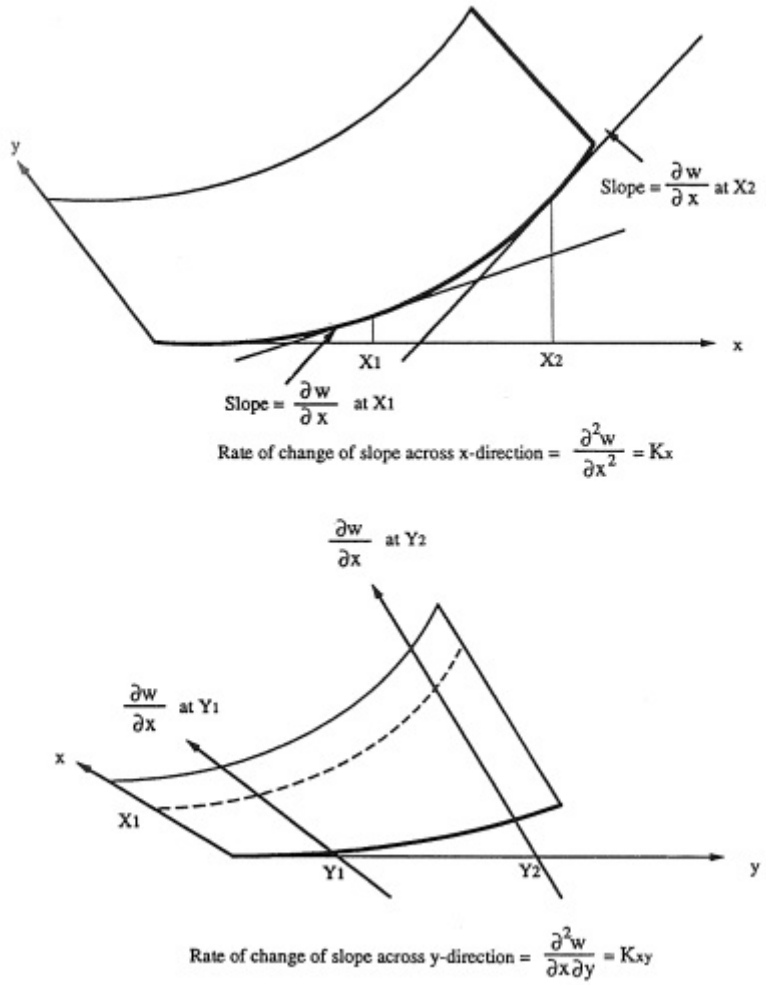

Figure 3-19. Introducing curvatures (Nettles, 1994)

By substituting equation (3-6) in (3-11) and given the equation (3-12), the constitutive equation for composite laminate can be written as:

$$\begin{bmatrix} N_x \\ N_y \\ N_{xy} \\ M_x \\ M_y \\ M_{xy} \end{bmatrix} = \begin{bmatrix} A_{11} & A_{12} & A_{16} & B_{11} & B_{12} & B_{16} \\ A_{21} & A_{22} & A_{26} & B_{21} & B_{22} & B_{26} \\ A_{61} & A_{62} & A_{66} & B_{61} & B_{62} & B_{66} \\ B_{11} & B_{12} & B_{16} & D_{11} & D_{12} & D_{16} \\ B_{21} & B_{22} & B_{26} & D_{21} & D_{22} & D_{26} \\ B_{61} & B_{62} & B_{66} & D_{61} & D_{62} & D_{66} \end{bmatrix} \begin{bmatrix} \varepsilon_x^0 \\ \varepsilon_y^0 \\ \gamma_{xy}^0 \\ K_x \\ K_y \\ K_{xy} \end{bmatrix}$$

3-13 (Reddy, 2004)

Where

$A_{ij} = \sum_{k=1}^{n} [\overline{Q_{ij}}](z_k - z_{k-1})$

B_{ij}=1/2 $\sum_{k=1}^{n}[\overline{Q_{ij}}](z_k{}^2\text{-}z_{k-1}{}^2)$

D_{ij}=1/3 $\sum_{k=1}^{n}[\overline{Q_{ij}}](z_k{}^3\text{-}z_{k-1}{}^3)$

3-14

Where z_k-z_{k-1} is the thickness of the kth layer.

Since in this work, the type of composite is a symmetric laminate, the geometric mid-plane is the neutral plane of the composite plate and all the components of the $[B]$ are equal to zero.

$[A_{ij}]$ is known as the extensional stiffness matrix and it shows the relation between the normal stresses and strains (Nettles, 1994).

$[D_{ij}]$ is known as the bending stiffness matrix and it shows the relation between the amount of plate curvature with the bending moments (Nettles, 1994).

$[B_{ij}]$ is known as the bending-extensional coupling stiffness matrix and it shows the relation between the bending strains and normal stresses (Nettles, 1994).

3.5.4 Investigation of Composite Laminated Plates (One-Dimensional Structure)

In composite laminated plates, when the width (*b*) of a plate is very small compared with the length and the loading is such that the deflections are only function of one direction, the composite laminate can be considered as a laminated beam (Reddy, 2004).

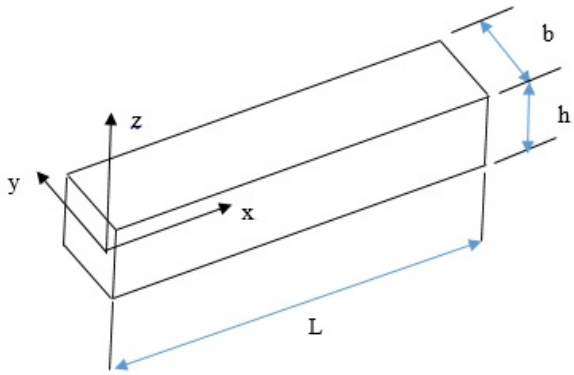

Figure 3-20. Beam (one-dimensional) structure (Mukhopadhyay, 2005).

- ***Exact analytical (closed-form) solution***

In this study, exact analytical solutions are developed for three point bending, tension and inter-laminar shear testing of GFRP composite, then the numerical solutions developed by computational Finite Element method (ANSYS) are verified by the closed form solutions.

For bending of symmetrically laminated beams according to composite laminated plate theory (Reddy, 2004), it is assumed that:

$$M_y = M_{xy} = 0$$

3-15

Therefore the constitutive equation of classical laminate plate theory for symmetric laminates are given by:

$$\begin{bmatrix} M_x \\ 0 \\ 0 \end{bmatrix} = \begin{bmatrix} D_{11} & D_{12} & D_{16} \\ D_{21} & D_{22} & D_{26} \\ D_{61} & D_{62} & D_{66} \end{bmatrix} \begin{bmatrix} K_x \\ K_y \\ K_{xy} \end{bmatrix}$$

3-16

And

$$\begin{bmatrix} K_x \\ K_y \\ K_{xy} \end{bmatrix} = \begin{bmatrix} d_{11} & d_{12} & d_{16} \\ d_{21} & d_{22} & d_{26} \\ d_{61} & d_{62} & d_{66} \end{bmatrix} \begin{bmatrix} M_x \\ 0 \\ 0 \end{bmatrix}$$

3-17

Where $[d_{ij}]$ is the inverted of $[D_{ij}]$

From (3-6) and (3-12), in-plane stresses in the Kth ply can be determined

$$\begin{bmatrix} \sigma_x \\ \sigma_y \\ \sigma_{xy} \end{bmatrix} = z \begin{bmatrix} \overline{Q_{11}} & \overline{Q_{12}} & \overline{Q_{16}} \\ \overline{Q_{21}} & \overline{Q_{22}} & \overline{Q_{26}} \\ \overline{Q_{61}} & \overline{Q_{62}} & \overline{Q_{66}} \end{bmatrix} \begin{bmatrix} K_x \\ K_y \\ K_{xy} \end{bmatrix}$$

3-18

By substituting (3-17) in the above equation:

$$\begin{bmatrix}\sigma_x\\ \sigma_y\\ \sigma_{xy}\end{bmatrix} = \frac{z}{b}\begin{bmatrix}\overline{Q_{11}} & \overline{Q_{12}} & \overline{Q_{16}}\\ \overline{Q_{21}} & \overline{Q_{22}} & \overline{Q_{26}}\\ \overline{Q_{61}} & \overline{Q_{62}} & \overline{Q_{66}}\end{bmatrix}\begin{bmatrix}d_{11} & d_{12} & d_{16}\\ d_{21} & d_{22} & d_{26}\\ d_{61} & d_{62} & d_{66}\end{bmatrix}\begin{bmatrix}M_x\\ 0\\ 0\end{bmatrix}$$

3-19 (Reddy, 2004)

In three point bending, $M_x = {Fx}/{2}$, where $0 < x < {L}/{2}$, L= distance between two supports,

And therefore, the maximum in-plane stress occurs at $x = {L}/{2}$.

Inter-laminar shear stresses can also be calculated (Reddy, 2004);

$$\sigma_{xz} = \frac{F}{2b}(\overline{Q_{11}}d_{11} + \overline{Q_{12}}d_{12} + \overline{Q_{16}}d_{16})(\frac{(z^2 - z_k^2)}{2})$$

3-20 (Reddy, 2004)

where $0 < z < h/2$ and $z_k = h/2$

If the laminated beam is subjected to a tension load of P ($N_y = N_{xy} = 0$) (Mukhopadhyay, 2005), the in-plane stresses for the kth layer:

$$\begin{bmatrix}\sigma_x\\ \sigma_y\\ \sigma_{xy}\end{bmatrix} = \begin{bmatrix}\overline{Q_{11}} & \overline{Q_{12}} & \overline{Q_{16}}\\ \overline{Q_{21}} & \overline{Q_{22}} & \overline{Q_{16}}\\ \overline{Q_{61}} & \overline{Q_{62}} & \overline{Q_{66}}\end{bmatrix}\begin{bmatrix}\varepsilon_x^0\\ \varepsilon_y^0\\ \gamma_{xy}^0\end{bmatrix}$$

3-21

And from constitutive equation (3-13),

$$\begin{bmatrix}\varepsilon_x^0\\ \varepsilon_y^0\\ \gamma_{xy}^0\end{bmatrix} = \begin{bmatrix}a_{11} & a_{12} & a_{16}\\ a_{21} & a_{22} & a_{26}\\ a_{61} & a_{62} & a_{66}\end{bmatrix}\begin{bmatrix}N_x\\ N_y\\ N_{xy}\end{bmatrix}$$

3-22

where $[a_{ij}]$ is the inverted of $[A_{ij}]$

Therefore:

$$\begin{bmatrix}\sigma_x\\ \sigma_y\\ \sigma_{xy}\end{bmatrix}=\begin{bmatrix}\overline{Q_{11}} & \overline{Q_{12}} & \overline{Q_{16}}\\ \overline{Q_{21}} & \overline{Q_{22}} & \overline{Q_{16}}\\ \overline{Q_{61}} & \overline{Q_{62}} & \overline{Q_{66}}\end{bmatrix}\begin{bmatrix}a_{11} & a_{12} & a_{16}\\ a_{21} & a_{22} & a_{26}\\ a_{61} & a_{62} & a_{66}\end{bmatrix}\begin{bmatrix}N_x\\ 0\\ 0\end{bmatrix} \text{ and } N_x=\frac{P}{b}$$

3-23 (Mukhopadhyay, 2005)

3.6 X-Ray 3D Micro-Computed Tomography (µ-CT)

X-Ray Computed Tomography is a reconstructive technique based on a large number of X-ray absorption images. The technique is sensitive to differences in X-ray absorption which is principally governed by the density of a material. Thus, dense materials absorb x-rays more readily than more open materials.

In X-ray micro-computed tomography, an X-ray source irradiates the specimen. A detector registers the transmitted X-rays, and it calculates the different intensities of the absorbed X-rays. The intensities show a discrepancy because of the difference in X-ray absorption. Materials with low density absorb less X-rays than materials with high density. The benefit of the CT is the ability to illuminate the specimen with X-rays in all directions for every slice. Thus, either the specimen or the source of X-ray can be swapped. At specified distances a number of slices can be scanned from the involved parts of the specimen (Stock, 1999). A data retransformation allows an accurate 3D-recreation of the specimen density distribution.

To achieve a high resolution, the specimen should be relatively small. With a big specimen, the resolution will be reduced, as seen from the equation (**3-24**).

$$Resolution = \frac{number\ of\ pixels}{object\ diameter}$$

3-24

3.6.1 Samples

The microstructure of the GFRP composite laminate was examined using four-sided samples with a size of 5×15×40 mm. The size of specimen is limited by the specification of the X-ray instrument Two specimens were cut from GFRP plates and two other specimens were cut from fatigue loaded test specimens, one fatigued in air and the other one, fatigued in sea water.

3.7 Water Uptake

In order to examine the influence of immersion in liquids on the GFRP composite material studied in this project, test coupons were immersed in sea water and distilled water over an extended period of time. GFRP composite specimens were preconditioned by immersion in seawater and distilled water at room temperature for various times prior to mechanical testing. The two types of preconditioning are:

- De-ionized water for up 720, 1440, 2160 hours at room temperature
- Sea water for up 720, 1440, 2160 hours at room temperature

In order to measure the water uptake, the mass change for the specimens was recorded at regular time intervals using an electronic balance.

As received specimens and aged specimens were subjected to quasi-static 3PB tests (a very common loading situation in tidal turbine blade applications). The ultimate flexural strength (UFS) and flexural Young modulus (E_f) were determined with the aid of the video gauge (DIC method) for strain measurement as described in (3.4). Three specimens were tested for each condition.

3.8 Fatigue Testing

3.8.1 Designing Flexural Fatigue Test

For simplicity and considering the typical loading on a tidal turbine blade, among different types of standard tests, a three point bending (3PB) fatigue test was selected in this study to determine fatigue life and failure mechanisms of the GFRP composite. Compared to other standard test methods, the 3PB test configuration introduces compressive, shear and tensile stresses/strains in the same specimen. As a result of the bending load, tensile stresses in the lower side and compressive stresses in the upper side of test specimen are developed and also shear stresses are generated in the middle (neutral axis), therefore all possible failure modes due to theses stresses can be assessed. The main reasons for designing 3PB configuration of fatigue rig to evaluate the composite blade performance and durability are discussed as follows:

1. Simulation of the main loading mode on a tidal turbine blade

The initial design of 3PB fatigue test rig was developed on the basis of typical bending loads acting on tidal turbine blades. As it is shown in chapter 5, hydrodynamic axial loads act on the blade surface causing the blade to bend. Due to the varying tidal current velocity in the marine

environment, fluctuating axial loads are generated on the blade. The fluctuating axial loads on the blade are approximated as cyclic bending loads. Therefore in order to emulate the bending behaviour of blade during its operation in sea water, a 3PB fatigue rig with a sea water tank was developed in this project.

2. Prediction of potential failure modes on tidal turbine blades

A single 3PB test is a good representative of a sample subjected to tensile, compressive and shear stresses/strains. Therefore all failure mechanisms due to the tensile, compressive and shear stresses on a single 3PB test specimen can be evaluated. Identifying these failure modes can make a positive contribution to predict and understand the main failure modes on GFRP composite tidal turbine blade subjected to thrust/bending load while exposed to sea water conditions. As it is shown in chapter 10 and 6, the stress/strain distribution through the thickness direction in a composite blade (at hot spot) and a 3PB test specimen (at the centre of sample) are similar to each other, meaning that, the composite blade experiences a similar gradient of 3PB stresses/strains due to the thrust load. In addition, the 3PB configuration of the fatigue test can be easily adapted to immersion in liquids. That is why in the designing process of the 3PB fatigue test rig, a chamber was included. Therefore the 3PB load can be applied on multiple samples while samples are in direct contact with sea water.

3. Minimizing the scattering of results

Usually axial fatigue testing is chosen for evaluation of fatigue behaviour of FRP composites, however, from a mechanical perspective, in axial fatigue tests using straight sided tabbed specimens may lead to scattering of results due to the tab de-bonding during fatigue tests and also it can cause failure at grips particularly for high stress/strain levels. Bending fatigue tests are easier to conduct due to the simplicity of specimens made without end tab bonding, therefore experimental scatter is reduced.

3.8.2 Designing and Manufacturing Process of 3PB Fatigue Rig

The design of the rig was originally developed and the ideas sketched by hand, then drawn out fully on AutoCAD and ANSYS Workbench environments. All of the fabricated components have been machined and built individually in the mechanical workshop using a variety of engineering equipment such as CNC and manual milling machines, standard bed lathes and drilling machines. The rig has been made from various materials to suit each area of use.

The main components and materials used in the manufacturing process of the fatigue rig (Figure 3-21 to Figure 3-23) are described as follow;

1. 316 stainless steel tank with polycarbonate viewing panels (part 1), all machined to size with drilled and tapped holes for easy assembly, a drain valve (part 2) was fitted to the bottom side and the tank has been fixed together with M5 stainless steel socket head bolts, sealed with silicone sealant to make it watertight.
2. 316 stainless steel flex assembly (part 3), has been made from flat plate with 10 mm rollers to give 3 point bending at the same dimensions as for static 3PB samples, As the original testing carried out on the Tinius Olsen test frames to determine the flexural strain.
3. The outer frame (part 4) is fabricated from 400mm×400mm×12mm thick mild steel, with 25mm diameter × 650 long support pillars connected by M10 socket head bolts to house the tank assembly, support the motor/gearbox (part 5), drive shaft with phosphor bronze bush (part 6), cam (part 7) and load cell (part 8). The stroke connected via the cam is manually adjustable (part 9) with two spanners to achieve the required deflection. This is set at a percentage of the failure strain. The whole assembly was bolted together for easy assembly in case of repair, modification or cleaning.

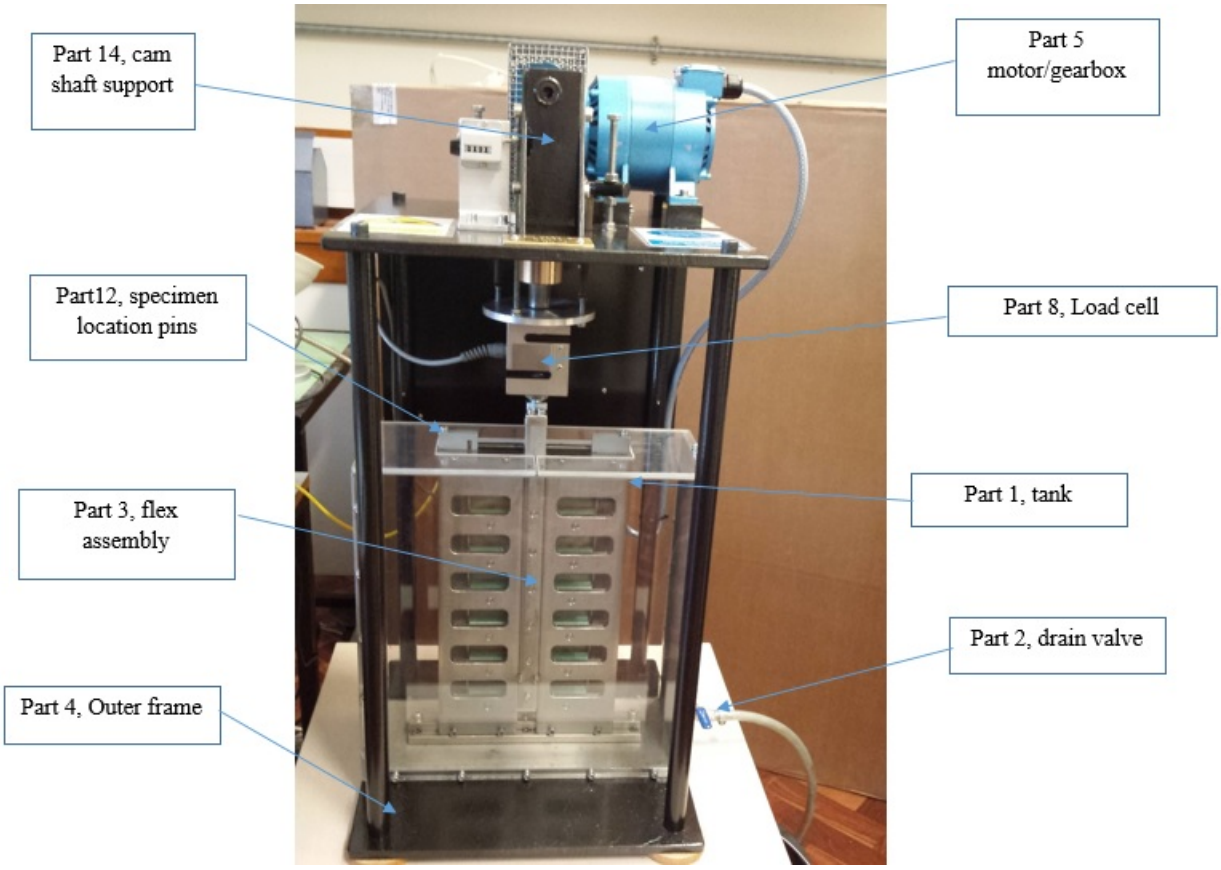

Figure 3-21. Components of Flexural Fatigue Test Rig (lateral side).

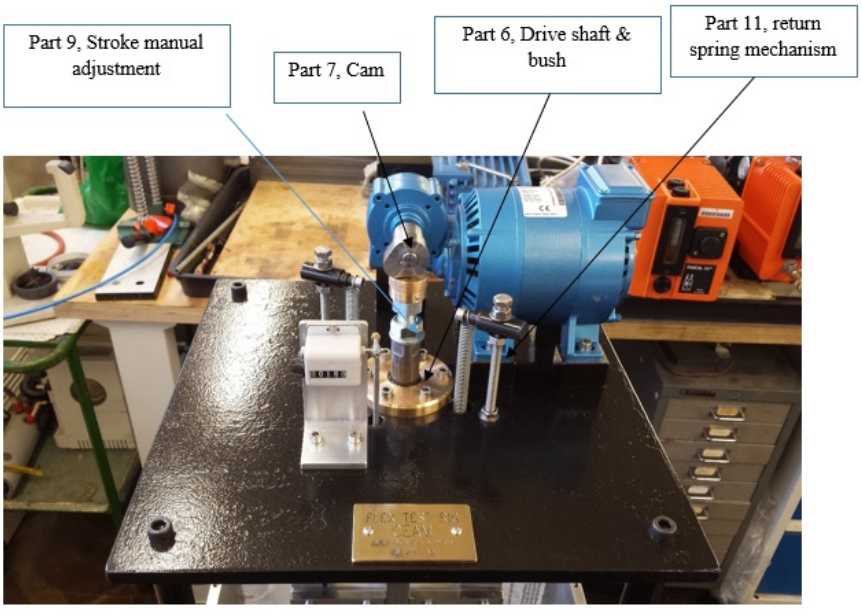

Figure 3-22. Components of Flexural Fatigue Test Rig (top side).

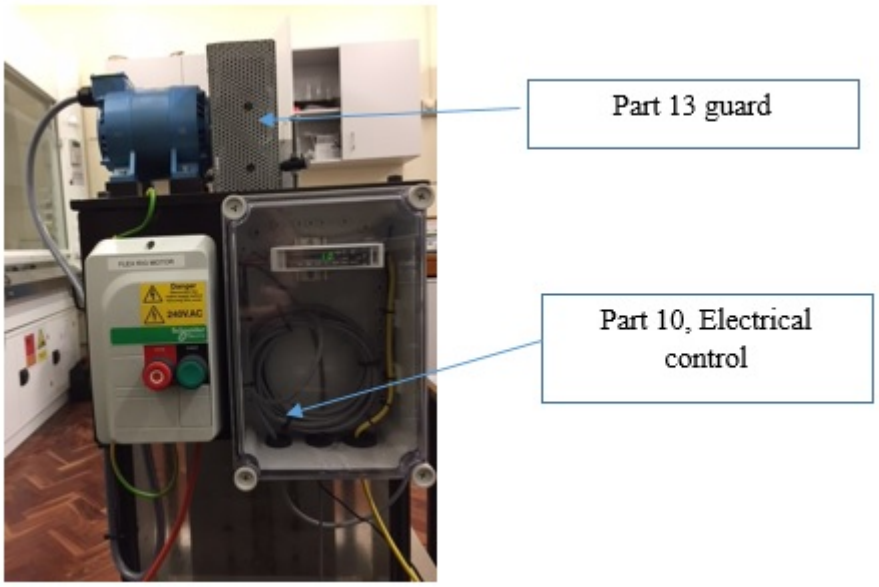

Figure 3-23. Electrical control equipment.

The main purpose of the motor is to generate rotational movement and the cam drive is used to convert the rotational movement into linear movement to apply deflection at the center of the test specimens.

The drive motor and gearbox have been selected to suit the required load and speed, (1Hz or 1 stroke per second). The amount of movement with the cam was finally determined at different offset from 2mm to 10mm.

A suitable load cell and controller (Tedea-Huntliegh Model 616, 2000Kg capacity) and a Pico data logger and software to operate the system were incorporated in the rig (part 10). The Pico data logger was used to record the data from the load cell.

The machine was tested with only a few minor additions to be made. These were;

- Adjustments to the return spring mechanism (part 11).
- New size offset cam (part 7)
- Specimen location pins (part 12)
- Guard for rotating shaft (part 13)
- Cam shaft support (part 14)

The fatigue rig, then, can run for extended periods of time with very little maintenance apart from a few drops of lubricating oil each day to the cam and bush assembly, also topping up the water level in the tank every 2 to 3 days, usually due to natural evaporation.

3.8.3 Performing a Fatigue Test

As it was mentioned before, the testing arrangement for the flexural fatigue tests was the same as those in a quasi-static 3PB test. A fatigue test rig, capable of exerting cyclic loads of up to 15kN was designed and manufactured to enable fatigue tests to be carried out on several GFRP composite test coupons at once (Figure 3-24).

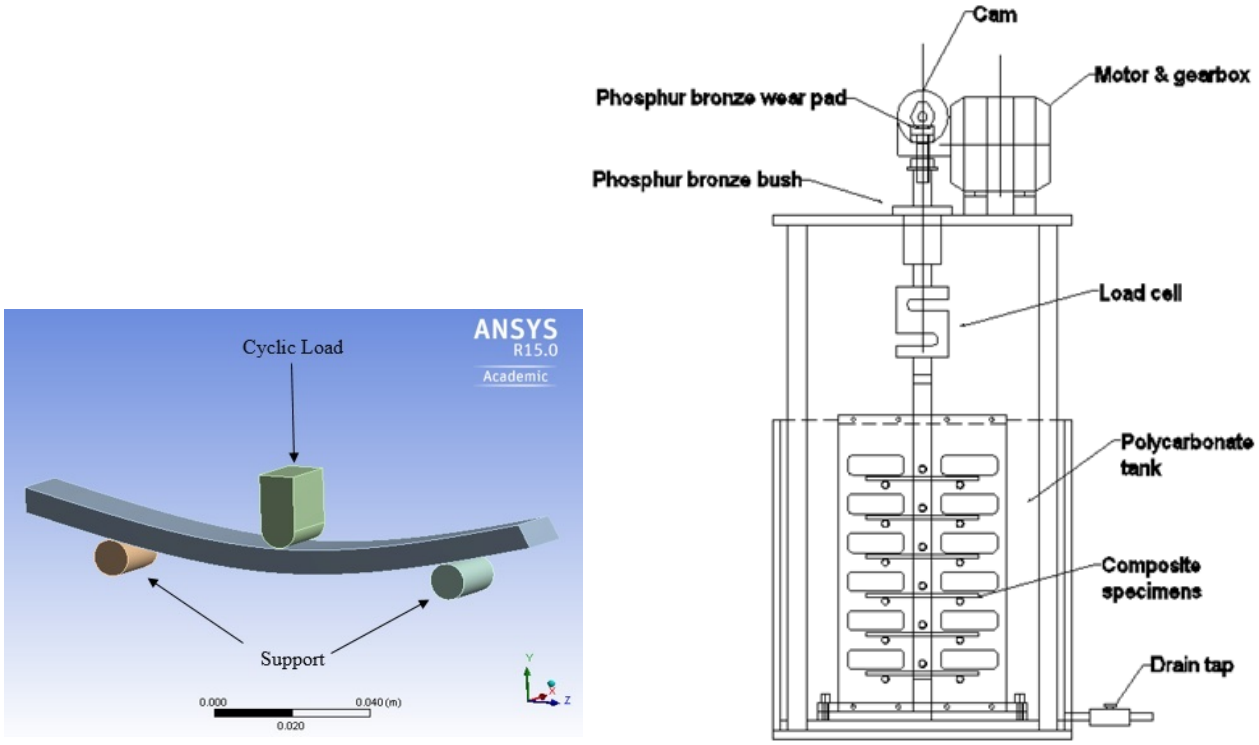

Figure 3-24. 3PB configuration of fatigue test specimen under cyclic loads and Exploded-view schematic of 3PB fatigue rig.

Fatigue tests were conducted in the 3PB mode at the frequency of 1*Hz* in two different environments, i.e. sea water and air. A total of 60 samples were prepared, 30 for each environment. The final dimensions of each test coupon were 150×15×5 mm. 30 samples were tested in fatigue loading while exposed to air with the 3PB mode; the other 30 specimens were also tested in fatigue loading while immersed in sea water with the same configuration at room temperature.

The fatigue tests were conducted under strain control mode. The tests were performed under cyclic strains and a strain ratio of R=0.1 (the ratio of the minimum strain to the maximum strain in one cycle) according to the ES BN ISO13003 (Iso, 2003). In this way the minimum displacement of the sample was maintained a little higher than zero to prevent the specimen movement and the variation of the loaded point during the fatigue test. Using low frequency (1Hz) allows the prevention of undesirable heating leading to a reduction of the fatigue life of the specimens. Also using the strain ratio of 0.1, the occurrence of impact when passing zero strain level can be avoided. Different strain levels (applied maximum strain) were used based on the proportion of the maximum midpoint displacement at the flexural strain (i.e. from 30% to 90% of maximum strain). The fatigue test involved cycling parallel sided specimens with a constant strain level until failure. A data logger which is connected to the load cell in the fatigue rig recorded the load-time response during fatigue tests, at the frequency of 100Hz enabling the observation of the variation of load versus time. As the bending fatigue tests are conducted under deflection control mode, the applied load, required to keep the given deflection constant, decreases with the number of cycles. In other words stiffness degradation of composites during fatigue tests can be confirmed via the output from the computer which is connected to the data logger and the load cell. The data logger shows a diagram of load variations with respect to the life time during the fatigue test. As can be seen in Figure 3-25, the stiffness of composites under cyclic loading decreases with time. This means that after an initial drop in flexural stress, the mechanical properties of the composite test specimen degrade gradually during the fatigue test. Initially the flexural stress drops rapidly and then the degradation follows an almost linear trend with the increase in the number of cycles. Therefore the load decreases slowly but near the end of the fatigue test the load decreases very rapidly indicating that the damage of test specimen is catastrophic. According to this figure, after an initial drop in stress, there is no significant reduction in mechanical performance before 40,000 seconds and the stiffness drops suddenly at 40,000 seconds in which this can be attributed to fatigue damage accumulation. Ultimate failure of composite material happens in a few testing cycles after this.

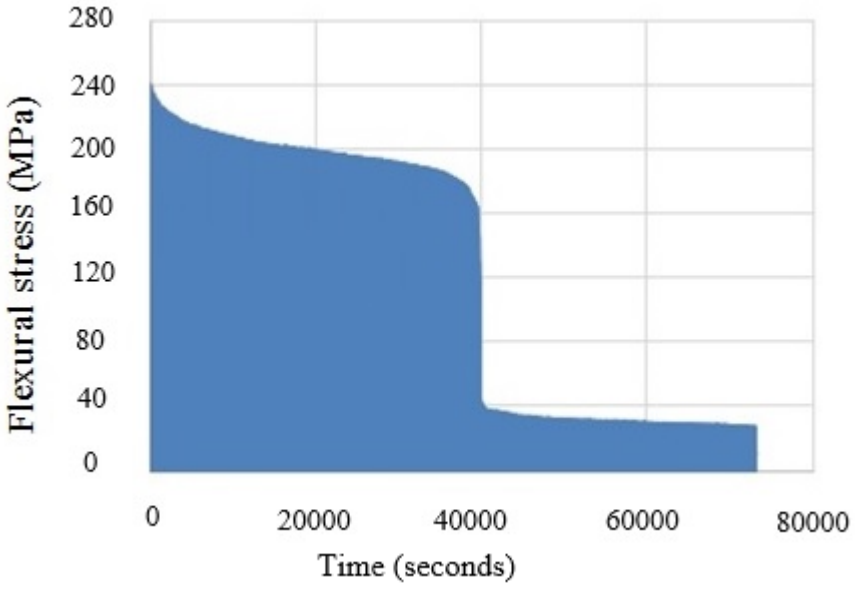

Figure 3-25. Stress versus time during the fatigue testing.

During the bending fatigue tests, sporadically the tests have been interrupted to determine the bending modulus and strength by means of a static 3PB test and the failure was observed by the stiffness reduction over the whole fatigue life of the samples. Post static bending tests on fatigued samples also included a DIC measurement to obtain a full-field strain map. During the fatigue tests, the damages on the specimen surface were also monitored using microscopic techniques and recorded during these examinations. In the very high cycles/low stress level tests, microscopic examinations suggest to stop the test once the stiffness reduction rises above 40%, since beyond this limit it is difficult to link the failure mechanisms to stiffness loss. As a consequence, the fatigue failure criterion is chosen as the number of cycles (N_{40}) at % 40 stiffness reduction in the strain-life diagram for very low stress levels (below than 0.7% strain level). Finally adopting a constant displacement mode and also considering the different displacement levels, strain-life curves were determined in both the air and the sea water environment. Macroscopic and microscopic observation of fatigue loaded samples revealed that damage develops and failure occurs mainly in the central part of the sample where stiffness degradation occurs, as expected in a 3PB test. It must be noted that in 3PB test, normal stresses are maximum in the top and bottom surface of sample in the central area and inter-laminar shear stress is maximum in the neutral axis, therefore failure is expected to occur in the central part of the samples and this is what happened in practice during quasi-static and fatigue testing of composite sample in 3PB configuration (chapter 7, Figure 7-5 and chapter 8, Figure 8-13 and Figure 8-16).

3.9 Reflected Light Microscopy of Woven GFRP Composite

Light microscopy is commonly used for failure analysis and it has been used for many decades to deliver understanding into the microstructure of FRP composites. The widest use of light microscopy for FRP composites is for determining ply counts, fibre orientations and void content.

In this study reflected-light microscopy was used to determine the above parameters in polished sample of the woven GFRP composite and also to investigate the failure mechanisms. Over the years many polishing methods for composite materials have been used but, there is no standard to reference. Throughout this study the easiest, most cost-effective and reproducible methods are used.

3.9.1 Specimen Preparation and Mounting

The first step that determines the quality of the microstructural information which can be acquired using light microscopy is the specimen preparation. Depending on the type of information which is desired tensile, 3PB, shear and fatigue specimens were sectioned, documented and labelled. In most analyses, the composite samples were sectioned through the z-axis and viewed normal to the z-x or z-y plane. An abrasive saw with coolant was used to cut large plates of composites (300mm×300mm×25mm) down to the specific dimensions required for tensile, 3PB, shear and fatigue samples. Using this type of band saw minimizes damage to the specimen. The use of coolant is necessary, because rising in temperature during cutting can alter the microstructure of the polymer matrix. In some cases to view the samples from the top surface, the samples were ground down to the required size with 80 or 120 grit silicon carbide (SiC) papers. Before mounting (casting resin), the samples were thoroughly cleaned to remove any debris from the cutting or sectioning process. This was done by using a fine brush, soap and water.

3.9.2 Specimen Mounting

Composite samples with surface features require support to ensure a flat planar surface. So polishing un-mounted samples may cause fibre pull-out or other type of damage. Epoxy resin was used as mounting medium because it has the least shrinkage during curing and good adhesion. Casting resins were cured at room temperature.

3.9.3 Grinding and Polishing

Grinding and polishing of mounted samples are required to make the surface planar and to prepare the composite specimen for microscopic analysis. Grinding removes surface layers to eliminate sectioning and mounting-induced artefacts. Sectioning artefacts include large cracks, micro-cracks and induced matrix strains. Following grinding, the samples have been polished. Polishing results in a better quality surface with less roughness. After the final step of polishing, the specimen should be free of artefacts when viewed at a magnification of 100.

Grinding and polishing were carried out using silicon carbide papers and diamond-coated disks. The first stage of grinding was aggressive enough to remove the material quickly and easily but not so aggressive as to induce damage to the sample. In all steps, water was used as a lubricant and to remove sample particles. The water also cools the specimen surface and eliminates heat damage.

The most common sequences of grit size for polishing composites which were used in this project are as follows (Hayes and Gammon, 2010):

1. Rough Grinding:
   This was done using silicon carbide (SiC) papers with various grit sizes: 120, 240, 400, 600, 800, 1200, and 2500 P: (sample movement counter direction to platen)
2. Polishing
   This was done using alumina slurry with different sizes: 15µm, 5.0µm and 0.3µm (de agglomerated alumina suspension (12 g alumina powder to 1 L distilled water), silk cloth, and counter direction
3. Final Polishing (alumina slurry)

I. 0.05µm de agglomerated alumina suspension (5g alumina powder to 1 L distilled water) or a commercial premixed 0.05 µm de agglomerated alumina suspension diluted with distilled water, neoprene cloth (pad), complementary direction

Movement of the specimens counter to the polishing platen rotation was used for composite sample preparation until the final polishing step. Countermovement of the sample increases the removal rate but also provides better sample control when grinding or polishing by hand. The speed of the platen was set as high as possible, not exceeding 1000 rpm.

3.10 Scanning Electron Microscopy (SEM)

The scanning electron microscope (SEM) uses a focused electron beam to produce a wide range of signals at the surface of samples. Due to the electron/specimen interaction, derived signals are used to disclose information about the specimen/object including microstructure and crystalline structure of materials making up the specimens. Therefore high magnification images can be obtained. When it is used in combination with the energy–dispersive X-ray spectroscopy (EDX), the composition of separate phases also can be evaluated.

3.10.1 SEM Principle

The scanning electron microscope is used to observe the surfaces of samples. When the sample is bombarded with the beam of electrons, secondary electrons are emitted from the specimen surface and they can be captured in a suitable detector. Therefore topography of surface can be visualized by scanning the electron probe over the sample and gaining of an image from the captured secondary electrons.

In SEM, a beam of electron is produced by an appropriate source, usually a tungsten filament or LaB_6 crystal. The beam of electrons is accelerated through a high voltage and transmitted through a system of apertures and electromagnetic lenses to generate a thin electron beam. Then the electron beam impacts the specimen surface and is scanned across it by means of scan coils. The electrons emitted from the sample are collected by a detector which outputs a current proportional to the number of electrons produced. The beam scanning the sample surface is synchronized with a spot on the screen- as the detector catches more electrons from a specific feature, therefore brightness increases. Once there are fewer electrons, the spot on the screen gets darker (Figure 3-26).

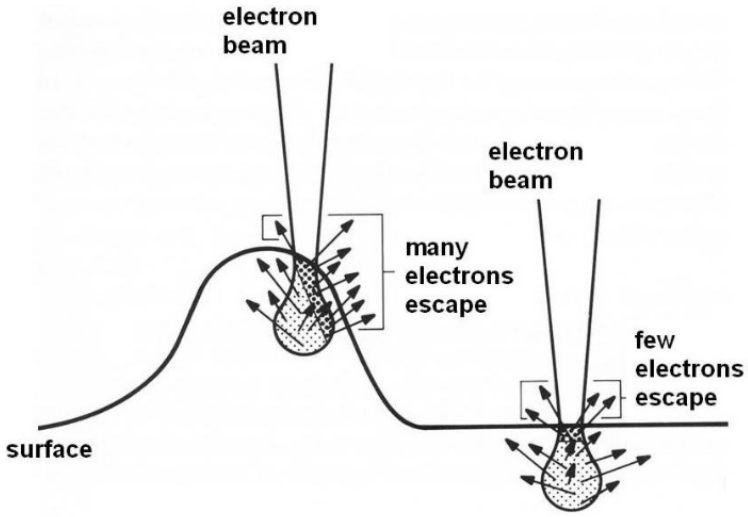

Figure 3-26. Schematic drawing of the primary electrons and scatter electrons, extra secondary electron will be emitted from edges, making them appear brighter (Egerton, 2006).

Essential components of all SEMs include the electron source (gun), electron lenses including condenser and objective lenses to generate an electron beam, scanning coils to move the electron beam, sample stage, detectors, data output devices, mechanical part (supply of power, system of vacuum, system of cooling, stage or floor free of vibration, room without magnetic and electric field environments). Figure 3-27 illustrates a cutaway inside an electron microscope.

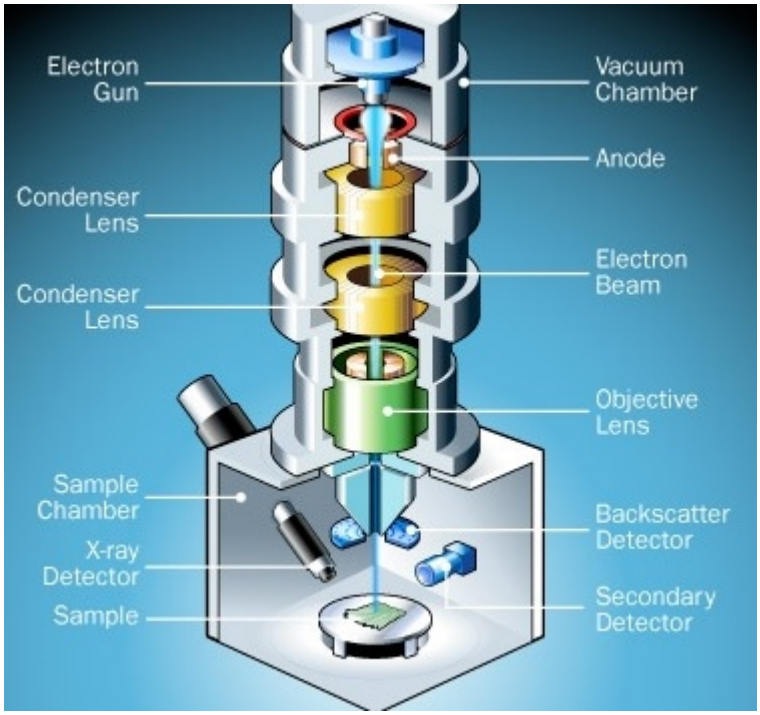

Figure 3-27. cutaway of electron microscope (Watt, 1997).

- ✓ ***Electron Gun***

The electron gun which is usually a thermionic emission gun, generates electron beams. Thermo-electrons are released from a tungsten filament wire. This is done by heating the filament at elevated temperature (3000K). By applying a positive voltage (between 1 to 30kV) to the metallic anode plate, thermo-electrons are grouped as an electron probe flowing into the anode plate. Electron beams flow through the central anode hole. Other emitter materials include LaB_6 delivers high brightness beams.

- ✓ ***Condenser and Objective Lenses***

In an electron microscope magnetic lenses are used to control the electron beam emitted by the gun. By passing an electric current through a coil, a magnetic field is created and a lens action is generated on an electron beam. By placing a lens below the electron gun, the diameter of the electron beam can be adjusted. Two-stage lenses, which incorporate the condenser and objective lenses, are placed below the electron gun. The electron beam formed by the electron gun is concentrated by the two-stage lenses, and a small electron beam is generated.

- ✓ ***Sample Stage***

The sample stage in the SEM can perform horizontal and vertical movement of sample, sample tilting and rotation. The field of view can be selected by horizontal movements of the sample, while the image resolution and depth of focus can be changed by vertical movement

- ✓ ***Secondary Electron Detector***

A scintillator detector is usually used to detect the secondary electrons released from the sample. By coating a fluorescent substance on the tip of the detector and applying a voltage to it, the secondary electrons emitted from the sample are collected and light is generated when they impact the fluorescent screen. The light is converted to electrons and they are amplified as an electric output signal. Usually a collector which is a supplementary electrode is located before the detector tip. Applying a few hundred volts to this collector helps the fluorescent substance to attract secondary electrons emitted from the sample. Thus changing the voltage, allows controlling the number of secondary electrons which can be collected.

The scanning on the screen is matched with the electron detector resulting in brightness variations, which depend on the number of the secondary electrons. Thus SEM images are formed from secondary electrons. A different detector can also be used to collect backscattered primary electrons with high energy. The backscatter images are sensitive to variations in atomic number within the sample.

- ✓ ***Vacuum System***

Vacuum of inside of the SEM system and specimen chamber should be kept at 10^{-3} to 10^{-4} Pascal to prevent electron/gas molecule collisions. As a consequence in order to exchange the samples, the entire sample chamber should be vented at the time of sample exchange.

3.10.2 Specimen Preparation for SEM Analysis

In this study SEM was used to analyse the fracture surfaces of GFRP composites after tensile, 3PB, shear and bending fatigue tests. This was used to obtain information about the multiple failure mechanisms of the GFRP composite. The following sequences were adopted to prepare GFRP specimens for SEM analysis:

- ✓ ***Cutting***

After performing mechanical tests including tensile, 3PB, shear and fatigue tests on GFRP composite coupons, failure areas from the specimens were cut with a suitable size and a cross section of the specimen was prepared for either light or electron microscopic observation.

- ✓ ***Mechanical Polishing***

Cross section of specimens were embedded in a resin and polished as described in section (3.9.3). During the mechanical polishing processes, the abrasive discs are changed from rough to fine and lastly, a polished cross section with a mirrored surface is created.

- ✓ ***Mounting Specimens***

In this stage, a thin band of silver paint was applied to the mounted samples in order to ensure electrical conductivity between the sample and the sample holder. During the SEM examination of non-conductive specimens, in order to avoid the effect of charging, coating, low acceleration voltage, tilt observation and low vacuum SEM observation are usually advised. In the SEM examination of GFRP composite specimens, the conductive coating method was used. In this method a highly conductive thin gold layer is coated on a non-conductive specimen. In order to replicate the true surface of the sample, it is important to make a very thin film, however too thin coating might result in charging as the coating film is incomplete.

- ***Coating***

The ion sputtering (using diode sputtering) method was used to produce the gold coating. In this method, positive ions, which are created by a glow discharge in a low vacuum of about 10Pascal, sputter the target metal and the sample is coated. Thickness is controlled by the sputtering time and is of the order of a few nm for good SEM images

3.11 Energy-Dispersive-X-Ray (EDX) Spectroscopy

Energy-dispersive X–ray spectroscopy (EDX) or energy-dispersive X-ray micro-analysis, is a characterization technique used to analyse the elemental composition of a sample. The EDX analysis system works as an incorporated feature of a SEM. It relies on the fact that the interaction of an electron beam with a substance produces a variety of emissions, including X-rays (Figure 3-28).

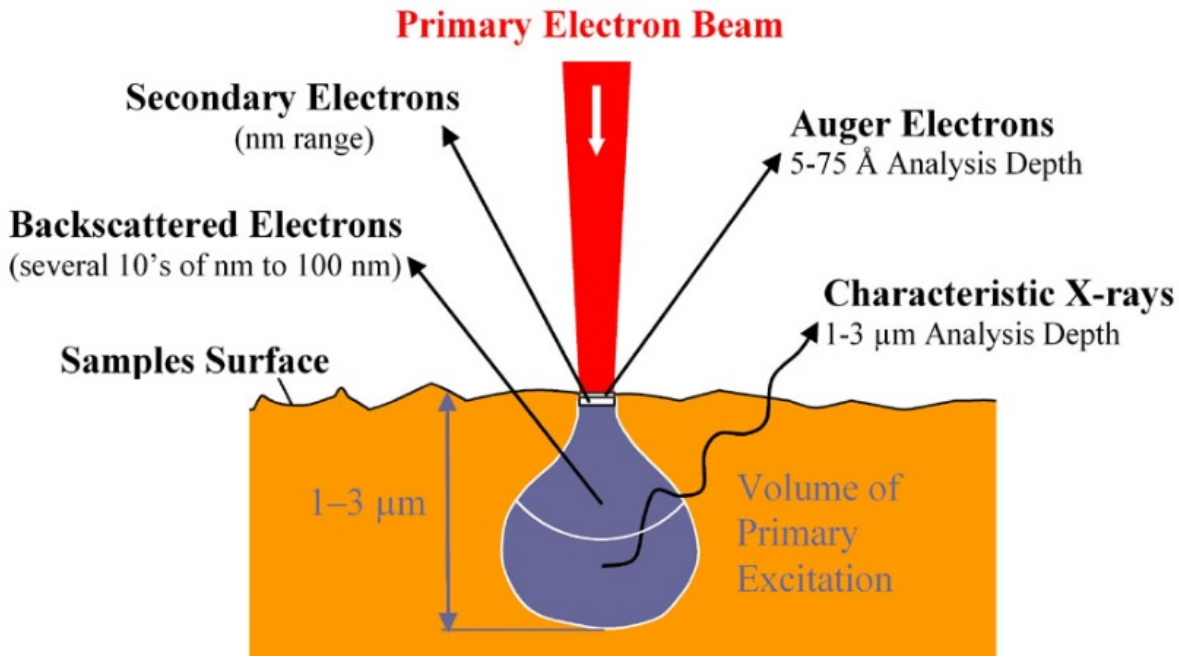

Figure 3-28. Schematic illustration of electron-matter interactions, showing the volumes involved in the radiation of different electrons and electromagnetic waves from the specimen (Van Grieken and Markowicz, 2001).

Figure 3-29 illustrates the diagram of the generation of the characteristic X-rays. As explained before, when the substance is bombarded with an incident electron beam, numerous electrons and electro-magnetic waves are released from the material. An atom within the material encompasses unexcited electrons in separate energy levels bound to the nucleus. The incident

electron beam may stimulate an electron in an internal shell, discharging it from the shell while forming an electron vacancy. This vacancy position created by an ejected core shell electron is occupied by a higher energy electron from an outer shell, in this process the transferring outer electron gives up some of its energy by emitting an X-ray whose energy corresponds to the energy difference between the outer and the inner shell. These X-rays are entitled 'characteristic X-rays' since their wavelengths and energies are characteristic of specific elements.

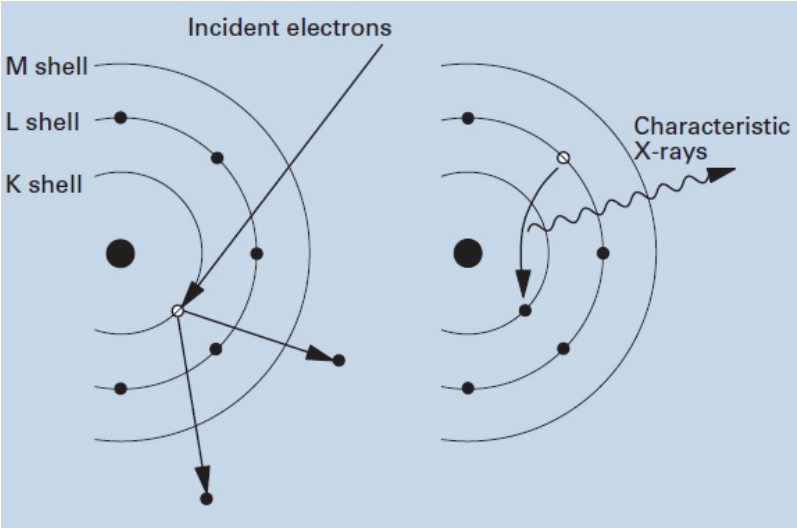

Figure 3-29. Basics of generation of characteristic X-rays (Van Grieken and Markowicz, 2001).

3.11.1 EDX Spectrum

An EDX spectrum is the output of EDX analysis. It shows peaks equivalent to the energy levels for which the majority of X-rays have been received. Each of these peaks are specific to an atom, and thus matches to a particular element. A higher peak intensity in a spectrum reveals a higher concentration of an element in the substance. An EDX spectrum identifies the type of X-ray corresponding to each of its peaks. For instance, a peak equivalent to the energy possessed by X-rays discharged by an electron in the L-shell going down to the K-shell is recognised as a K-alpha peak. Similarly the peak matching to X-rays emitted by M-shell electrons moving to the K-shell is identified as a K-beta peak (Figure 3-30).

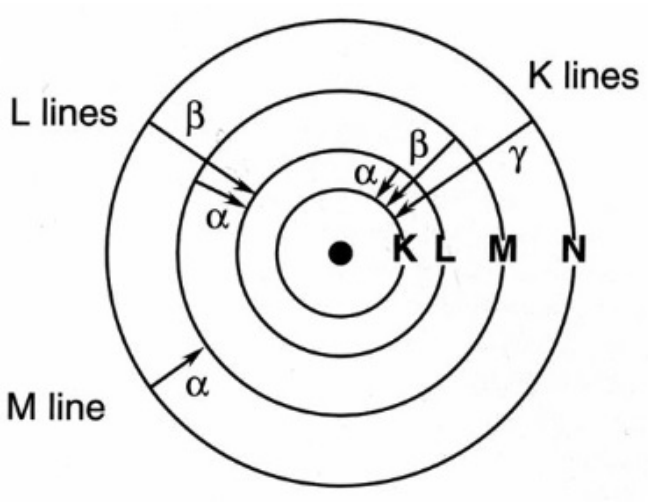

Figure 3-30. In EDX spectrum, constituents/elements are detected according to the energy of the X-rays released by their electrons once these electrons move from a higher-energy level to a lower-energy one (Van Grieken and Markowicz, 2001).

3.11.2 EDX Equipment

In EDX set up, the primary components are:

- Excitation source (electron beam)
- X-ray detector
- Pulse processor
- Analyser

The detector is used to translate X-ray energy into electrical signals. This information is sent to a pulse processor to ensure that single photon energies are recorded (overlapping peaks are ignored) and transfer them onto an energy analyser to display and analyse the data.

3.11.3 EDX of GFRP Composite Sample

In this study during the SEM analysis of GFRP samples, EDX analysis was also performed to examine the effect of sea water on the fatigue behaviour of GFRP specimens. This was done by performing EDX analysis near the matrix cracks, longitudinal and transverse micro-cracks, inter-laminar cracks, delaminated areas, and fibre breakage areas of the fatigued samples in both sea water and air. By comparing EDX spectra of specimens in these two different environments, variations in the chemical composition due to the sea water will be an indicator of the sea water effect.

As the GFRP specimen is a non-conductive sample, its surface need to be coated with a conductive material. Therefore for EDX analysis of GFRP samples in this study, carbon coating

was used, since gold coating reduces the intensity of X-rays which escape the sample and reach the detector.

3.12 Glass Transition Temperature using Differential Scanning Calorimetry

The Glass Transition Temperature (T_g) is one of the most important properties of any epoxy resin. It is a temperature region where the thermosetting polymer changes from a hard, rigid state to a soft, pliant and rubbery state. Epoxy resins are categorized as thermosetting materials and they are chemically cross-linked during the curing process, therefore unlike thermoplastic materials which undergo melting or reflowing at elevated temperature, the ultimate cured epoxy resin experiences a small softening (phase change) when heated.

DSC is a technique that evaluates the change of a material's heat capacity (C_p) as a function of temperature. The change in the amount of heat needed to increase the temperature of a specimen is evaluated with respect to temperature. Both the specimen and a reference are kept at almost the same temperature during the testing. In DSC a specimen of known weight is heated or cooled and the variations in its heat capacity are traced with regard to variations in the heat flow. This allows the user to identify the transitions such as melting, glass transitions, phase changes, and curing. The outcome of a DSC test is a curve of heat flux as a function of temperature.

One of the most important parameter affecting glass transition temperature of epoxy resins is humidity. The glass transition temperature (T_g) of epoxies can be considerably reduced by moisture uptake, an aspect which should be taken into consideration when designing for humid applications such as tidal turbine composite blades.

Chapter 4

Finite Element Modelling

4 Finite Element Modelling

As was mentioned in Figure 3-1, a methodology for fatigue life prediction of composite tidal turbine blades has been proposed. The methodology involves Finite Element modelling of composite blades. This chapter initially deals with modelling and designing of quasi-static mechanical testing of composite samples including tension, shear and 3PB test specimens and finally modelling and designing of a composite blade in the FE software (ANSYS) is explained. In chapter 7, it is shown how the DIC method was used to validate the FE results of mechanical tests on GFRP composite samples in 0/90 fibre orientation, therefore confidence was acquired regarding the FE model of a GFRP composite turbine blade. In this chapter (chapter 4) it is shown how different modules in the ANSYS environment (ACP and ANSYS static structural) were used for modelling a turbine blade. The most important steps regarding FE modelling of a turbine blade such as designing the blade geometry, defining the boundary conditions and the mode of loading, improving mesh density, selecting a suitable element type and material characteristics including fibre orientations and composite properties are explained in details in the following sections.

4.1 Finite Element Modelling (FEM) Using ANSYS

In this study in order to model all mechanical testing of the GFRP composite test coupons, different parts of the integrated modular structure of ANSYS including ANSYS Workbench, ANSYS Composite Pre-post (ACP) and ANSYS n Code design life were employed (Release, 2012). The mechanical performance and the fatigue life of a full-scale tidal turbine blade have been investigated using the same ANSYS modules. The FE method enables testing in a virtual environment before manufacturing prototypes of products. In the field of Finite Element Analysis of composite tidal turbine blades, ANSYS is widely used for stress/strain analysis and prediction of fatigue life.

4.1.1 ANSYS Workbench

ANSYS Workbench is a platform which incorporates simulation/modeling technologies and CAD systems. The power of ANSYS Workbench is due to the ANSYS solver algorithms. The aim of ANSYS Workbench is to verify and improve a product in a virtual setting.

ANSYS Workbench enables a geometry to be built with its "preprocessing" functions. Correspondingly, a Finite Element mesh which is necessary for calculation and simulation is

created. After defining the boundary conditions and performing the simulation, the outcomes can be presented in numerical and/or graphical form.

4.1.2 ANSYS Composite Pre-Post (ACP)

Engineering layered composites involves complex operations including material selection, total and individual layer thickness and stacking sequences, fibre orientations, failure analysis and parameterization. The engineering challenge for designing and analyzing layered composites is to assess how well the completed product will perform under real working conditions. Computer modelling and simulation is suitable for this task when stresses, deformations as well as a variety of failure criteria are taken into consideration. ANSYS Composite Prep-Post which is an add-in to ANSYS Workbench offers all the required functionalities for FE investigation for layered composite structures.

In the pre-processing stage, based on the geometry and the FE mesh, the boundary conditions and composite definitions are applied to the component or structure. After the solution is found, post-processing is employed to assess the behaviour of the laminate. In the case of an unacceptable design or failure, the geometry or laminate structure must be modified or improved and the calculation is then iterated until a successful solution is found.

ACP has two pre-processing and post-processing modes. In the former mode, all composite definitions are generated and mapped to the geometry with the FE mesh. These definitions are reassigned to the FE model and reallocated to the solver input file. In the post-processing mode, after a finalized solution and the import of the result file(s), results including failure and components of strains/stresses can be identified and pictured graphically.

4.1.3 ANSYS n Code Design Life

ANSYS n Code Design Life is an extension of ANSYS Mechanical and Workbench used for predicting fatigue life. It employs the results of FE analysis, from ANSYS Mechanical or other similar FE programs to estimate stresses and strains, and accumulated damage from exposure to alternating loading.

ANSYS n Code Design Life provides an all-inclusive diagnostic and analytical fatigue process model. Using this tool, complex loading such as fatigue cycles based on real-life forces can be created.

In this work, an experimental strain-life curve was obtained for the GFRP composite, therefore, the strain-life approach was used to predict the fatigue life of composite blades.

4.2 Finite Element Modelling of 3PB and Tensile tests

4.2.1 3PB Test Configuration

Numerical simulations of mechanical tests were performed using ANSYS Composite Pre-Post FE Software. The simulations were conducted for 3PBT test specimen employing a reference fibre reinforced polymer made up of glass fibres in the matrix of epoxy resin in which the mechanical properties (Table 4-1) have been found experimentally. In chapter 3 section 3.3, mechanical tests including tension and shear tests were done in order to determine tensile and shear properties. The results of tension and shear tests (i.e. tensile, shear elastic modulus and Poisson's ratio) in chapter 6, Table 6-2 and chapter 7, Table 7-3 are used for FE modelling of all mechanical tests. Figure 4-1 shows the boundary conditions imposed on the FE model of 3BT coupons. The two supporting points at either end of the parallel sided specimen are fixed for translation at $z = 0$ and a flexural load is applied opposite to the supporting points. The FE model of 3PB test specimen is meshed with element type SHELL (planar element) appropriate for laminated composite components (ANSYS; Matthews *et al.*, 2000b). Modelling of a laminated composite with SHELL elements is efficent as there is no need for multiple elements through the thickness of composite components (Canino, 2016). This results in less nodes/elements and faster running and reduced computational time of FE analysis. In addition, when it comes to comparing with SOLID elements, SHELL elements are better matched with componenets with sharp edges and complex design (Hameed *et al.*, 2015). For FE modelling of all mechanical tests of GFRP laminated composites and FE modelling of full scale turbine blades (Hermann *et al.*, 2005; Grogan *et al.*, 2013), the same element type SHELL 181 has been used (Canino, 2016). In general, given the layered nature of FRP laminated composite materials, only certain types of elements can be employed efficiently for the Finite Element analysis of composites. For FE analysis of thin to reasonably thick shell composnents, the element SHELL181 is appropriate (ANSYS). Given the dimensions of composite samples for FE modelling of all mechanical tests, initially a thin surface was modelled in ANSYS workbench, and then using ACP process, the laminate is made by laying plies over one another so that the required thickness of the laminate is achieved. In this project, this element type was selected by ANSYS ACP.

Element SHELL 181 is a four-node element and at each node, 6 degrees of freedom (DOF) exist: 3 translations in the x, y, and z directions, and 3 rotations about the x, y, and z axes. Figure 4-2 illustrates the geometry, locations of node, and the coordinate system of this element. Four nodes I, J, K, and L define the element. SHELL 181 is used for layered applications for modelling FRP or sandwich composite shells and it is suitable for various applications (linear, large rotation, and/or large strain nonlinear). Also, when it comes to comparing different shell element types, this element can eliminate problems of convergence. In other words, in FE analysis of composite components, using SHELL 181 compared with some other SHELL elements, convergence is obtained with the use of lower number of elements. The mesh sensitivity study was carried out to study the convergence of the maximum flexural stress in the sections used for the data reduction. Convergence tests were conducted on a GFRP model of the flexural test specimen. An appropriate number of elements was obtained by improving mesh density. The stabilization of the flexural stress was the criterion for convergence. The convergence is gained with the use of approximately 1000 or more elements. In addition, using this number of element type (Shell 181), the flexural stress/strain of GFRP was almost the same to that obtained by close form solution (chapter 6, section 6.3.2). The most important steps which are employed to simulate the GFRP composite test specimen with 0°/90° fibre orientations in ANSYS Composite Pre-Post are Rosette, Oriented element sets and modelling ply groups commands. Simulation of plies was conducted on the basis of scanning electron micrographs of biaxial fibres with rosette commands to represent the reference fibre orientations. According to the micrograph, the thickness of GFRP composite test specimens is composed of 24 plies (Figure 4-3). The thickness of each lamina was set to 0.21 mm.

Table 4-1. Measured mechanical properties of glass fibre reinforced epoxy resins (detailed in chapter 6, section 6.2.1, Table 6-2 and chapter 7, section 7.4, Table 7-3), E- Young's Modulus, ν – Poisson's ratio, G – Shear Modulus.

Mechanical properties	E_x(GPa)	E_y(GPa)	ν_{xy}	G_{xy}(GPa)
GFRP	21.6	21.6	0.25	3.52

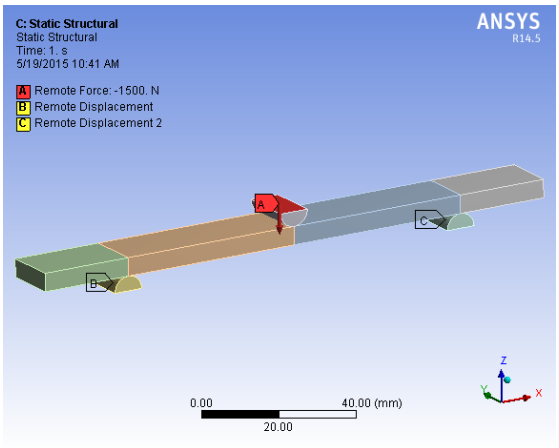

Figure 4-1. Load application and boundary conditions for 3PBT $\boldsymbol{F_z}$= load applied in z direction; $\boldsymbol{U_x \neq 0}$,$\boldsymbol{U_y \neq 0}$ and $\boldsymbol{U_z}$= 0 are displacement on the x, y, z directions; $\boldsymbol{ROT_x = 0}$, $\boldsymbol{ROT_y \neq 0}$ and $\boldsymbol{ROT_z = 0}$ are rotation around x, y, z directions.

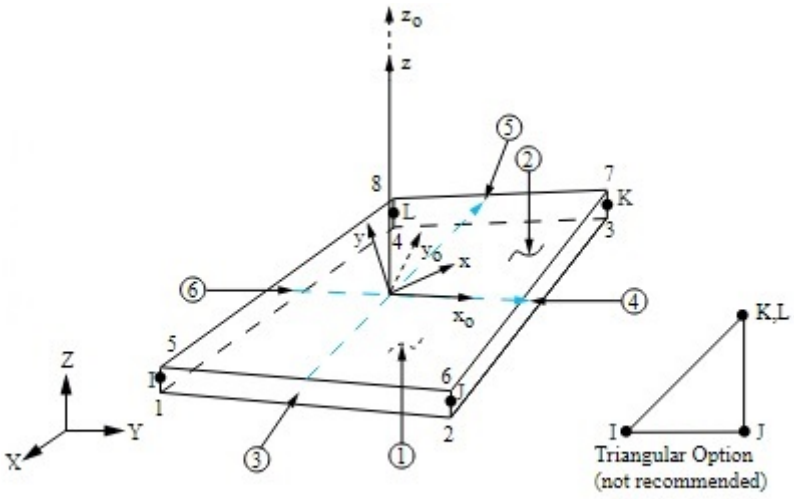

Figure 4-2. Element Geometry of Shell 181 for FE modelling of GFRP laminated composite samples subjected to 3PB, tension and shear tests and FE modelling of full scale GFRP laminated composite turbine blade (ANSYS).

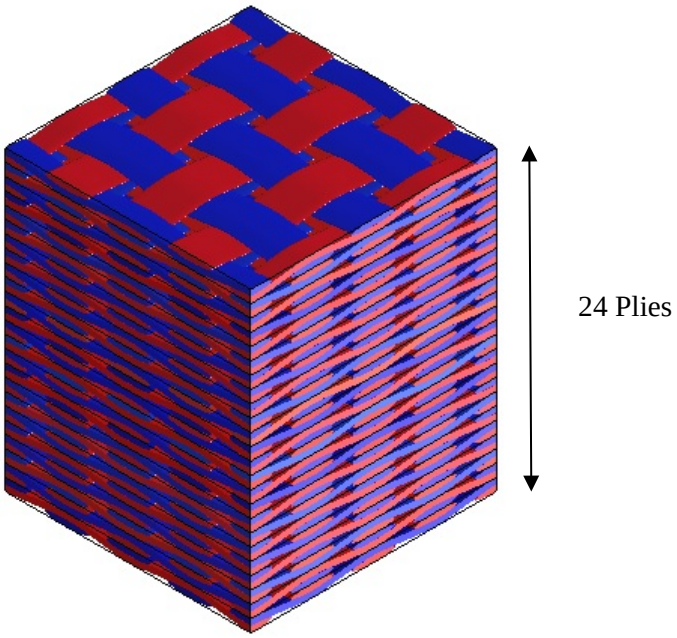

Figure 4-3. Number of plies for FE simulation of GFRP specimen, thickness of each ply was set to 0.20833 mm. 24×0.20833= 5 mm

4.2.2 Tensile Test Configuration

A typical FE mesh of the tensile test specimen is shown in Figure 4-4. The FE model is meshed with the element type SHELL appropriate for modelling of laminated composite structures and components (ANSYS; Matthews *et al.*, 2000a). The FEM includes the geometry of the specimen, the boundary conditions and material characteristics including fibre orientations and composite properties (Table 4-1). A mesh sensitivity study (convergence test) was conducted to investigate the convergence of the tensile stress in the sections used for the data reduction. An appropriate number of elements are obtained by improving mesh density. The stabilization of the tensile stress was the criterion for convergence. The convergence is obtained with the use of approximately 1000 or more elements. In addition using this number of element SHELL 181, the tensile stress/strain of GFRP sample obtained was close to that given by closed form solution (chapter 6, section 6.3.4).

To define boundary conditions, the FE model was locked for displacement in the x direction on the left side of the tensile specimen and also was locked in the z direction in the clamp areas. On the right side of the specimen various displacements were applied in the x direction. The movement was controlled to get the same load applied as in the experiment.

The simulation was conducted for tensile test specimens employing reference fibre reinforced epoxy resins made up of glass fibres for which the mechanical properties (Table 4-1) have been found experimentally (results of tension and shear tests in chapter 6 and 7).

Simulation of plies was conducted on the basis of µ-CT images and scanning electron micrographs of biaxial fibres with rosette commands in order to represent the reference fibre orientation. Thickness of the GFRP composite tensile test specimen is composed of 24 plies (Figure 4-3). The thickness of each ply was set to 0.21 mm according to µ-CT results (chapter 9) and SEM micrographs. Figure 4-4 shows the FE model of the tensile specimen.

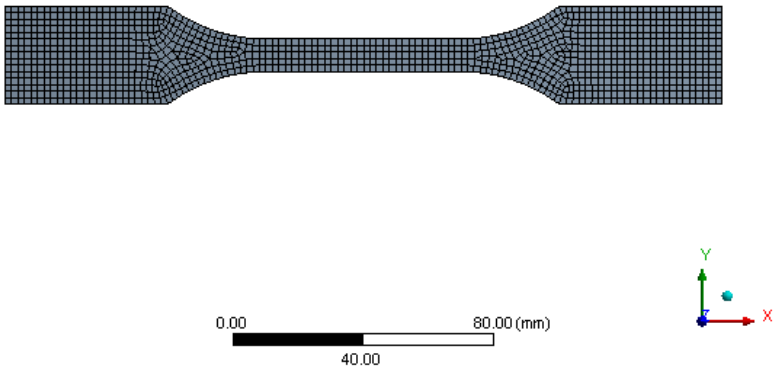

Figure 4-4. Finite element mesh of a tensile test specimen

4.2.3 Iosipescu Shear Configuration

A typical FE mesh of Iosipescu shear test specimen is shown in Figure 4-5. The FE model is meshed with the element type SHELL appropriate for modelling of composite laminated structures and components (ANSYS; Matthews *et al.*, 2000a). The FEM involves the creation of geometry of the specimen, the application of loading (contact interaction between clamps and specimen) and material characteristics including fibre orientation and composite properties. A mesh sensitivity study was undertaken by investigating the convergence of the maximum shear stress. Convergence tests were conducted on a composite model of the Iosipescu shear test specimen. An appropriate number of elements are obtained by improving mesh density. The stabilization of the shear stress was the criterion for convergence. Convergence was obtained with the use of approximately 1000 or more elements.

To define boundary conditions, the model was locked in displacement in the y direction of the left side of the shear specimen at the top and bottom and also was locked in the x direction at the far left. On the right side of the specimen various displacements were applied in the y direction at the top and bottom (Figure 4-5). The displacement was set to get the same load applied in the experiments. The simulation was conducted for Iosipescu shear test specimens employing reference fibre reinforced composite in which their mechanical properties (Table 4-1) have been found experimentally.

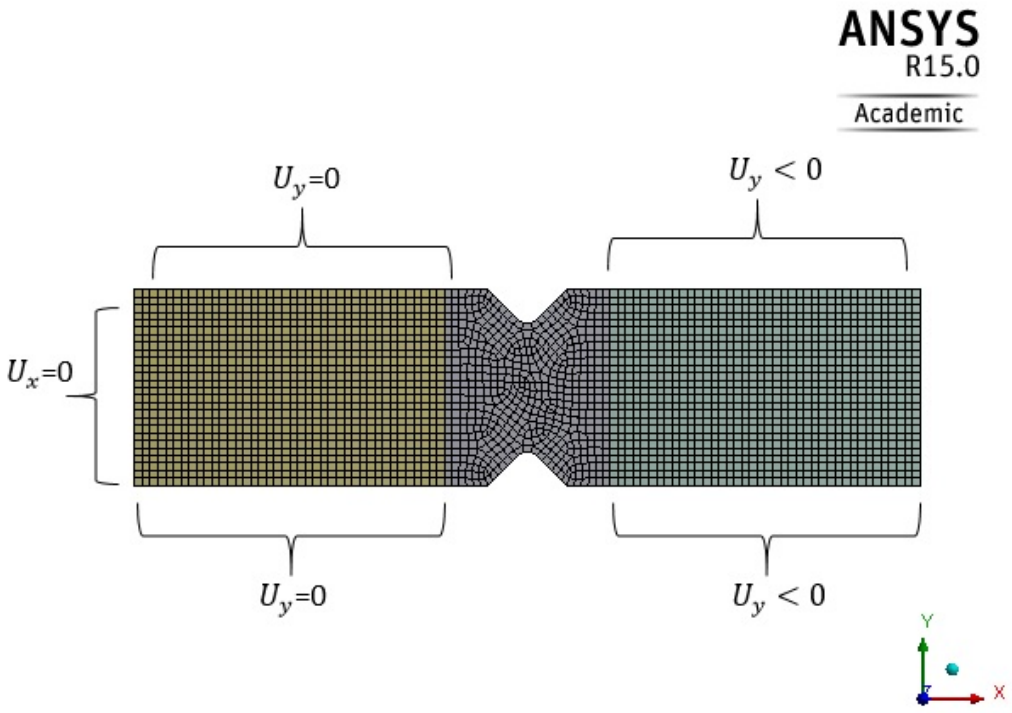

Figure 4-5. Finite element mesh of an Iosipescu shear specimen and boundary condition.

4.3. Finite Element Structural Model of Tidal Turbine Blade

The FE model and analysis of blade begins with output from the hydrodynamic analysis, in the form of blade loadings. Considering the blade as a cantilever beam and tangential/axial forces at each blade station output from the stream tube model, the strain/stress distribution, critical elements/hot spots and fatigue life of turbine blades are evaluated.

4.3.1. Material Selection

The selection of materials for tidal turbine blades involves several factors, such as stress distribution, stress concentration and the sea water environment where turbine systems work. In order for the blade to withstand hydrodynamic loadings from tidal currents, a high specific

strength and stiffness material is required. In addition, stiffness degradation of the material due to the environmentally affected fatigue must be taken into account. Since blade materials are subjected to fatigue loads while they are exposed to harsh sea water conditions, fibre reinforced polymer composites, which have been used widely in the wind turbine industry, are a good candidate material in the case of tidal turbine industry.

A GFRP composite material was used for FE model of the blade. The material properties and layer orientation of the composites is shown in Table 4-2. The mechanical properties have been measured according to the experimental techniques mentioned in chapter 3. The results are detailed in (chapter 6, section 6.2.1, Table 6-2 and chapter 7, section 7.4, Table 7-3). Fatigue data obtained from experiments presented in section 8.2.1 in the form of Strain-Life diagrams was used as input data for fatigue analysis of the blade.

Table 4-2. Measured material properties for the FE model of the blade. Material properties were determined experimentally in this project (detailed in chapter 6, section 6.2.1, Table 6-2 and chapter 7, section 7.4, Table 7-3)

Materials	Glass/Epoxy
Longitudinal modulus , E_1 (GPa)	21.6
Transverse modulus , E_2 (GPa)	21.6
In plane shear modulus, G_{12}(GPa)	3.52
Major Poisson's ratio, ν_{12}	0.25
Layup sequences	woven
Thickness of plies (mm)	0.21

4.3.2. Element Selection for FE Model of Blade

One of the elements available in ANSYS which is capable of structurally modelling laminated composite materials is SHELL (*ANSYS, Inc.Element Reference*). It is believed that SHELL is the most well suited element for modelling the skin geometry of the wind and tidal turbine blade (ANSYS; Matthews *et al.*, 2000a; Hermann *et al.*, 2005; Shokrieh and Rafiee, 2006; Lee *et al.*, 2015; Canino, 2016). It is designed for simulating shell structures with a wide range of thicknesses.

4.3.3. Modelling Blade Geometry

This section outlines the process used to create the blade geometry. Static structural and fatigue analysis were performed using ANSYS Composite Pre-Post and ANSYS n Code Design life, respectively.

The results have been analysed and the areas on the blade which experience high stress/strain concentration were detected. These data can be used for optimization of the blade by adjusting the stacking sequence or increasing the thickness of the blade shell. A convergence criterion was used for selecting the suitable number of elements for the FE model.

The design of the blade commences with the selection of hydrofoil sections and their distribution in the span-wise direction. For the reference tidal turbine blade, hydrofoils designed for wind turbines were used, such as NACA4415 aerofoil series, whose description can be found in NACA's documentation (*NACA Airfoil Generator*).

An FE model of a tidal turbine blade was designed using ANSYS workbench 15.0 and the analyses of the blade were performed with this software. Initially key points have been defined and then they were connected with curves, finally the surface and the body are generated by surrounding areas. The key points are listed in a text file, which was imported in the ANSYS. The *x, y* coordinates can be obtained by specifying the chord lengths and the thickness of each cross-section in NACA's documentation. The chord length varies throughout the blade. The blade chord length is 2000 mm at 1.5 m distance from the root. It tapers to a chord length of 920 mm at the tip. These coordinates are exported to an Excel worksheet in two columns. Subsequently the foil coordinates were turned into key points. A 2-D sketch of the root was obtained by importing the points generated from the excel spreadsheet. Each set of foil points were fitted with a spline function, enclosing the foil. This gave a smooth transition between points. This process was carried out for other cross-sections along the length of the blade from root to the tip. Each plane was offset from the next by a specified distance; finally this gave the blade a length of 11 metres. Two new planes were created to add the connector points for the blade to the hub. A 2-D sketch of circles (with diameter of 1000 mm) and ellipses (with diameters of 1200 mm and 800 mm) were created on these planes spaced at a certain distance. The skin/loft function was used to create a surface body by joining all the aerofoils together. Two shear webs are inserted at 15% and 50% of chord length back from the leading edge (Figure 4-6). Table 4-3 shows the general specifications of the FE model of the blade.

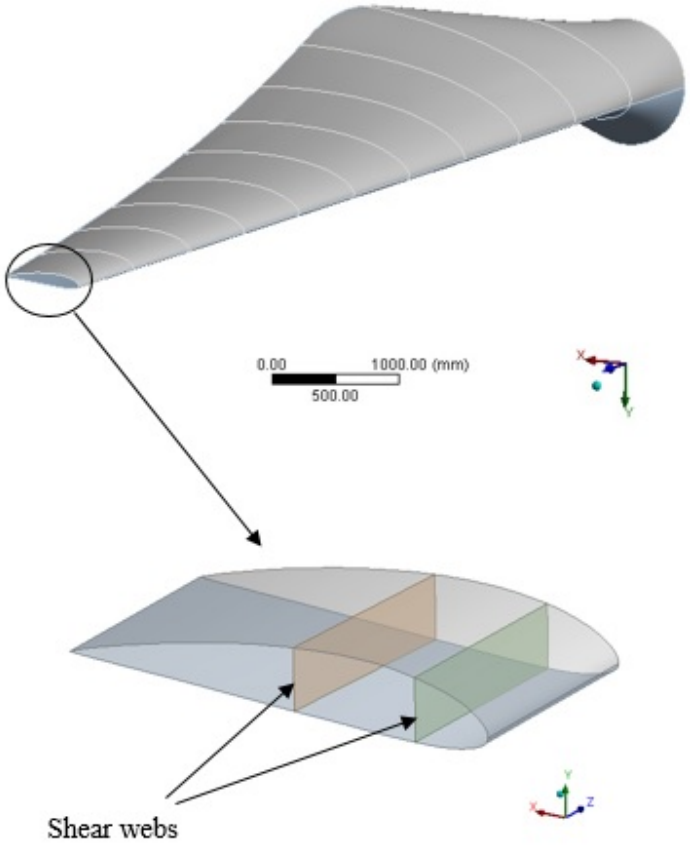

Figure 4-6. FE model of tidal turbine blade, the two shear webs were inserted between the top and bottom skin of the blade at 15% and 50 % of chord length back from the leading edge.

Table 4-3. General specification of FE model of tidal turbine blade.

Parameter		Value
Cross Section	Maximum camber	4%
	Maximum camber position	40%
	Thichness of camber	25%
Characterization of Blade	Length	11000 mm
	Maximum chord	2000 mm
	Station of maximum chord from root	2000 mm
	Minimum chord	920 mm
	Max Twist	20°
	Upper shell area	17.3 m^2
	Down shell area	16.8 m^2
	Thickness variation of blade surface from root to tip (mm)	140-50
	Thickness of shear webs	30 mm

ANSYS Composite Pre-Post (ACP) was used to create laminates on the surface of the blade. Different commands were used to simulate composite blade;

- Fabrics. This command was used for defining thickness of composite.
- Stack Ups. This command was used for defining ply orientation.
- Element Sets. Division of blade into two up and down shells.
- Rosette; Represents reference fibre direction and laminate orientation in each ply.
- Oriented Element Sets; for building the shell thickness. Laminate orientation a, in each upper and down shell were defined using Oriented Element Sets command.
- Modelling Ply Groups; making laminate using defined Fabrics in stage 1.

The basic composite lay-up used for the FE model of the blade is shown in Table 4-4. The same lay-up configuration (0°/90°) was used for all sectors of the blade.

Table 4-4. Composite lay-up used in the FE structural model of the blade.

Sector	Composite lay-up
Top skin	(0°/90°)
Bottom skin	(0°/90°)
Shear webs	(0°/90°)

4.3.4. Composite Ply Drops

With ACP process, the composites are made by laying plies over one another so that the required thickness of the laminate is achieved. The laminates made in this manner are flat since the thickness of each ply is uniform throughout the component. In practice, however, tapering of laminates is necessary in many structural components. The tapering is introduced by terminating plies at different locations. In other words, in order to optimize the weight of the structure, the thickness of the panel can be tailored to the local stress distribution. These thickness variations may be well produced by so-called ply drop-off. In these zones (ply drop-off zones) out of plane stress concentrations may initiate delamination failures. This is a critical failure mechanism and several investigations have been performed about damage and delamination propagation in these ply drop areas (Thomsen *et al.*, 2000; Steeves and Fleck, 2005; Ganesan and Liu, 2008). Design guidelines have been proposed to avoid, or minimize damage initiation for simple specimen geometry, for example by using several ply drops (Mukherjee and Varughese, 2001). The present study addresses the fatigue and mechanical

behaviour of blades with several ply-drop off configurations defined to meet the turbine blade industry design guidelines (DNV, 2015).

Figure 4-7 shows a schematic of ply drop-off in the GFRP composite tidal turbine blade used in this project. The laminate tapers from root of the blade (thick section) to the blade tip (thin section) as a result of the ply drop-off. The use of ply drop-off results in substantial saving in composite material and hence, it is cost effective. However, ply drop-off causes a discontinuity within the composite laminate and consequently, it introduces stress concentrations at the drop points. This leads to failure of the components through delamination and/or failure of the resin.

Inter-laminar stresses induced at the drop-off may cause failure long before the ultimate load carrying capacity of the laminate is attained. The potential paybacks in dropping plies may be compromised through a reduction of strength and stiffness of the composite blade. Therefore, the dropping-off of plies has to be executed in a mode that does not influence the strength and stiffness of the composite to a great extent.

Ply drop-off in laminated composites has been recognized as a stress raiser (Wilklns, 1982; Curry *et al.*, 1992). Several experimental and analytical studies have been reported regarding various aspects of this problem. A detailed review is available in (Varughese and Mukherjee, 1997). In these studies, the effect of three design parameters including the number of plies dropped-off at a single station, the distance between consecutive drop-offs (stagger distance) and the lay-up of a dropped sub-laminate on the strength of the composite blade have been considered.

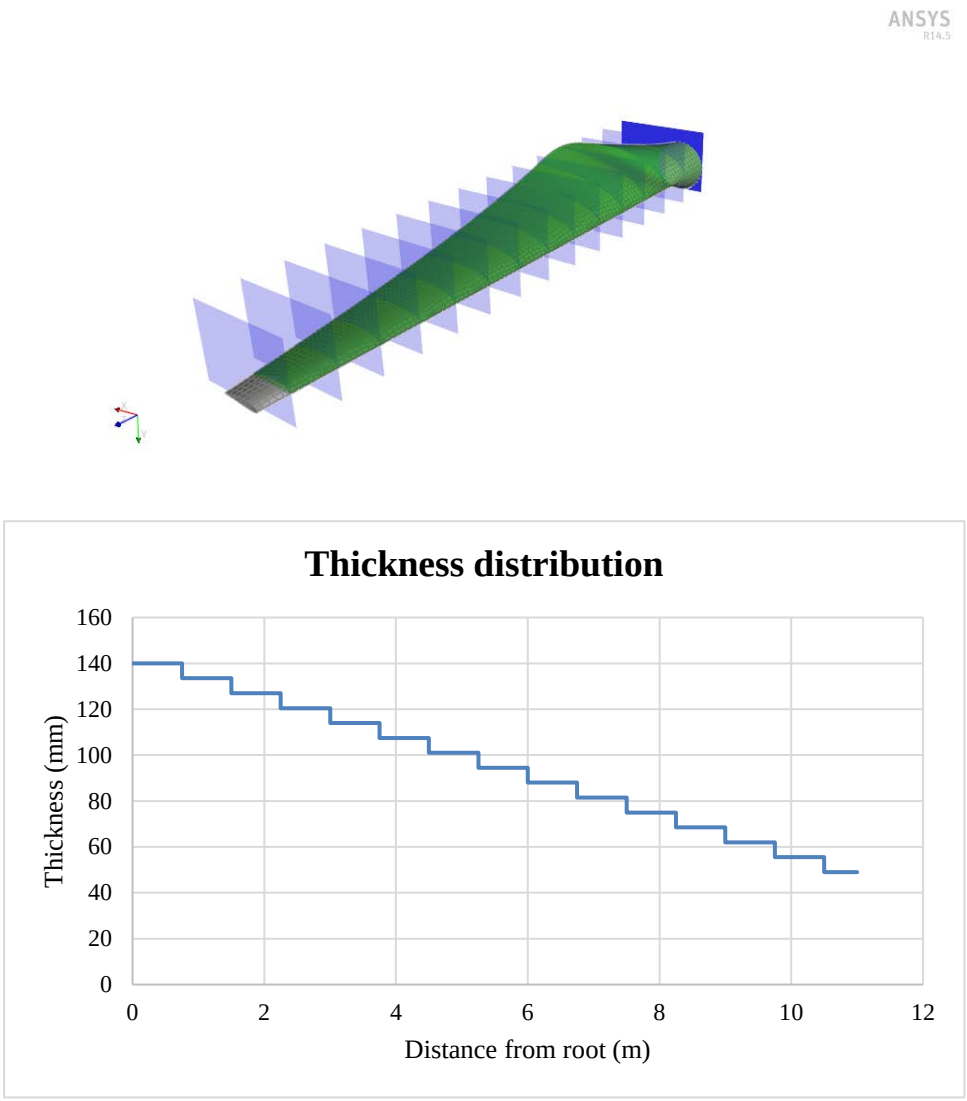

Figure 4-7. Composite blade ply drops and thickness distribution.

Figure 4-7, shows GFRP composite blade studied in this project with ply drops along the span-wise section of the blade. After designing the blade profile, the geometry was imported into ANSYS Composite Pre-post (ACP) where the *Parallel rule* command was used to create ply-drops along the length of the blade by incrementally terminating plies from root to tip. In the tapered area, the plies are dropped, from about x to x-6.5 mm plies, by respecting the typical design guidelines for ply drop-offs (ANSYS).

4.3.5. Convergence Criterion

For evaluation of the results from the FE model of the tidal turbine blade, the convergence criterion was taken into consideration. An appropriate number of elements are obtained by increasing the mesh density. The stabilization of the stress and tip deflection are the criteria for convergence. Figure 4-8 shows the results of the convergence analysis. Convergence is acquired with the use of approximately 75,000 or more elements.

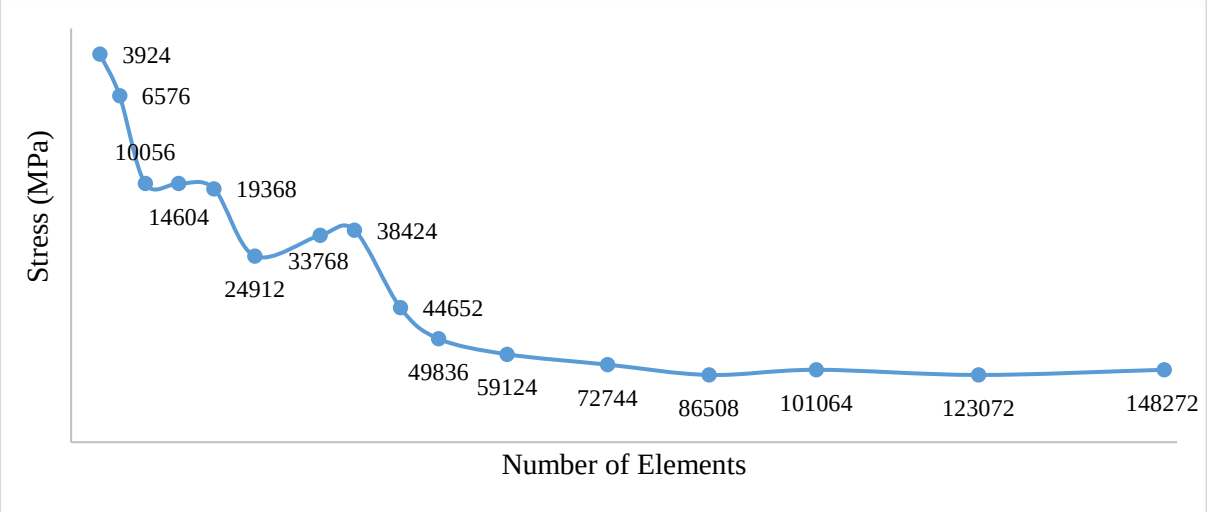

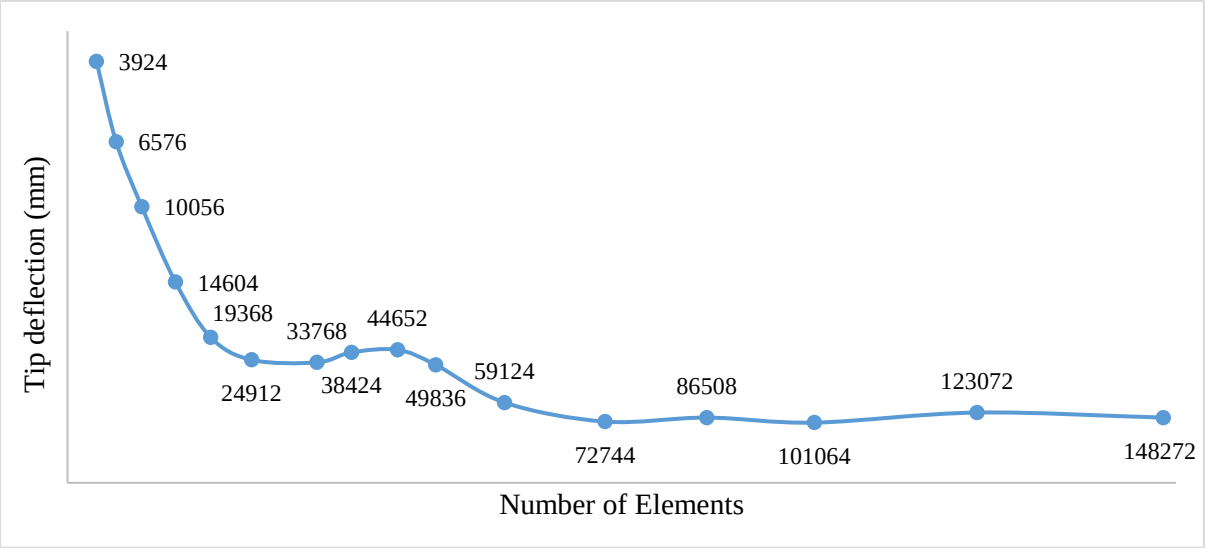

Figure 4-8. Convergence based on (a) Von-Mises Stress , (b) Tip deflection.

4.4. Fatigue Analysis

In order to perform a fatigue analysis, the blade geometry, the mechanical properties of the blade material and the loading-time history on the blade have been transferred into the ANSYS n code design life module. Considering the FE model of the blade and the mechanical properties which were experimentally determined, the time-series loads as the main fatigue loads on the tidal turbine blade also need to be identified. The method for determining hydrodynamic loads (tangential and axial forces) and loading-time history for the FE model of the tidal turbine blade is discussed in the next chapter.

Chapter 5

Hydrodynamic Analysis

5. Hydrodynamic Analysis

With reference to the fatigue life prediction methodology (Figure 3-1), this chapter addresses hydrodynamic loading. As it was mentioned before, in this study a fatigue life prediction methodology was proposed on the basis of FE analysis of the blade. One of the main requirements in performing FE analysis on the blade, is to predict the magnitude of hydrodynamic loads acting on the blade. Using information about the blade geometry (chord length and twist angle distribution), tidal current velocity and angular velocity, a hydrodynamic model can be developed and therefore the amount and distribution of axial and tangential loads on the blade can be estimated. Emphasis is made on the thrust load as it causes bending of blade and create a flap-wise bending moment near the blade root. Consequently the main issue regarding the first stage of the fatigue life prediction methodology, Figure 3-1, is met in this chapter. In the following sections, more details of the hydrodynamic blade models are discussed.

5.1. Hydrodynamic Model

In order to determine the axial (thrust) and tangential forces acting on the tidal turbine blade, a hydrodynamic model based on Blade Element Momentum Theory (BEMT) (Ingram, 2005) and Stream Tube (Kennedy *et al.*, 2012) methods were developed using a MATLAB code (Appendix 3 and 4). The MATLAB code which is based on the local relative fluid blade velocities/forces (Kennedy *et al.*, 2012) was provided by the project partner from the Strathclyde University and subsequently was verified by an EXCEL file (Appendix 5) using the same equation detailed in (Kennedy *et al.*, 2012). Both BEMT and Stream tube momentum methods have the same principle and the difference is mainly related to induction factors involved in equations. This hydrodynamic model and MATLAB code have been validated using input parameters and information provided in (Kennedy *et al.*, 2012; Grogan *et al.*, 2013).

BEMT is usually used for the analysis of tangential and axial loads acting on wind turbine blades. It is implemented in this project to the case of tidal turbine blades where the major difference is the density of sea water and air. In fact in modelling tidal turbine blades and hydrodynamic loads acting on blades, it is supposed that the quantity of sea water current which passes through the area of the rotor disc losses some of its kinetic energy to provide the impetus to rotate the blade (Grogan *et al.*, 2013; Fagan *et al.*, 2016). In BEMT the area of the rotor and therefore the blade is divided into the number of elements at a radius of (r) and length of (δr)

along the blade length (Grogan *et al.*, 2013). In each of these blade elements, chord length can be set until the loads from sea water current on the blade is balanced by the momentum thrust (Grogan *et al.*, 2013). The process is performed along the span of the blade for each element and the total thrust and torque forces are calculated. It must be noted that determining the chord length was outside the scope of this project, therefore in this work, the chord length was defined as an input parameter for the hydrodynamic model (MATLAB code, Appendix 3) and it is not determined by the code.

In BEMT, the axial and tangential forces can be derived using the angle of attack, flow angle and twist angle for each element which can be calculated from the incident resultant velocity (Ingram, 2005). Figure 5-1 shows the relative incident water velocity (W) and it's axial (V_d) and rotational (tangential) (V_t) components on a single blade element. In fact the angle of attack (α), is dependent on the tidal current velocity, rotational speed of turbine blade and axial/ tangential induction factors of a and a' (Ingram, 2005). Induction factors indicate a reduction of the tidal stream speed between the rotor disc and the free stream. An iterative process is used to determine induction factors a and a'(Ingram, 2005).

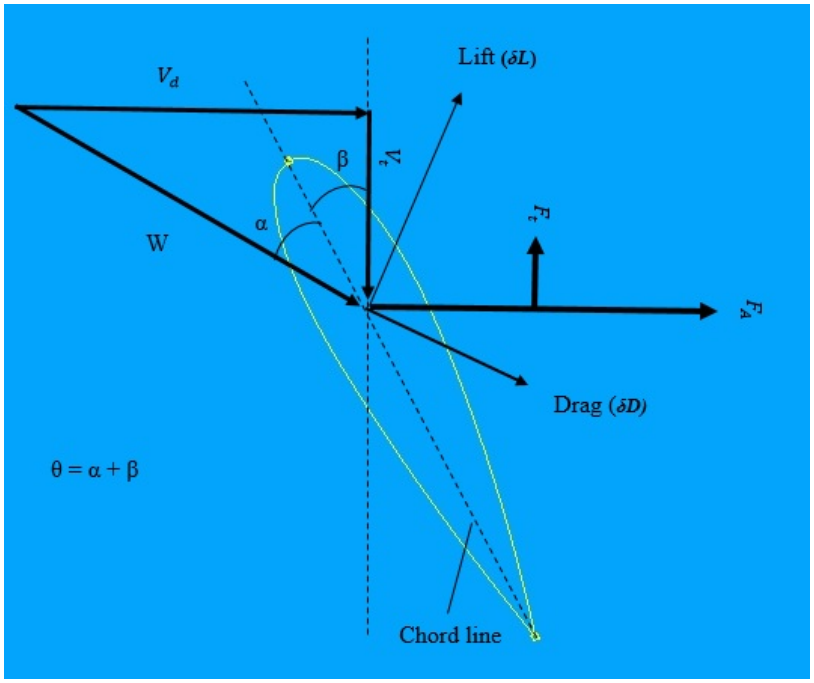

Figure 5-1. Diagram showing the directions of velocities and the force directions (The lift force (δL) and the drag force (δD)) on a turbine blade element (Fagan *et al.*, 2016).

In this study, stream tube model (Kennedy *et al.*, 2012) was used for prediction of axial and tangential forces on the blade. It must be noted that for the stream tube model (Appendix 3),

the fraction of axial velocity remaining at the exit of the stream tube (i.e. ζ in Table 5-1) was set to 0.33 in the MATLAB code, assuming that the water velocity in each of the blade elements has slowed to 0.33 of its initial velocity (Kennedy *et al.*, 2012).

The BEMT analysis is conducted by defining the number of elements and the geometry of the blade. The blade chord length is 2000 mm at 2 m distance from the root. It tapers to a chord length of 920 mm at the tip.

The axial velocity at the rotor disc is given by;

$$V_d = V_0(1- a)$$

5-1

Where V_0 is the free stream velocity of the seawater current. The rotational (tangential) velocity of a blade element, is given by

$$V_b = \omega r$$

5-2

Where ω is the angular velocity of blade. The net tangential velocity, V_t, is;

$$V_t = (1+ a') V_b$$

5-3

The resultant velocity is then (Figure 5-1),

$$W = \sqrt{(V_d{}^2 + V_t{}^2)}$$

5-4

And the angle between the resultant relative velocity and the rotational plane of the rotor is;

$$\Theta = \alpha + \beta$$

5-5

Where β is the pitch angle and Θ is the angle between relative velocity and the rotational plane of the rotor.

The lift force (δL) and the drag force (δD) generated for each blade element along the blade can be calculated using following equations:

$$\delta L = 0.5\rho c W^2 C_L \, \delta r$$

$$\delta D = 0.5\rho c W^2 C_D \, \delta r$$

5-6

In the above equations, C_L and C_D are lift and drag coefficients respectively, c is the chord length for each blade element and ρ is the density of the fluid. Then the drag and lift forces are translated into axial and tangential forces acting on a blade element by

$$F_A = \delta L \cos\Theta + \delta D \sin\Theta$$

$$F_t = \delta L \sin\Theta + \delta D \cos\Theta$$

5-7

Consequently, with the information about the magnitude of the axial and tangential forces acting on each blade element, the total thrust and torque forces acting on a blade can be calculated.

In addition, the XFOIL code (Drela and Youngren, 2008) was used to generate the lift and drag coefficients for the angle of attack. The hydrodynamic model used in this work is based on (Kennedy *et al.*, 2012; Grogan *et al.*, 2013). A full description of the equations used in stream tube (MATLAB code) has been provided by (Van Briel and Van Leuven, 1985; Ingram, 2005; Kennedy *et al.*, 2012). The input parameters for the hydrodynamic program based on the stream tube model are summarized in Table 5-1.

Table 5-1. Input conditions to the BEM and stream tube model

Parameter	value
Water velocity	2.5 (m/s)
Angle of attack	6°
Number of blades	3
RPM	10
Water density	1025 kg/m^3
Water viscosity	0.0013155 Pas
ζ	0.33
Blade length	11 m
Number of stream tube/blade elements	45

The normal and extreme tidal current velocity for which the turbine blade is expected to work, were chosen as 2.5 and 3 m/s respectively. This tidal current velocity was obtained from a potential site around Scotland (Stronge) for tidal turbine installation.

In general, the rotor size needs to be determined based on the limitation and constraints in which the tidal turbine devices can be installed (Walkington and Burrows, 2009; Kennedy *et al.*, 2012; Grogan *et al.*, 2013). These constraints include water depth at which the tidal turbine can operate, the depth which the support structure of turbine blade can be installed, the bending moment at the root of the blade (Grogan *et al.*, 2013).

The tangential and axial force distributions calculated by the stream tube model via equations (5-6 and 5-7) are depicted in Figure 5-2. The thrust force which can cause bending of blade acts perpendicular to the air foil chord line and the tangential force which can cause torque (power generating) acts parallel to the aerofoil chord line (Grogan *et al.*, 2013). Figure 5-3 shows the axial loads on the FE model of the blade. The resultant hydrodynamic forces are applied to the FE model as 'surface traction distribution' (Grogan *et al.*, 2013) and act through the quarter chord of the blade section (Spera, 1994; Kennedy *et al.*, 2012).

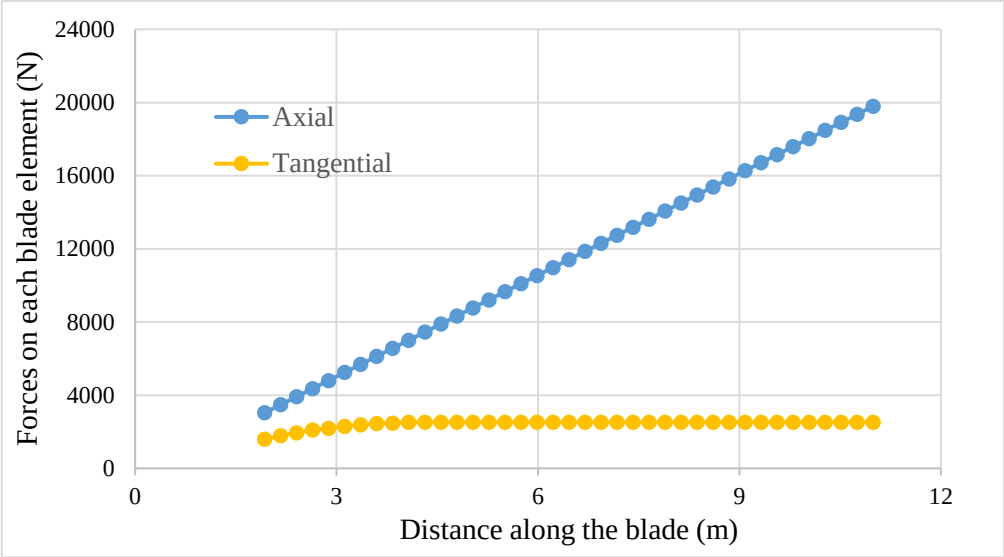

Figure 5-2. Distribution of axial (out-of-plane) and tangential (in-plane) forces from hydrodynamic model at 2.5 m/s tidal current velocity.

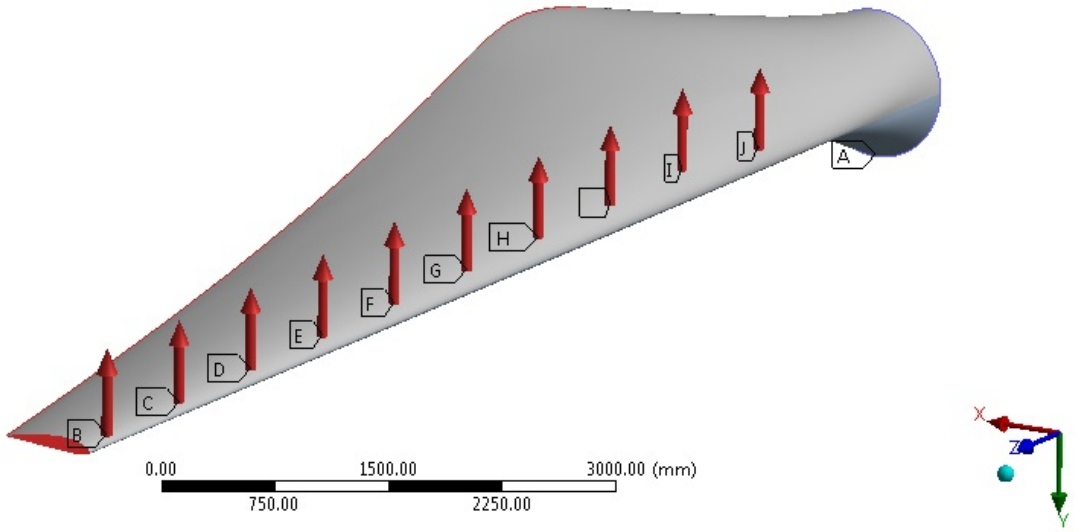

Figure 5-3. Schematic model of 11 meter blade showing axial forces.

Figure 5-4 shows the variation of maximum root flap-wise bending moment as a function of tidal current velocity. It is clear that increasing the water velocity from 1.5 to 3 m/s (i.e. two fold) results in increasing of the bending moment by four times.

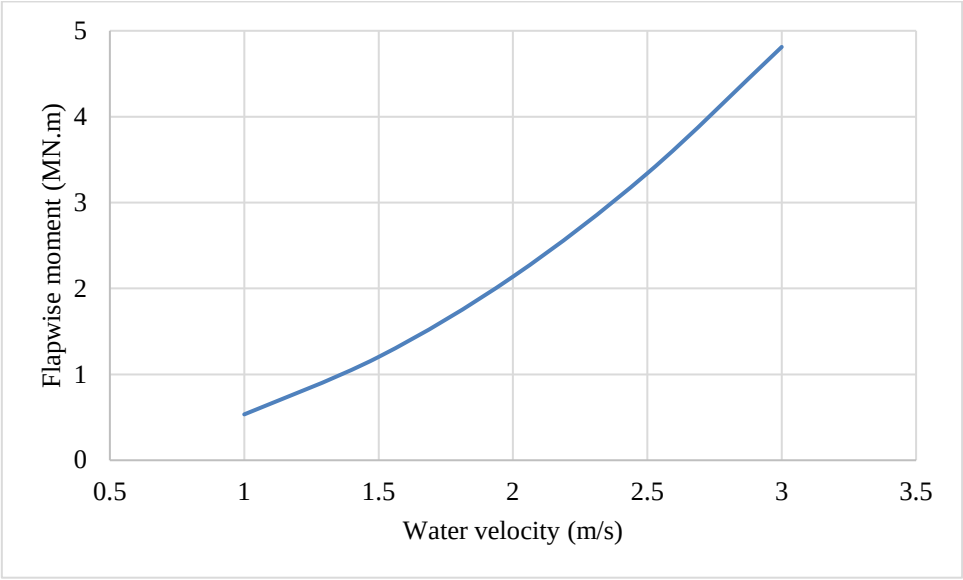

Figure 5-4. Effect of water velocity on max bending moment as predicted using hydrodynamic model.

5.2. Fatigue Loads on Tidal turbine Blades

The fatigue loads on a tidal turbine blade are caused by the variations in the tidal current velocity and the rotation of the rotor.

The most important factor in fatigue analysis of tidal turbine blades is the loading spectrum. Therefore, the loading spectrum of tidal turbine blade must be determined for fatigue analysis of any constituent in operation. In general, tidal turbine blades are subjected to alternating loads originated from the variation of tidal currents. As a result of the effect of low and high tide, the velocity of a tidal current varies with respect to time. The tidal model which was assumed in this project has two high and two low tides per day with the level varying by about 20% in a repeating monthly cycle. Figure 5-5 shows a typical tidal current velocity at any time (*t*) which is due to variation in tidal height with respect to time (Stronge). By making some basic approximation, tidal current velocity at any time can be estimated from tide height. Varying currents will cause changes in loading and consequently these varying loads on turbine blades will produce cyclic loads. It must be noted that the tidal turbine studied in the project has yaw system and therefore it yaws once the direction of tidal current velocities reverse.

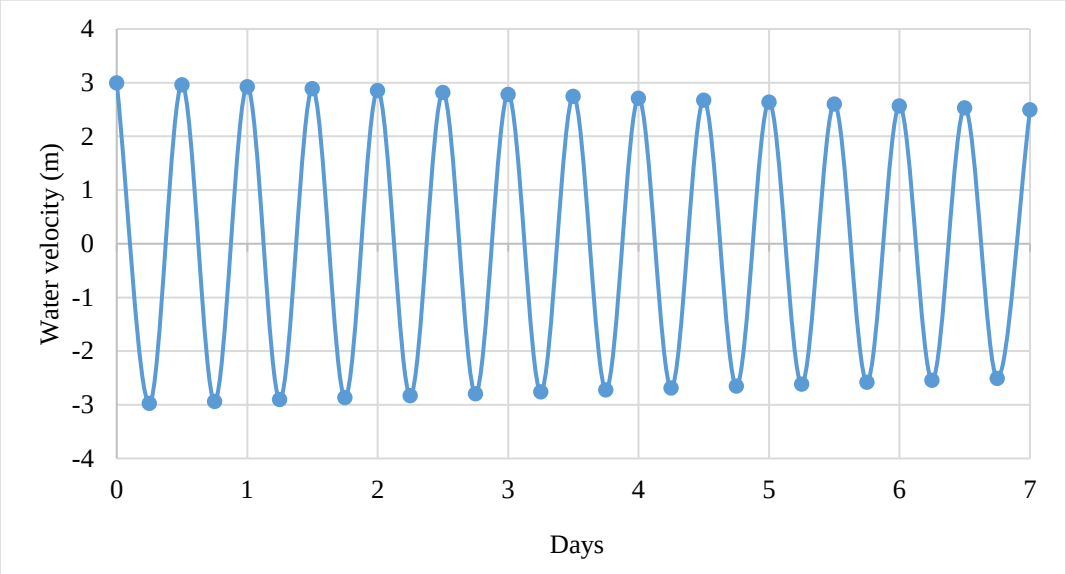

Figure 5-5. Sinusoidal model for water velocity.

To calculate loading variations on a blade, about 7 days (168 hours) of water velocity profile (velocity-time series) was considered. From time series velocity data, the tangential and axial force profile (loading spectrum) corresponding to a model of water velocity on a turbine blade (Figure 5-5) was determined. This was done using stream tube momentum model. For simplicity in this analysis, 10 blade elements were defined in MATALB code. Figure 5-6 and

Figure 5-7 show schematically the variation of tangential and axial loads on each blade element section along the span of the FE model of the blade. This loading spectrum was implemented for fatigue analysis via ANSYS n code design life as input data. In this study, for fatigue analysis, a 90% reduction of bending strains due to the axial and tangential forces in tidal turbine was considered corresponding to fatigue loading ratio of 0.1. It must be noted that the strain ratio of fatigue testing explained in section 8.2, is 0.1.

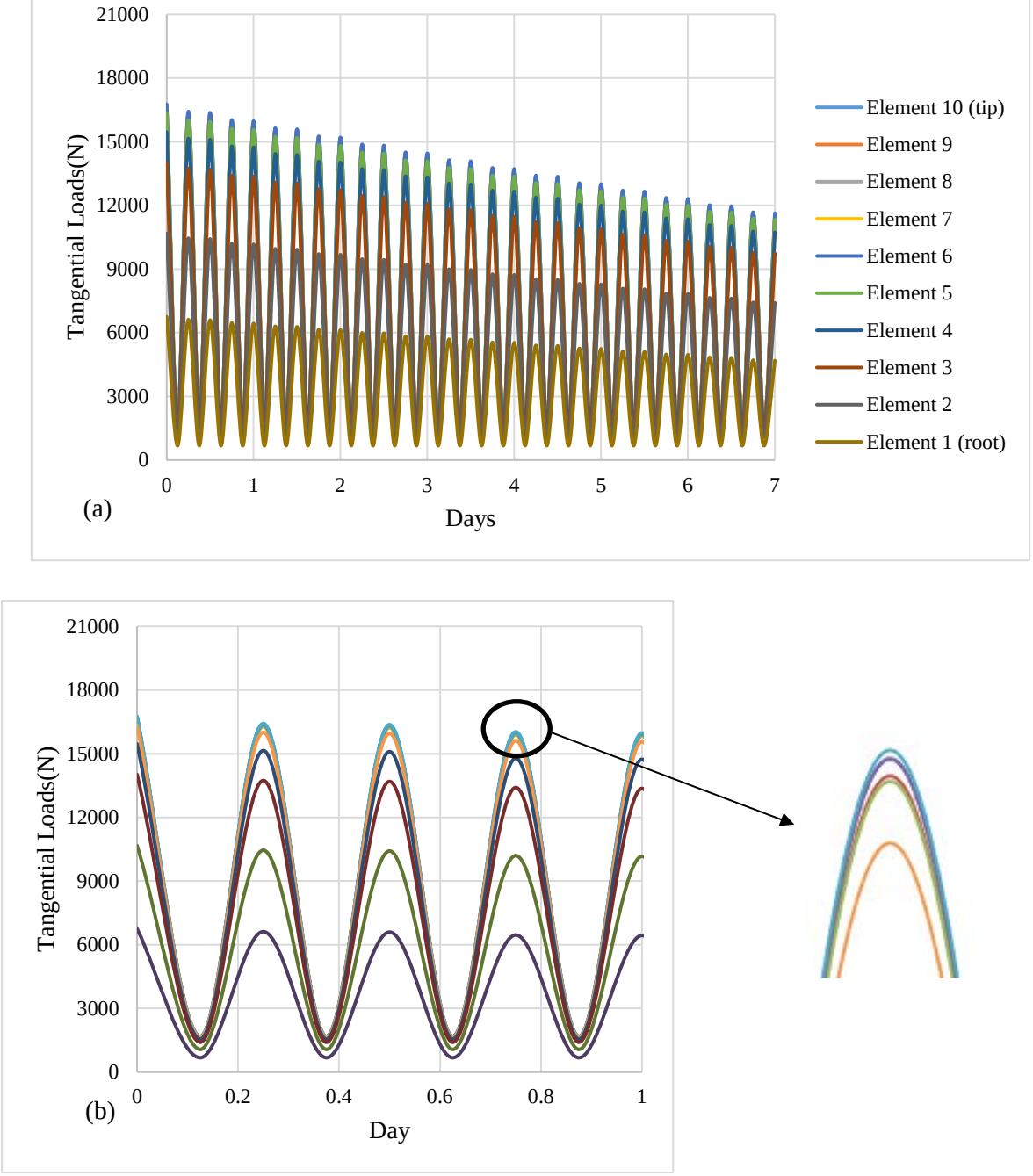

Figure 5-6. Schematic variation of tangential loads on tidal turbine blade (a) 7 days, (b) one day period. Each curve corresponds to the variation of tangential loads on each blade element. For hydrodynamic analysis, the blade was divided to 10 elements/stream tubes.

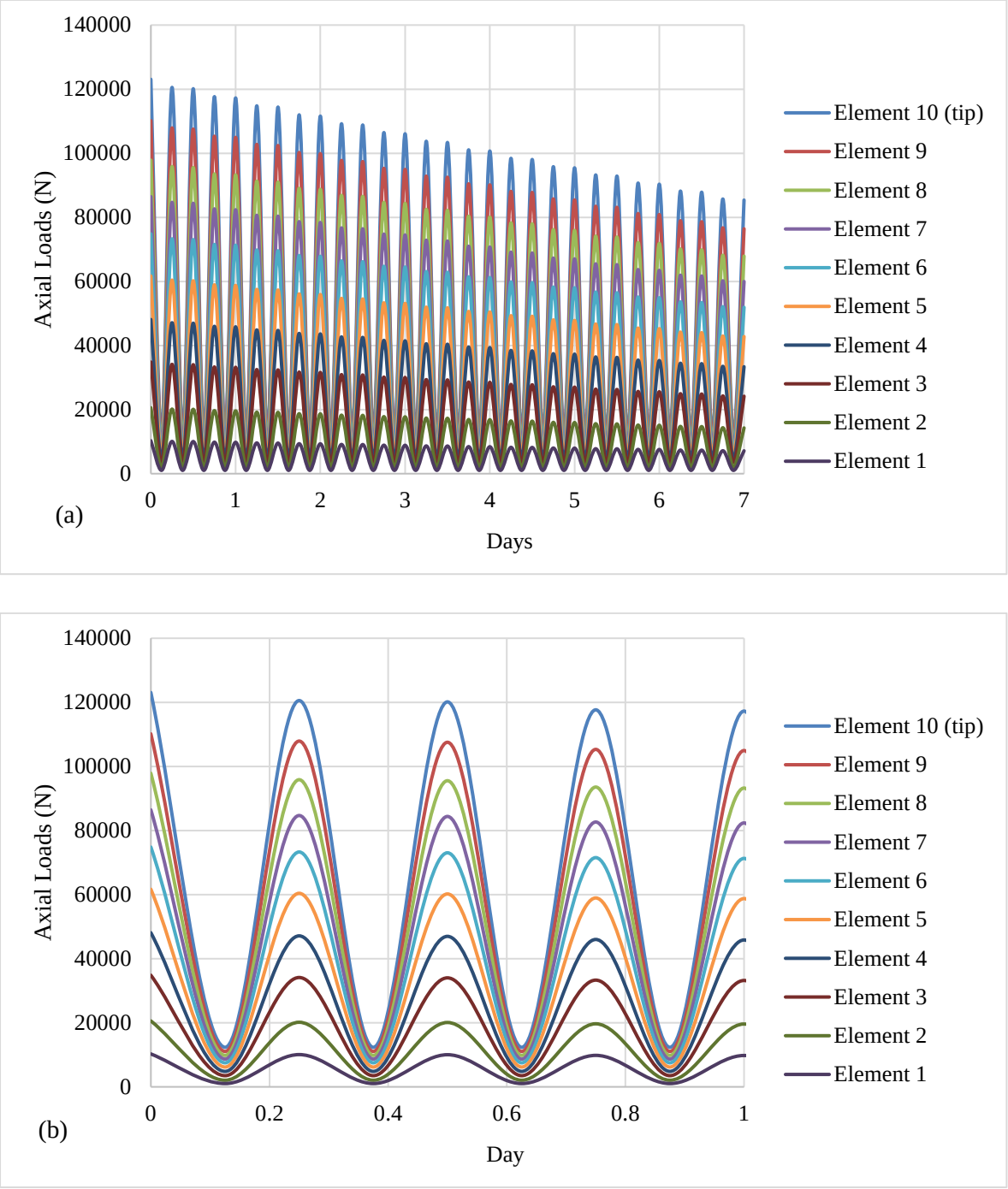

Figure 5-7. Schematic variation of axial loads on tidal turbine blade during (a) 7 days and (b) one day period. Each curve corresponds to the variation of axial loads on each blade element. For hydrodynamic analysis, the blade was divided to 10 elements/stream tubes.

5.3. Summary

In this chapter, a hydrodynamic model based on stream tube momentum approach was used in order to determine the hydrodynamic loads acting on the FE model of the blade. This was done by developing a MATLAB code (appendix 3 and 4), in order to predict the fluid-blade force distribution, therefore the boundary condition and mode of loading required for FE model of the composite blade were defined. Two normal and extreme tidal current velocities (i.e. 2.5 and 3 m/s) were considered and the corresponding hydrodynamic loads were determined and applied to the FE model of the blade. The level of thrust loads are greater than the level of tangential loads (approximately 6 times) meaning that the thrust loads can cause high flap-wise bending moment at the blade root. Therefore variation of the high-flap-wise bending moment as a function of tidal current velocities for evaluation of the structural performance (and fatigue life prediction) of tidal turbine blades was evaluated. To predict the fatigue life of composite blade, the loading history (time-series of thrust and tangential loads) was determined by the same MATLAB codes. This was done on the basis of velocity fluctuation pattern which is due to the tidal movement. As a result time-series of loading was applied to the FE model of the composite blade and it resulted in the time-series of strains (cyclic strains) that the blade experience during each tidal movement.

Chapter 6

Quasi-static Mechanical Tests

6. Quasi-static Mechanical Tests

With reference to Figure 3-1, this chapter addresses the requirement of FE structural analysis of a blade in terms of the mechanical properties required (stress-strain response of the composite). As was mentioned before a fatigue life prediction methodology was proposed which is on the basis of experimental mechanical properties. A series of tests including tension, shear and three point bending were carried out in order to obtain mechanical properties of the composite used for FE analysis. These tests are conducted on composite samples made of GFRP. Tension and shear properties in the form of stress-strain data were obtained and used as input data for the FE model of a blade. DIC contributed strain measurement to build the stress-strain curves of composite under mechanical testing and from these curves the information for FE analysis was obtained.

Since one of the performance limiting issues regarding FRP composites is their failure modes, which can significantly affect the behaviour of FRP composite tidal turbine blades, in this chapter characterization and failure analysis techniques including optical/scanning electron microscopy and DIC, were used to characterize potential failure mechanisms. Identifying these failure mechanisms when the composite samples are subjected to tension, shear and bending fatigue loads, can increase our understanding about limiting issues in the use of composites in tidal turbine blades.

In addition, since laminated composites are anisotropic, the effect of fibre orientation on all tension, shear and bending tests of composite samples has been investigated; this can increase our confidence in the use of these materials for components with complex geometry.

Because the results of FE analysis of the blade have not been validated using experiments on a real blade, in order to acquire confidence about the results of FE model of blade, all mechanical tests on GFRP test coupon with 0/90 fibre orientation used in this study were simulated by the FE software (ANSYS). Then the FE calculated strain fields were compared with DIC strain fields and the agreement between these two methods in terms of strain distribution have been used to validate the FE model. In addition, FE results of mechanical testing (tension, inter-laminar shear and 3PB test) were validated using closed form solutions.

In the following sections details of mechanical testing including the construction of stress-strain curves, failure analysis of composites using SEM and DIC and the FE modelling of mechanical tests are discussed. It must be noted that the results presented in the following

sections are unique to this particular fibre architecture and cannot be generalized for other woven composites.

6.1. Quasi-Static 3PB and Tensile Tests

6.1.1. 0°/90° Fibre Orientation

Initially microstructural analysis was used to reveal information about the microstructure. This was done using light and electron microscopic techniques described in chapter 3. The reinforcement material consists of longitudinal and transverse bundles of glass fibres as shown in Figure 6-1. The fibres, having an average diameter of 10**μ**m are grouped into the bundle of fibres which are intertwined and oriented in the form of a plain woven fabric (orthogonally oriented). The bunch of fibres has an oval-shaped cross-sectional appearance with an average width and height of about 750**μ**m and 100**μ**m respectively. 24 plies of fabric were laminated until 5 mm thickness achieved. Figure 6-1 shows a micrograph of this composite from both cross-section (lateral side) and top surface of the initial plate.

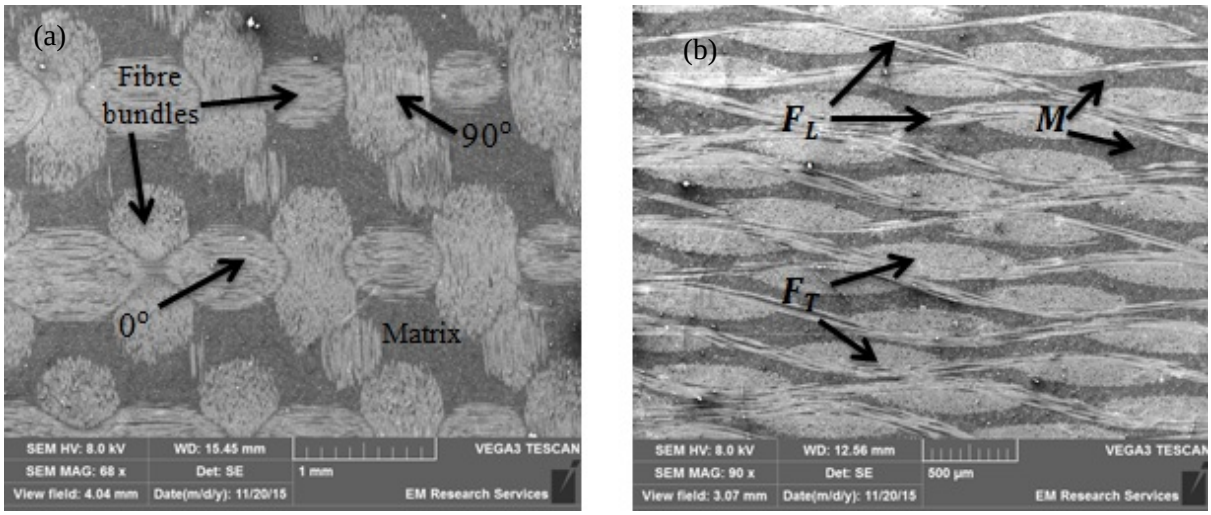

Figure 6-1. Scanning electron micrographs showing (a) the microstructure of the top surface of the sample showing the direction of fibre bundles at longitudinal and transverse axis, (b), and the cross section of GFRP composite. The micrograph shows the cross woven of microstructure with biaxial fibre alignment ($\boldsymbol{F_T}$ - transverse fibres, $\boldsymbol{F_L}$ - longitudinal fibres, M-bulk matrix)

GFRP samples were subjected to 3PB and tensile tests to evaluate static flexural and tensile properties. The results of 3PB and tensile tests including the modulus of elasticity, ultimate strength are listed in Table 6-1. Tensile and flexural strength in this table are in agreement with the mechanical properties of this composite provided by the manufacturer (Appendix 2). It must be noted that bending modulus in this table is actually the effective elastic modulus (E_{eff})

which was obtained by equation 3-1. Tensile and flexural modulus are dependent not only upon the fibre and matrix properties, fibre angles and fibre volume fraction but also on the stacking sequences (Gilchrist *et al.*, 1998). In all cases of 3PB testing of composites, failure initiated on the compression and tension side, under the loading roller. Cracks and some delamination propagated from the initial damage until final failure of the test specimen. Cracks were also observed to grow along the adjacent transverse bundles of fibres in the woven laminates. The failure on the tensile side occurred in the form of fractures (Figure 6-2) within the glass fibre bundles and cracking of the matrix between the bundles.

Table 6-1. Mechanical properties of GFRP composites (raw data of tension and 3PB test results are detailed in appendix 1). * Compression test was conducted at the research institute in Iran.

test	Mechanical properties	GFRP
3PB	Effective Elastic Modulus, E_{eff} (GPa)	21±1
	Ultimate Flexural Strength UFS (MPa)	465±15
Compression*	Compressive Elastic Modulus, E (GPa)	19.5±1
	Ultimate compressive Strength UCS(MPa)	290±10
Tension	Tensile Elastic Modulus, E (GPa)	21.6±1
	Ultimate Tensile Strength UTS(MPa)	320±10
	Poisson's Ratio	0.25

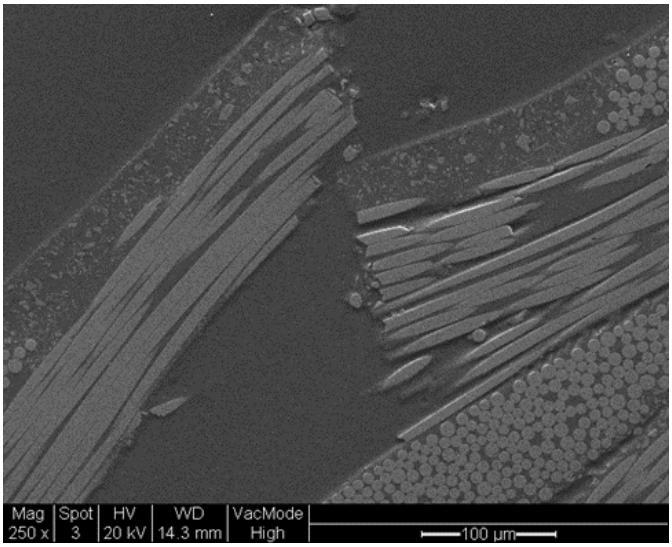

Figure 6-2. Tensile failure of a woven GFRP composite under three point bending test.

In tension, in the early loading stage, local fibre breakage occurred followed by stress redistribution. After this, interfacial de-bonding between fibres and matrix occurred and this is followed by fibre fracture in the form of fibre pull out that leads to the final failure. As seen in (Figure 6-3a) on the fracture surface of the composite, bundles of fibres were pulled out which confirms interfacial de-bonding between the fibres and matrix. This shows that the interfacial bond strength is exceeded before the tensile failure strength of the composite is reached (Godara and Raabe, 2007). The top surface view of the fracture edge of the composite specimen after failure in tension shows a straight fracture edge with transverse fibres pulled out (Figure 6-3 (c and d)).

From the load-displacement curves obtained in 3PB tests (Figure 6-7), it can be observed that, initially load rises correspondingly with displacement; the material shows a linear elastic behaviour until the point of fracture under the highest load. In 3PBT, it is possible to identify that after an initial settlement, the trend is linear-elastic until a certain stress value. After this point micro-cracks start to appear in the area around the loading roller. Then the load increases but the curve slope is lower due to the crack propagation. As a result of bending, shear stresses are developed at the neutral axis of the test specimen. Due to the high magnitude of the shear stresses induced in the polymer matrix near the neutral axis, inter-laminar cracks can be observed in the matrix. Also, due to the differences between stress magnitudes induced in adjacent plies, delamination occurred. Figure 6-4 shows the inter-laminar-cracks associated with delamination. In the 3PB test the failure in the compression side occurs due to buckling of the fibres while on the tension side failure occurs due to fibre breakage in tension.

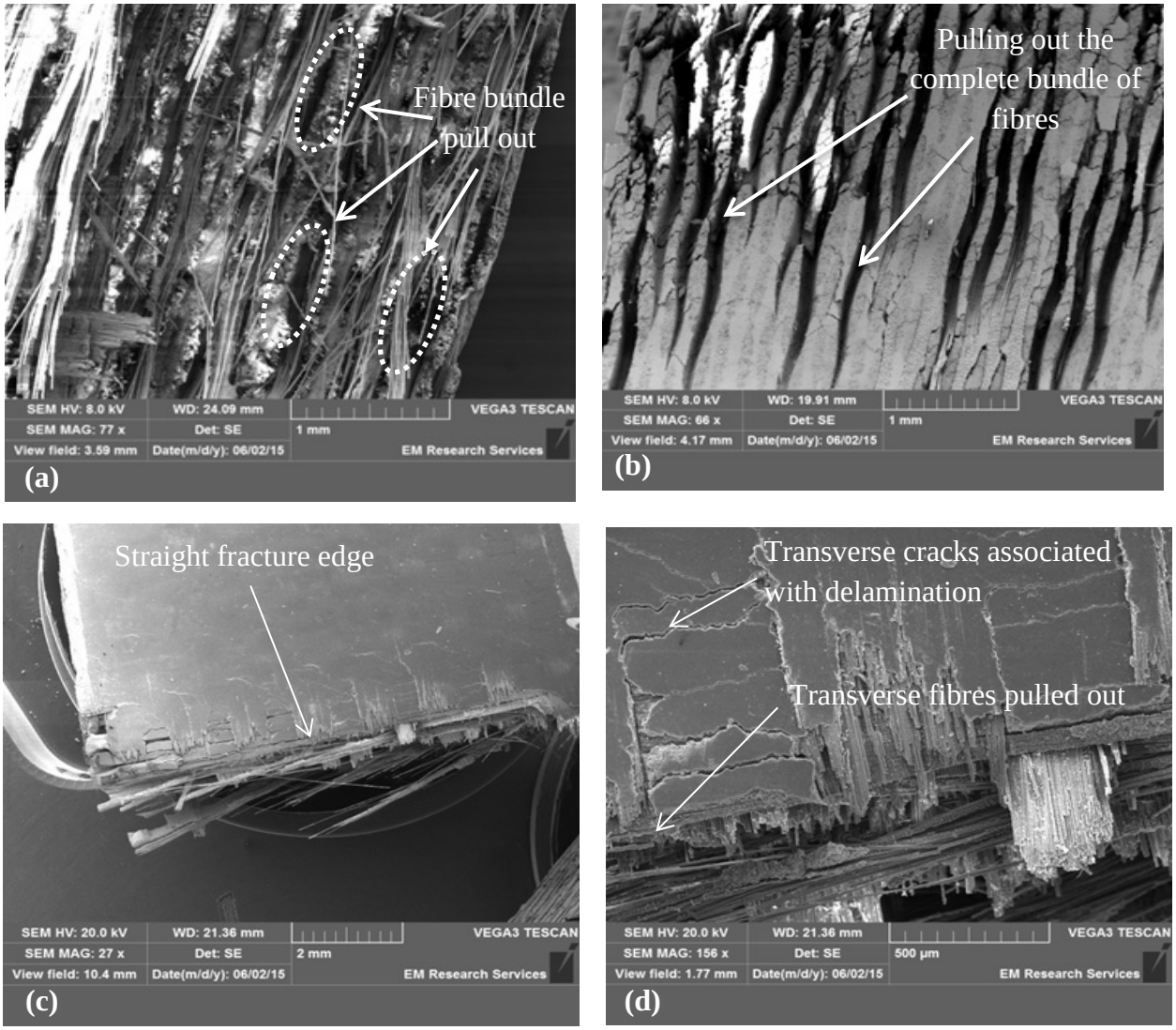

Figure 6-3. Scanning electron micrographs of the fracture surface of GFRP composite samples (a) bundle of fibres pulled out from epoxy resin (b) pulling out of complete fibre bundles from lateral side view, (c) straight fracture edge, (d) transverse fibres pulled out, transverse cracks associated with delamination.

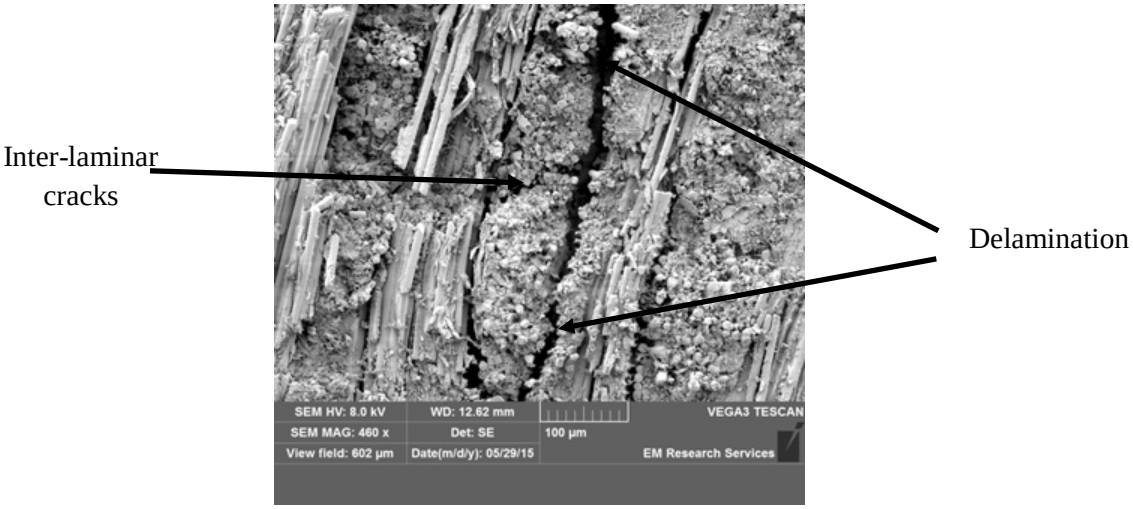

Figure 6-4. Scanning electron micrograph from lateral side of GFRP composite specimen after failure in static 3PB test.

6.1.2. Three point bending strength versus tensile strength

As it can be seen from the Table 6-1, the bending strength is higher than the tensile strength for glass fibre reinforced polymers. The bending strength would be identical as the tensile strength if the material were not inhomogeneous. In fact, most materials in particular FRP composites have small or large defects/imperfections which causes stress concentration locally, effectively leading to a localized weakness. When a FRP composite material is subjected to flexure only the extreme fibres are at the maximum stress/strain so, if those fibres are free from imperfections/flaws, the flexural strength is dominated by the strength of those undamaged fibres. However, if the same composite material is subjected to only tensile loads then all the fibres in the material are at the similar stress and failure occurs when the weakest fibre reaches its limiting tensile strength. Therefore, it is common for flexural strengths to be greater than tensile strengths for the same material.

By ignoring the effects of defects of any kind, it is obvious that the material fails under a bending force which is lesser than the equivalent tensile force.

For a rectangular test specimen, the resultant stress under an axial load is given by

$$\sigma = {}^{F}/_{bh}$$

Where F is the axial load (force) at the fracture point, b and h are the width and the thickness of test specimen

The resultant stress for a rectangular test specimen under a load in a 3PB configuration is given by:

$$\sigma = {}^{3FL}/_{2bh^2}$$

Typically, L (distance between the support span) is much larger than h, so the fraction of $3L/(2h)$ is greater than one.

Aside from the above discussion regarding the difference between flexural strength and tensile strength, any differences between these two properties are to be expected to be statistical in nature. One usually wouldn't expect to see too much difference in these strength values for a ductile material (e.g., metals), however this may certainly not be the case for technically brittle materials, such as ceramics and certain composites (e.g. FRP composites). The strength of brittle materials is very sensitive to the size of the sample; larger components often exhibits inferior strengths because their strength depends on the population of the defect/flaw and therefore, with a larger specimen, there is a greater statistical chance of finding a larger defect/flaw. Many years ago Leonardo da Vinci actually established that larger and/or longer wires had lower strengths than shorter ones. Comparing the strengths measured in tensile versus flexure tests, the active statistical surface or volume of test specimen that experiences the highest stresses are very different. For similar sizes of specimens, the entire sample surface/volume experiences the highest stresses in tension, whereas in flexure the highest stresses will only be on the top loading surface, i.e. the active sampling volume is much smaller.

In other words, in a tensile test, the maximum tensile stresses are experienced throughout the entire volume of the test specimen; in bending (where the sample experiences tensile stress above the geometric mid-plane and compressive stresses below), the maximum tensile stresses are concentrated in a small region on the top surface above the geometric mid-plane. Consequently for the comparable sized test specimen, the tensile sample experiences the maximum stresses throughout its entire gauge length, i.e., over a much bigger volume than the equivalent flexure sample, In brittle materials (e.g. FRP composites) which are highly sensitive to the population of the defect, this change in statistical sampling volume means that strength measured in tensile tests are expected to be lower than the corresponding strength measured in bending, because there is a higher statistical likelihood of finding a larger flaw. Similar arguments about the difference between the flexural and tensile behaviour of fibre reinforced polymer composites have been discussed in the literature showing that flexural

strength is normally higher than the tensile strength (Bullock, 1974; Whitney and Knight, 1980; Wisnom, 1992; Hild *et al.*, 1994; Maalej and Li, 1994; Ahmed and Vijayarangan, 2008).

Tensile data on FRP composites generated from a bending test, typically yield a higher strength than witnessed from a standard tensile test specimen. According to a statistical-strength theory based on a Weibull distribution, the existence of s stress slope in the bending test results in an increase in tensile strength as compared to the tensile test under uniform stress (Whitney and Knight, 1980). Both experiment and theory suggest that the flexural strength is significantly greater than the tensile strength (Hild *et al.*, 1994).

The effects of defects (e.g. entrapped air bubbles) in GFRP composite studied in this project was investigated by scanning electron microscope (Figure 6-5). Entrapped air in composites that is not removed during manufacturing can lead to the creation of voids in the cured composite. As a results, given the above discussion regarding the effects of defects on the mechanical properties (i.e. flexural and tensile properties) of composite, the difference between flexural and tensile strength of glass fibre reinforced polymer composites is due to the effects of defects in Figure 6-5.

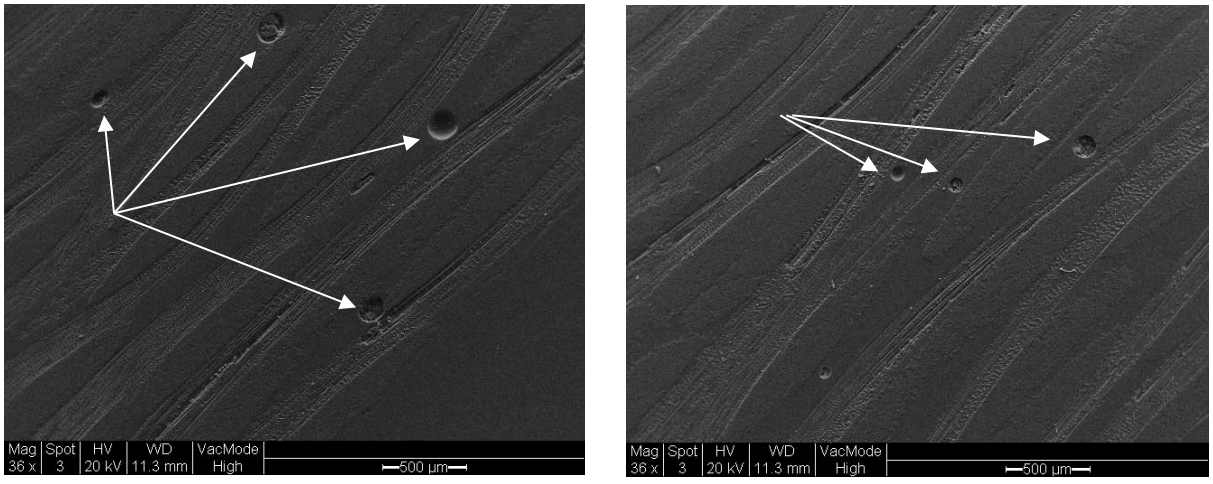

Figure 6-5. Scanning electron micrograph showing the entrapped air bubbles and the voids distributed throughout the GFRP composite samples.

6.2. Effect of Fibre Orientation of GFRP Composites on Mechanical Properties

Figure 6-6 and Figure 6-7 show the effect of fibre orientation on tensile and flexural behaviour of the GFRP composite laminate. The change in the fibre orientation from 0°/90° to ±45° with respect to the tensile and bending load axis results in a substantial reduction in strength and increased ductility of the composites in both tension and flexure. The material showed approximately 60% drop in failure strength in bending and tension tests. These differences show that the tensile and flexural strength are sensitive to the fibre arrangement with regard to the external load (Papanicolaou *et al.*, 2004).

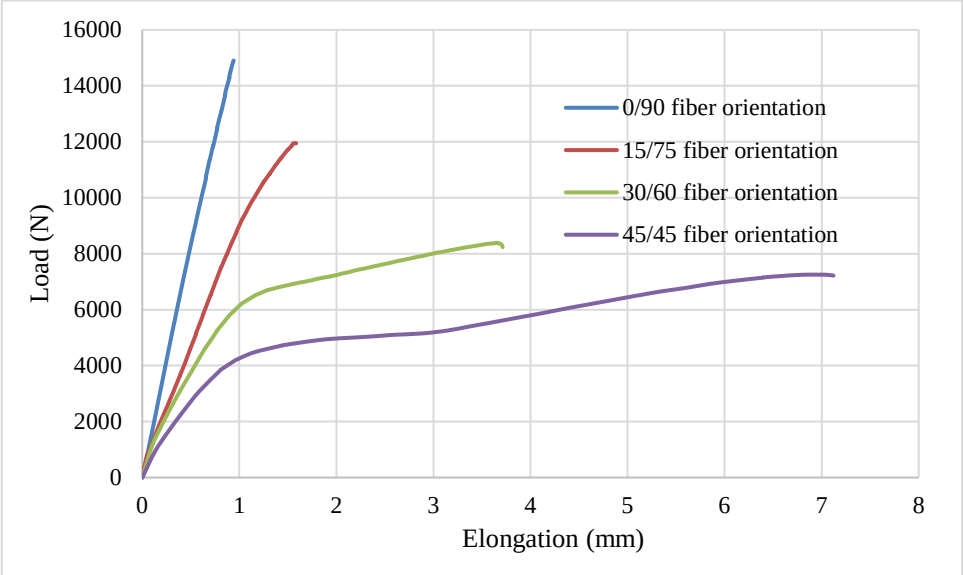

Figure 6-6. Effect of fibre orientation on load-elongation curves of GFRP composites under tension test.

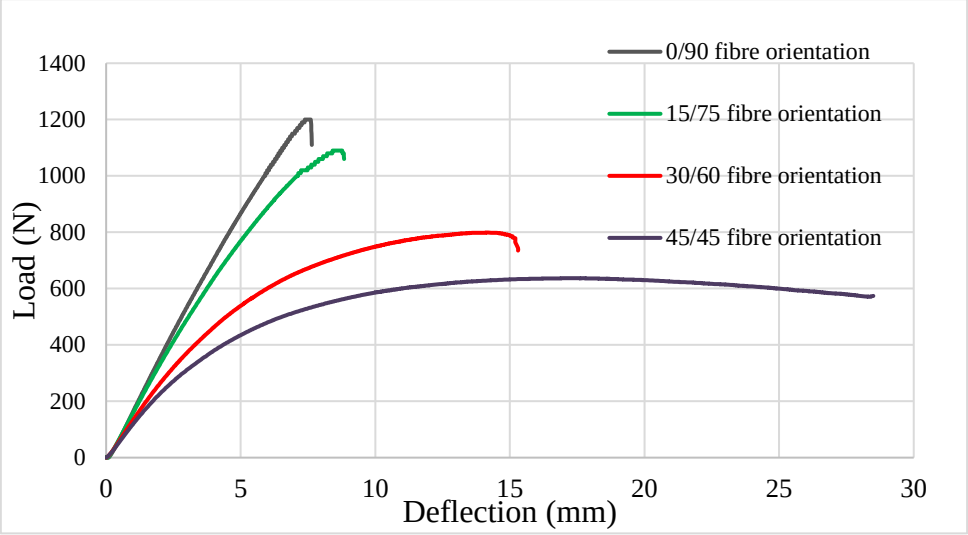

Figure 6-7. Effect of fibre orientation on load-displacement curves of GFRP composites under 3PB test.

It can be concluded that when the fibres are oriented at 0°/90°, failure is dominated by the fibre fracture, while at the ± 45 fibre configuration deformation at the polymer matrix is responsible for the failure of the composite.

6.2.1. Tensile Properties

Designing composite structures for various applications necessitates a better understanding of their mechanical behaviour and failure mechanisms under external loading. In this section a method was developed for the assessment of tensile properties of woven glass fibre reinforced composites. The technique is based on a Finite Element (FE) modelling for stress/strain evaluation and Digital Image Correlation (DIC) for strain/displacement field measurement. The DIC technique was used in a two point tracing configuration for longitudinal and transverse measurements to calculate the elastic modulus and Poisson's ratio. In addition, full-field DIC strain maps were evaluated to show the areas on the specimen surface where damage initiation and propagation occurs. DIC also showed anisotropy of the strain distribution, depending on the fibre orientation with respect to the main loading axis. SEM was used to observe the fracture surfaces in order to evaluate the effect of fibre alignment on failure modes.

Tensile stress-strain curves were constructed using the strain data extracted from DIC measurements and the engineering stress calculated from $\sigma = {}^{F}/_{A}$ where A is the cross-sectional area (A=b×h) and F is the applied load. Figure 6-8 shows the effect of fibre orientation on the tensile stress-strain behaviour of the GFRP composite material. Each point in the figure relates to a load step at which the deformation is measured. Fracture strains in these plots correspond to maximum strains (strain at fracture).

Table 6-2 shows a summary of the mechanical properties of the composite for different fibre configurations.

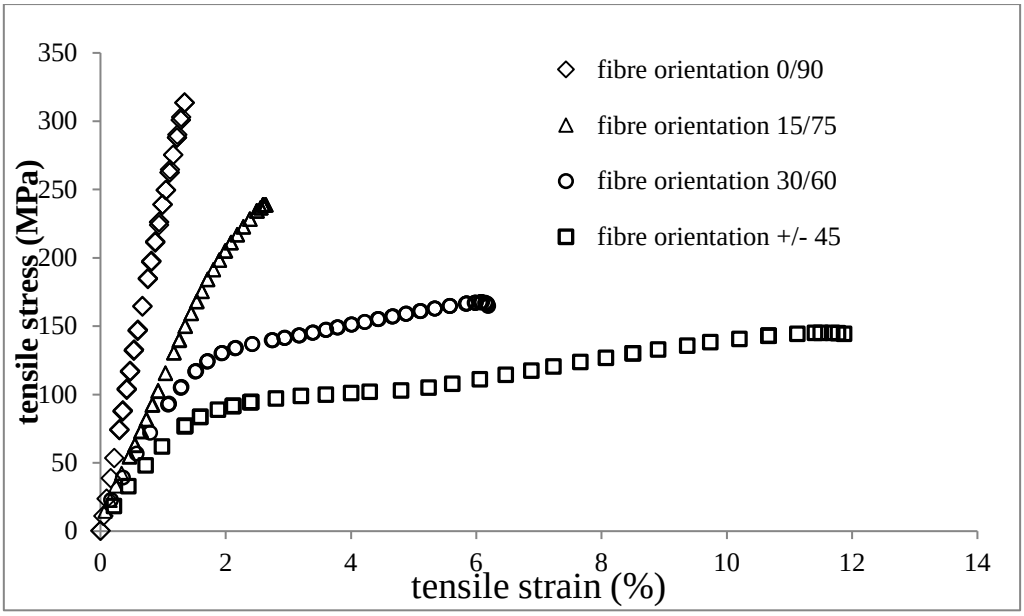

Figure 6-8. Tensile stress-strain curves showing the anisotropy; fracture strains in these plots corresponds to maximum strains.

Table 6-2. Mechanical properties of GFRP derived from the stress-strain curves of composites showing the effect of fibre alignment on tensile properties.

Fibre orientation relative to main loading axis	**Modulus of elasticity (GPa)**	**Ultimate strength (MPa)**	**Failure strain (%)**	**Poisson's ratio**
0°/90°	21.6±0.5	320±20	1.60±0.2	0.25±0.02
15°/75°	15.7±0.7	235±12	3±0.5	-
30°/60°	11.2±0.6	165±10	6.2±0.6	-
±45	9.5±1	145±10	12.5±0.7	-

- ***0°/90° Stacking Sequence***

When fibre orientation changes from 0°/90° to ±45°, a substantial reduction in the ultimate tensile strength and an increase in strain, as a measure of ductility of the material can be observed. This indicates that the tensile behaviour of this material strongly depends on the fibre alignment (Papanicolaou *et al.*, 2004). This behaviour of composites is due to the fibre configuration influencing the load distribution. When the fibres are oriented at 0°/90°, applied tensile load is transmitted by the reinforcing fibres parallel to the tensile loading axis, therefore the material shows increase in failure strength which is due to the high strength of the fibres.

Compared to the stiff glass fibres, the epoxy resin matrix has a much lower stiffness and it is not able to resist the applied load, so it fails quickly by fracture without any significant plastic deformation. Figure 6-9 shows scanning electron micrographs of the fracture surface of the composite with 0°/90° oriented fibres. As it can be seen in Figure 6-9(a) on the fracture surface, clusters of fibres are pulled out. The corresponding lateral view (Figure 6-9b), confirms interfacial de-bonding between the fibres and the matrix. This shows that interfacial bond strength is overcome before the tensile failure strength of the composites is reached (Godara and Raabe, 2007). The uneven topography surface of longitudinal pulled-out fibres and the smooth surfaces of transverse fibres indicate that the maximum applied load is taken by longitudinal fibres (parallel to tensile loading axis Figure 6-9 (c)). It is worth noting that the surface of polymer matrix is relatively smooth showing no signs of plastic deformation at the failure point.

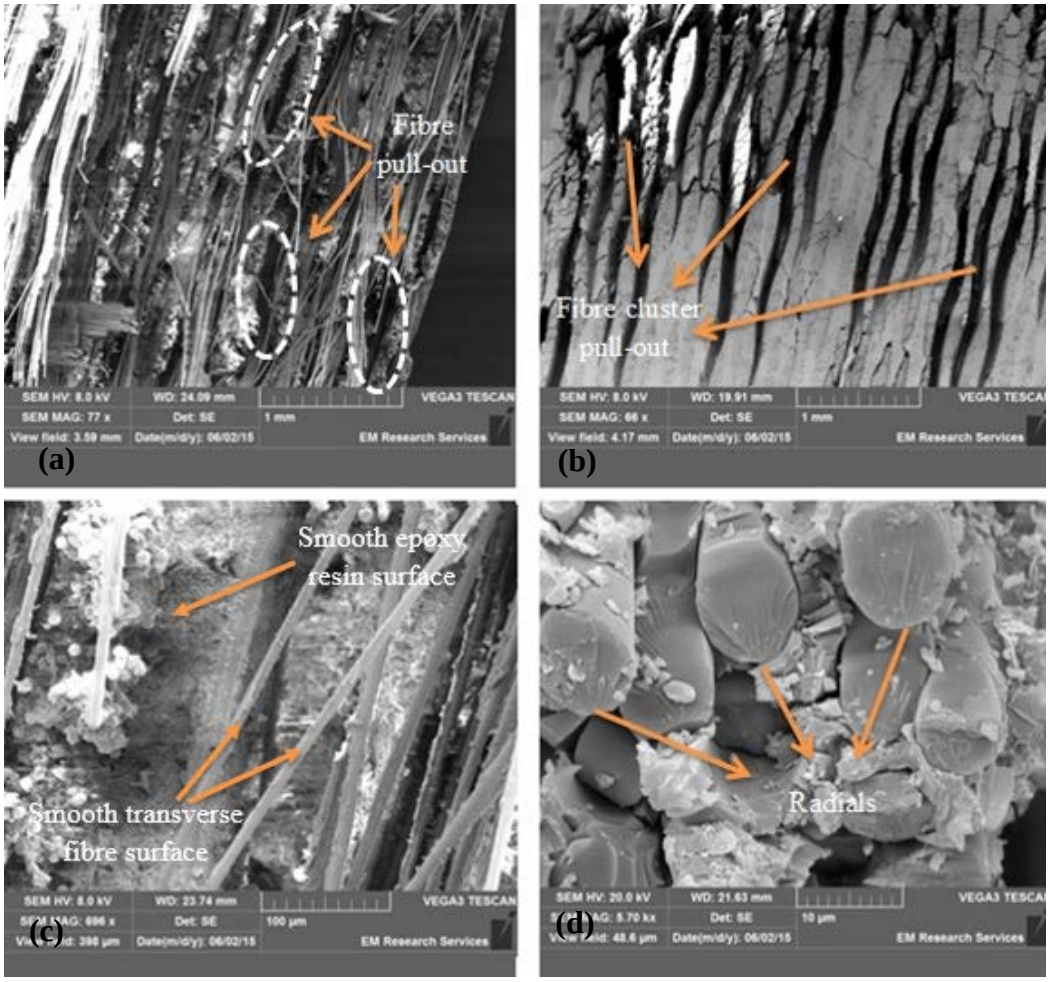

Figure 6-9. Scanning electron micrographs of the fracture surface of composite samples, 0°/90° fibre configuration (a) cluster of fibres pulled out from epoxy resin (b) pulling out of fibre clusters from lateral side view, (c) detailed view (coarse surface of longitudinal pull-out fibres, soft surfaces of epoxy resin and transverse fibres), (d) radials showing crack propagation direction across the glass fibres.

The fracture edge from the top surface view of the specimen with longitudinal and transverse fibre direction is straight. Transverse cracks in the epoxy matrix indicate that during pulling-out of longitudinal fibres, transverse fibres are also pulled-out (Figure 6-10).

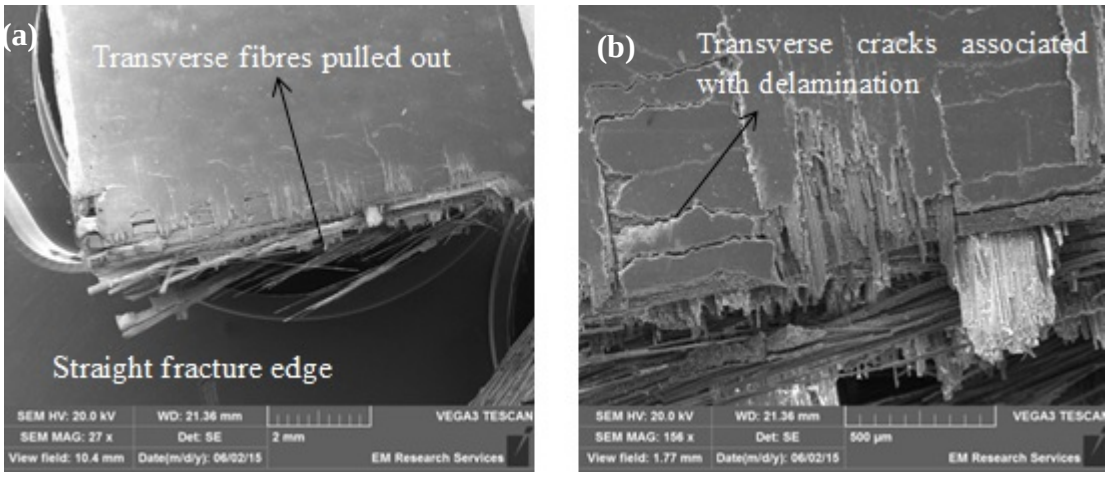

Figure 6-10. SEM micrographs revealing the top surface of a sample with the longitudinal and transverse fibre configuration indicating a straight edge with transverse failure of the fibres. (a) Low magnification, (b) high magnification

- ***±45 Stacking Sequence***

When the fibres are oriented at -45°/+45° with respect to tensile loading axis, an appreciable higher ductility relative to 0°/90° fibre orientation is seen which is related to the less strain limiting effect of glass fibres. When fibres are oriented at -45°/+45°, the applied tensile load is divided between fibres and matrix. If the induced shear stress in the matrix exceeds its shear strength, plastic shear deformation is developed in the matrix and the failure is dominated by matrix and interfacial properties. Unlike the topography of the fracture surface of the 0°/90° fibre orientation specimen, in which the surface of fibre bundles was rough and polymer surface was smooth, the surfaces of both fibres and epoxy resin matrix of the sample with ±45° fibre orientations is uneven indicating that the applied load was distributed between fibres and polymer matrix (Figure 6-11). This results in the higher strain to failure of sample and its lower strength.

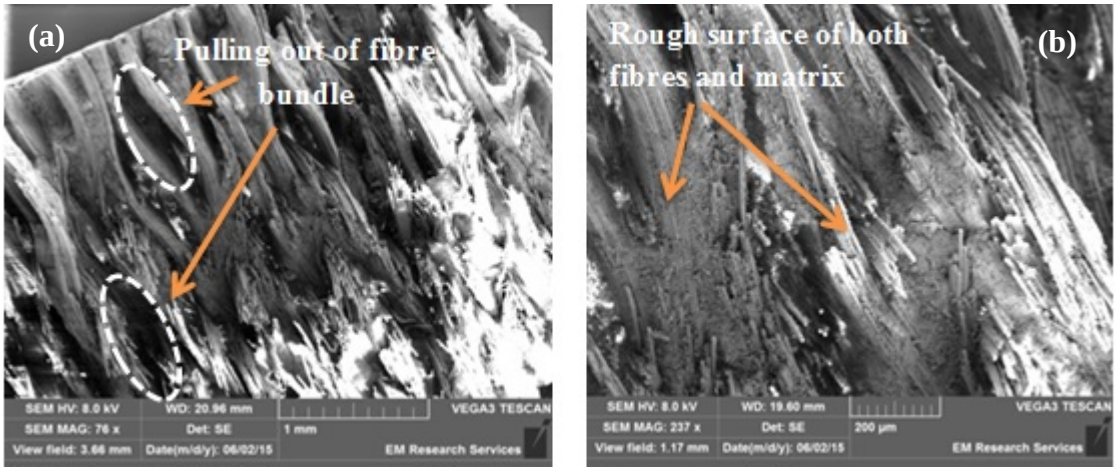

Figure 6-11. Scanning electron micrographs of the fracture surface of composite samples,-45°/+45° fibre configuration (a) cluster of fibres pulled out from epoxy resin (b) fracture surface showing rough surface of both fibres and epoxy resin

Scanning electron micrographs of the fracture edge of the specimen with fibre orientation at ±45° show that failure occurs at several angled planes (Figure 6-12). Formation of shear lips near the edge of specimen indicates that interfacial de-bonding occurs between different layers. Compared to the specimen with 0°/90° fibre orientation, in the ±45° specimen the epoxy resin has additional space to extend between reinforcements in the loading direction. Furthermore due to the less constraining effects of fibres in ±45° sample compared to the 0°/90°, creation of resin-shear bands is more pronounced.

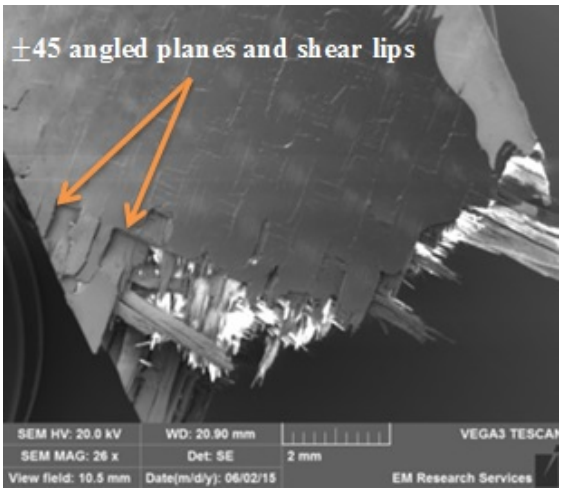

Figure 6-12. SEM micrograph revealing the top surface view of a sample with -45/+45 fibre configuration indicating multiple angled fracture planes.

6.2.2. Investigation of the Anisotropy Effect of Glass Fibre Reinforced Composites on Tensile Properties Using Digital Image Correlation (DIC)

Until recently in quasi-static mechanical testing of structural composite materials only conventional strain gauges or two point based strain measurement devices were exploited. Using conventional strain gauges for assessment of the stress-strain properties of structural materials does not reveal information regarding the strain concentration or gradient of strain-fields. This is due to the limitations imposed by the size of the gauges. This information can be obtained when using a full-field measurement method, in particular, Digital Image Correlation (Brynk *et al.*, 2012; Grédiac and Hild, 2012). Also using this novel experimental technique, restrictions regarding specimen dimensions to obtain a uniform displacement distribution can be eliminated. Due to the advances of computers and image acquisition equipment, the DIC based methodology has been widely implemented for full-field displacement measurement of heterogeneous materials using a formulation of tracking the digital images obtained from the specimen surface before and after deformation (Godara and Raabe, 2007; Laurin *et al.*, 2012; Crupi *et al.*, 2013). The DIC method has been effectively implemented in many applications related to mechanical testing of materials. There are many literature examples of DIC measurements in tests with monotonic (Brynk *et al.*, 2012; He *et al.*, 2012; Qin *et al.*, 2012) as well as dynamic loading conditions (Giancane *et al.*, 2010b; Makeev, 2013). There are also well documented examinations and investigations about strain measurement on the surfaces of the structures and components made up of composites materials (Godara and Raabe, 2007; Laurin *et al.*, 2012).

The aim of this section was to carry out tension tests on dog-bone specimens made of glass fibre reinforced composites in which strain is mapped using a DIC system. Composite specimens with two different fibre orientation were tested. The DIC system was also used in a two point tracing configuration for longitudinal and transversal strain measurements. The outcomes of these measurements were used to determine the elastic modulus and Poisson's ratio required in the designing procedure and development of the composite tidal turbine blade. The acquired strain maps indicated that there is inhomogeneity of strain and its dependence on the fibre arrangements. Strain maps/distributions also revealed the areas on the specimens where delamination will take place.

- ***Qualitative Examination of the Localized Strains***

The development of the strain at the mesoscale was considered with the DIC system and the effects of the fibre configurations at 0°/ 90° and ±45° relative to the main axis loading in tension were identified (Figure 6-13 and Figure 6-14). The attained strain field maps are presented against the background of the original and un-deformed images of the tested sample surfaces. Due to moderately high deformation of the sample, particularly for the sample with $\pm$45° fibre orientation, some parts of the measurement area were removed from the analysis, therefore no strain maps were obtained from the lower regions of these samples. The full field strain maps were obtained for a predefined zone in the longitudinal section of the tensile test samples. For each test specimen, four strain maps with growing imposed tensile stress/strain are presented. In order to achieve full field strain maps, the displacement gradient tensor and the consequential Lagrange strain tensor components were computed at each stages of movement. The ultimate strain map was presented in terms of the Von Mises strain. The Von Mises strain (ε_V) is specified by equation;

$$\varepsilon_V = [2/3(\varepsilon_{xx}{}^2 + \varepsilon_{yy}{}^2 + \varepsilon_{zz}{}^2)]^{0.5} + 1/2(\varepsilon_{xy}{}^2 + \varepsilon_{yz}{}^2 + \varepsilon_{xz}{}^2)$$

6-1

Where ε_{ii} denotes the normal strain and ε_{ij} denotes the shear strain. Due to the 2-D strain analysis performed in this work, the Lagrange strain tensor components ε_{zz}, ε_{yz} and ε_{xz} were set to zero.

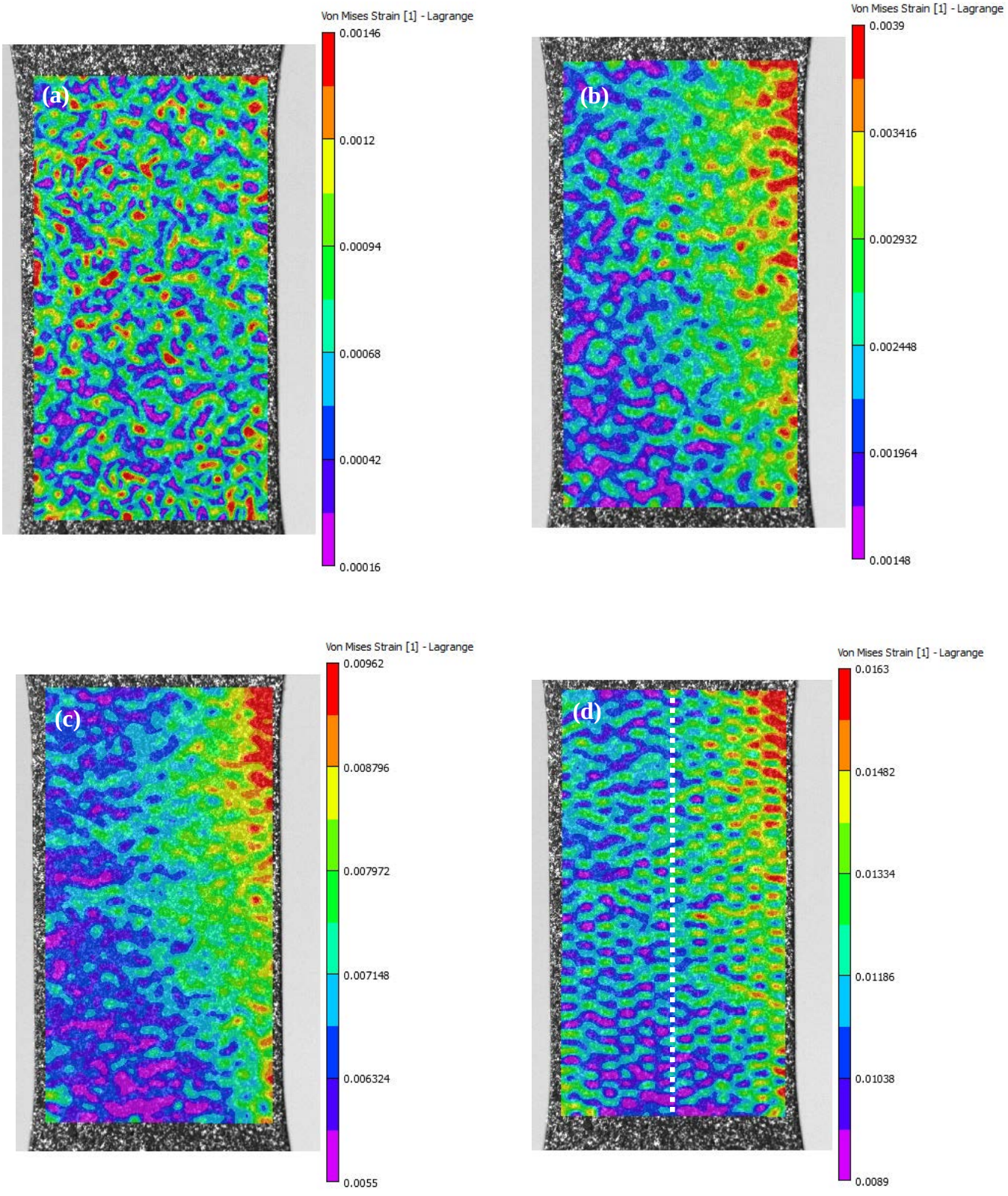

Figure 6-13. Inhomogeneous dissemination of the Von Mises strain displaying areas with high and low strain values in the test sample with fibre alignment at 0°/90°. The extents of the field image match the geometry of the strain examination region 10×30 mm. The white flecked line in the strain map shows the location of the slices used for the strain contours and profiles. (a) Applied tensile strain: 0.1%, (b) applied tensile strain: 0.3%, (c) applied tensile strain: 0.8%, (d) applied tensile strain: 1.3%.

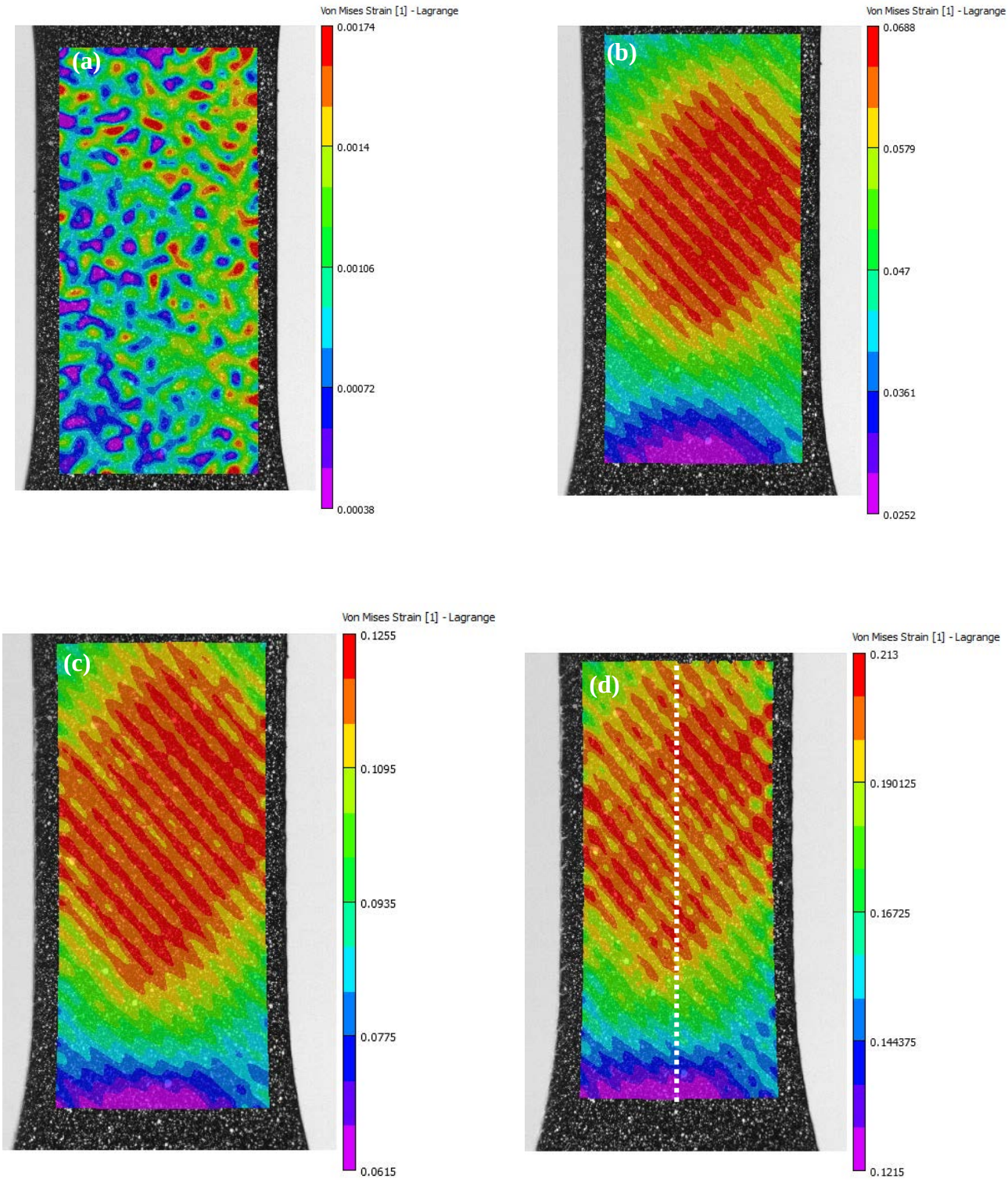

Figure 6-14. The accumulated plastic Von Mises strain showing inhomogeneity distribution in the test sample with fibre alignment at ±45°. The sizes of the displacement field image match the geometry of the strain examination region 10×30 mm. The white flecked line in the strain map marks the location of the segments used for the strain profiles. (a) Applied tensile strain: 0.1%, (b) applied tensile strain: 4%, (c) applied tensile strain: 9%, (d) applied tensile strain: 13%.

Comparing the strain maps of the composite with 0°/90° and ±45° fibre orientation (Figure 6-13 and Figure 6-14) and their relevant stress-strain curves, the higher elongation to break for sample with ±45° fibre orientation may be associated with later strain localization and smoother strain distribution for this specimen which is obviously noticeable when comparing their strain maps. In other words the strain maps for sample with ±45° fibre orientation shows heterogeneity of strain distribution in the form of strain bands oriented 45° to the applied force direction. Delamination in the case of composite samples with 0°/90° fibre orientation initiates near the edge of the sample and is located in a few distinct places simultaneously. The strain map for samples with ±45° fibre orientation revealed that delamination begins in more limited zones situated in the central area of the sample width.

- ***0°/90° Fibre Orientation***

The distribution of the accumulated Von Mises strain in the region of interest in the longitudinal section of the tensile specimens with fibre configuration at 0°/90º is shown in Figure 6-13. Averaging the values of ε_V on each row it is possible to monitor the strain development and to clearly detect the image matching to final failure. In each of these four strain maps, the intensities of localized strain are greater than the applied tensile strain giving an indication that composite displays an inherent mechanical inhomogeneity. The creation of localized strain areas observed in the strain maps is related to the micro-structure of the sample. The distribution of the polymer matrix at the intersection areas of the longitudinal and transverse fibre bundles and among fibre bundles creates diverse regions prone to excess deformation. The volume of the epoxy resin near the boundaries of the glass fibre bundles is relatively large, however, in regions where the fibre bundles intersect each other the volume is smaller and deformation is reduced. The micrograph (Figure 6-15) displays the development of such different regions.

- ***±45° Fibre Orientation***

The evolution of the Von Mises strain for the composite sample with ±45° fibre alignment is relatively homogeneous at lower imposed loads. With additional increase in the imposed load, there is a change from homogeneous to inhomogeneous distribution. This is shown by the introduction of the high and low strain domains in the strain maps in Figure 6-14 when plastic flow in the matrix occurs. In comparison with GFRP composite with 0°/90° fibre configuration, this is observed at more elevated applied load. The early homogenous strain field maps can be understood by an equivalent distribution of the applied load between the polymer matrix and

the reinforcing fibres. The coarse fracture surfaces of ±45° oriented fibres with a multi-directional microstructure and plastic flow of the polymer matrix endorse the above statement (Figure 6-11).

- ***Quantitative Examination of the Localized Strains***

In order to evaluate the strains in the high and low strain territories, sectional examination of the localized strain was carried out. The effect of the fibre orientation in regard to the main loading axis is important. The location of the segment along the main axis was chosen after witnessing the localized strain in the strain map just before rupture (noticeable with a white flecked line (Figure 6-13 and Figure 6-14). The four curves in Figure 6-16 and Figure 6-18 exhibit the progression of the Von Mises strain for the strain fields displayed in Figure 6-13 and Figure 6-14 correspondingly, at each level of imposed tensile strain.

- ***Sectional Examination of the Localized Strain in 0°/90° Fibre Orientation Sample***

The profile of Von Mises strain for the samples with fibres arranged at 0°/90° is shown in Figure 6-16. The strain accumulation is inhomogeneous as indicated by numerous local maxima and minima. These oscillations in the curves indicate the inhomogeneous nature of the Von Mises strain alongside the length of the tensile test sample. The maximum difference between the maxima and the minima is between 10-30% of the mean strain and the behaviour for the different strain levels is similar, just moved to greater Von Mises strain with increasing load. The average space between the adjacent maxima and minima is not regular which is in agreement with the inhomogeneous microstructure of the composite material particularly at the top surface (Figure 6-15). These localized strain accumulations are due to the localized plastic deformation of the matrix and the micro-damage such as interfacial failure which ultimately results in de-bonding, micro-cracks, or fibre breakage.

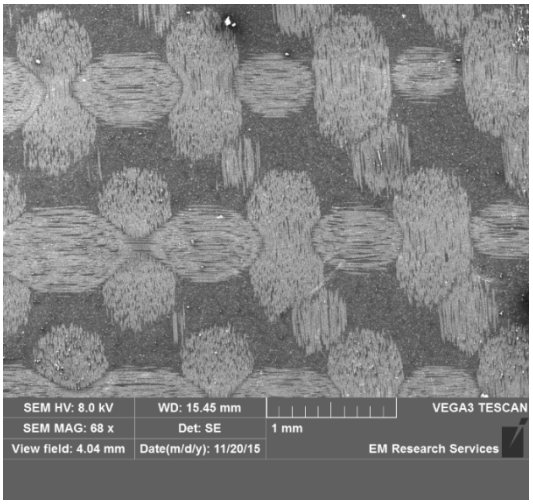

Figure 6-15. Micro-structure of the top surface of the sample revealing the arrangement of fibre packages at 0°/90°.

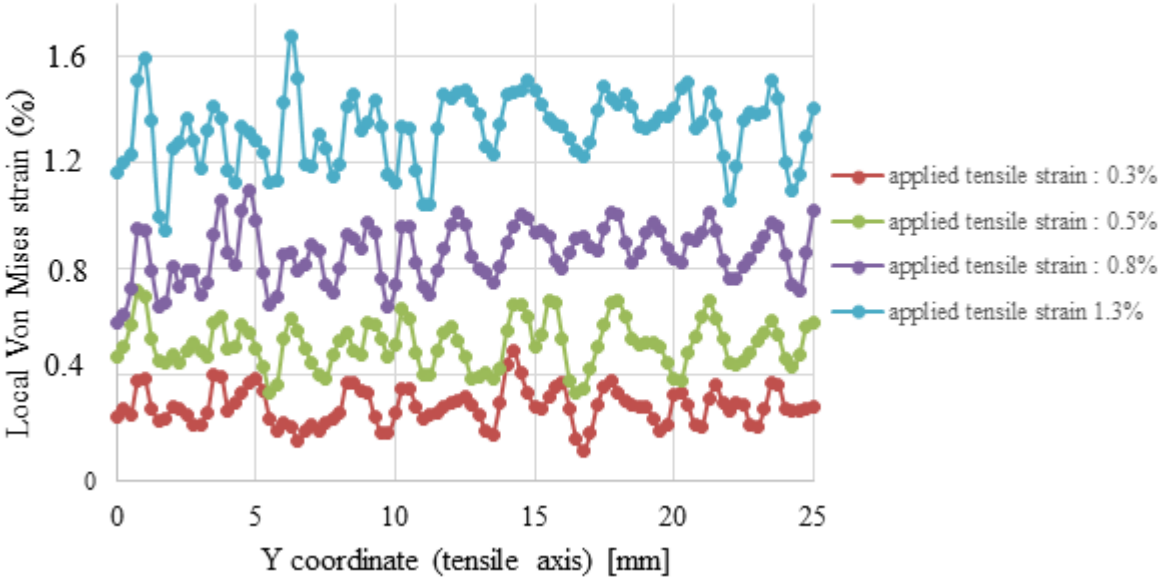

Figure 6-16. Sectional examination of the development of the Von Mises strain distribution alongside the length of the test sample with the fibre configurations at 0º/90º.

- ***Sectional Examination of the Localized Strain in specimen with ±45° Fibre alignment***

At small loads the profile distribution of the accumulated Von Mises strain curves in Figure 6-18 displays an almost linear pattern suggesting an identical distribution of the deformation.

The pattern changes to periodic at larger loads. This suggests a different mechanisms of load distribution for the ±45° compared to the 0°/90° fibre alignment involving plastic deformation of the matrix. The maximum difference between the maximum and the minimum is around 2-4% of the mean strain which is discernible at future stages of the deformation. The average spaces between the adjacent maxima and minima is asymmetrical and is in agreement with the inhomogeneous micro-structure as seen in Figure 6-17.

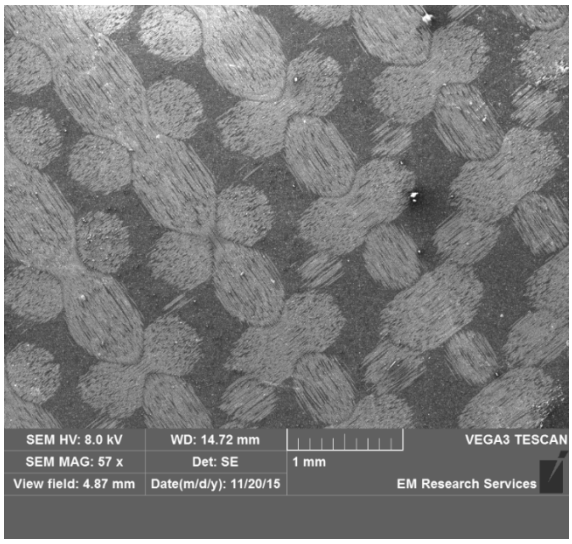

Figure 6-17. Micro-structure of the top surface of the sample revealing the configuration of fibre packages at ±45°.

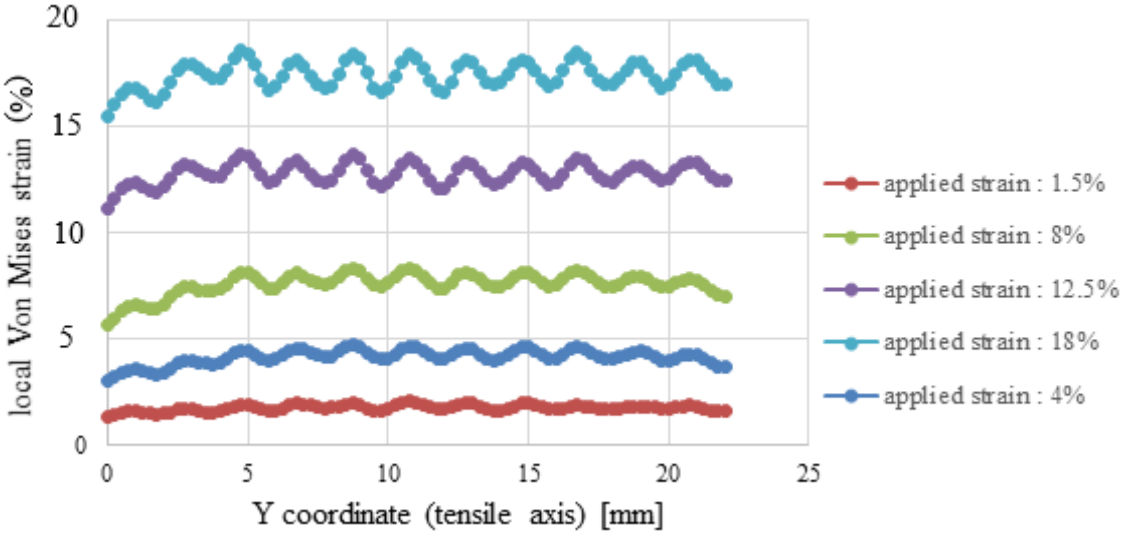

Figure 6-18. Sectional examination of the accumulated Von Mises strain distribution alongside the length of the test specimen with the fibre alignments at ±45º.

6.2.3. Effect of Fibre Orientation on Flexural Properties

Table 6-3 summarizes the mechanical properties resulting from the 3PB stress-strain curves of composite sample.

Table 6-3. Mechanical properties of the composite materials subjected to 3PB load showing the effect of the fibre arrangement.

Fibre orientation relative to main loading axis	Ultimate strength (MPa)	Failure strain (%)
0°/90°	475±10	2.1±0.1
15°/75°	430±24	2.65±0.1
30°/60°	310±21	4.5±0.15
±45	245±17	8.6±0.2

Once the fibre angle changes from 0°/90° to ±45°, the number of micro-cracks increases drastically in the 3PB test specimen (Figure 6-19). In the 0°/90° fibre orientation, the low ductility of the fibres results in a low ductility of the composite laminate. As the specimen angle increases, the failure mode becomes controlled by interfacial properties and matrix deformation. In the ±45° fibre orientation the yielded matrix has more space to extend between fibres and in the loading direction, consequently there is less restraining effect of fibres compared with 0°/90°. The final failure modes are matrix cracking, delamination as well as fibre buckling in the compression and tension side.

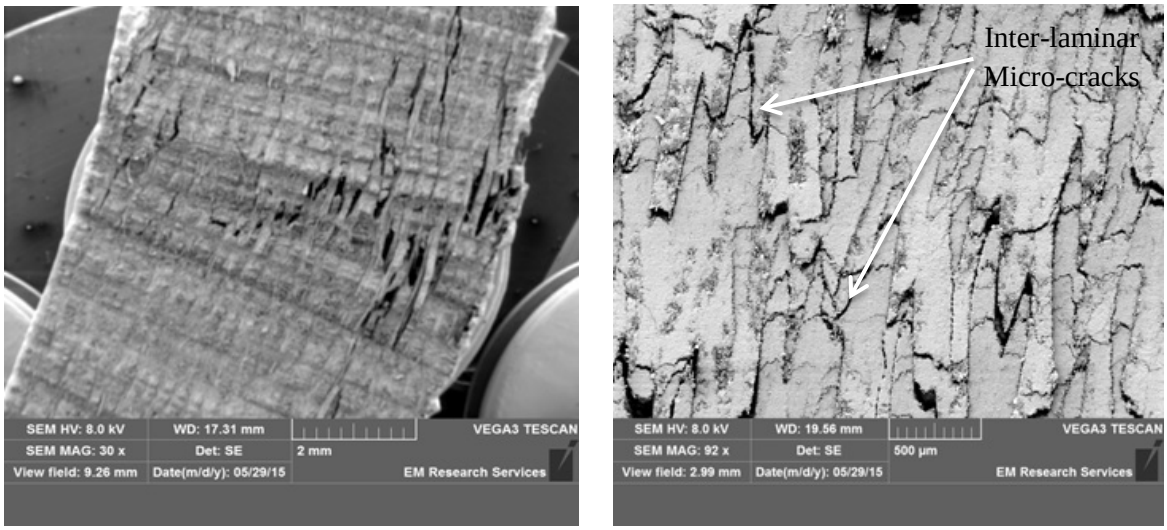

Figure 6-19. SEM micrograph of 3PB test specimen with ±45 fibre orientation showing increased number of micro-cracks with increasing the fibre orientation angle. (a) Low magnification, (b) high magnification.

6.2.4. Linear Elasticity and Tsai-Hill theory

Variation of elastic modulus and failure strength as a function of fibre orientation angle (α), based on the Linear Elastic theory and Tsai-Hill criterion can be stated by equation (6-2) (Agarwal *et al.*, 2006; Mortazavian and Fatemi, 2015).

$$\boldsymbol{E_\alpha = [\frac{cos^4\alpha}{E_1} + \frac{sin^4\alpha}{E_2} + 0.25\left(\frac{1}{G} - \frac{2\nu}{E_1}\right) sin^2 2\alpha]^{-1}} \qquad \text{(Linear elasticity theory)}$$

$$\boldsymbol{\sigma_\alpha = [\frac{cos^4\alpha}{\sigma_1^2} + \left(\frac{1}{\tau^2} - \frac{1}{{\sigma_1}^2}\right) sin^2\alpha\, cos^2\alpha + \frac{sin^4\alpha}{{\sigma_2}^2}]^{-0.5}} \qquad \text{(Tsai-Hill criterion)}$$

6-2

Where E_1, E_2 are elastic moduli in longitudinal and transverse direction respectively and G is the shear modulus. σ_1, σ_2 and τ are longitudinal and transverse tensile strength and shear strengths in material reference axes, and ν is Poisson ratio.

The model was applied to the experimental data for composite samples (Table 6-2) and the results are illustrated in Figure 6-20. The shear properties were obtained using the Iosipescu shear test which is discussed in section 7.4.

By substituting the properties from Table 6-2, the variation of elastic modulus and failure strength corresponding to different fibre orientation were predicted. Table 6-4 shows the calculated percentage difference between predicted and experimentally obtained tensile properties. It is clear that linear elasticity theory predicts the off-axis elastic modulus and failure strength to a good approximation.

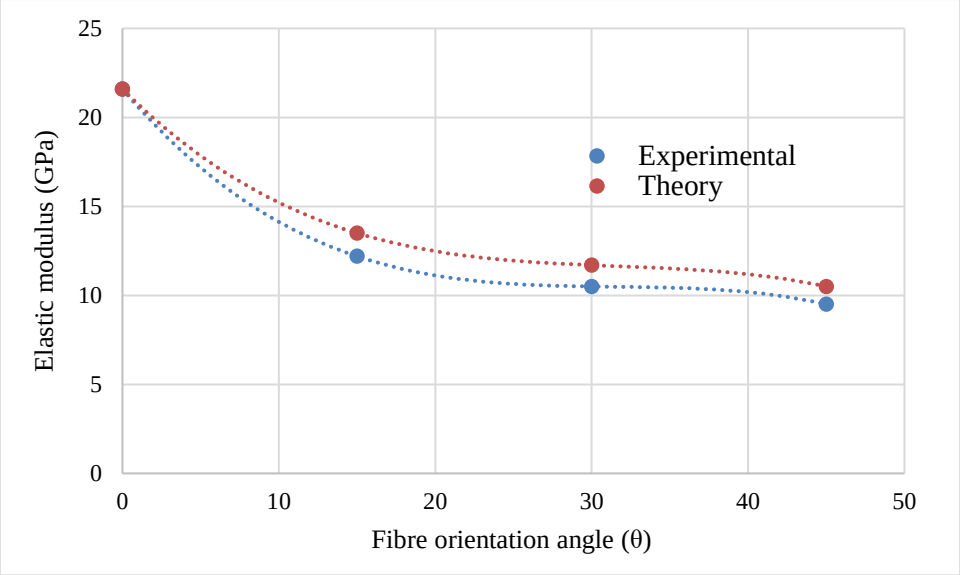

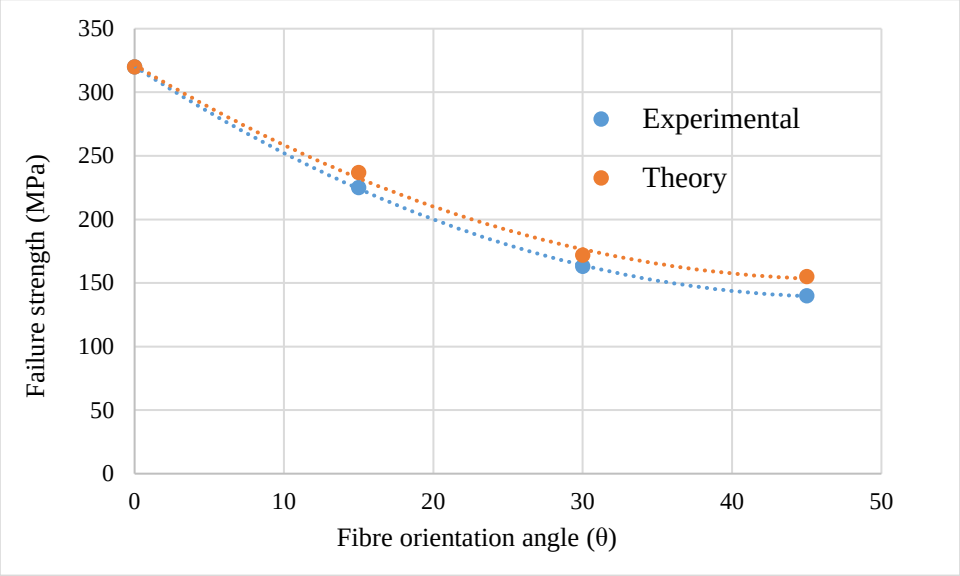

Figure 6-20.Variation of elastic modulus and failure strength with fibre orientation angle.

Table 6-4. Percentage difference between theoretical and experimental.

Fibre orientation angle	Elastic modulus difference (%)	Failure strength difference (%)
0°/90°	0	0
15°/75°	8	7
30°/60°	8	8
±45°	6	9

6.3. Finite Element Analysis Results of Tensile and Bending Tests

6.3.1. 3PB test, 0°/90° fibre orientation

With respect to the mechanical properties of GFRP obtained from the experiment (Table 6-5), Figure 6-21 shows the results from ANSYS simulation of 3PB/tensile tests and the experimental data, indicating a reasonable compatibility between numerical analysis and experiments. Small deviations show the effects of potential manufacturing defects and flaws such as voids. These deviations were probably caused by the poor fibre-matrix adhesion and the fibre misalignment during stacking and manufacturing. The angle between fibre bundles can promote the formation of voids. The other reason for the formation of voids is air entrapment between the plies. Entrapped air in composites that is not removed during manufacturing can lead to the creation of voids in the cured composite. The poor fibre-matrix adhesion in the present material can be seen from the very clean glass fibres in Figure 6-22. The crimp (i.e. the undulation of the warp and weft fibres) in the laminate which is responsible for the large resin pockets, especially in the cross–over areas between the weft and warp bundles could be the other reason for this deviation. A discrepancy between flexural strength obtained by FEA and the experimental value is evidenced, associated with delamination and micro-cracks in the sample.

Table 6-5. Material properties for woven glass fibre reinforced epoxy resin laminate used in FE model (ANSYS).

Type of mechanical testing	**Material characteristics for a biaxial woven fabric composite**	**GFRP**
Tension	Longitudinal elastic modulus E_x(GPa)	21.6
	In-plane transverse modulus E_y(GPa)	21.6
	Major Poisson's ratio ν_{xy}	0.25
	Longitudinal ultimate tensile strength (MPa)	320
	In-plane transverse ultimate tensile strength (MPa)	320
Shear	In-plane shear modulus (GPa)	3.52
	In-plane ultimate shear strength (MPa)	80
	Inter-laminar shear modulus (GPa)	2.1
	Inter-laminar shear strength (MPa)	40
Compression	Longitudinal compressive modulus (GPa)	20
	In-plane transverse compressive modulus (GPa)	20
	Longitudinal compressive strength (MPa)	290
	In-plane transverse compressive strength (MPa)	290

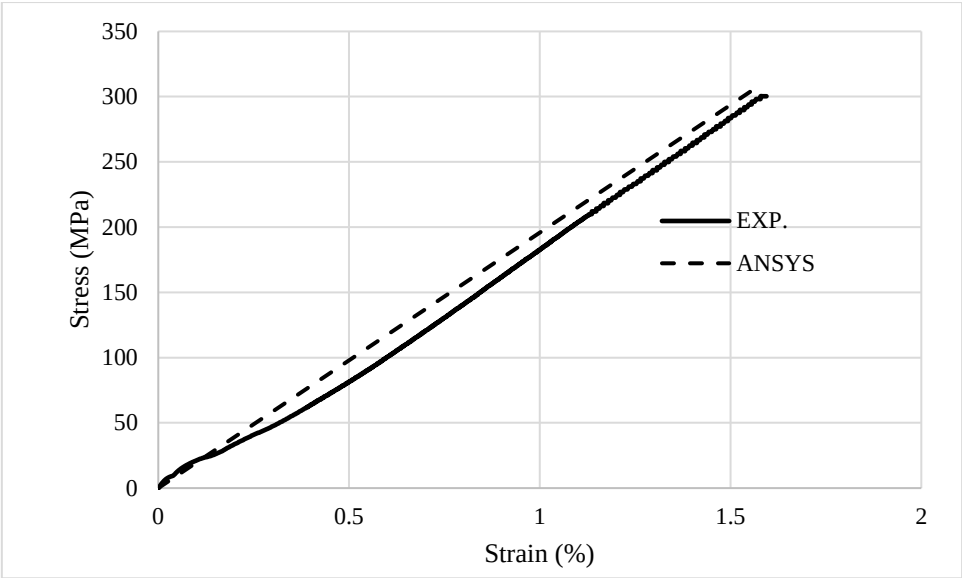

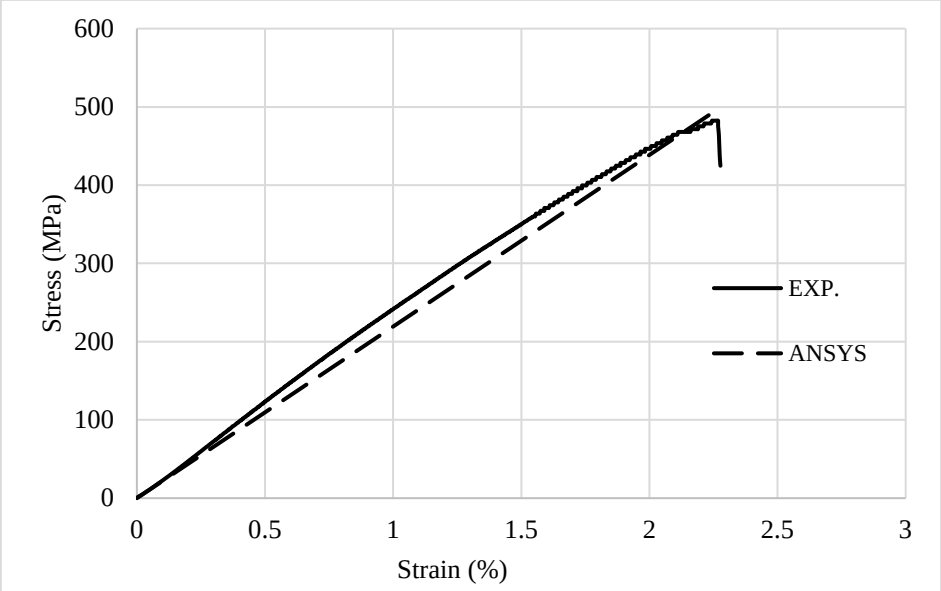

Figure 6-21. Experimental/numerical comparison of stress-strain curves of GFRP composite under (a) tension and (b) three point bending, the standard uncertainty in the experimental data is maximum 5N. (The maximum strain in these plots corresponds to the failure strain).

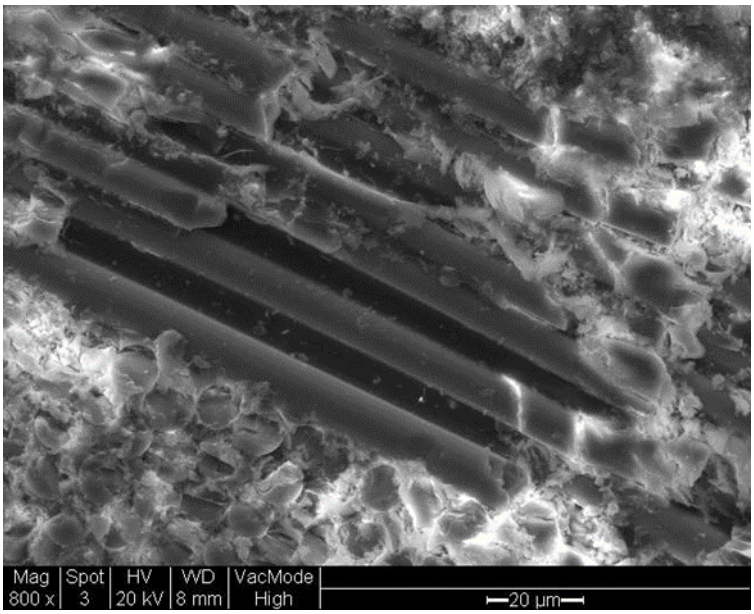

Figure 6-22. Clean fibres on the fracture surface showing the poor adhesion between the fibres and the matrix.

Figure 6-23 to Figure 6-27 show contour maps of deflection, normal and shear stresses/strains induced within plies through the thickness of 3PB test specimen in the applied load direction, just before the point of rupture in the load-deflection curve. The bending stresses/strains are maximum in the outer surface and inter-laminar shear stress is maximum in the middle of the specimen. The maximum stress failure criteria predicts fibre breakage (fibre tension and fibre buckling) near the top/bottom surface of the sample associated with the maximum normal stress in Figure 6-24 and Figure 6-25. Delamination failure is predicted at mid span of test specimen corresponding to the maximum inter-laminar shear stress in Figure 6-27.

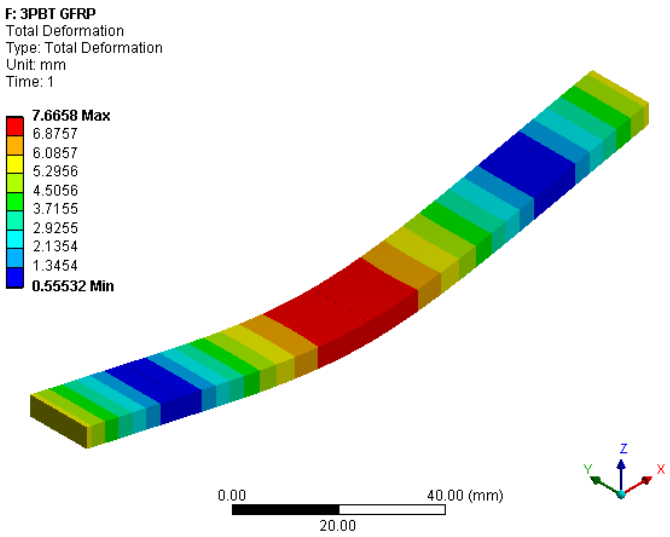

Figure 6-23. Deflection contour showing that maximum deflection occurs at the center of test specimen in 3PB test (load = 1200 N).

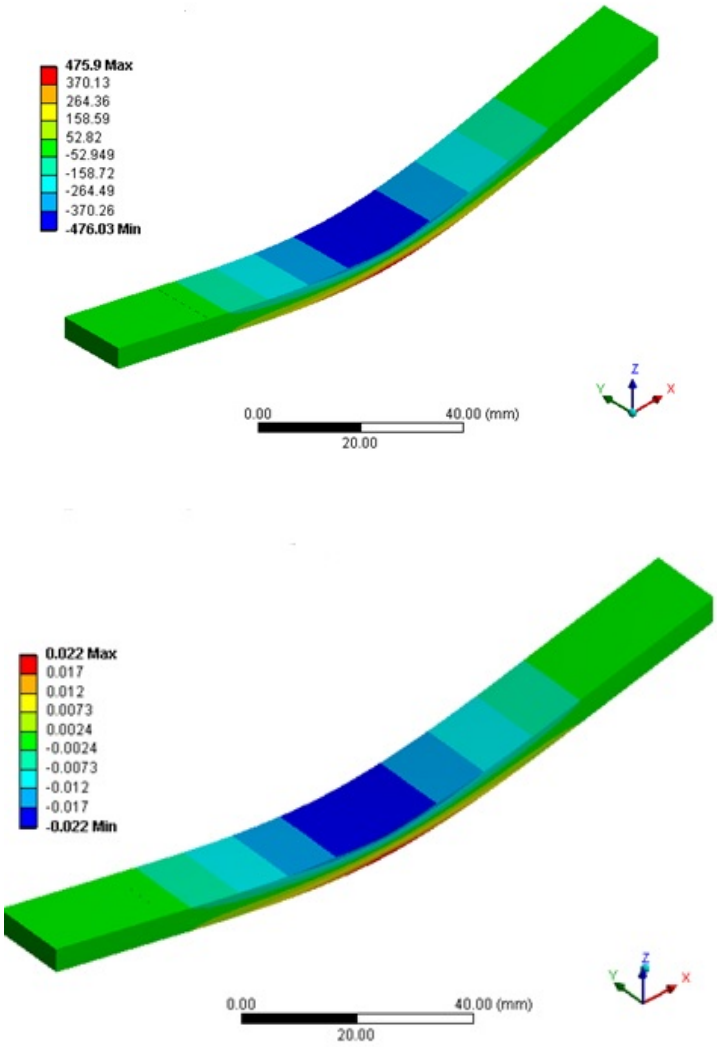

Figure 6-24. Normal stress/strain distribution in 3PB at the maximum loading (1200 N).

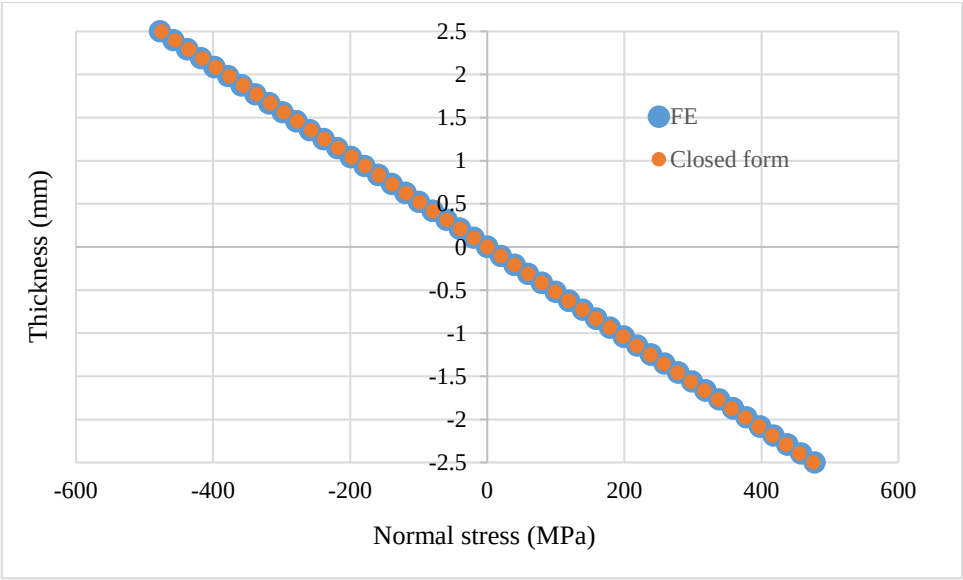

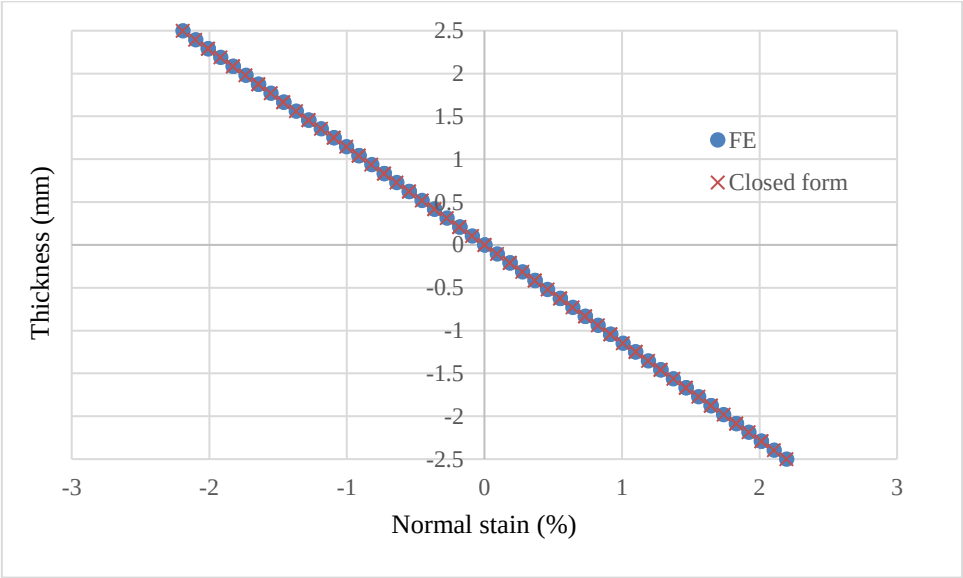

Figure 6-25. Variations of stress/strain through layers and laminate thickness (lateral view) at the centre of test specimen where maximum loading (1200 N) applied. Comparison has been made between overlapping numerical and analytical data.

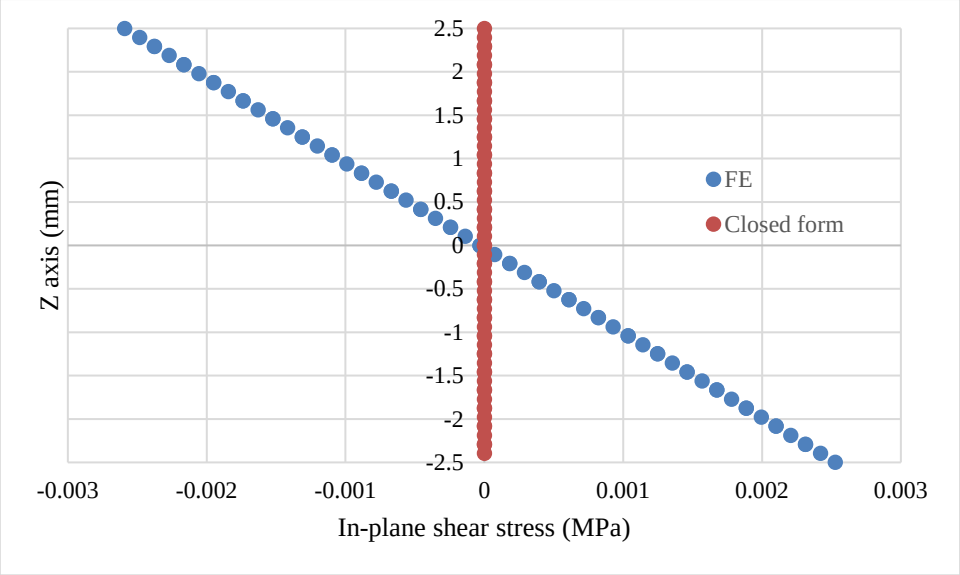

Figure 6-26. Variations of in-plane shear stress through laminate thickness at the centre of test specimen where maximum loading (1200 N) applied. Comparison has been made between numerical and analytical data. The maximum value of in-plane shear stress obtained from FE model is 0.0025 (MPa) which is almost zero, meaning that there is negligible difference between these values obtained by closed form solution.

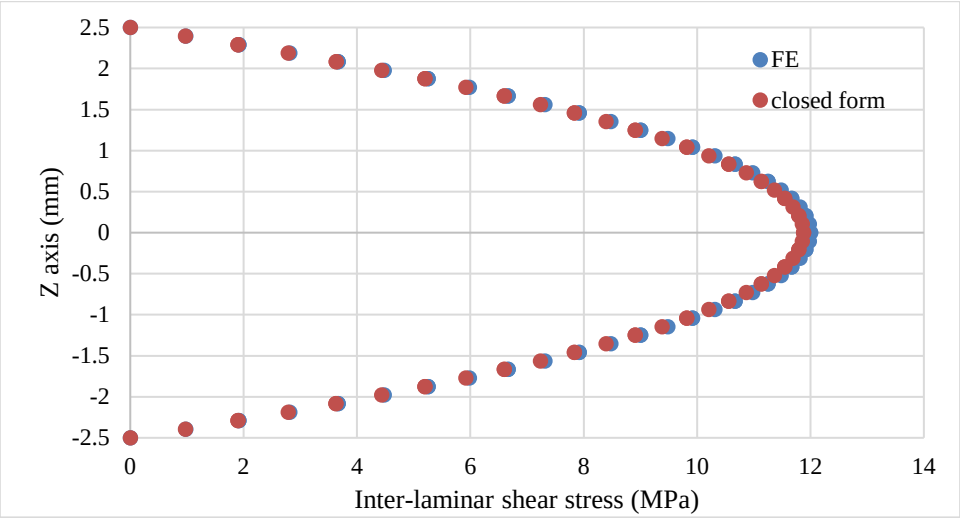

Figure 6-27. Variations of inter-laminar shear stress through layers and laminate thickness (lateral view) at x= L/4 from the centre of sample (load at the centre=1200 N). Comparison has been made between overlapping numerical and analytical data.

6.3.2. Closed Form Solution of 3PB test

Given equations (3-3, 3-4 and 3-14), the matrix of reduced stiffness, compliance matrix and bending stiffness are calculated as below:

$$Q = \begin{bmatrix} 23.04 & 5.76 & 0 \\ 5.76 & 23.04 & 0 \\ 0 & 0 & 3.52 \end{bmatrix} \quad , Q^{-1} = \begin{bmatrix} 0.0462 & -0.0115 & 0 \\ -0.0115 & 0.0462 & 0 \\ 0 & 0 & 0.284 \end{bmatrix}$$

$$D = \begin{bmatrix} 240 & 60 & 0 \\ 60 & 240 & 0 \\ 0 & 0 & 36.66 \end{bmatrix} \quad , \quad D^{-1} = \begin{bmatrix} 0.0044 & -0.0011 & 0 \\ -0.0011 & 0.0044 & 0 \\ 0 & 0 & 0.02727 \end{bmatrix}$$

From equations (3-19 and 3-20) normal, in-plane and inter-laminar shear stresses at the load of 1200 (N) are calculated as below:

σ = 190× z (MPa) and from equation (3-6) ε = 0.877×z (%)

τ = 0

$\sigma_{(x,z)}^{(k=1-24)}$ = 1.9 × (6.25-z^2)

Where: – *h/2* (bottom side of sample) ≤z ≤ +*h/2* (upper side of sample), F = 1200 N, b = 15 mm, L = 100 mm, h = 5 mm and ply thickness is 0.2083 mm

Therefore, according to above solution, Figure 6-25 and Figure 6-27 show that closed form solution agrees with the results of FE model of the 3PB test.

6.3.3. Tension, 0°/90° fibre orientation

Normal and shear stress/strain distribution contours in the tensile test specimen are depicted in Figure 6-28 showing the gauge length area of test specimen where potential failure such as fibre pull out and fibre/matrix interfacial de-bonding are predicted. According to the maximum stress failure criterion, just before the point of fracture, failure is predicted.

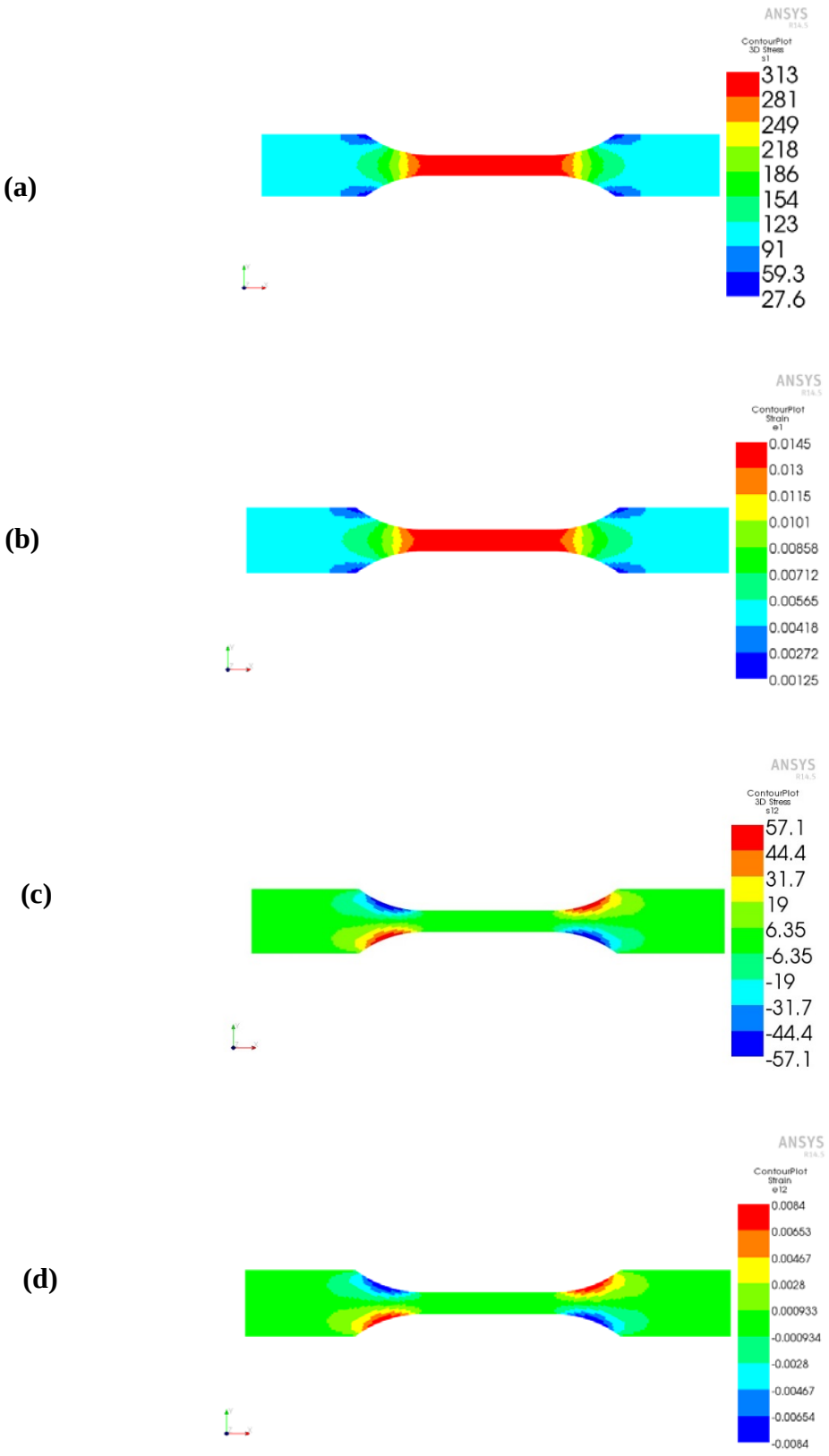

Figure 6-28. (a and b) Normal stress/strain distribution, (c and d) shear stress/strain distribution at the max load of 15000 N (GFRP with 0°/90° fibre orientation).

6.3.4. Closed Form Solution of tension test

Given equations (3-3, 3-4 and 3-14) the matrix of reduced stiffness and extensional stiffness matrix are calculated as below:

$$Q = \begin{bmatrix} 23.04 & 5.76 & 0 \\ 5.76 & 23.04 & 0 \\ 0 & 0 & 3.52 \end{bmatrix} \quad , Q^{-1} = \begin{bmatrix} 0.0462 & -0.0115 & 0 \\ -0.0115 & 0.0462 & 0 \\ 0 & 0 & 0.284 \end{bmatrix}$$

$$A = \begin{bmatrix} 115.2 & 28.8 & 0 \\ 28.8 & 115.2 & 0 \\ 0 & 0 & 17.6 \end{bmatrix} \quad , \quad A^{-1} = \begin{bmatrix} 0.0092 & -0.0023 & 0 \\ -0.0023 & 0.0092 & 0 \\ 0 & 0 & 0.0568 \end{bmatrix}$$

From equation (3-23), the normal and in-plane shear stresses at the load of 15000 (N) are calculated as below:

σ = 300 MPa (refer to Figure 6-28 (a) for comparison)

From equation (**3-5**), ε = 1.4% (refer to Figure 6-28 (b) for comparison)

τ = 0 (refer to Figure 6-28 (b) for comparison, the stress values should be compared with the stress values within the gauge length).

Cross section of tensile sample is h×b= 5mm×10mm

6.3.5. Effect of Fibre configuration-3PB test

The effect of fibre orientation on normal and shear stresses in the thickness direction at the center of 3PB specimen is illustrated in Figure 6-29 and Figure 6-30. The normal stress variation shows that the maximum value of tensile and compressive stress at upper and lower surface decrease as a function of fibre orientation. The maximum value of the shear stress in the XY plane increases with increasing fibre orientation. This explains the increased ductility and decreased strength in the bending specimen with ±45°compared to 0°/90° fibre orientation.

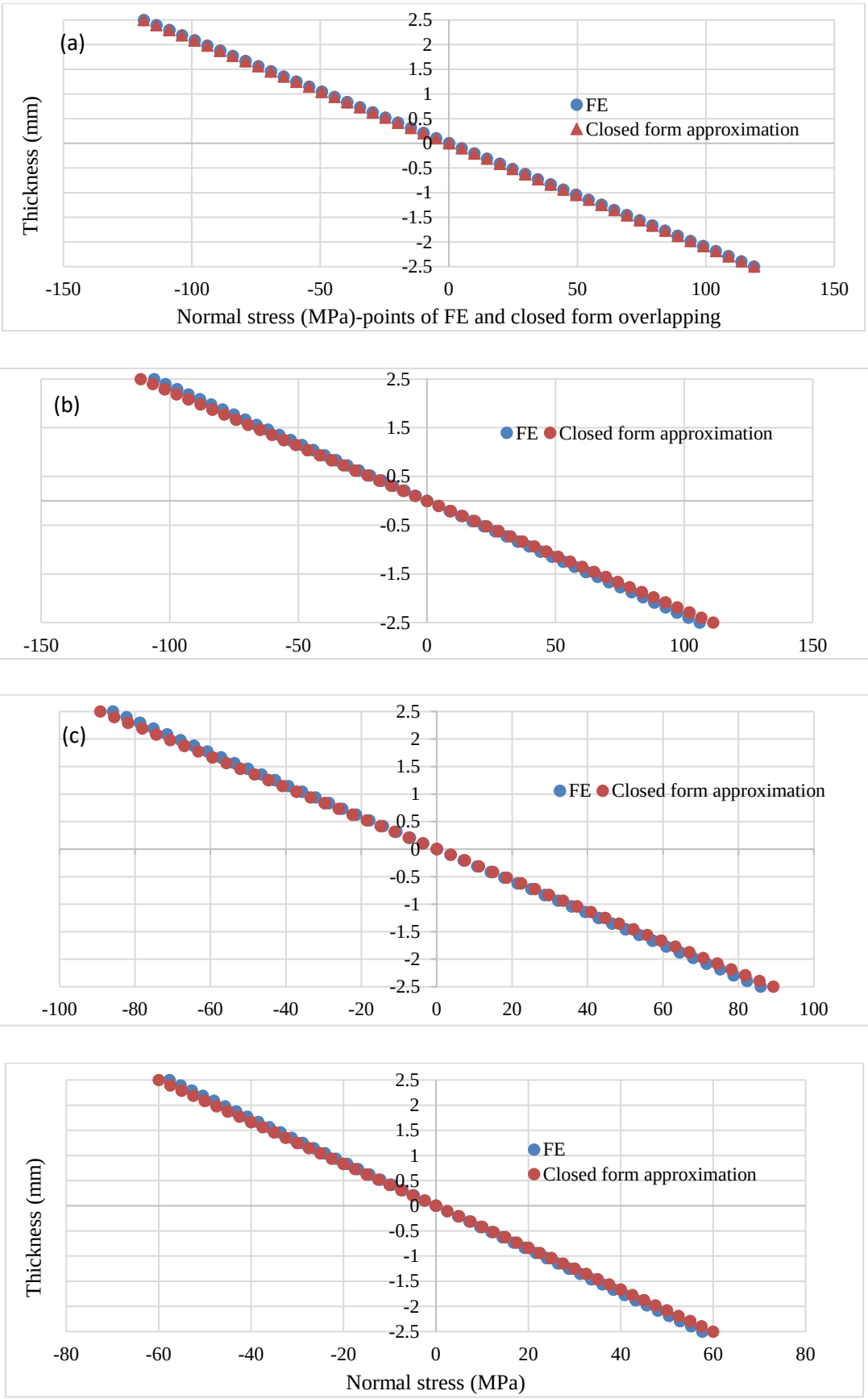

Figure 6-29. Effect of fibre angle on normal stress throughout the thickness of laminate, applied load= 300 N, (a) 0°, (b) 15°, (c) 30°, (d) 45° lay ups.

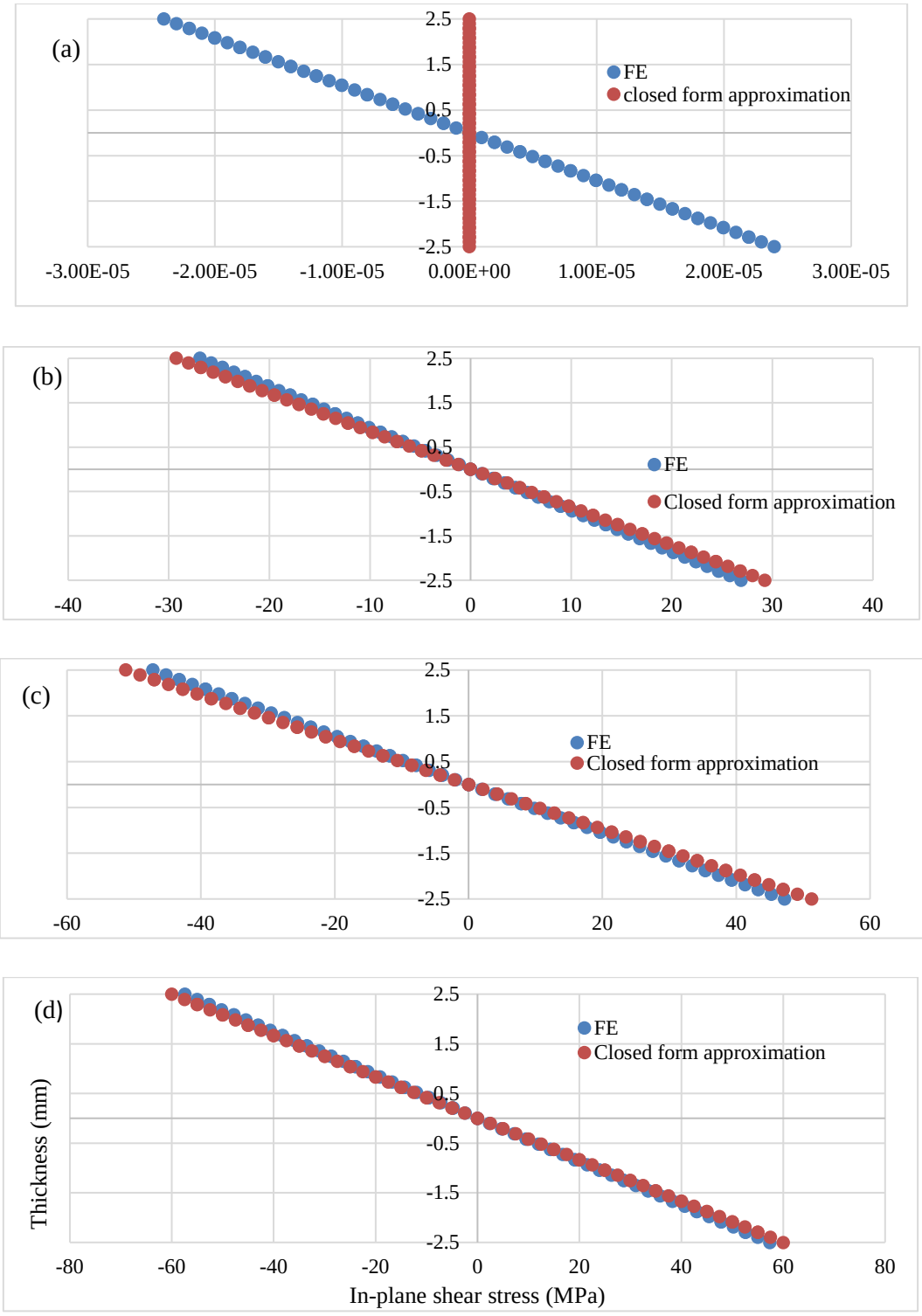

Figure 6-30. Effect of fibre angle on in-plane shear stress throughout the thickness of laminate, applied load= 300 N, (a) 0°, The maximum value of in-plane shear stress obtained from FE model is 0.000025 (MPa) which is almost zero, meaning that there is very negligible difference between these values obtained by closed form solution, (b) 15°, (c) 30°, (d) 45° lay ups.

6.3.6. Closed Form Solution of 3PB test

Given equations (3-5, 3-14, 3-19 and 3-7,) for various fibre orientation, normal and in-plane shear stresses at the load of 300 (N) are calculated as below:

a) **0°**

$$Q = \begin{bmatrix} 23.04 & 5.76 & 0 \\ 5.76 & 23.04 & 0 \\ 0 & 0 & 3.52 \end{bmatrix}$$

$$D = \begin{bmatrix} 240 & 60 & 0 \\ 60 & 240 & 0 \\ 0 & 0 & 36.66 \end{bmatrix} \quad , \quad D^{-1} = \begin{bmatrix} 0.0044 & -0.0011 & 0 \\ -0.0011 & 0.0044 & 0 \\ 0 & 0 & 0.02727 \end{bmatrix}$$

$\sigma = 47.5\times z$

$\tau = 0$

b) **15°**

$$Q = \begin{bmatrix} 21.76 & 7.04 & -2.217 \\ 7.04 & 21.76 & 2.217 \\ -2.217 & 2.217 & 4.8 \end{bmatrix}$$

$$D = \begin{bmatrix} 226.65 & 73.32 & -23.09 \\ 73.32 & 226.65 & 23.09 \\ -23.09 & 23.09 & 50 \end{bmatrix} \quad , \quad D^{-1} = \begin{bmatrix} 0.0054 & -0.0021 & 0.0034 \\ -0.0021 & 0.0054 & -0.0034 \\ 0.0034 & -0.0034 & 0.0232 \end{bmatrix}$$

$\sigma = 44.5\times z$

$\tau = 11.7\times z$

c) **30°**

$$Q = \begin{bmatrix} 19.2 & 9.6 & -2.217 \\ 9.6 & 19.2 & 2.217 \\ -2.217 & 2.217 & 7.3 \end{bmatrix}$$

$$D = \begin{bmatrix} 200 & 100 & -23.09 \\ 100 & 200 & 23.09 \\ -23.09 & 23.09 & 76.66 \end{bmatrix} \quad , \quad D^{-1} = \begin{bmatrix} 0.0074 & -0.0041 & 0.0035 \\ -0.0041 & 0.0074 & -0.0035 \\ 0.0035 & -0.0035 & 0.015 \end{bmatrix}$$

$\sigma = 35.6\times z$

$\tau = 20.54\times z$

d) **45°**

$$Q = \begin{bmatrix} 17.92 & 10.88 & \sim 0 \\ 10.88 & 17.92 & \sim 0 \\ \sim 0 & \sim 0 & 8.64 \end{bmatrix}$$

$$D = \begin{bmatrix} 186.65 & 113.32 & \sim 0 \\ 113.32 & 186.65 & \sim 0 \\ \sim 0 & \sim 0 & 90 \end{bmatrix} \quad , \quad D^{-1} = \begin{bmatrix} 0.00848 & -0.00515 & \sim 0 \\ -0.00515 & 0.00848 & \sim 0 \\ \sim 0 & \sim 0 & 0.011 \end{bmatrix}$$

$\sigma = 24 \times z$

$\tau = 24 \times z$

The above results of closed form solution for different fibre orientations, show that the FE model of 3PB test agrees well with the closed form solution (Figure 6-29 and Figure 6-30).

6.3.7. Effect of Fibre orientation-Tension test

The tensile behaviour is similar to the bending behaviour in respect to fibre configuration. Figure 6-31 and Figure 6-32 show graphically the influence of fibre orientation on normal and shear stresses induced in individual plies during tensile testing. The maximum normal stresses in individual plies decreases with increasing angle (Figure 6-31).

Shear stress variations with respect to the fibre orientation angle (Figure 6-32) show that changing the orientation angle from 0°/90° to ±45° the shear stress increases. Higher shear stresses cause shear band formation. This explains the lower strength observed in ±45 fibre orientation than 0°/90°. The shear bands correspond to the 45° oriented strain bands which were observed in the DIC strain map (Figure 6-14). This is also confirmed by resin-shear band formation which was observed in the SEM (Figure 6-12). In conclusion there is a good agreement between SEM observation, FE modeling and DIC strain maps for specimens with ±45° fibre orientation.

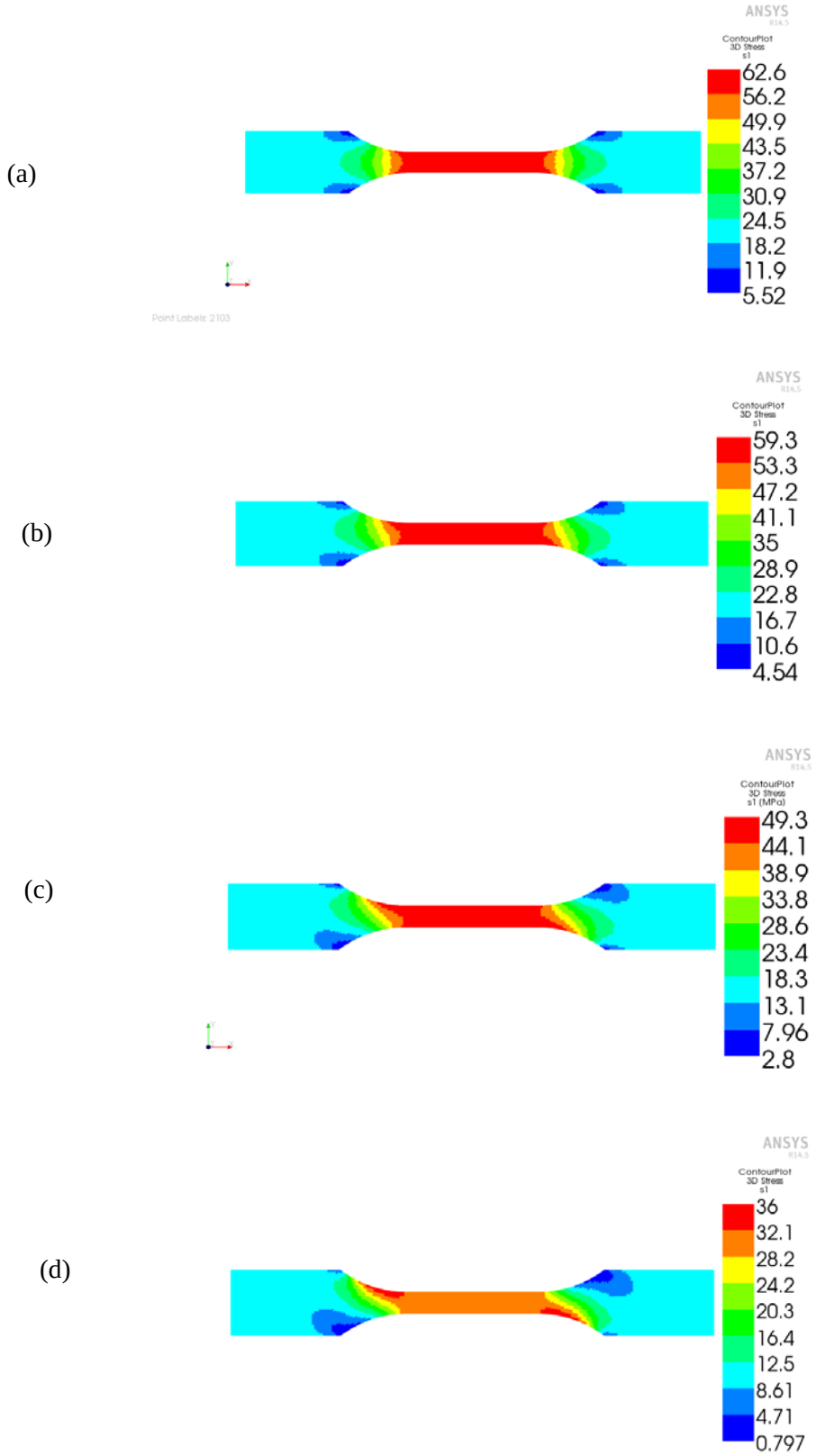

Figure 6-31. Effect of fibre angle on normal stress distribution, load = 3000N (a) 0°, (b)15°(c) 30° (d) 45° lay ups.

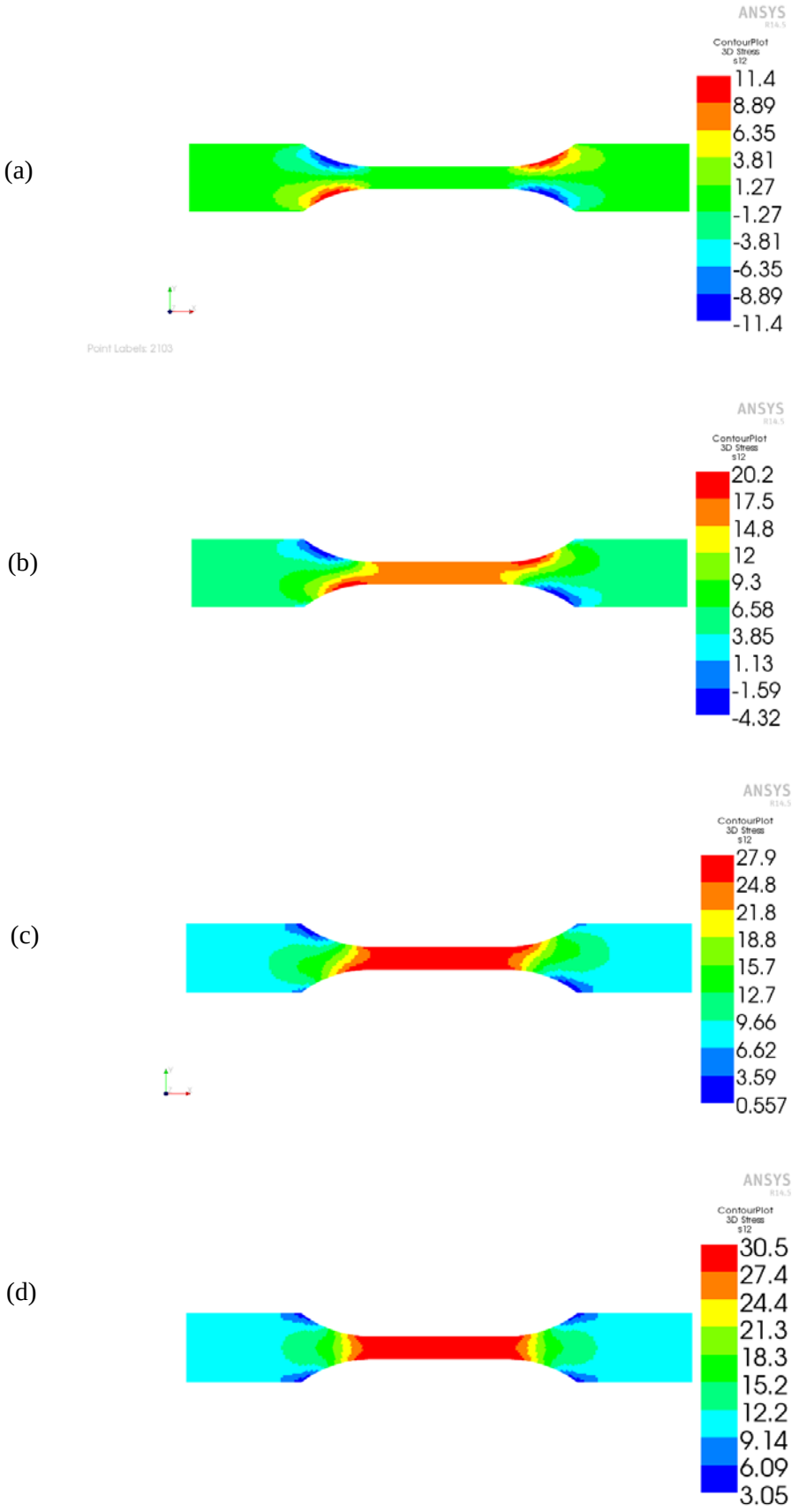

Figure 6-32. Effect of fibre angle on in-plane shear stress distribution in tension, load = 3000N (a) 0°, (b)15°(c) 30°(d) 45° lay ups.

6.3.8. Closed Form Solution of tension test at gauge length

Given equations (3-5 , 3-14, 3-24 and 3-7) for various fibre orientations the normal and in-plane shear stresses at the load of 3000 (N) are calculated as below:

a) 0°/90°:

$$Q = \begin{bmatrix} 23.04 & 5.76 & 0 \\ 5.76 & 23.04 & 0 \\ 0 & 0 & 3.52 \end{bmatrix}$$

$$A = \begin{bmatrix} 115.2 & 28.8 & 0 \\ 28.8 & 115.2 & 0 \\ 0 & 0 & 17.6 \end{bmatrix} \quad , \quad A^{-1} = \begin{bmatrix} 0.0092 & -0.0023 & 0 \\ -0.0023 & 0.0092 & 0 \\ 0 & 0 & 0.0568 \end{bmatrix}$$

σ = 60 MPa (refer to Figure 6-31 (a) at the gauge length area)

τ = 0 (refer to Figure 6-32 (a) at the gauge length area)

b) 15°

$$Q = \begin{bmatrix} 21.76 & 7.04 & -2.217 \\ 7.04 & 21.76 & 2.217 \\ -2.217 & 2.217 & 4.8 \end{bmatrix}$$

$$A = \begin{bmatrix} 108.8 & 35.2 & -11.08 \\ 35.2 & 108.8 & 11.08 \\ -11.08 & 11.08 & 24 \end{bmatrix} \quad , \quad A^{-1} = \begin{bmatrix} 0.0113 & -0.0044 & 0.0072 \\ -0.0044 & 0.0113 & -0.0072 \\ 0.0072 & -0.0072 & 0.0483 \end{bmatrix}$$

σ = 57 MPa (refer to Figure 6-31 (b) at the gauge length area)

τ = 15.7 MPa (refer to Figure 6-32 (b) within the gauge length area)

c) 30°

$$Q = \begin{bmatrix} 19.2 & 9.6 & -2.217 \\ 9.6 & 19.2 & 2.217 \\ -2.217 & 2.217 & 7.3 \end{bmatrix}$$

$$A = \begin{bmatrix} 96 & 48 & -11.08 \\ 48 & 96 & 11.08 \\ -11.08 & 11.08 & 36.8 \end{bmatrix} \quad , \quad A^{-1} = \begin{bmatrix} 0.0155 & -0.0086 & 0.0072 \\ -0.0086 & 0.0155 & -0.0072 \\ 0.0072 & -0.0072 & 0.0315 \end{bmatrix}$$

σ = 45 MPa (refer to Figure 6-31 (c) at the gauge length area)

τ = 26 Mpa (refer to Figure 6-32 (c) within the gauge length area)

d) 45°

$$Q = \begin{bmatrix} 17.92 & 10.88 & \sim 0 \\ 10.88 & 17.92 & \sim 0 \\ \sim 0 & \sim 0 & 8.64 \end{bmatrix}$$

$$A = \begin{bmatrix} 89.6 & 54.4 & \sim 0 \\ 54.4 & 89.6 & \sim 0 \\ \sim 0 & \sim 0 & 43.2 \end{bmatrix} \quad , \quad A^{-1} = \begin{bmatrix} 0.0176 & -0.0107 & \sim 0 \\ -0.0107 & 0.0176 & \sim 0 \\ \sim 0 & \sim 0 & 0.023 \end{bmatrix}$$

σ = 30 MPa (refer to Figure 6-31 (d) at the gauge length area)

τ = 30 MPa (refer to Figure 6-32 (d) within the gauge length area)

The results from closed form solutions show that FE results of tension test for all fibre orientation angle (Figure 6-31 and Figure 6-32) are validated.

Table 6-6 and Table 6-7 show the percentage difference between predicted normal and in-plane shear stresses using FE and closed form approximation in tensile test.

Table 6-6. Percentage difference between FE and closed form predicted longitudinal normal stresses.

Fibre orientation (degree)	FE results (MPa)	Closed form approximation (MPa)	Percentage difference (%)
0	62	60	3
15	59.3	57	4
30	48	45	6
45	31.5	30	5

Table 6-7. Percentage difference between FE and closed form predicted in-plane shear stresses.

Fibre orientation (degree)	FE results (MPa)	Closed form approximation (MPa)	Percentage difference (%)
0	0	0	0
15	16.7	15.7	7
30	27.5	26	6
45	30.5	30	2

In order to investigate the effect of fibre orientation on the failure criteria in the FE model of tensile test specimens, a constant load was applied on the specimen. Figure 6-33 to Figure 6-36 show that Tsai-Hill factor changes corresponding to the fibre orientation in the FE model. In

specimens with 15°/75° and 30°/60° fibre configuration, as a result of shear/normal stresses induced within the fibres oriented at 15° and 30° the fracture surface is also oriented. When the fibres are oriented at $\pm$45°, due to the balanced shear and normal stresses induced in both $\pm$45° direction, the fracture surface is relatively flat.

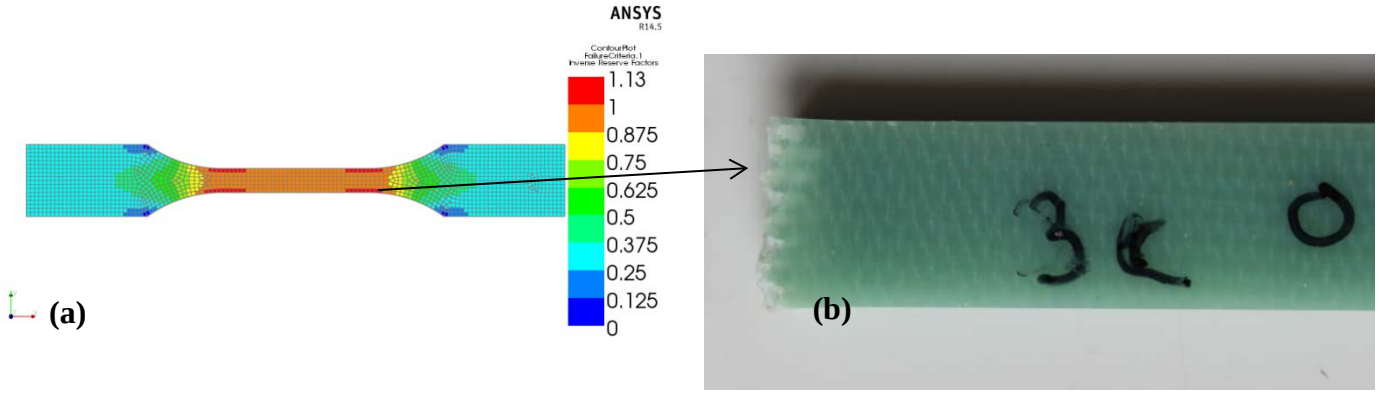

Figure 6-33. Predicted (FE) and actual location of failure (a) Tsai-Hill failure criterion, (b) top fracture surface of tensile test specimen with 0°/90° fibre orientation.

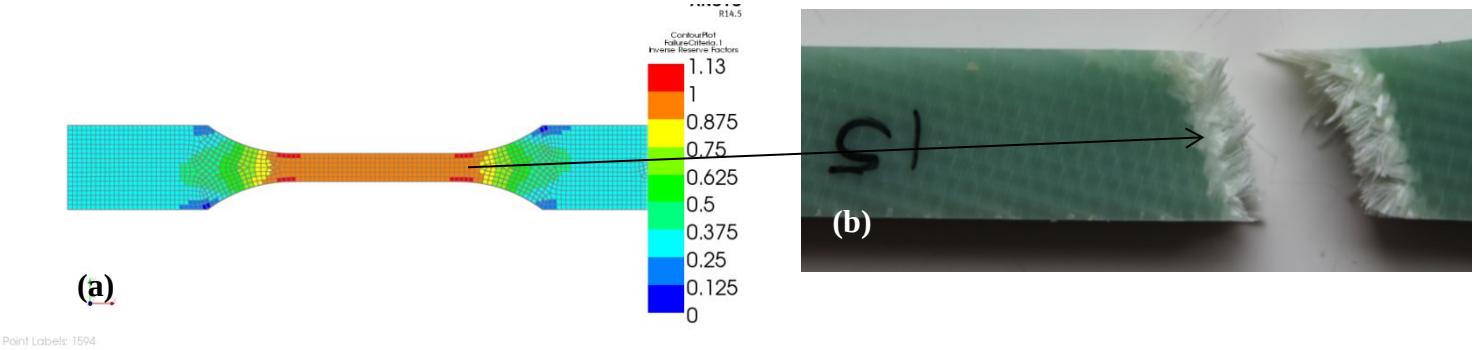

Figure 6-34. Predicted (FE) and actual location of failure (a) Tsai-Hill failure criterion, (b) top fracture surface of tensile test specimen with 15°/75° fibre orientation.

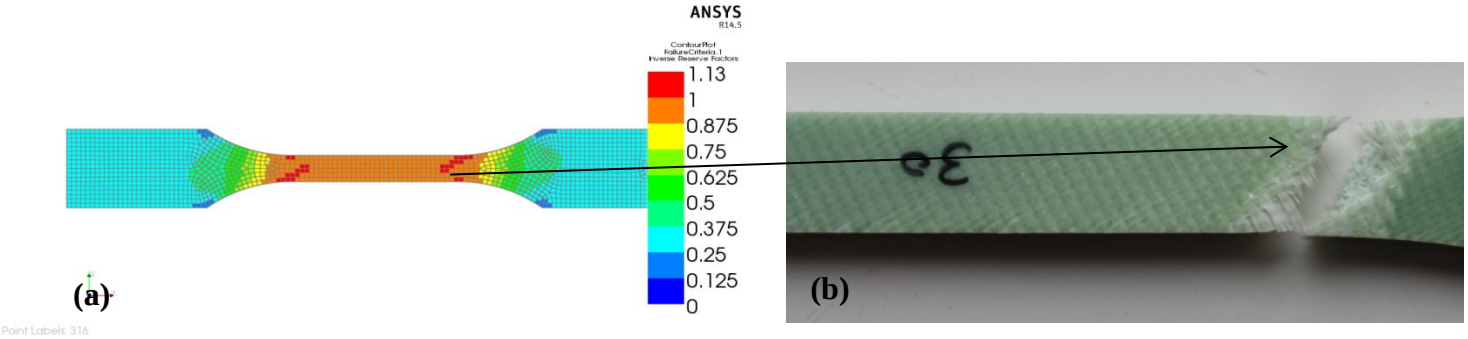

Figure 6-35. Predicted (FE) and actual location of failure (a) Tsai-Hill failure criterion, (b) top fracture surface of tensile test specimen with 30°/60° fibre orientation.

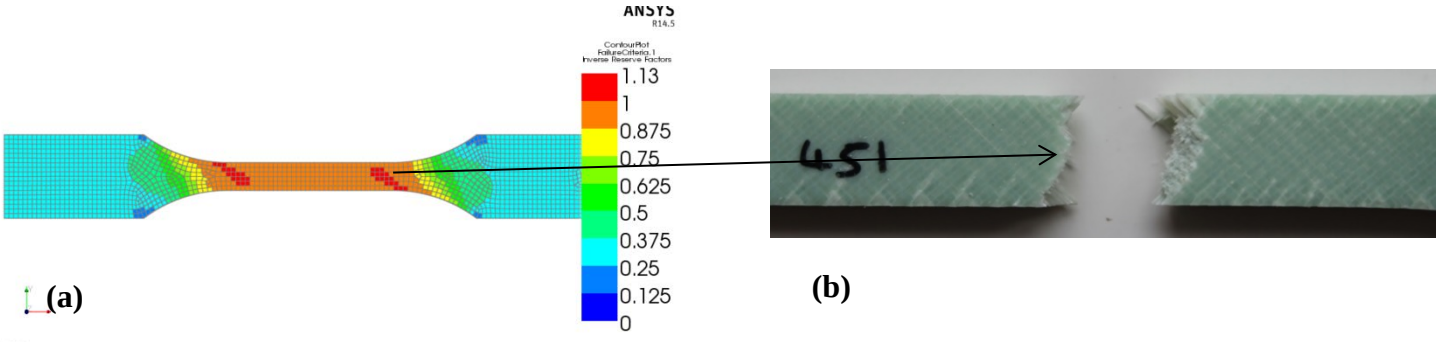

Figure 6-36. Predicted (FE) and actual location of failure (a) Tsai-Hill failure criterion, (b) top fracture surface of tensile test specimen with -45°/+45° fibre orientation

Given the mechanical properties of GFRP composite (Table 6-5) studied in this work and based on Figure 6-33 to Figure 6-36, a comparison between failure load occurred in the tensile test specimen and Tsai-Hill predicted failure load is shown in Table 6-8. A good agreement between FE model and experiment is observed.

Table 6-8. Comparison between tensile failure load and Tsai-Hill failure load predicted by FE model.

Fibre orientation	Experimentally failure load	Tsai-Hill predicted failure load	Difference (%)
(0°/90°)	15750	16000	1.5
(15°/75°)	11250	11750	4.2
(30°/60°)	8000	8600	6.5
(+45°/-45°)	7000	7750	9.6

6.4. Summary

In order to determine mechanical properties for FE model of GFRP composite turbine blade, a series of tests including tensile, shear and 3PB were conducted in conjunction with a full field strain measurement technique via DIC system. Therefore stress-strain response in each of these mechanical tests were assessed on the basis of DIC strain measurements.

In addition DIC strain localization maps contribute to the analysis of damage development during the composite sample deformation in each of mechanical test. The digital image correlation technique for measuring displacement and/or strain during tension tests of GFRP composite materials, allowed for the determination of parameters from stress-strain plots where these parameters cannot be obtained by using conventional strain gauges or an electro-mechanical extensometer. Strain gauges do not perform well on rough composite surfaces. For example, the Poisson's ratio can be calculated by longitudinal and transverse strain measurement via DIC. Strain distribution maps could also be evaluated for the moments just after the onset of delamination. DIC strain maps illustrate that strain distribution depends on the fibre orientations and indicates the zones where delamination took place. Analysis of such strain distribution maps for two-directional woven GFRP specimens aided in assessment of the greater elongation of plain weave reinforced composites with $\pm 45°$ in comparison with 0°/90° fibre orientation. The outcomes reveal the applicability of the image correlated system in precise strain calculation during tension testing of GFRP specimens and the effect of their anisotropy. In addition to determination of elastic constants, image correlated technique contributed to a better evaluation of the failure modes in glass epoxy composites and can be employed for verification of the FE models of these materials.

In order to evaluate the fibre orientation effect in a GFRP composite during a tensile test, an experimental methodology was adopted which develops a capability to examine the structural integrity of the GFRP composite material. The heterogeneous mechanical behaviour of the laminated composite and the various damage modes detected by the failure analysis techniques (i.e. fractography) indicated the effect of the fibre configuration. The concurrent full-field strain measurement indicated that there is a strong link between the distribution of imposed deformation and the microstructure of the material. An improved assessment of the material performance was obtained from the high density of data points in the strain maps. Creation of strain gradients during the development of whole strain fields can be explained by the original microstructure of the material. For example the strain localizations in the material with the fibre

alignment at 0°/90° and the relative homogeneous distribution of the strains in the material with the fibre alignment at ±45° at lower loads. The intensities of localized strain are greater compared to the applied strain of the GFRP material which additionally indicates opportunity for enhancement in behaviour of the GFRP material by adjusting the fibre configuration with respect to the external applied force. Supplementary advances in the plotting and recording procedures could play a pivotal part not only in the development of the high-tech side of safe design, but also in identifying the appropriate applications for the existing polymer based fibre reinforced composites. Experimentally generated results can be compared and matched to FE analysis models for validation.

The effect of fibre configuration on tension properties of woven glass fibre reinforced epoxy resin was assessed. Based on the experimental results, scanning electron micrographs, the full field strain measurement maps and the FE investigation conducted, the subsequent discussions can be made;

- ✓ Specimens machined in the $\pm 45°$ fibre orientation exhibited significantly lower tensile properties than those in longitudinal or transverse directions. Also the $\pm 45°$ fibre orientation specimens showed a greater ductility, as compared to 0°/90° fibre directions. There are two reasons for this behaviour:

1- Strain limiting effect of fibres.
2- Matrix shear band formation.

In this chapter the finite element modelling results have been validated by comparison with closed form solutions and experimental measurements. The importance of fibre orientation has been highlighted. In the next chapter a more detailed analysis of the strain distribution in a woven composite has been undertaken using the DIC method

Chapter 7
Digital Image Correlation

7. Digital Image Correlation

Using the DIC method, the stress-strain response of composites subjected to static loads can be evaluated, therefore following the first step in methodology flowchart (Figure 3-1), DIC is necessary to provide the mechanical properties of composites for FE fatigue life prediction of turbine blades.

In addition, with reference to chapter 1 section 1.2, one of the main objective of this work is to identify performance controlling issues so that confidence can be attained for using GFRP in tidal turbine applications. The life controlling factors in the use of composite materials for load bearing components like tidal turbine blades are mainly associated with failure mechanisms. In other words, when laminated composites are subjected to static and fatigue loads, numerous damage modes can be activated leading to the premature failure of materials unless controlled. Detecting these failure modes can make positive contribution to understanding the safety factors which need to be defined and implemented when using composites for tidal turbine blades. The DIC technique was employed in this study to analyse damage development and strain localization during the static and cyclic deformation. In particular, during the fatigue testing of composites in a sea water environment, the effect of penetration of sea water in the resin cracks was observed using DIC strain map. Diffusion of sea water in composites can facilitate crack propagation and fibre degradation. Although SEM/EDX technique is used to characterize these failure modes, DIC can provide more information about localized strain in the damage zones. As a result, employing DIC in this study can eliminate limiting factors in the design of composite turbine blades.

For characterizing and obtaining mechanical properties of GFRP, a methodology based on the combination of DIC and FEM for full field strain assessment was used. The DIC system provides experimentally generated strain fields and therefore validation is obtained by comparing DIC and FE calculated strain maps. Consequently DIC and FEM strain field agreement can increase our confidence about the results of FE modelling of tidal turbine blades.

In the following sections, results of DIC maps during tension, shear and bending deformation of GFRP composites are discussed in more detail.

7.1. Comparison of FE and DIC Strain Fields

The DIC full-field surface displacement evaluation is based on the examination of images of the sample surface with an arbitrary texture (Sutton *et al.*, 2009). Figure 7-1 to Figure 7-4 show random textures (speckle patterns) created on three point bending, Iosipescu shear, tensile and short beam shear sample surfaces using black and white spray paints. The DIC software VIC-2D (Solutions, 2009) has been employed in this work for evaluation of strain fields on the sample surface. The VIC-2D software determines two-dimensional positions before and after deformation by following the grey intensity levels (speckle pattern) in small subsets all over the sequence of obtained images.

For the analysis of the tensile, shear and bending test specimens in this work, 35 × 35 pixel subsets (analogous to approximately 0.5 mm × 0.5 mm) have been used. The displacements determined in this method were then mathematically differentiated using the strain computation algorithm in the VIC-2D software. This is done in order to compute the Green–Lagrange surface strain tensor components.

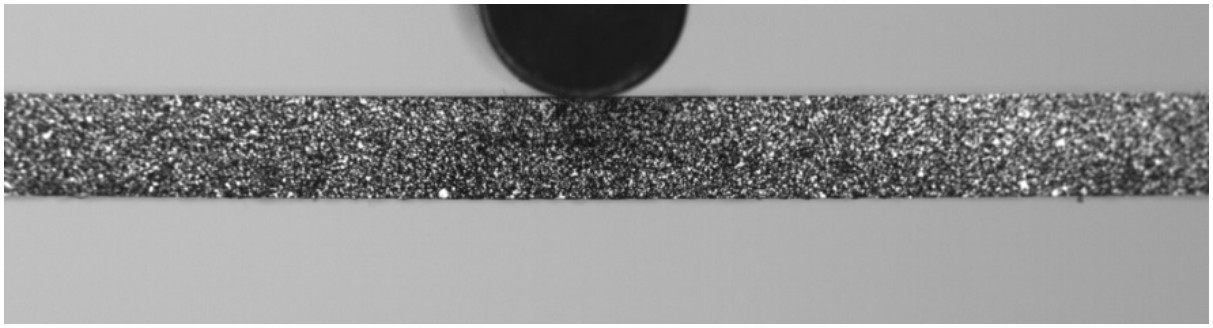

Figure 7-1. Random spot arrangement formed on 3PB specimen surface by painting black and white colour

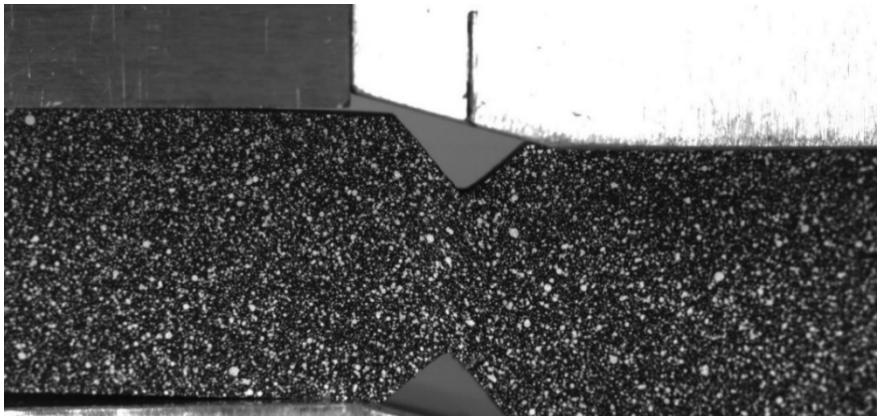

Figure 7-2. Random spot arrangement generated on Iosipescu shear test specimen surface by painting black and white colour.

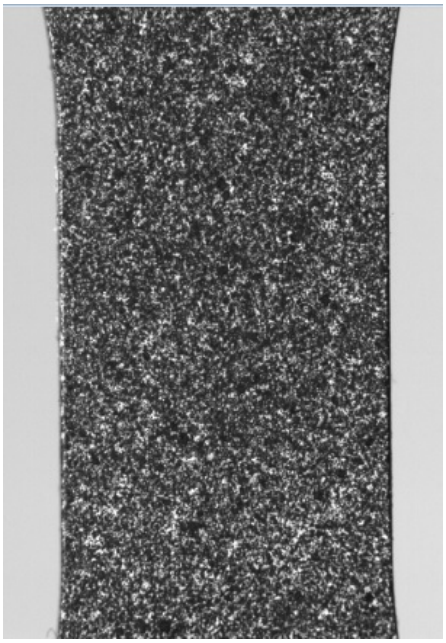

Figure 7-3. Random spot arrangement created on tensile test specimen surface by painting black and white colour.

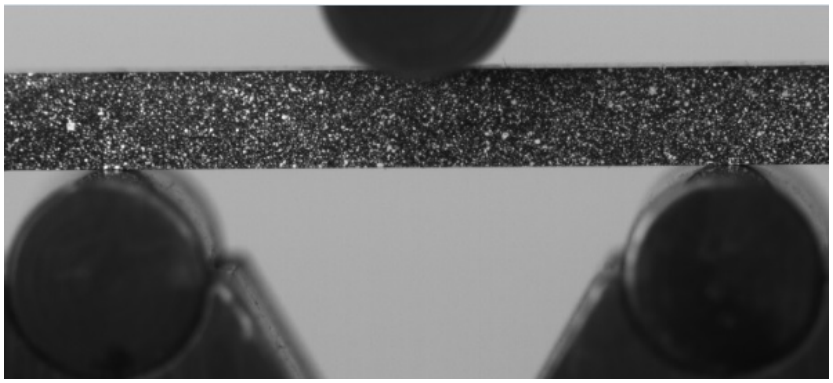

Figure 7-4. Experimental setup for a short beam specimen in inter-laminar shear test

7.2. 3PB Test

The DIC technique was used to evaluate the stress–strain relations of a glass/epoxy composite in the 3PB test. The specimen with a span-to-thickness ratio of 20 is loaded in three-point bending configuration so that shear, tensile and compressive failure may occur.

Figure 7-5 shows DIC and FEM calculated strain fields obtained in a 3PB specimen (GFRP sample with 0/90 fibre orientation). The FEM-calculated stress fields (Figure 7-6) are related to the strain fields. The FEM strain fields can be compared with the experimentally-created strain fields to further validate the precision of the material properties used in FE analysis. The

comparison for stress has been made in the context of the closed form solution. The closed form solution in section 7.2.1 indicates that both FE calculated stress and strain fields agree with the strain fields obtained by DIC method with an accuracy of 90%. The verification was carried out at a 70% of fracture load.

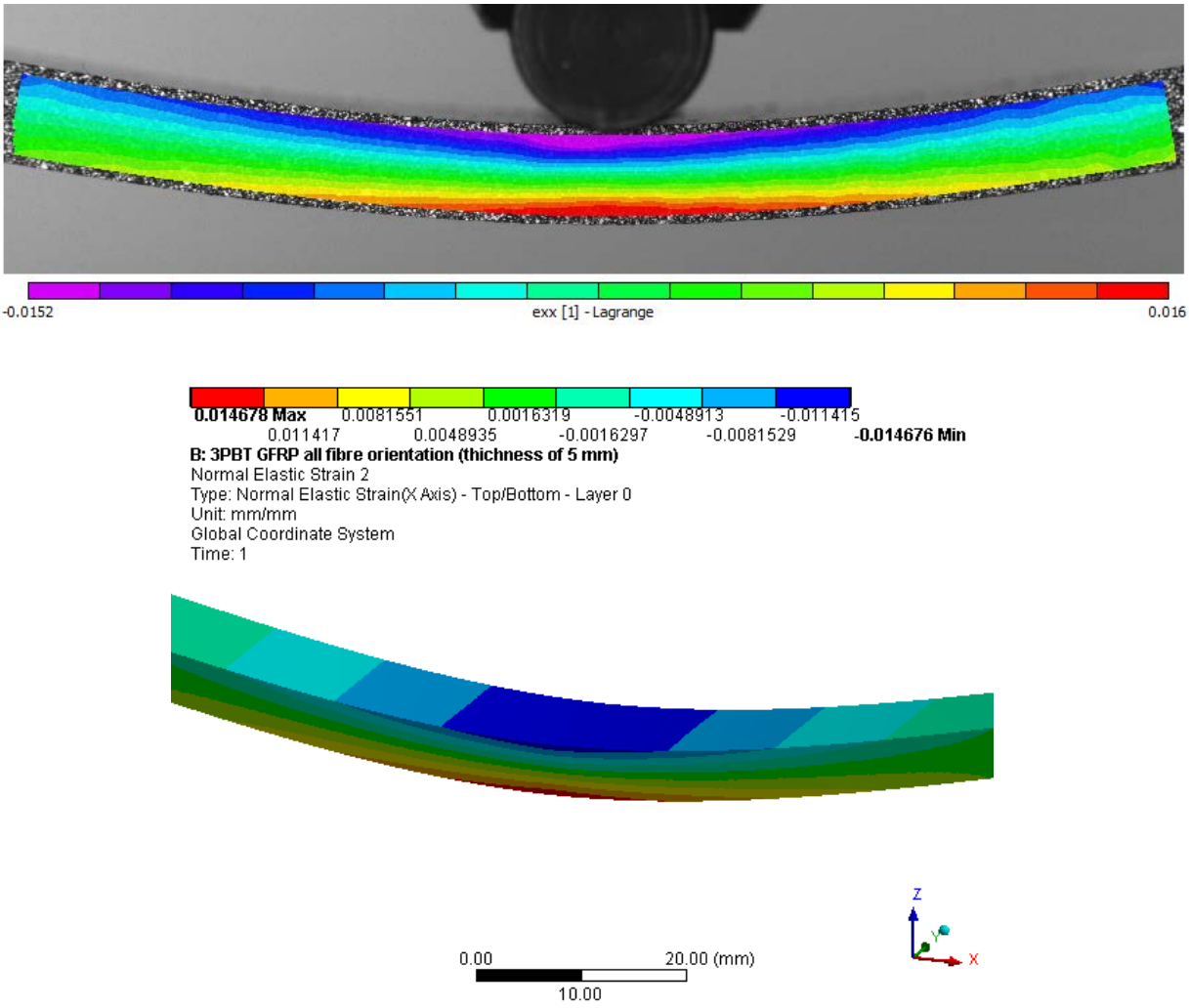

Figure 7-5. Comparison between FE and experimentally generated (DIC) axial strain fields under 3PB test sample (0/90 fibre orientation) at 800 N.

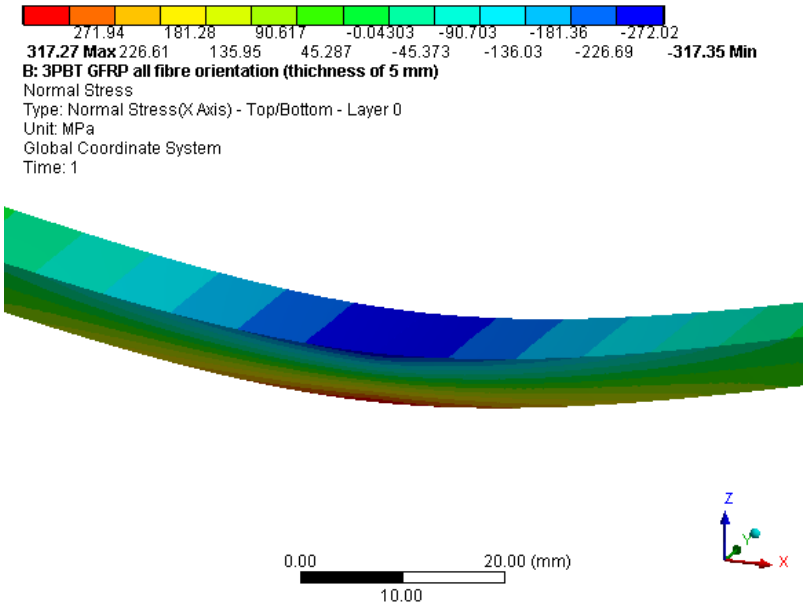

Figure 7-6. FE predicted axial stress distribution under 3PB test (0/90 fibre orientation) at load 800 N.

7.2.1. Closed form solution

Given the equations (3-3, 3-4 and 3-14) stresses at the load of 800 (N) are calculated as below:

$$Q = \begin{bmatrix} 23.04 & 5.76 & 0 \\ 5.76 & 23.04 & 0 \\ 0 & 0 & 3.52 \end{bmatrix} \quad , Q^{-1} = \begin{bmatrix} 0.0462 & -0.0115 & 0 \\ -0.0115 & 0.0462 & 0 \\ 0 & 0 & 0.284 \end{bmatrix}$$

$$D = \begin{bmatrix} 240 & 60 & 0 \\ 60 & 240 & 0 \\ 0 & 0 & 36.66 \end{bmatrix} \quad , \quad D^{-1} = \begin{bmatrix} 0.0044 & -0.0011 & 0 \\ -0.0011 & 0.0044 & 0 \\ 0 & 0 & 0.02727 \end{bmatrix}$$

From equation (3-6 and 3-19);

$\sigma_{(x,x)}^{(k=1-24)} = 127 \times z$, at z=2.5mm, $\sigma_{(x,x)}^{(k=1-24)}$=318 N (refer to Figure 7-6 for comparison)

$\sigma_{(x,y)}^{(k=1-24)} = 0$

$\varepsilon_{(x,x)}^{(k=1-24)} = 5.86 \times z$, at z=2.5 mm, $\varepsilon_{(x,x)}^{(k=1-24)}$= 1.47% (refer to Figure 7-5)

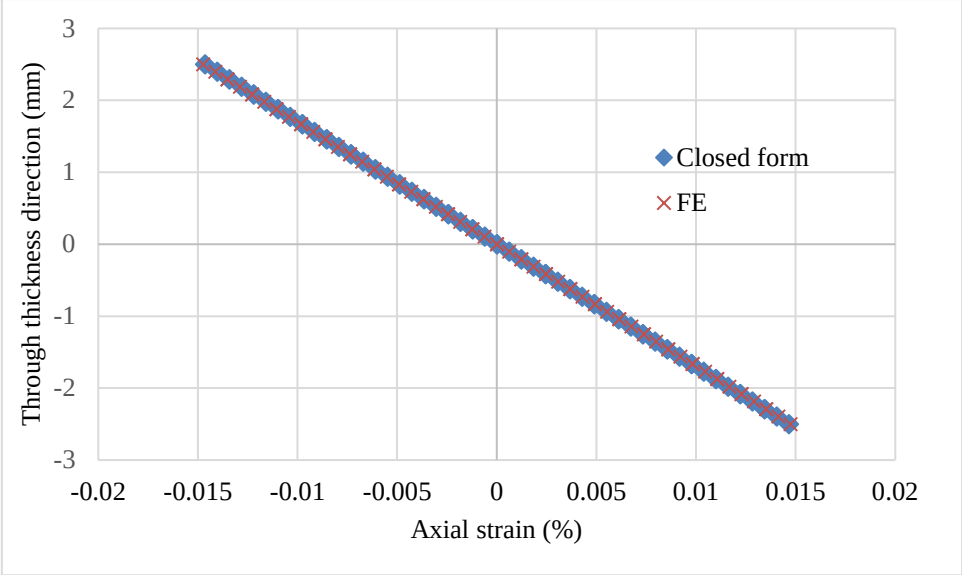

Figure 7-7. Variations of axial strain through layers and laminate thickness (lateral view) at the centre of test specimen where maximum loading of (800 N) applied. Comparison has been made between overlapping numerical and analytical data.

7.3. Tensile Test

The DIC technique was used for the evaluation of the tensile stress–strain response of a GFRP composite. Figure 7-8 shows characteristic axial, transverse and shear strain fields acquired in a glass/epoxy tensile sample using a DIC system.

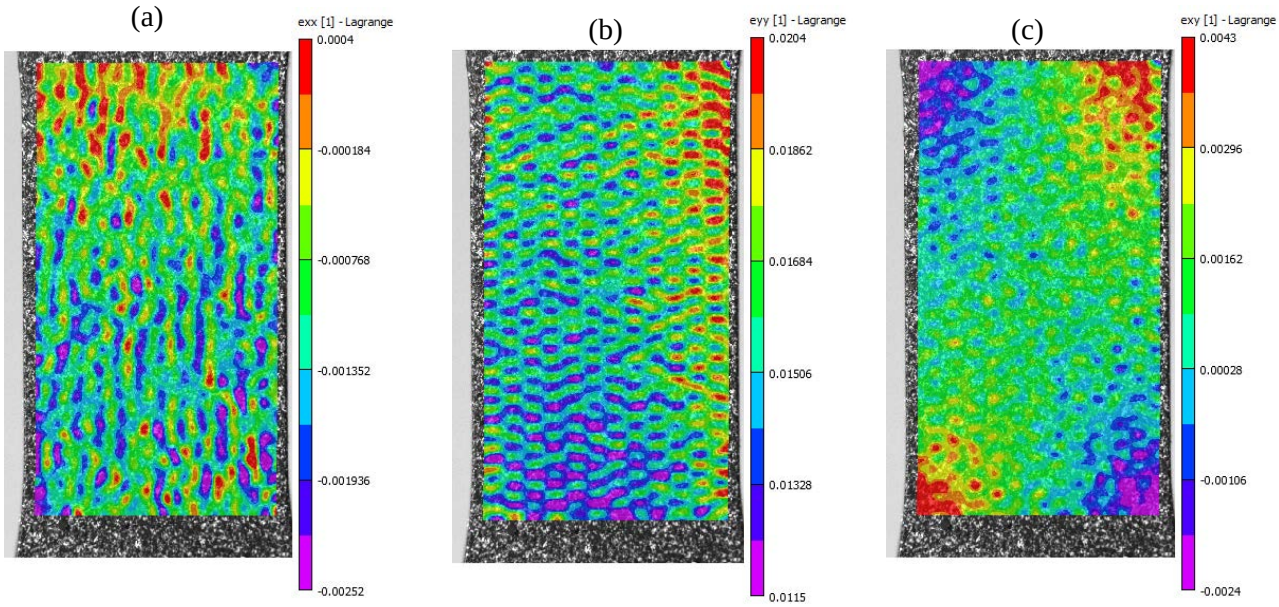

Figure 7-8. Lagrange strain tensor components for a tensile specimen, images were registered just after delamination occurred, (a) axial, (b) transverse, (c) shear strain.

As mentioned before in order to simulate tensile testing, ANSYS composite Pre-post was used. In order to make a comparison between the FEM and DIC strain distribution the composite sample must be modelled. This simulation was carried out using the FE-DIGIMAT software (Digimat, 2011). Since the DIC technique captures the outmost layers of composite during the deformation, for simplicity only one layer of composite sample as a representative volume element (RVE) is shown in Figure 7-9.

Table 7-1 and Table 7-2 list the mechanical properties of constituents and yarn specifications which are used for simulation in RVE (Figure 7-9).

Table 7-1. Mechanical properties of GFRP constituents which are defined in FEM-DIGIMAT for above RVE ('CES EduPack 2017,').

	Density(gr/cm^3)	Young's Modulus (MPa)	Poisson's ratio
Epoxy Resin	1.15	3500	0.35
E-Glass	2.55	72000	0.22

Table 7-2. Yarn specification based on X-Ray micro-computer tomography results (chapter 9).

Warp yarn count	10 (yarn/cm)	
Weft yarn count	10 (yarn/cm)	
Filament count	560	
Fibre diameter	0.01 mm	
Yarn cross-section	Height	0.1 mm
	Width	0.750 mm

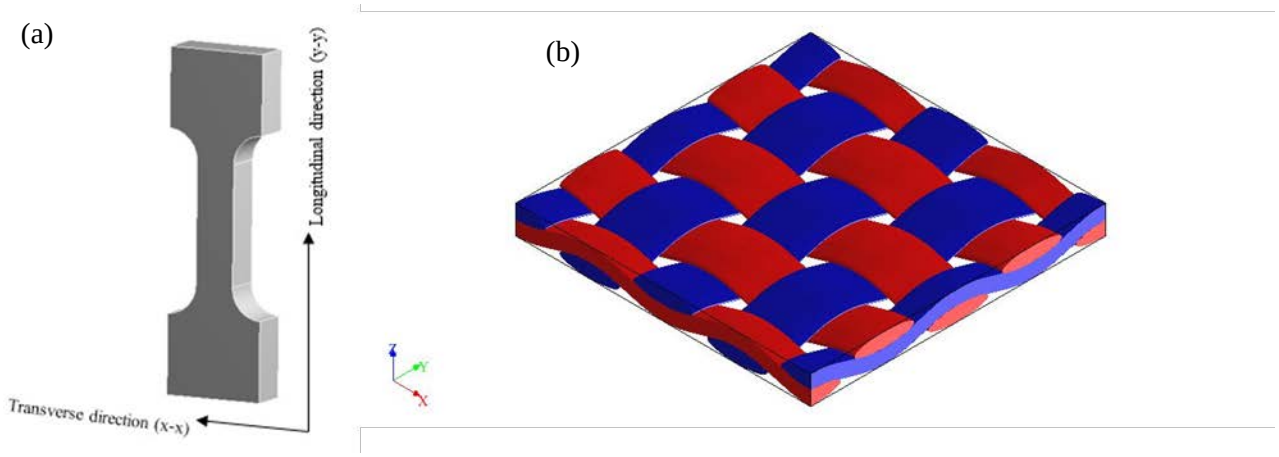

Figure 7-9. Tensile test specimen simulation, (a) ANSYS, (b) Representative volume element (RVE) with FE-DIGIMAT

Comparisons are drawn for strain fields on the sample surface within the low load regime in terms of Von Mises strain. Figure 7-10 shows the Von Mises strain determined by the two methods. A good agreement in terms of strain distribution is observed.

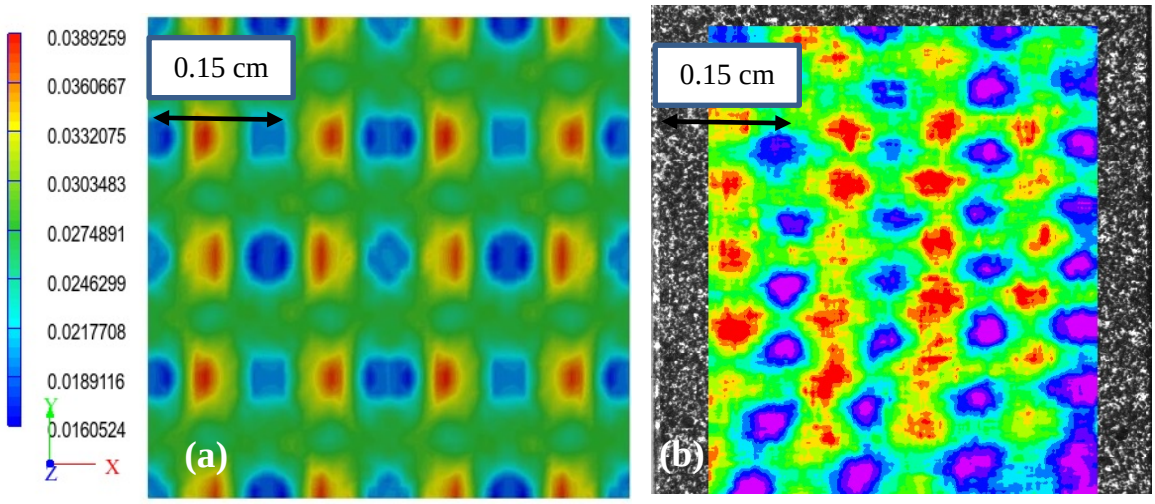

Figure 7-10. Full field Von Mises strain map, (a) FE-DIGIMAT, (b) DIC.

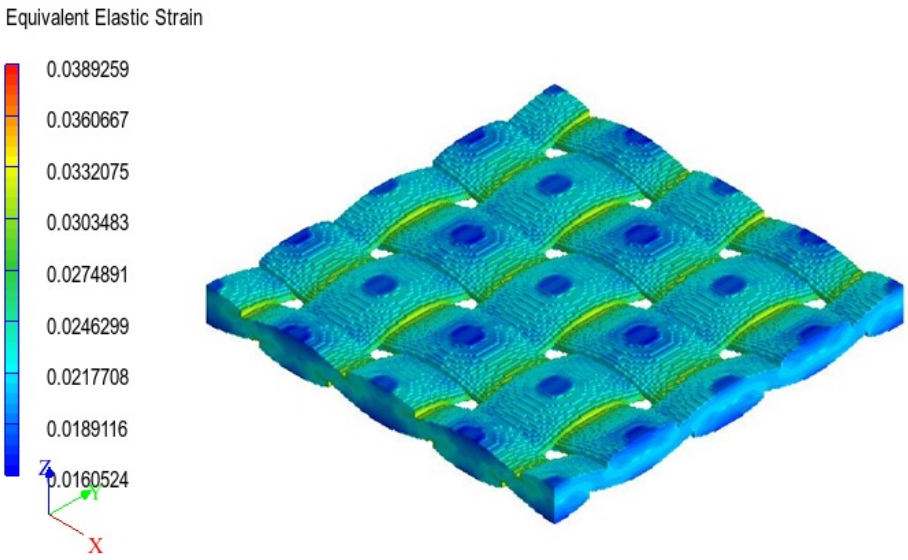

Figure 7-11. 3D-FE strain map

A 3D-FE strain map is shown in Figure 7-11. Comparing the FE and DIC strain maps with the microstructure of the composite (Figure 6-1) reveals that high strain value in Figure 7-10 and Figure 7-11 in both DIC and FE strain maps corresponds to the epoxy resin region while, intermediate value of strain occurs in the regions with transverse yarn and low strain value in the regions with longitudinal yarn.

7.4. Iosipescu Shear Test

The objective of this section is to use the Iosipescu shear test method and assess its capability to qualify and quantify the shear properties of GFRP laminates. An Iosipescu test fixture has been manufactured to examine the in-plane and through-thickness (inter-laminar) shear properties of cross-ply woven glass fibre composites.

To better understand the material behaviour under shear testing, surface shear strain was monitored using the DIC system. DIC allows, for various loading levels, to reach a full field shear strain measurement, therefore the strain distribution on the area between notches can be investigated. The obtained strain maps show heterogeneity of strain localization and its dependency on the fibre orientation. The strain maps also show the areas where damage accumulation takes place. Experimentally produced strain fields were compared with FE strain fields to validate the precision of in-plane shear strain measurements.

In this study in order to understand the influence of fibre orientation under both in-plane and inter-laminar shear stress, the laminate was cut at different off-axis angles (0°, 45°) to give specimens with two different stacking sequences ([0°/90°], [+45/−45]). At least five tests were carried out for each shear plane and the average value for shear strength and modulus, with their standard deviations were determined. The in-plane shear strength is measured from the load prior to the non-linear behaviour while the inter-laminar shear strength is calculated on the basis of the successive load drops in the shear stress-strain curves corresponding to the onset of delamination. Representative DIC images for in-plane shear test coupons and the effect of fibre orientation are compared with FEM maps and are shown in Figure 7-12 to Figure 7-17. The strain values in these figures indicates that the FE predicted in-plane shear strain fields agree with experimentally generated (DIC) strain fields by almost 90%.

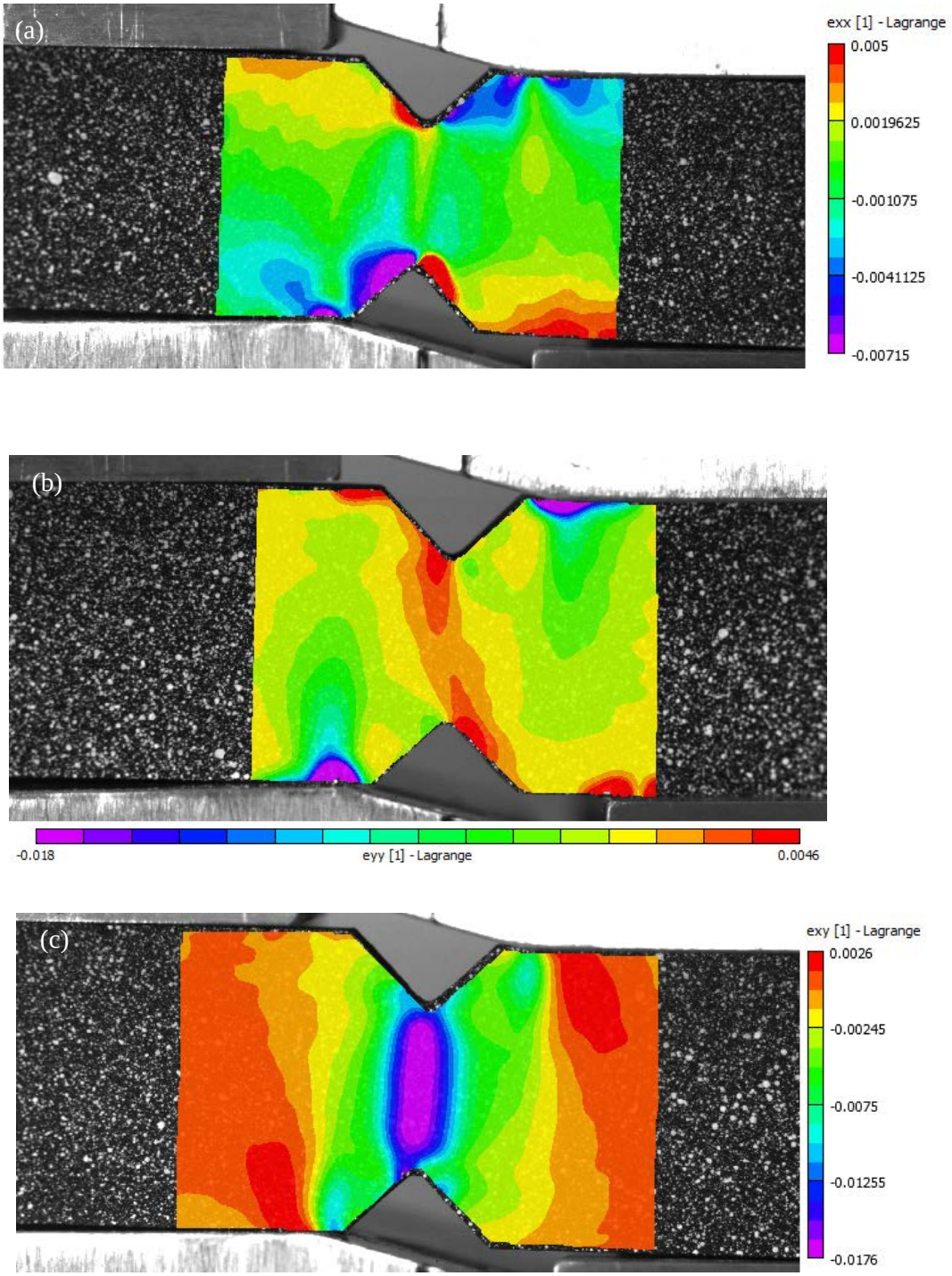

Figure 7-12. DIC in-plane strain field components, Equivalent longitudinal/transverse/shear strain maps, 0°/90° fibre orientation, (a) axial, (b) transverse, (c) shear strain.

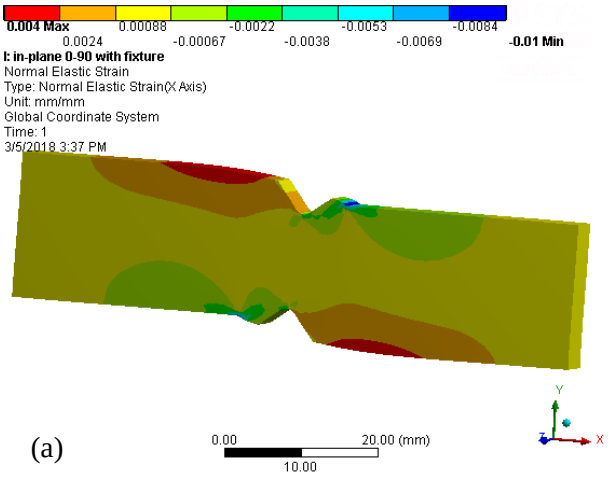

(a)

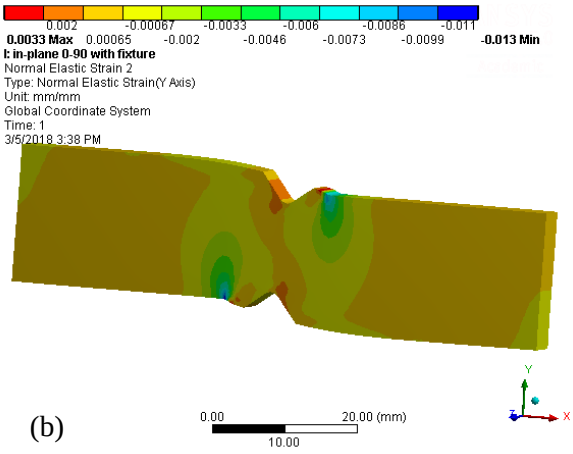

(b)

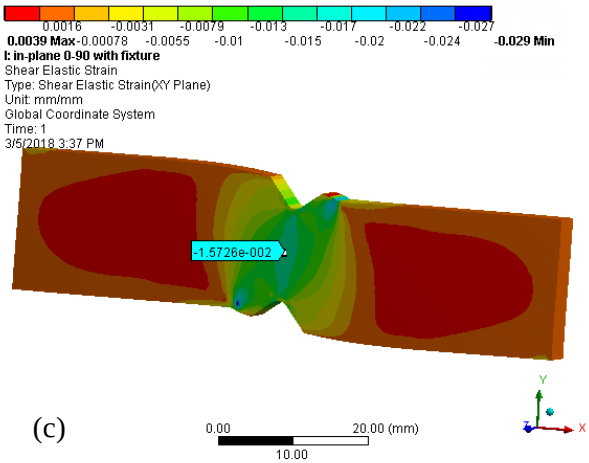

(c)

Figure 7-13. FEM (ANSYS) in-plane strain field components, Equivalent longitudinal/transverse/shear strain maps, 0°/90° fibre orientation, (a) axial, (b) transverse, (c) shear strain.

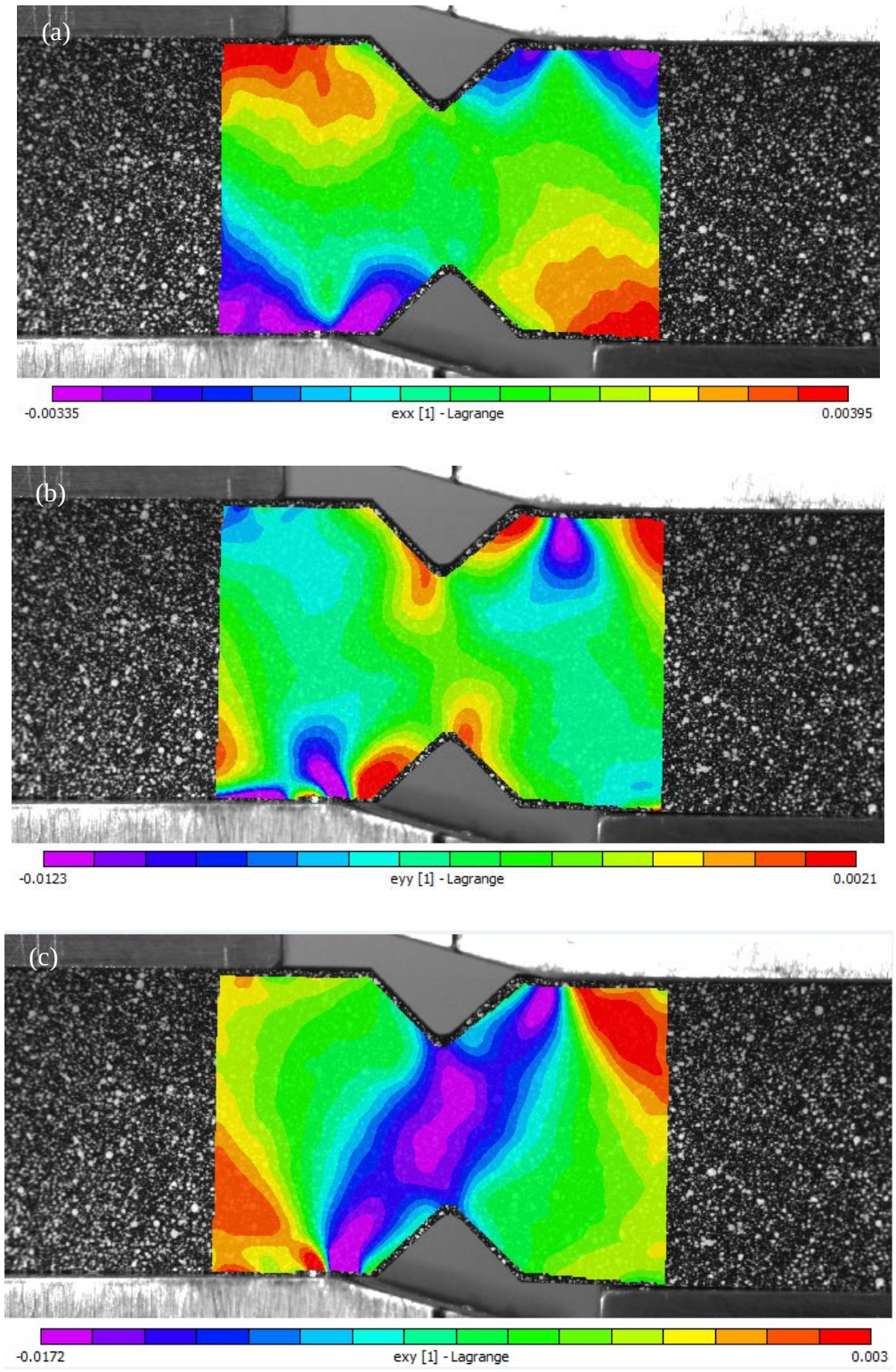

Figure 7-14. DIC in-plane strain field components, Equivalent longitudinal/transverse/shear strain maps, ±45° fibre orientation, (a) axial, (b) transverse, (c) shear strain.

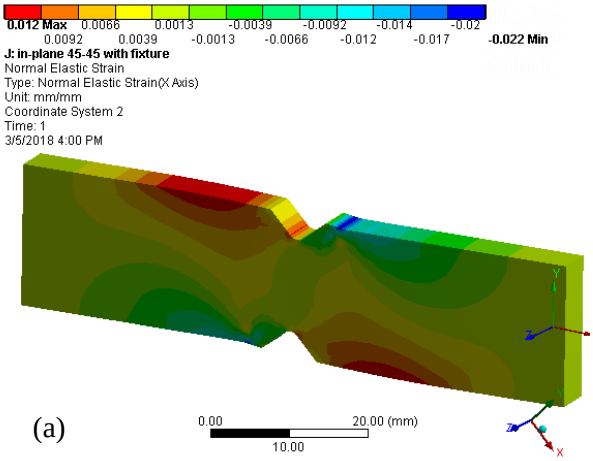

(a)

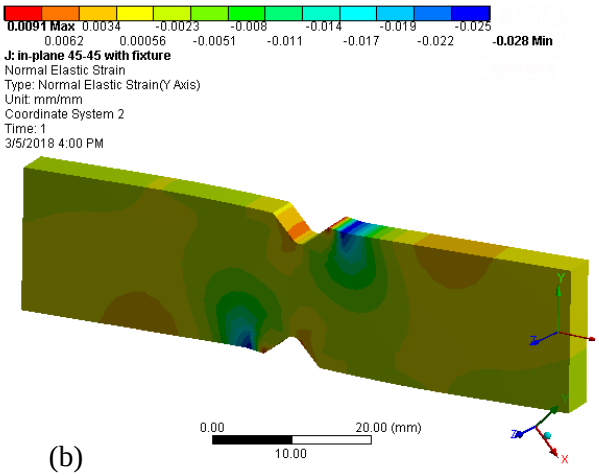

(b)

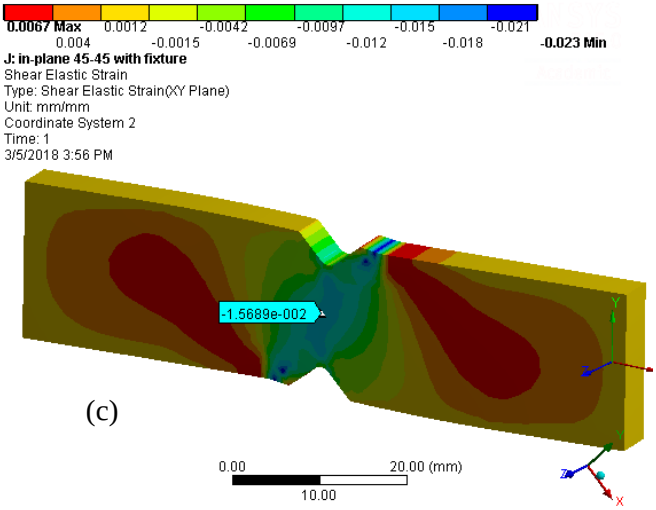

(c)

Figure 7-15. FEM (ANSYS) in-plane strain field components, Equivalent longitudinal/transverse/shear strain maps, ±45° fibre orientation, (a) axial, (b) transverse, (c) shear strain.

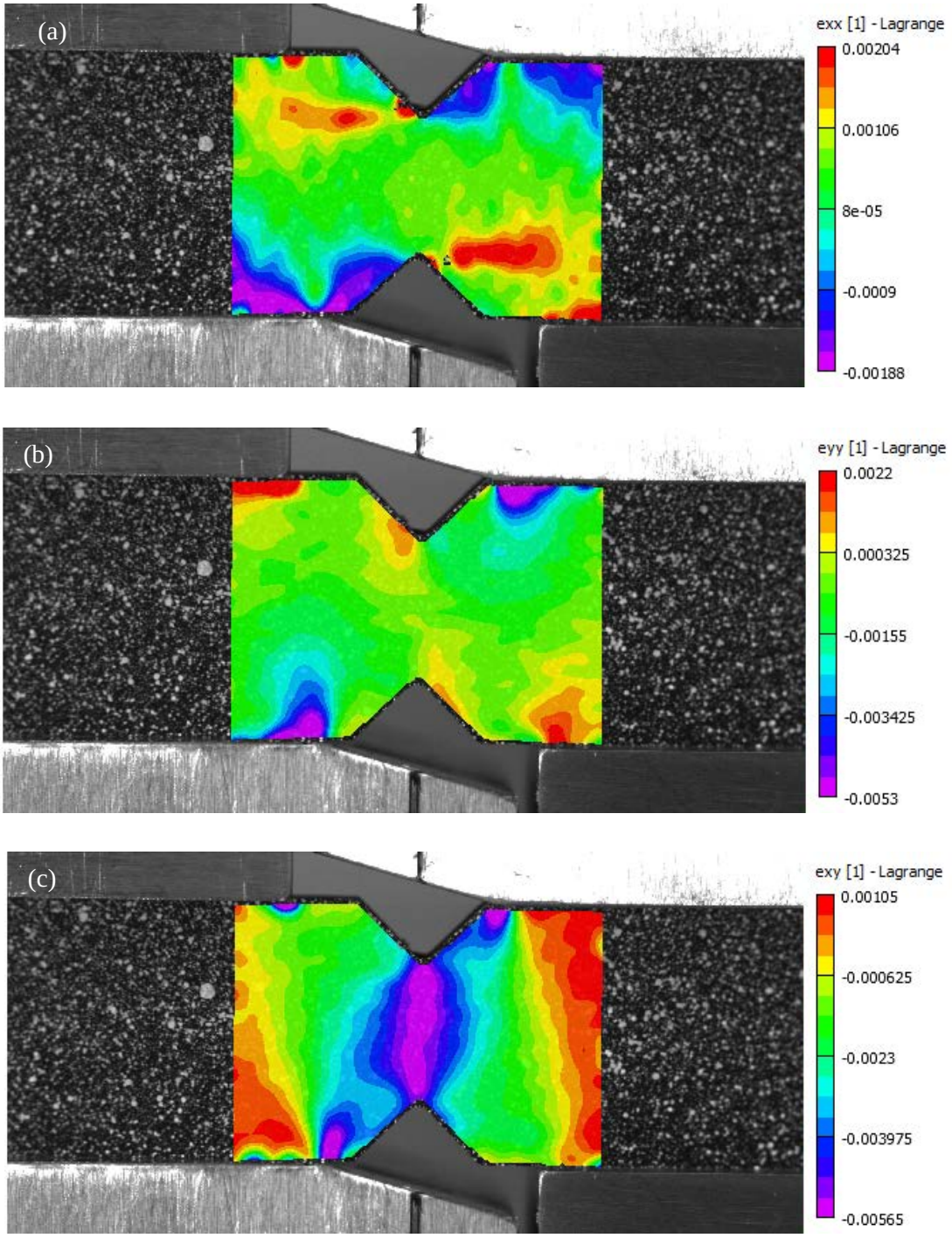

Figure 7-16. DIC inter-laminar strain field components. Equivalent longitudinal/transverse/shear strain maps, 0°/90° fibre orientation, (a) axial, (b) transverse, (c) shear strain.

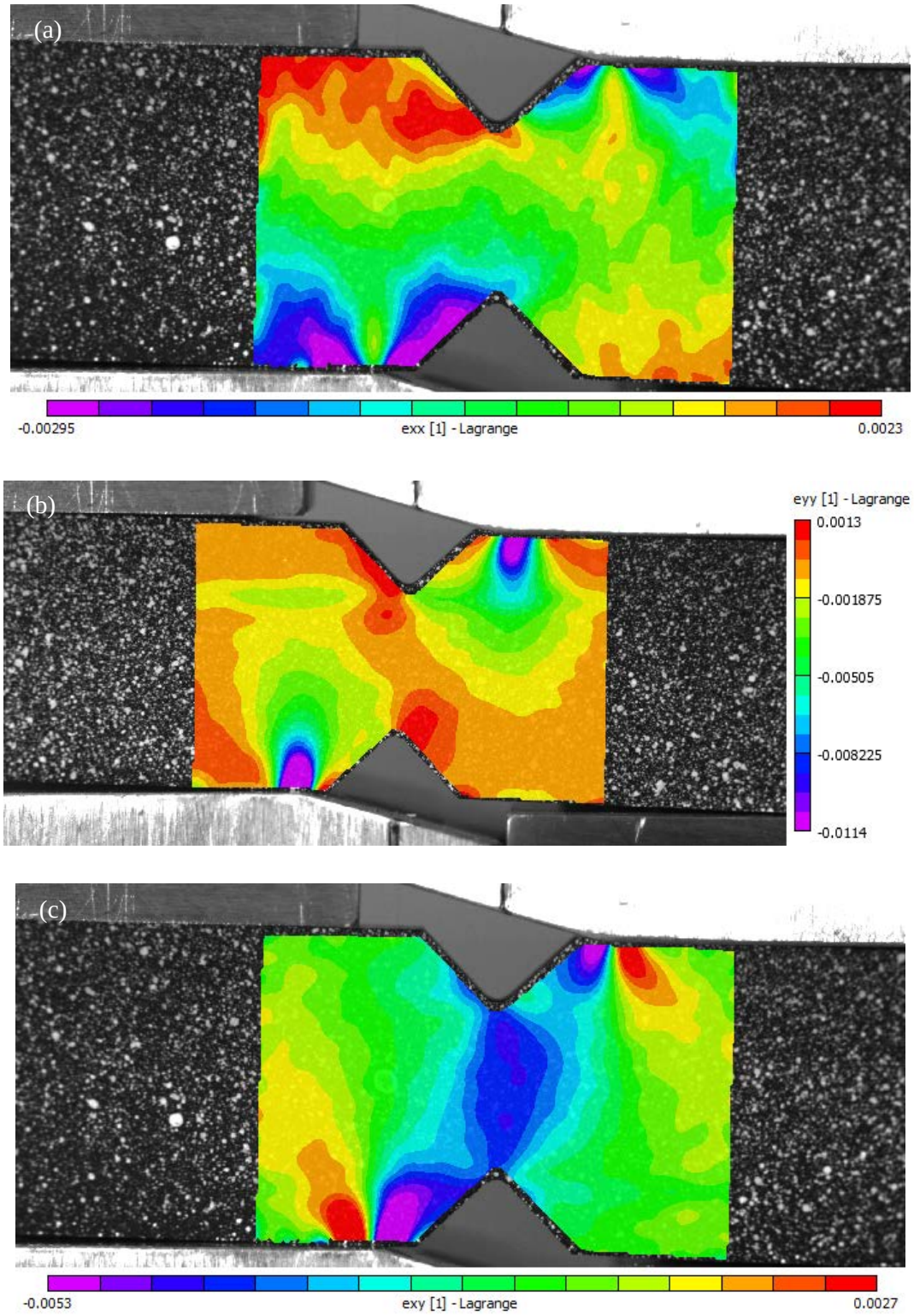

Figure 7-17. DIC inter-laminar strain field components. Equivalent longitudinal/transverse/shear strain maps, ±45° fibre orientation, (a) axial, (b) transverse, (c) shear strain.

From Figure 7-12 to Figure 7-17 it can be concluded that, the stacking sequence in the samples has an effect on the shear strain distribution. The shear strain field is non-symmetric for all fibre orientation and types of shear modes (inter-laminar and in-plane shear). From the DIC strain maps, strain concentration around the joining with the clamps is observed. Also shear strain is highest at the centre of the specimen. As expected for the composite specimen with $\pm 45°$ fibre orientation, the load conveyed by the clamp is re-distributed less than specimen with 0°/90° fibre orientation.

Comparing Figure 7-12 and Figure 7-14 it can be seen that the in–plane shear strain distribution in the area between the notch roots is less uniform when fibre orientation changes from 0°/90° to $\pm 45°$.

7.4.1. Inter-laminar and In-plane Shear Properties

The region between the two notches is ideally in a pure shear state and the shear stress–strain curves can be built using the shear strain data extracted from the image correlated system. The shear stress is determined from equation 7-1

$$\tau = \frac{F}{A} = \frac{F}{tw} \qquad \textbf{7-1}$$

Where A is the cross-sectional area between the roots of two V-notches, t is the thickness of sample, w in the distance between two notches and F is the applied load.

Figure 7-18 and Figure 7-19 show shear stress–strain data for both in-plane and inter-laminar shear specimens up to failure. One characteristic of these curves is the inflection between 10 and 20 MPa in inter-laminar shear testing regardless of fibre orientation. This knee was due to the failure of the transverse layers in the cross-ply laminates. Redistribution of stress between longitudinal fibres and matrix occurred leading to an increased shear stress.

From the shear stress–strain diagrams the modulus of elasticity was calculated at the initial portion of the curve. Table 7-3 shows the shear strength, the elastic shear modulus and the fibre orientation angle. In this table the shear modulus has been determined from the slope of the linear portion of shear stress-strain curve up to 0.005 strain level.

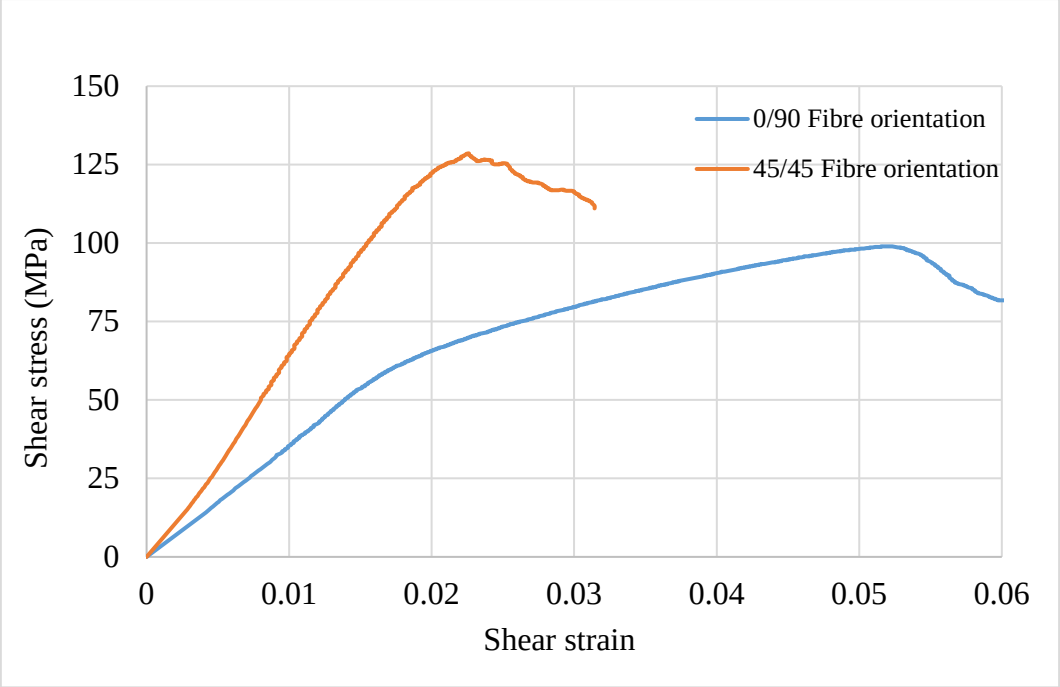

Figure 7-18. Effect of fibre orientation on in-plane shear stress-strain reaction.

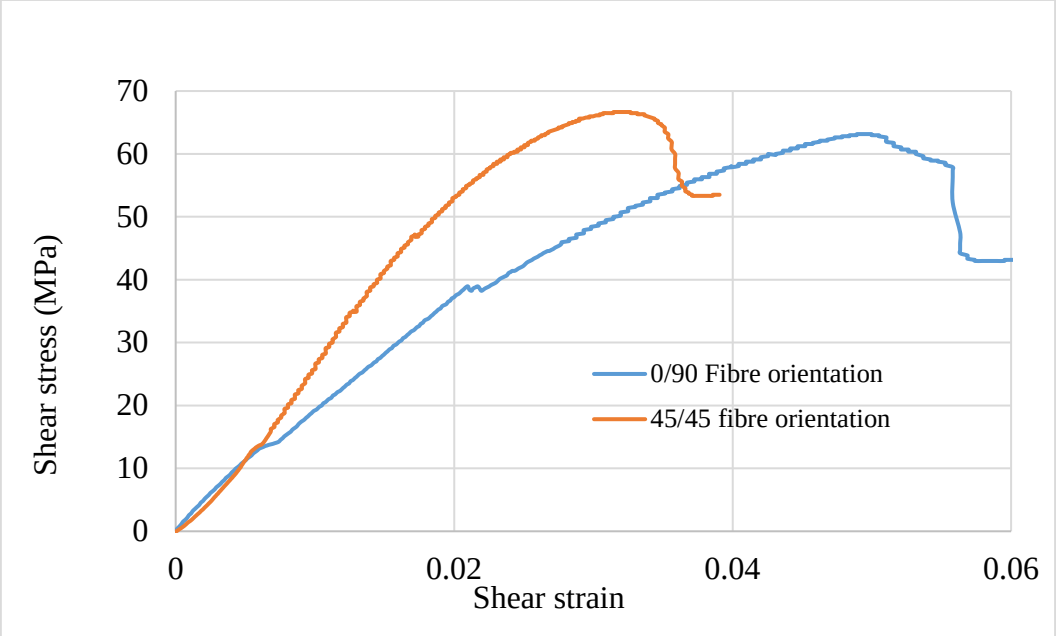

Figure 7-19. Effect of fibre orientation on inter-laminar shear stress-strain response of the composite.

Table 7-3. Shear properties of the composite.

	Fibre orientation	Shear strength (MPa)	Shear modulus (GPa)
In-plane	0°/90°	70±10	3.52±0.2
	±45°	110±10	6.00±0.3
Inter-laminar	0°/90°	45±10	2.22±0.15
	±45°	38±8	2±0.1

In the Iosipescu shear test, some investigators (Bhatnagar *et al.*, 1995) have considered the stress magnitude equivalent to the ultimate load as the shear strength while others (Morton *et al.*, 1992; Odegard and Kumosa, 1999) have considered the first load drop in stress-strain curves as the shear strength. Kashaba et al (Khashaba, 2004) defined the shear strength as the ratio of the load prior to the non-linear behaviour and the cross-sectional area . Regarding this work, shear stress-strain behaviour (Figure 7-18 and Figure 7-19) and DIC maps suggest the use of the latter definition of shear strength for in-plane shear testing.

For inter-laminar shear testing the first successive load drops (higher than the knee shape in Figure 7-19) in the stress-strain curves is considered. Delamination or inter-laminar shear cracking occurs at load levels lower than the ultimate load. The uncertainty about which strain should be used as the measure of the material property can be addressed by considering these failure criteria (indeed the first successive load drops after the knee shape in the inter-laminar shear stress-strain curves corresponds to the onset of delamination). The inter-laminar shear stiffness decreases slowly in a non-linear manner even after the beginning of delamination (Figure 7-19).

It must be noted that failure of the specimen can occur at the notch tip region due to the stress concentration caused by the notch geometry, material inhomogeneity and discontinuity at the free edges of the notches. In specimens with 0°/90° and ±45° fibre orientation, the inter-laminar shear stress–strain behaviour is moderately linear up to about 0.0053% and 0.0048% of shear strain respectively, where the knee shape was observed. By increasing the load, successive load drops were seen until fracture. This is caused by crushing at the inner loading points due to the stress concentration and/or crack initiation/propagation around the notch roots.

In general, the absence of reinforcement in the thickness direction results in lower inter-laminar shear strength compared to the in-plane shear strength. Therefore the composite laminates are susceptible to delamination.

The maximum in-plane shear strength is found for the specimen with 45° off-axis angle, i.e. [45/−45]. On the other hand specimens with 0° and 90° fibre orientation have the minimum in-plane shear strength. Conversely the maximum inter-laminar shear strength is found for samples with 0°/90° fibre alignment. On the other hand specimens with 45° off-axis angles have the minimum inter-laminar shear strength.

7.4.2. Strain distribution on the area between two notches

Using DIC method and FE calculations it is possible to analyse the distribution of the in-plane shear strains on the segment between two V-notches. The distribution of in-plane shear strain over the area measured by the DIC has identical shape as the curve achieved by FE model (Figure 7-20) but the experimental measurement are about 10% higher.

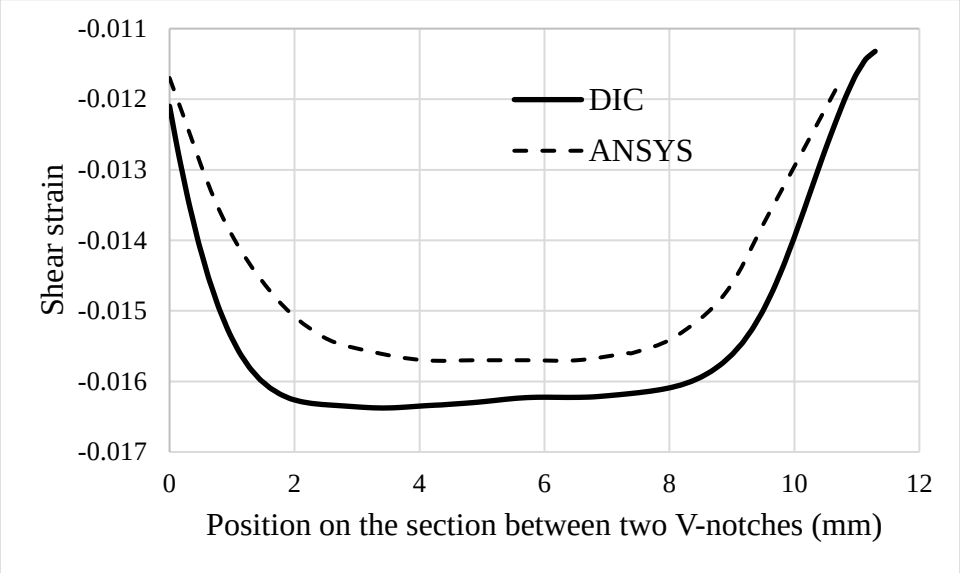

Figure 7-20. Distribution of in-plane shear strain on the section between the two V-notches, 0°/90° fibre orientation.

These figures indicate that in-plane shear strain reaches a maximum in the middle of the sample between the notches and it decreases when approaching the root of the notches. The shear strain is fairly uniform across 60% of the sample width between the two notches.

7.4.3. Mode of Failure in Iosipescu Shear Samples

All the curves have similar shape in the early stage of (Figure 7-18 and Figure 7-19). Just beyond this relative limit, they became non-linear because of the build-up of resin cracks. With increasing load the deviation from linearity increases as a result of crack growth along the fibre direction and failure of some fibres in the transverse direction. Beyond this point, the resistance

to pull-out of fibres and fibre bundles maintained all the applied loads. Observable large cracks were seen between the notches. In-plane shear specimens with 0°/90° and ±45° off-axis angles failed due to pure shear stress between the roots of the notches as shear cracks parallel to the loading direction that connected the two roots of the V-notches were detected. The cracks in the out-of-plane shear specimens with 0°/90° and ±45 off-axis angles were initiated at the roots of the V notches. With increasing load more cracks occurred around the notches instead of the central area making it impossible to measure the in-plane and inter-laminar shear strength when the measurement is based on the ultimate load. Therefore the proposed failure criterion in this work, the maximum load just prior to the nonlinear behaviour (in-plane shear strength) and the first load drop higher than knee shape in load-displacement curve (inter-laminar shear strength) may be useful in calculating the shear strength of the tested composite material.

7.5. Short Beam Shear (SBS) Testing

In this section, a methodology is developed for evaluation of inter-laminar shear behaviour of GFRP composites. This method is based on a combination of exact solution, FE analysis for stress calculation and the DIC technique for full-field strain measurement.

To further verify the accuracy of the inter-laminar shear tests, a total of 5 short beam shear specimens were tested following the ASTM standard D-2344 guidelines (Standard, 2010).

In a short beam shear test, a specimen with a low span-to-thickness ratio (typically 6) is loaded in three-point bending configuration so that an inter-laminar shear failure occurs. The maximum shear stress is

$$\tau_{max} = 0.75\frac{P}{A} \qquad \textbf{7-2}$$

Where *A* is the cross sectional area.

As shown in Figure 7-21 the short beam shear specimen is loaded similar to the 3PB test discussed earlier. The short beam specimens are 5 mm thick and 5 mm wide. The specimen length is 45 mm and the support length is 30 mm. The short beam specimens were loaded to failure at 2 mm/min cross-head displacement rate in the transverse material direction.

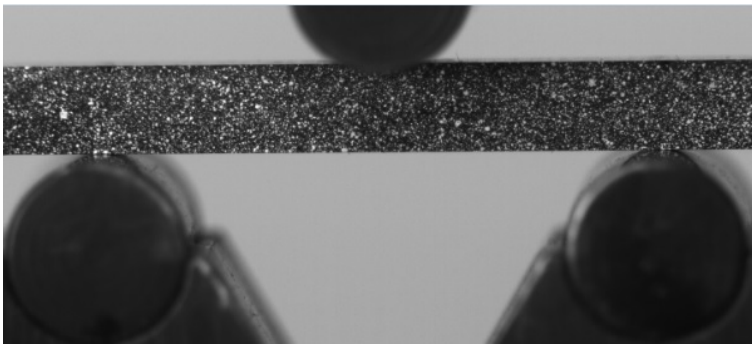

Figure 7-21. Loading conditions for a short beam specimen in inter-laminar shear test

7.5.1. Exact Analytical Solution of SBS test

Given the equations (3-3, 3-4 and 3-14) the matrix of reduced stiffness and bending stiffness are calculated as below:

$$Q = \begin{bmatrix} 23.04 & 5.76 & 0 \\ 5.76 & 23.04 & 0 \\ 0 & 0 & 3.52 \end{bmatrix}$$

$$D = \begin{bmatrix} 240 & 60 & 0 \\ 60 & 240 & 0 \\ 0 & 0 & 36.66 \end{bmatrix} \quad , \quad D^{-1} = \begin{bmatrix} 0.0044 & -0.0011 & 0 \\ -0.0011 & 0.0044 & 0 \\ 0 & 0 & 0.02727 \end{bmatrix}$$

From equation (3-20), the inter-laminar shear stress at the load of 475 (N) is calculated as below:

$$\sigma_{(y,z)}^{(k=1-24)} = \frac{-F}{2b} \times ((23.04 \times 0.0044) + (5.76 \times (-0.0011)) + (0 \times 0)) \times (\frac{(y^2 - y_k^2}{2})$$

Where F = 475 N, b = 5 mm

$$\sigma_{(y,z)}^{(k)} = 2.26 \times (6.25\text{-}y_k^2).$$

Figure 7-22 shows that there is close agreement between FE and closed form results of inert-laminar shear test specimen. The experimentally generated strain field is shown in (Figure 7-23).

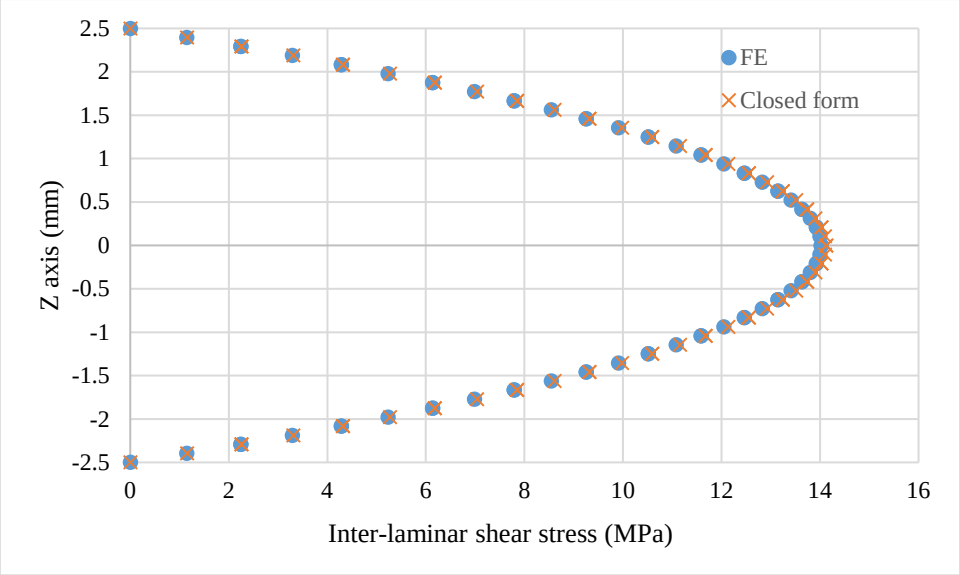

Figure 7-22. Variations of inter-laminar shear stress through layers and laminate thickness (lateral view) at x= L/4 from the centre of sample (load at the centre=475 N). Comparison has been made between overlapping numerical and analytical data.

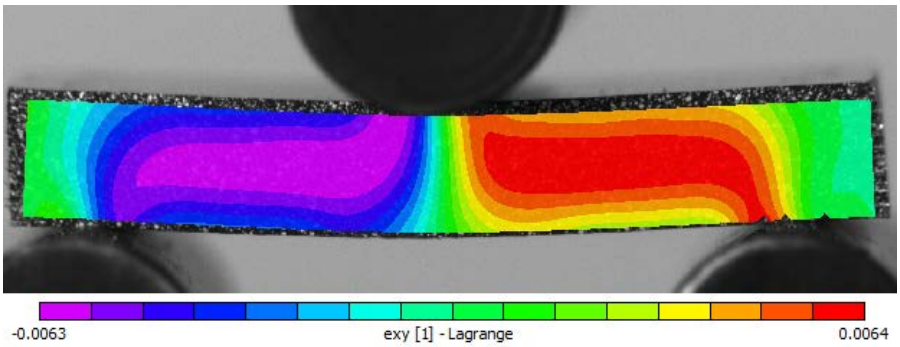

Figure 7-23. Characteristic shear strain distributions from DIC corresponding to the knee shape in inter-laminar shear stress-strain curve (Figure 7-19). (0/90 fibre orientation).

In this chapter a combination of DIC, closed form and FE analysis have been used to generate validated modelling data and approaches for static analysis of composite tidal turbine blades. The next chapter discusses the acquisition of durability data necessary for blade life calculations.

7.6. Summary

Full field strain map results of the GFRP composite subjected to the static tension, 3PB and shear show that the composite laminates have an inherent heterogeneous mechanical behaviour from the start of load application.

A method for precise evaluation of tensile, (in-plane) shear and bending stress– strain responses of GFRP composite materials is established in this work using the dog-bone, parallel sided and V-notched beam test specimens. The methodology is established on an integration of a finite element method for strain prediction and a digital image correlated system for strain assessment. Based on the surface strain components experimentally-generated strain fields reasonably agree with the FE-predicted strain maps. This work exhibits a suitable arrangement of DIC and FEM in the field of characterizing and evaluating composite material. The incorporation of full-field topographies of finite element and image correlated methods not only increases the precision of composite properties but also create a chance to obtain composite properties from experiments where a simple stress-strain estimate is not valid.

Results from the investigation of the effect of fibre orientation on tension, bending and In-plane Iosipescue shear testing show also that; the strength of GFRP composite is minimum for specimens with 45° off-axis angles. On the other hand specimens with 0°/90° fibre orientation have the maximum strength. However, the maximum inter-laminar shear strength is found for samples with 0°/90° fibre alignment and samples with 45° off-axis angles have the minimum inter-laminar shear strength.

Chapter 8
Durability and Fatigue Tests

8. Durability and Fatigue Tests of GFRP

With reference to the methodology of fatigue life prediction in chapter 3, Figure 3-1, the main objective of the present study is to evaluate environmentally affected fatigue behaviour of GFRP composites. This has been done in this work by designing a 3PB fatigue rig capable of applying cyclic bending loads on multiple composite samples while exposed to sea water. The main advantage of the fatigue test used in this project is that the composite blade performance under bending loads (i.e. thrust load from tidal current) in sea water is approximated using the design of fatigue rig. Since composite tidal turbine blades are subjected to harsh sea water conditions, a fatigue test rig was designed to emulate the blade environment. Therefore, realistic sea water affected fatigue data points (i.e. strain-life diagram) required for FE prediction of the blade, can be provided. This can inform the choice of the design safety factor which engineers need to consider for designing and manufacturing tidal turbine blades.

The fatigue performance of highly stressed composite components such as tidal turbine blades is highly dependent on the shape of the S-N curve of the composite, meaning that a steeper S-N curve indicates that the fatigue life of a composite component is lower compared to a composite component with a flatter S-N curve.

In this chapter, initially the S-N curves required for FE analysis of blade are generated in air and sea water, then the effect of sea water on fatigue performance of the composite is investigated using failure analysis techniques. Sea water affects the S-N curve in a regime of stress and environment dependence (high cycle fatigue) and a regime of stress dependence and environment independence (low cycle fatigue). Therefore another design challenge for engineers regarding a criterion for fatigue behaviour of composite blade in which regime the blade may operate in can be addressed.

A wide range of failure analysis techniques including DIC and SEM/EDX have been used to determine fatigue failure mechanisms. In addition, stiffness degradation (modulus decay) was used as an index for damage development and subsequently the main fatigue failure modes corresponding to stiffness degradation curves were identified. The major fatigue failure mechanism and its effect on fatigue life of GFRP composite was determined. Therefore the effect of this failure mode on the full composite blade in the context of fatigue life also can be assessed. As a result, fatigue performance limiting issues can be realized and confidence can be obtained in using a GFRP composite for tidal turbine applications.

In the following sections results of fatigue/durability testing and characterization techniques for determining fatigue failure modes are reported.

8.1. Durability Testing

8.1.1. 3PB Tests

The mechanical properties of as received GFRP specimens and those of specimens immersed in sea water and distilled water were determined. Figure 8-1 and Figure 8-2 show the flexural elastic modulus and flexural strength as a function of immersion time.

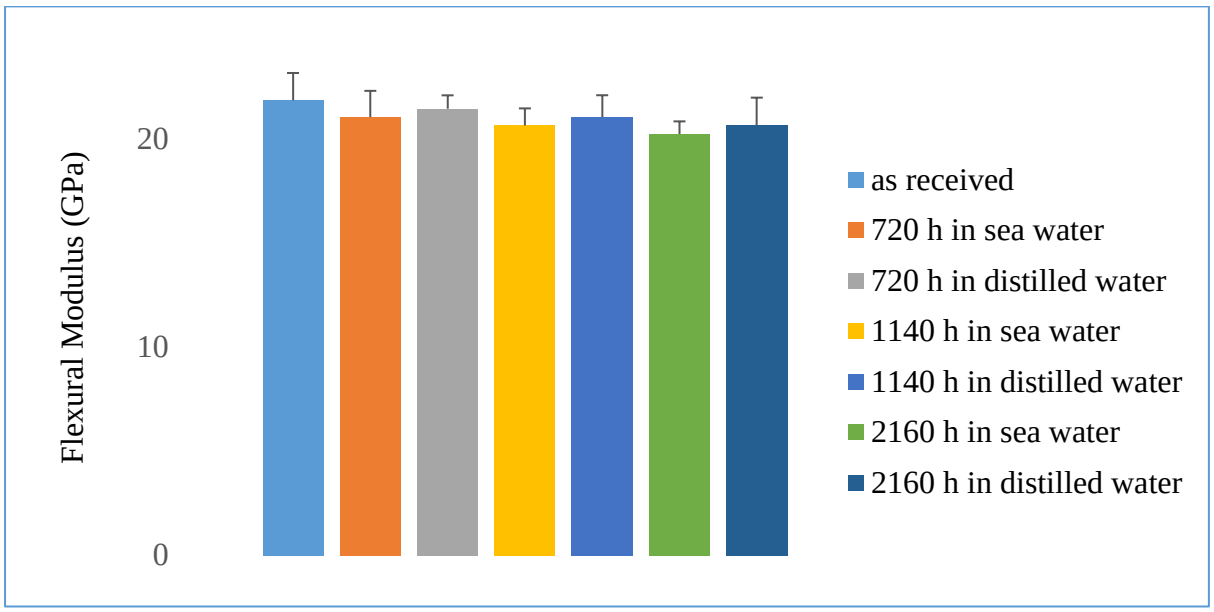

Figure 8-1. Bending elastic modulus of composite specimens before and after immersion.

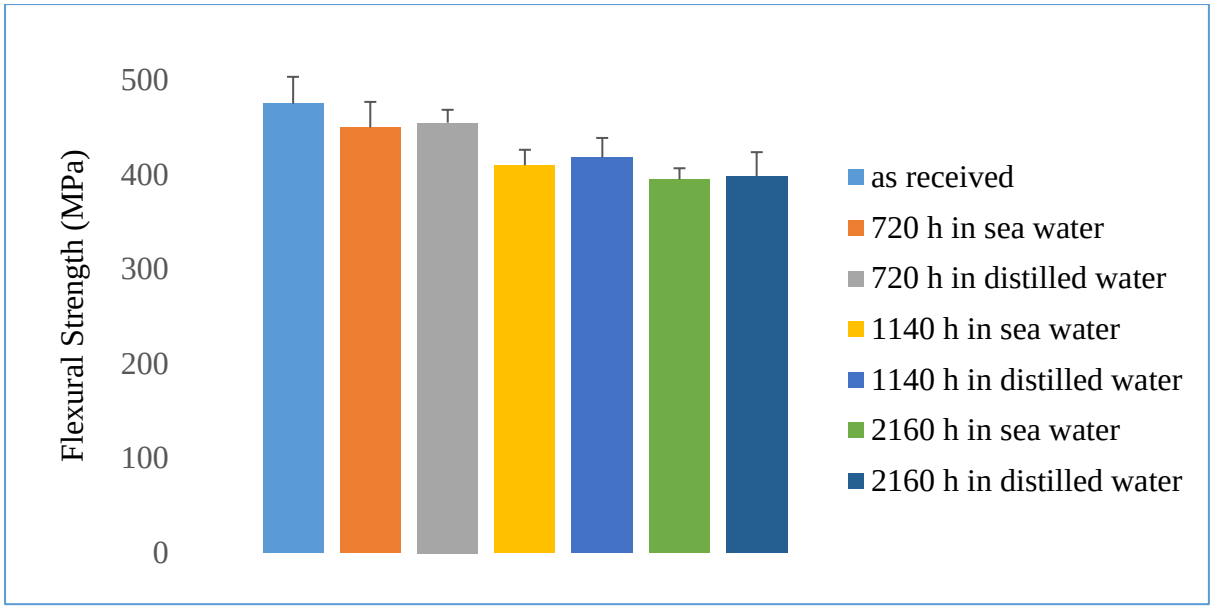

Figure 8-2. Bending strength of composite specimens before and after immersion.

Figure 8-1 shows that the immersion of samples in either sea water or distilled water has little effect on the bending elastic modulus. The bending strength after immersion showed some amount of degradation. The bending strength for samples held in sea water and distilled water after 2160 hours showed a decrease of 16% and 14%, respectively, relative to those specimens that were not immersed.

These results are in good agreement with data from previous investigations (Liao *et al.*, 1999a) on the environmental effect on composites where degradation of bending strength of composite samples was reported (Romanenkov, 1967; Bonniau and Bunsell, 1981; Martin and Gardner, 1981; Apicella *et al.*, 1982; Garg and Paliwal, 1982; Garg and Pawar, 1982; Rege and Lakkad, 1983; Sekine *et al.*, 1988; Komai *et al.*, 1991; am E Grami *et al.*, 1995; Bradley *et al.*, 1995). The degradation of strength in the environmentally affected specimens is related to degradation of three constituents: the glass fibres, the fibre/matrix interphase region, and the matrix (Schmitz and Metcalfe, 1966; Metcalfe and Schmitz, 1972; Vauthier *et al.*, 1995).

Macroscopic failure mechanisms under bending for the as-received samples and samples immersed in sea water at room temperature are similar to each other. The failure under bending commences with the formation of transverse resin cracks on the tension side (the bottom surface of the test specimen), followed by failure of the transverse and longitudinal bundles of fibres. Propagation of longitudinal cracks also occurs between bundles of fibres and the layers of fibre mats.

8.1.2. Water Intake

The amount of fluid (sea water and deionized water) absorbed by samples during immersion was measured by mass change. Representative results are shown in Figure 8-3. All of the tests were carried out at 21℃.

The absorption performance in the two fluids (i.e., sea water, distilled water) occurred as below: an initial weight gain can be seen but saturation did not occur after extended immersion. The mass increase in the material is influenced by the type of environment and concentration of the environment, however there is little or no difference between distilled water and sea water. For example, the average mass increase after 2160 hours immersion in sea water and distilled water are 0.4% and 0.41%, respectively.

The majority of the water ingress and water absorption occur at the cut faces/ends of the test samples where penetration along fibre/matrix boundaries is easiest. The shape of the mass gain curves in Figure 8-3 confirmed that the rate of diffusion of water into the composite limits uptake.

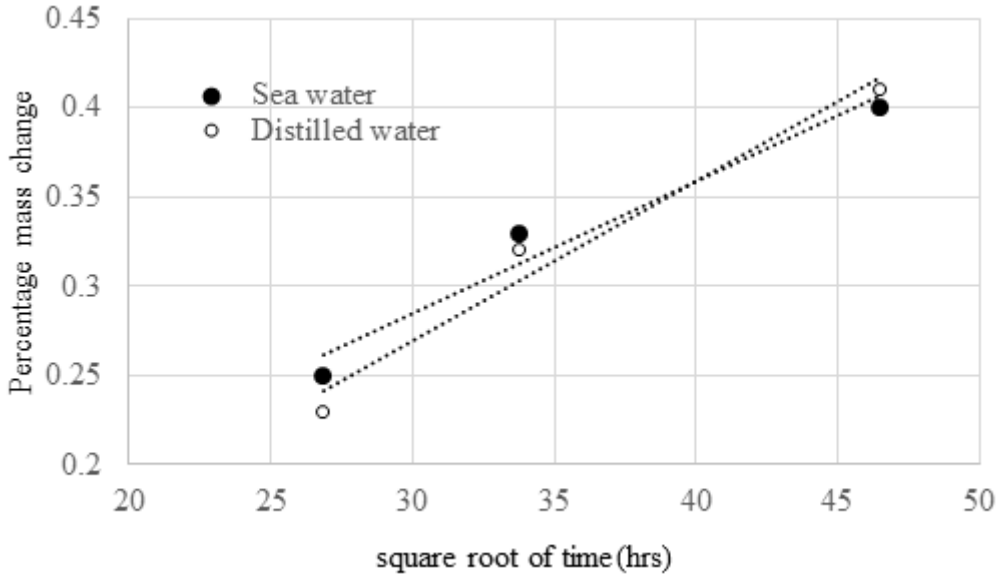

Figure 8-3. Mass change for the samples immersed in sea water and distilled water. Hollow symbols signify absorption data taken from samples immersed in distilled water while filled symbols represent absorption data taken from samples immersed in sea water (where the ordinate is the exposure time).

8.2. Three Point Bending Fatigue Tests

8.2.1. Strain-Life Diagrams

Strain-life diagrams were obtained for the GFRP in air and sea water at seven strain levels with five samples per level. In this study a power law equation (8-1) between maximum initial strain ($\varepsilon_{max,i}$) and fatigue life were found to be a good fit for the experimental data.

$$\varepsilon_{\max,\ i} = K(logN_f)^{-A} \qquad \textbf{8-1}$$

where N_f is the number of cycles that material can sustain before it fails, *K* and *A* are constants. These constants can be determined by fitting equation (8-1) to the data.

The fatigue test results for GFRP along with the corresponding fits, as per equation 8-1 are shown in Figure 8-4. Comparing the Strain-Life curves obtained in air and sea water reveals that sea water reduces fatigue life. It is clear that for GFRP at a particular cyclic strain level, the fatigue life in air is longer than in sea water.

As it can be seen in Figure 8-4, fatigue data points can be classified into two different regimes, a regime dependent on test environment, and a regime independent of test environment. For the samples tested at high strain levels, fatigue data points are almost overlapping, so low cycle fatigue can be categorized as environment-independent. A substantial difference in fatigue data points can be observed for the specimens tested at lower strain levels (strain $<$ 1.2%). For example at strain level of about 0.6%, samples tested in air, lasted longer cycles approximately 10^7, while specimens tested in sea water failed within about 10^6 cycles, consequently high cycle fatigue can be classified as environment dependent.

In Figure 8-4, as expected, the number of cycles to failure increases when the maximum fatigue strain level decreases. Damage initiates in the compression and tension sides close to a transverse bundle of fibres. Damage can be observed on the samples in the form of stress whitening which is due to matrix crazing. At elevated strain level the damage propagated through the thickness and finally failure on both tension and compression sides occurred. Usually during the fatigue testing tensile matrix cracking is one of the most important failure mechanisms that is apparent in the developing damage zone.

The power law coefficients determined by fitting the experimental data using the least-squares method are also shown in Figure 8-4. For prediction of the fatigue life of the composites under strain levels outside the testing range, equation 8-1 was used. The regression fitting parameter (*A*) is 0.84 and 0.88 for GFRP in air and sea water indicating the strength loss per decade of

cycles of the materials. The loss in strength per decade, is higher for GFRP composites when tests are performed in sea water.

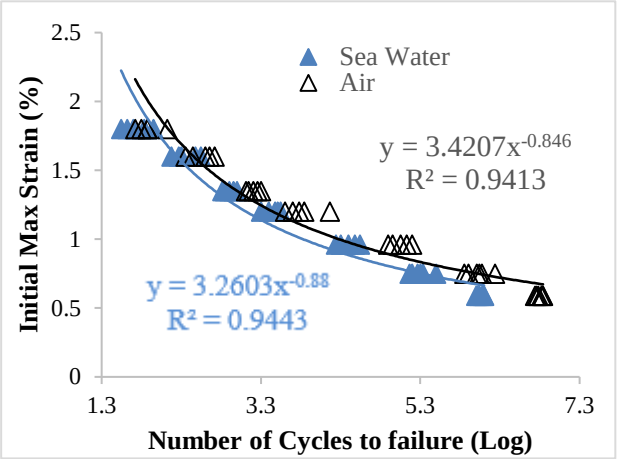

Figure 8-4. Strain –Number of cycles to failure curve.

8.2.2. Goodman Diagram

Strain or stress-life diagrams are generally built for tension-compression fatigue testing, however when the materials are under fatigue loading with a non-zero mean stress, the safe and unsafe regions regarding fatigue failure can be visualized in the form of a Goodman diagram. In the Goodman diagram, the abscissa represents the mean value of stress and the ordinate corresponds to the amplitude of stress. When the mean value is zero, the safe stress limit is identical to the endurance limit. When the stress amplitude is zero it is equivalent to the the static load case, so the safe limit is the ultimate flexural strength (UFS). In this study in order to build the Goodman diagram the endurance limit of the composite in both sea water and air were obtained by plotting a simple strain-life diagram (Figure 8-4), then the Goodman diagram (Figure 8-5) were constructed on the basis of a linear relationship between stress amplitude and mean stress and the value of UFS and endurance limit. The intersection of the lines with *x*-axis (mean stress) and *y*-axis (stress amplitude) are the UFS and the endurance limit, respectively. From this figure it is evident that below the lines are the safe areas in terms of fatigue failure. When the fatigue test is performed in sea water the safe area is reduced.

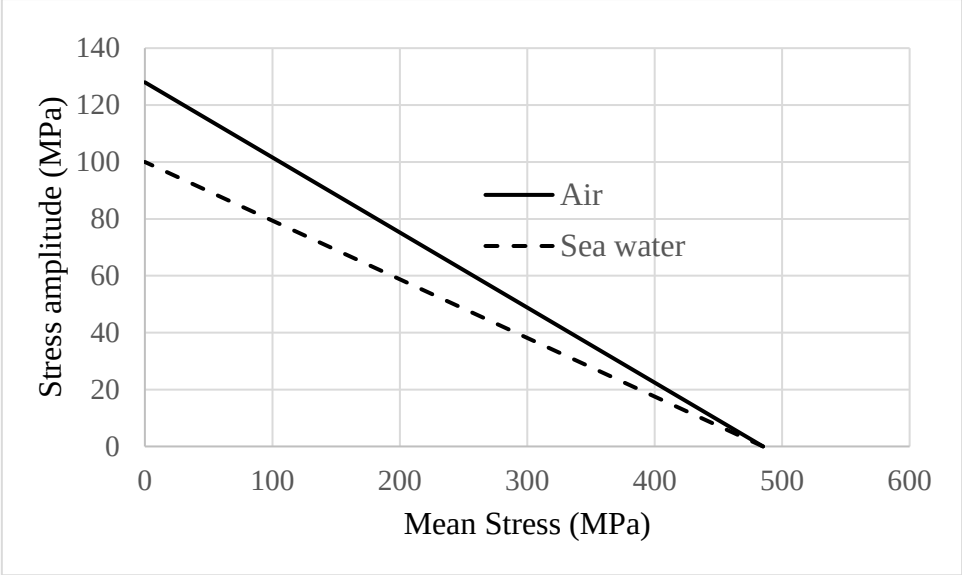

Figure 8-5. Goodman diagram showing safe and unsafe area for designing GFRP materials in terms of fatigue failure.

8.2.3. Effect of Carbon Fibres on Strain-Life Curves

In order to investigate the effect of increased stiffness of carbon fibres on bending fatigue behaviour of GFRP samples, GFRP composite samples containing carbon fibres were also subjected to bending fatigue test in both air and sea water condition. The composite material subjected to bending fatigue test is a multi-layered cross woven composite with an epoxy resin matrix reinforced with glass and carbon fibres. The composite is substantially glass fibre reinforced but it had additional carbon fibres in longitudinal direction between same plies (C-GFRP). Figure 8-6 shows the image from the top surface of C-GFRP before cutting for 3PB fatigue test. The green lines represent the bunch of carbon fibres which have an oval-shaped cross-sectional appearance. During the manufacturing process of woven glass/epoxy resin (GFRP), yarn of carbon fibres are placed between glass fabrics. This has been done in order to increase the stiffness of the composite in longitudinal direction. Performing tensile testing in the longitudinal direction (parallel to the unidirectional bundle of carbon fibres) of C-GFRP resulted in a tensile strength of 400 ± 10 (MPa) and a tensile elastic modulus of 26.5 ± 1 (GPa). Figure 8-7 shows the strain-life curve of C-GFRP obtained in the bending fatigue test in both air and sea water conditions. Comparing the power law equations of C-GFRP and GFRP in both air and sea water, indicates that placing unidirectional bundle of carbon fibres can increase the fatigue performance, and therefore using this composite can be an option of low cost candidate material for tidal turbine blades.

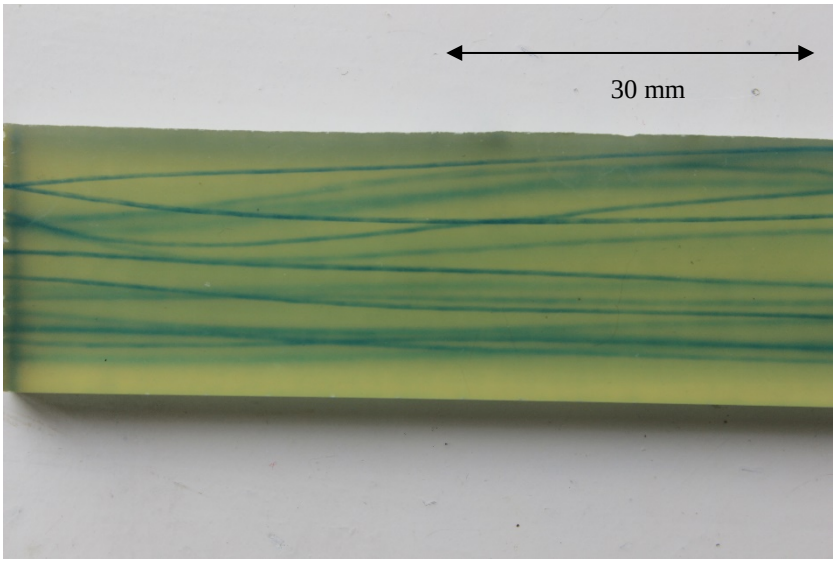

Figure 8-6. GFRP sample containing unidirectional bundle of carbon fibres (carbon fibre content is approximately 5%).

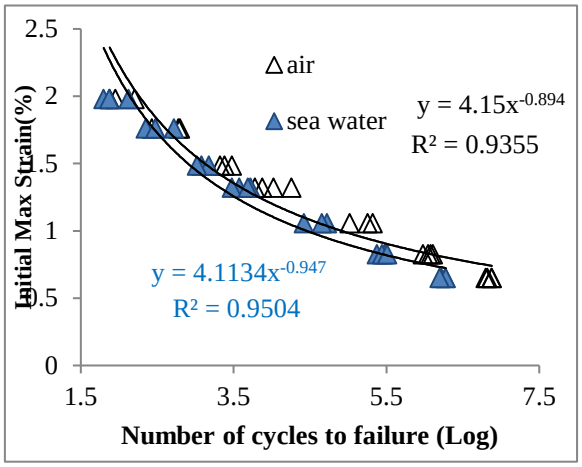

Figure 8-7. Strain –Number of cycles to failure curve.

8.2.4. Effect of Fibre Orientation on Strain-Life Curves

Similar to the work reported in section 6.2, the effect of anisotropy of the GFRP composite on fatigue behaviour was studied in this section. Two different fibre orientations (i.e. 0°/90° and ±45°) were subjected to the 3PB configuration of fatigue tests according to the standard test method specified by ES BN ISO13003 (Iso, 2003). Figure 8-8 shows the effect of fibre orientation on strain-life diagram. Similar to the result of the static 3PBT which showed reduced mechanical properties of the samples with ±45° fibre orientation, reduced fatigue life of the samples with ±45° fibre orientation was recorded. The fatigue properties of these

samples are dominated by the mechanical properties of polymer matrix rather than fibre reinforcements.

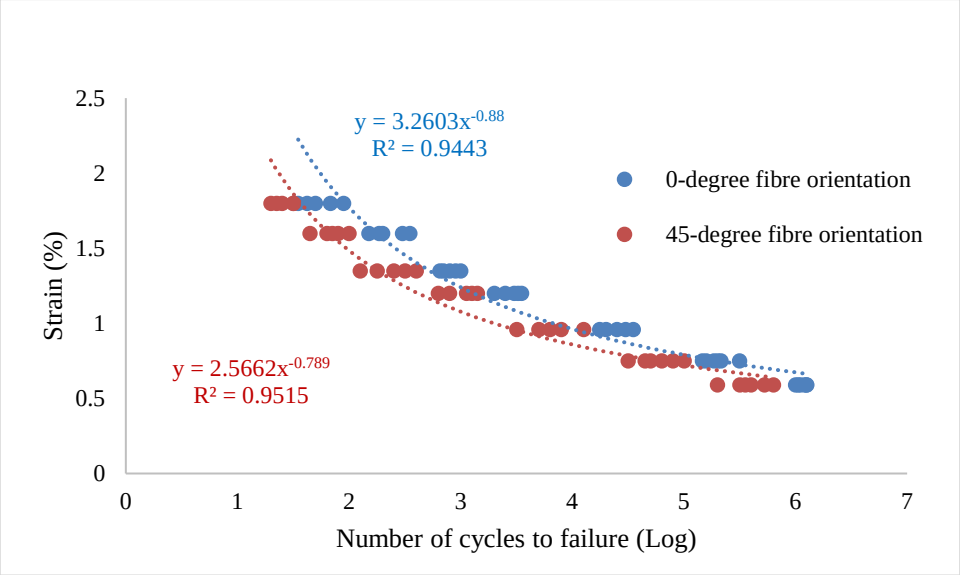

Figure 8-8. S-N curve of GFRP composite under different strain level in sea water.

8.2.5. Size Effect

In order to study the size effect on the fatigue results, two different thicknesses of test coupons (i.e. parallel sided test specimens with dimensions of 150mm×15mm×5mm and 150mm×15mm×6mm) were selected and subjected to 3PB fatigue tests. Although static mechanical testing (i.e. tensile and 3PB tests) of thicker samples showed superior mechanical properties compared to the thinner ones, the fatigue performance of thicker composites has not changed significantly except at low cycle conditions (Figure 8-9). Microscopic observation of the failure mechanisms on the fracture surface of failed composite samples revealed that the failure is due to the effect of delamination. In thicker composite samples a higher amount of delamination was observed.

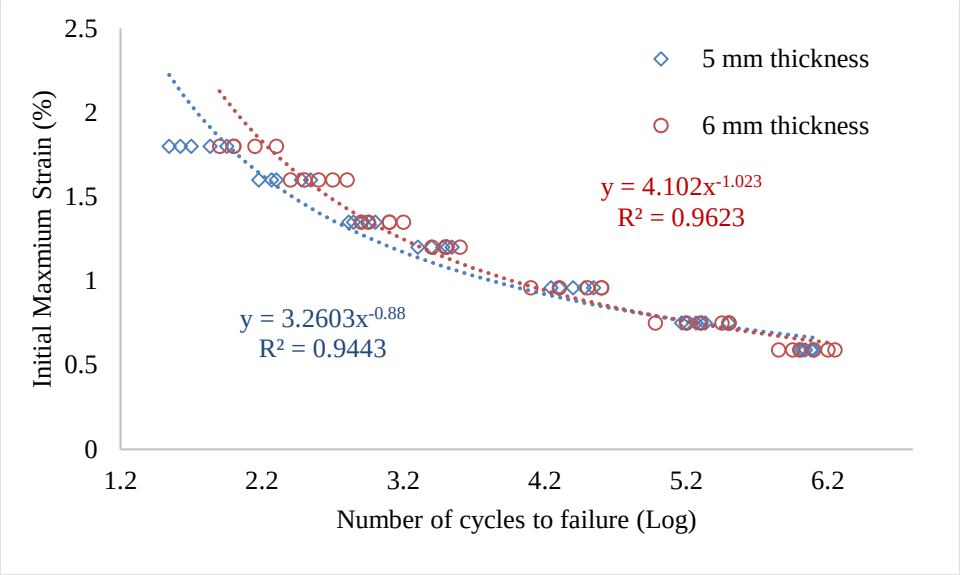

Figure 8-9. S-N curves of GFRP composite under different strain level in sea water. (For thicker sample the displacement was adjusted to get the same strain level).

8.3. Application of DIC in Fatigue

Most investigations of the fatigue of FRP composites reported in the literature were conducted using a tensile configuration, with less consideration to the fatigue behaviour under bending modes particularly in the case where the material is immersed in a fluid. The present investigation provides data for fatigue tests of specimens with sea water exposure. A large number of coupons were tested under the 3PB fatigue load configuration at various constant displacements in both sea water and air environment. Damage characterization and failure analysis were performed using the DIC method to identify the damaged zones on the test coupon surface and to track failure during the fatigue history. In order to characterize damage in GFRP composites, stiffness degradation has been monitored during the entire fatigue history. DIC results were used to determine the elastic modulus evolution associated with fatigue damage. Modulus decay gives evidence about damage localization and the gradual deterioration of mechanical properties of the composites during fatigue. A specific parameter is proposed for damage evaluation as a function of modulus decay. This parameter (stiffness degradation) is obtained using the DIC strain measurement system.

8.3.1. Fatigue Damage Evolution of GFRP Composite with DIC

In this section, a damage evaluation procedure based on the DIC technique, is presented. Fatigue damage development in GFRP composites under fatigue load using parallel sided

specimens is analyzed. Failure analysis based on the DIC methodology has been conducted to locate the damaged zones on the sample surface and to track failure modes during fatigue.

In this work, normal and shear strain were checked and observed in a number of 3PB coupons subjected to cyclic loads. Figure 8-10 shows an example of the random speckle pattern created using black and white spray paints on a sample with a delamination crack formed during fatigue testing.

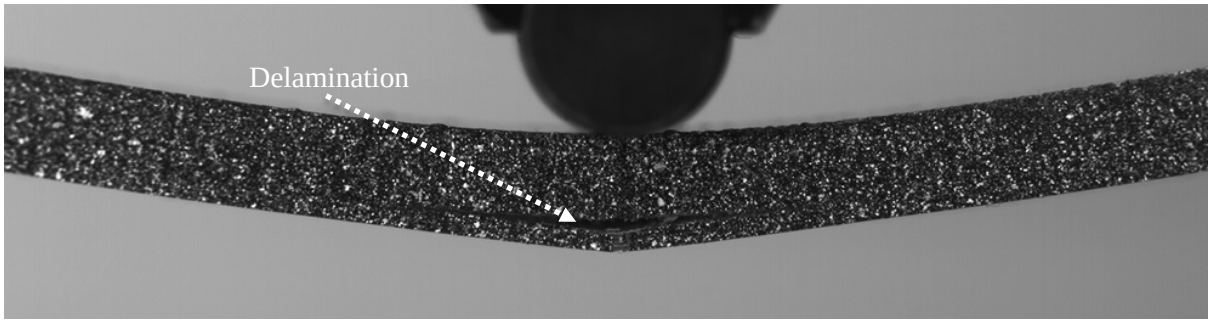

Figure 8-10. E-glass/epoxy three point bend fatigue test specimen failure at 5.5 million cycles in air.

Figure 8-11 and Figure 8-12 show results of strain analysis using a subset size of 33×33 pixels, corresponding to about 0.3 mm^2. Figure 8-11 and Figure 8-12 illustrate typical DIC analysis results for the surface strain components in the fatigue test of a cross-ply woven E-glass/ epoxy resin coupon, loaded in the x-z principal material plane, at a cyclic strain equal to 30% of the ultimate static strain in both, sea water and air respectively. The axial, transverse normal, and the shear strain components plotted in these figures are denoted as ε_{xx}, ε_{yy},and ε_{xy} respectively.

Figure 8-13 and Figure 8-14 show the normal engineering strain at different stages during the fatigue test. The maps shown in Figure 8-13 (e) and Figure 8-14 (e) have been captured at a stage in which delamination was visible on sample surface.

An increase in the flexural normal strain can be detected during the initial 90% of fatigue life in sea water and air conditions respectively, and a rapid and strong increase of the flexural normal strain happens shortly before the onset of delamination. A possible cause for this response is the increase in the non-observable damage accumulation in the epoxy resin prior to the noticeable cracking.

From Figure 8-13 and Figure 8-14, it is possible to identify that the damage phenomena are concentrated first in the central region near the tension and compression sides of the specimen (starting from the beginning of the sample lifetime) and progressively develop creating a concentrated damage region of the composite specimen. The fatigue specimens tested in air fail in tension while for samples tested in sea water, the failure modes are tension and compression suggesting that there may be a stress corrosion mechanism involved (Price and Hull, 1983).

It must be noted that using DIC system, the state of damage development can be assessed by tracking the strain evolution as the DIC can contribute to map the strain distribution during the different stages of fatigue life. In other words, strain localization maps showing strain evolution are recorded using DIC technique and this is done in order to analyse the damage development during the whole fatigue history of GFRP composite.

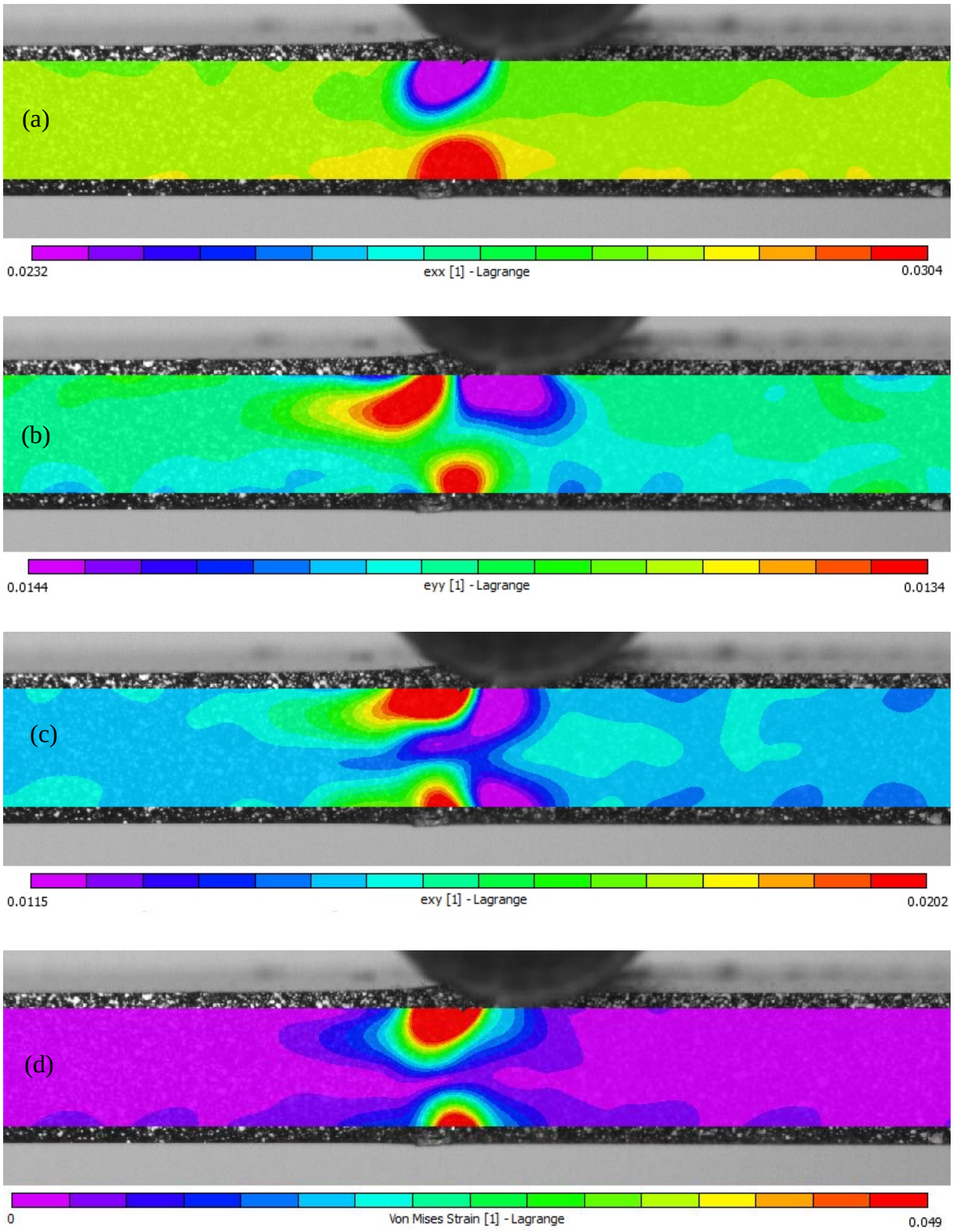

Figure 8-11. Strain components for a 3PB fatigue test (sea water) at peak cyclic strain equivalent to 30% of ultimate static strain and 1.300 million cycles. (a) Longitudinal strain, (b) transverse strain, (c) shear strain in x-y plane, (d) Von Mises strain.

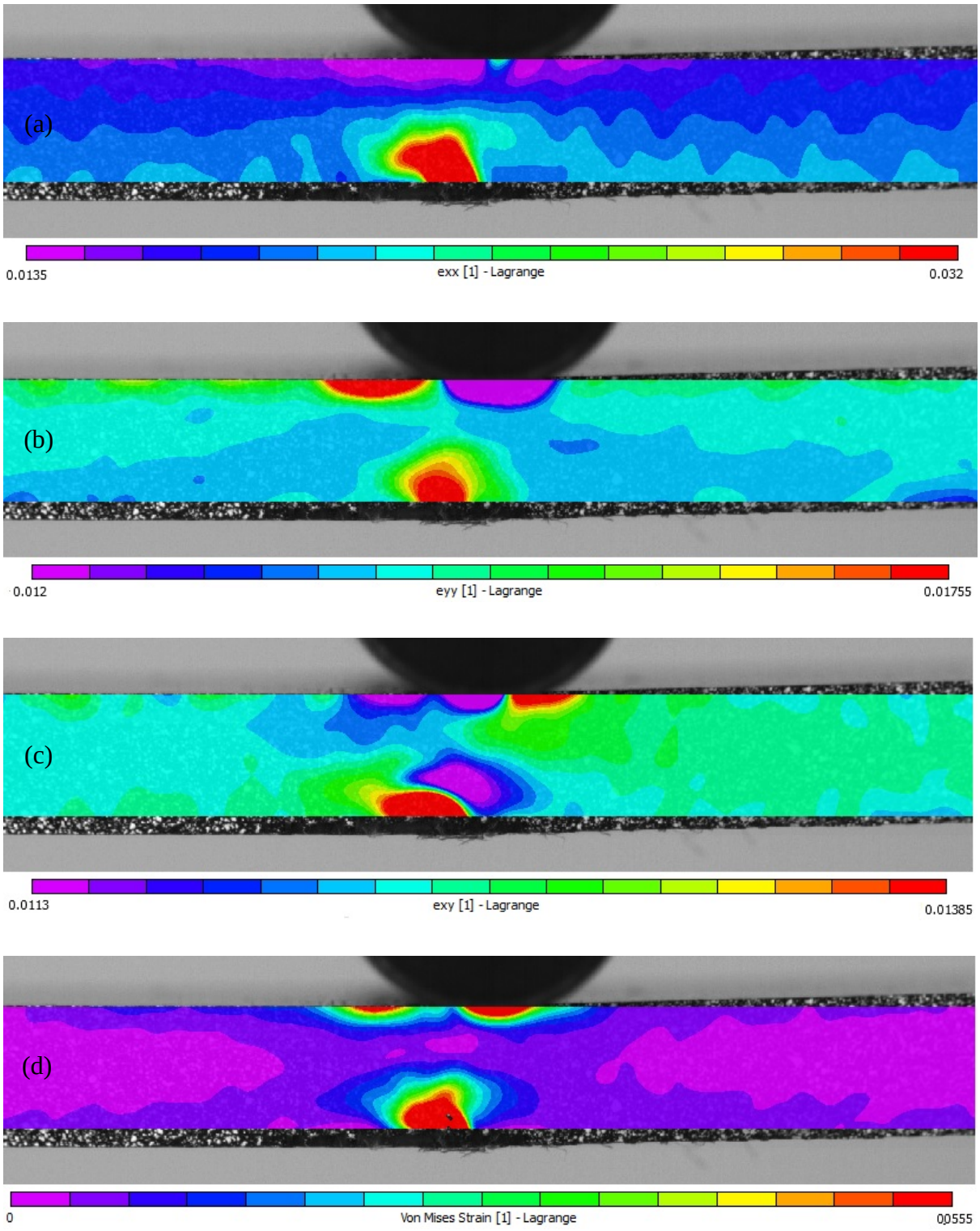

Figure 8-12. Strain components for a 3PB fatigue test (air) at peak cyclic strain equivalent to 30% of ultimate static strain and 5.900 million cycles. (a) Longitudinal strain, (b) transverse strain, (c) shear strain in x-y plane, (d) Von Mises strain.

1000 cycles

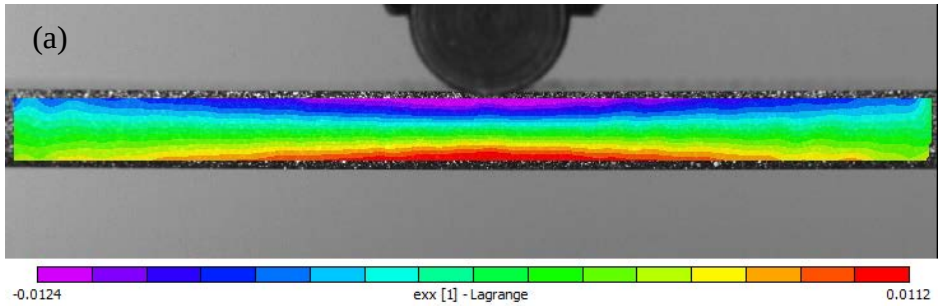

120,000 cycles

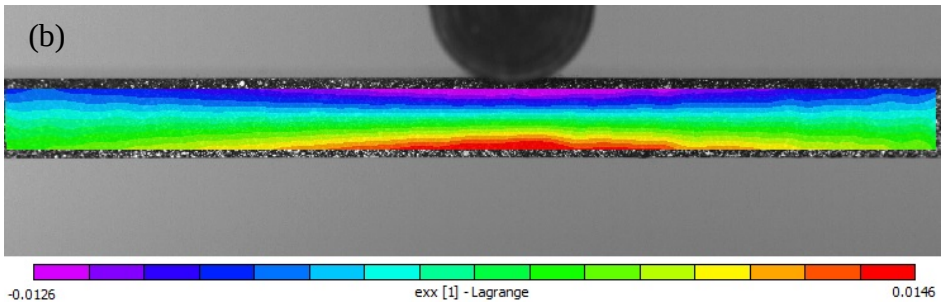

1000,000 cycles

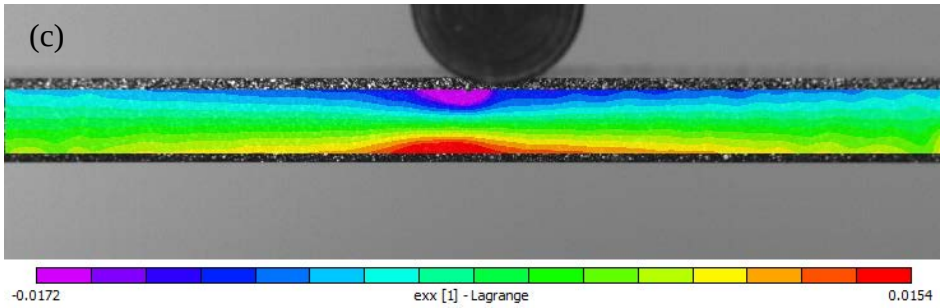

1,150,000 cycles

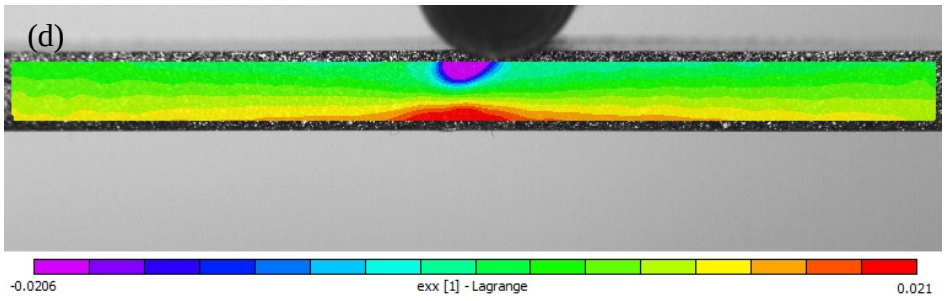

1,290,000 cycles

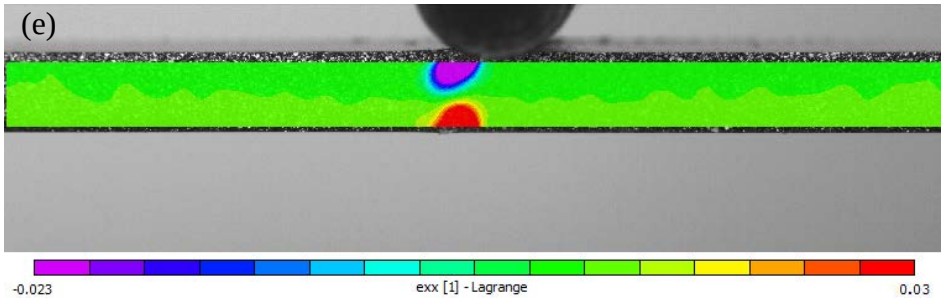

Figure 8-13. Bending strain for a 3PB fatigue test (sea water) at peak cyclic strain equivalent to 30% of the ultimate static strain and 1.300 million cycles.

1000 cycles

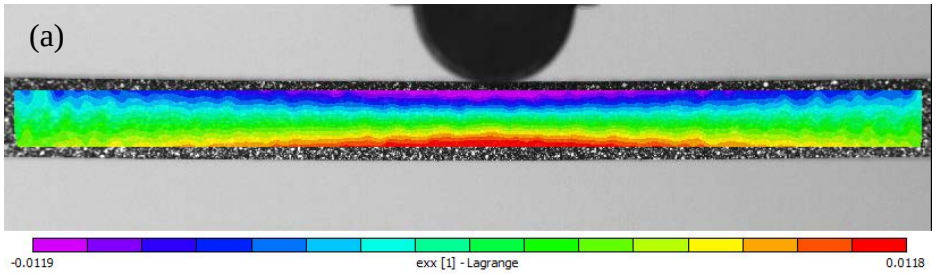

500,000 cycles

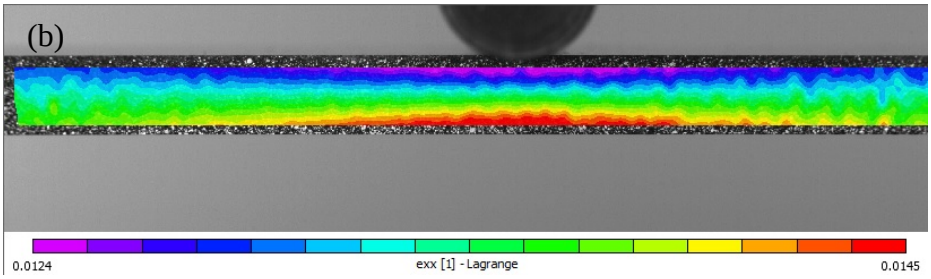

5,500,000 cycles

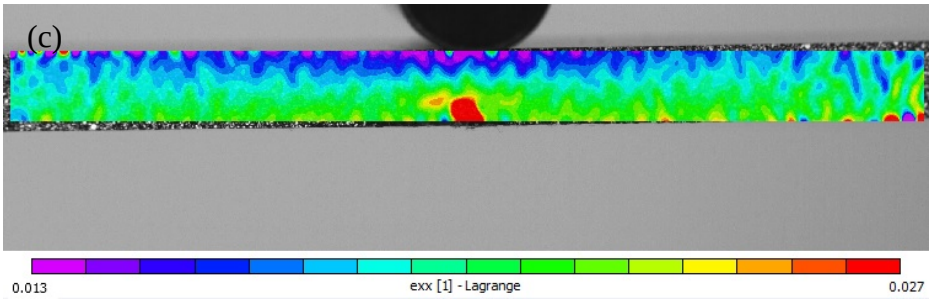

5,750,000 cycles

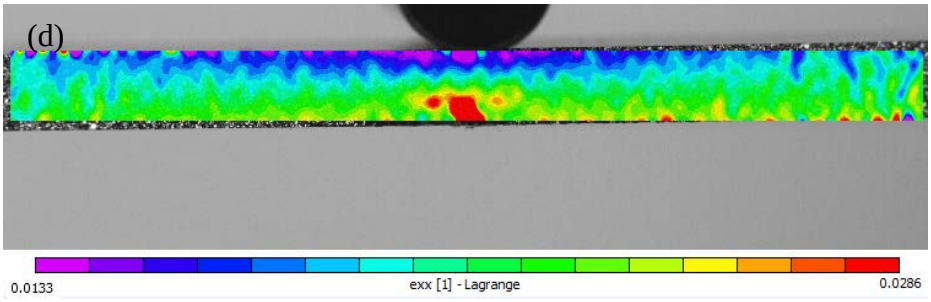

5,850,000 cycles

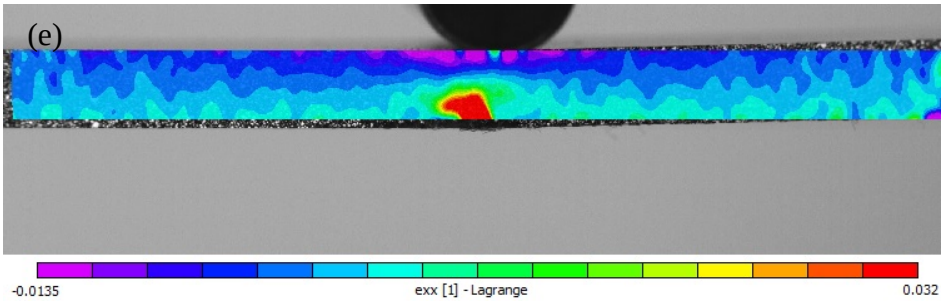

Figure 8-14. Bending strain for a 3PB fatigue test (air) at peak cyclic strain equivalent to 30% of the ultimate static strain and 5.900 million cycles.

Figure 8-15 and Figure 8-16 show the damage development during the last stage of fatigue life.

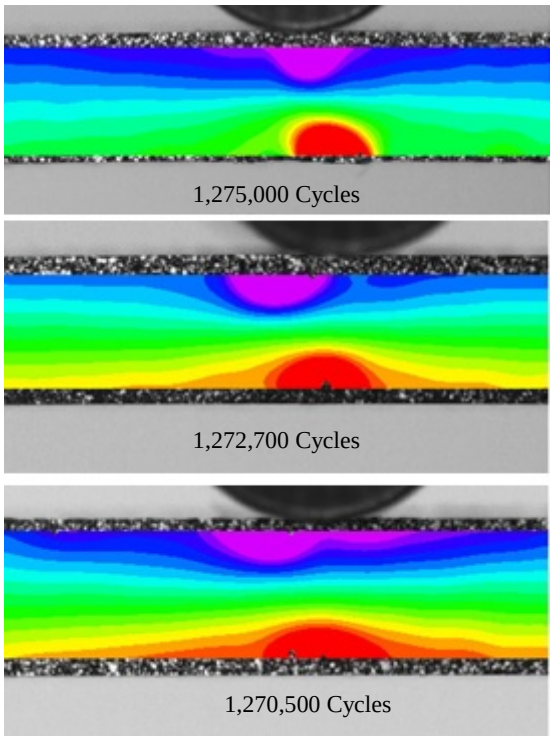

Figure 8-15. DIC strain map for a 3PB fatigue test (sea water environment) at peak cyclic deflection equal to 30% of the ultimate static deflection and 1.300 million cycles.

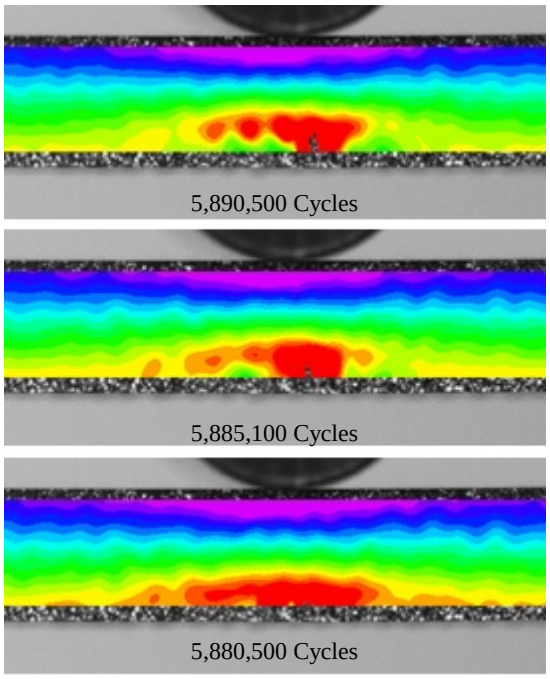

Figure 8-16, DIC strain map for a 3PB fatigue test (air environment) at peak cyclic deflection equal to 30% of the ultimate static deflection and 5.900 million cycles.

8.3.2. Fatigue Failure Mechanisms

Fatigue damage development is evaluated by quantitative measurement of changes in flexural elastic modulus and qualitative investigation of microstructural damage modes of the sample surface during the fatigue cycling. In order to investigate damage development of composites under flexural fatigue testing the tests have been interrupted after certain number of cycles chosen as a function of the fatigue life and then a quasi-static 3PB test was performed to determine residual flexural modulus as shown in Figure 8-17 and Figure 8-18 indicating the reduction of stiffness as a result of fluctuating loads. It has been well documented that variation in flexural elastic modulus is a sign of the failure state for composite materials (Stinchcomb and Reifsnider, 1979; Hahn and Chiao, 1980; Konur and Matthews, 1989; Agarwal *et al.*, 2006). Such a bending modulus degradation curve is characterized by a drop within the first 10% of life, followed by a rather flat region, representing a slower damage development rate to about 90% of life and then failure by a sudden drop during the last stages of life.

8.3.3. Elastic Modulus Evolution

Modulus decay was normalized with respect to maximum value of elastic modulus and the number of cycles to failure. The curves obtained in (Figure 8-17 and Figure 8-18) show two slope transition points and three different zones can be identified. The number of cycles corresponding to these slope transition points are located at around 10% and 90% of total life. The initial phase is dominated by a reduction in stiffness in the order of 10-15%, until an equilibrium stage is reached. This behaviour is probably induced by internal fibre-matrix viscoelastic interactions and crack accumulation in several stress concentration hot spots. The second stage which is a stable damage phase occupies 90% of the fatigue life and is placed in the same life percentage interval for all samples. In the second phase, the evolution of damage is linear and the slope remains constant regardless of the load level. The final stage is described by combination of defects and flaws leading to severe stiffness reduction.

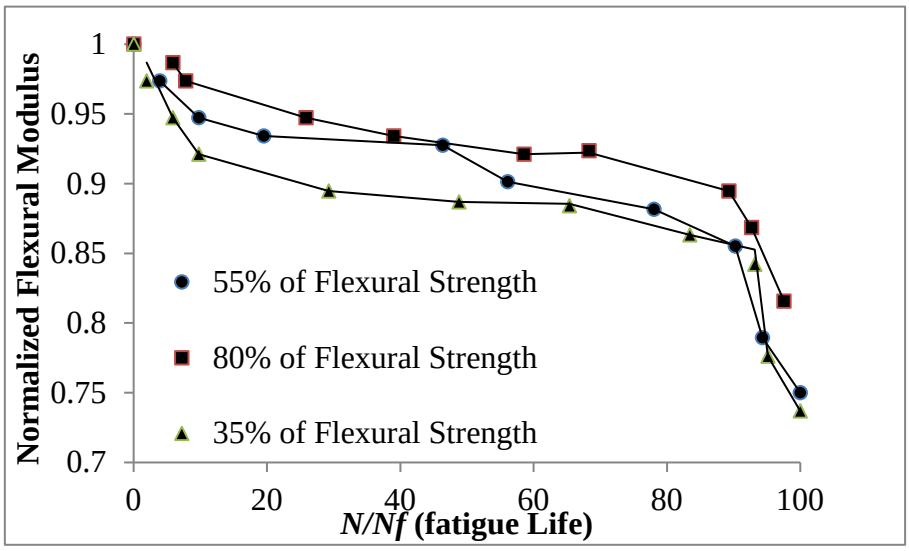

Figure 8-17. Modulus decay in GFRP composites during fatigue life in air.

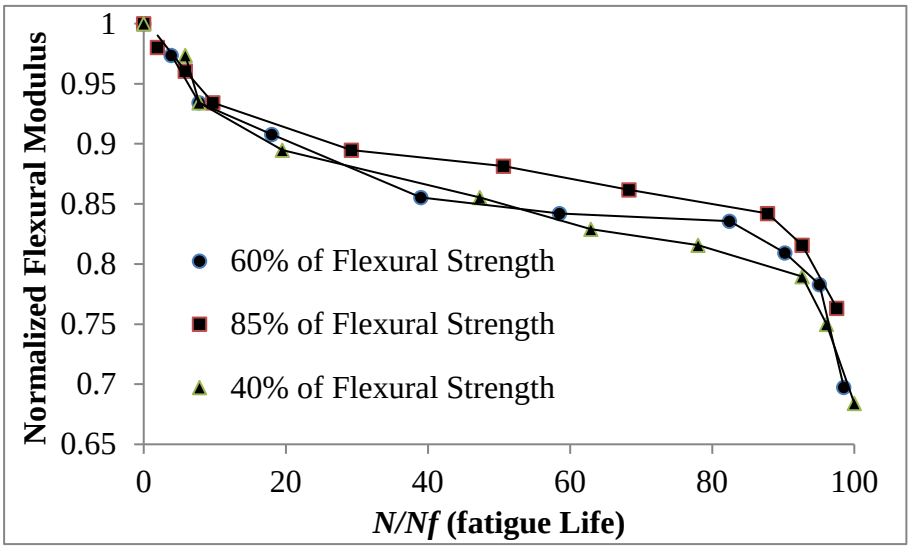

Figure 8-18. Modulus decay in GFRP composites during fatigue life in sea water.

8.3.4. Fatigue Damage Estimation

In order to assess and evaluate the damage state (D) in the fatigue test specimen in terms of residual life to failure, a knowledge of elastic modulus reduction is useful, provided that a constant displacement/strain level is applied. Young' modulus decay has been employed to quantify and characterize the damage state of composite materials for a long time (Kuo and Pon, 1997; Whitworth, 1997; Van Paepegem and Degrieck, 2002; Tang *et al.*, 2004).

In this project for the calculation of damage an expression is proposed which is a function of elastic modulus variation;

$$D = \frac{E_i - E}{E_i - E_f}$$

8-2

Where D takes a value between 0 and 1 and it is influenced by an initial elastic modulus, E_i, and the final elastic modulus, E_f.

Figure 8-19 and Figure 8-20 show the evolution of damage in the tested sample.

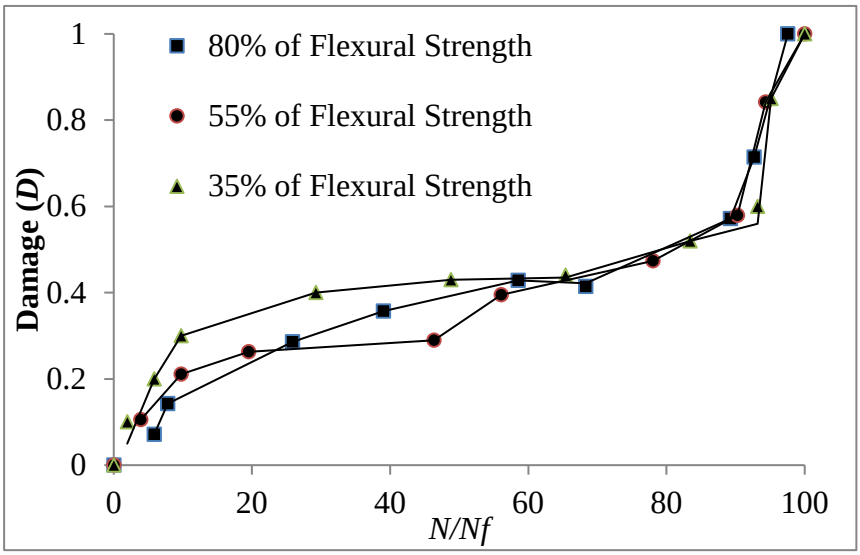

Figure 8-19. Damage accumulation in GFRP composites during fatigue life in air.

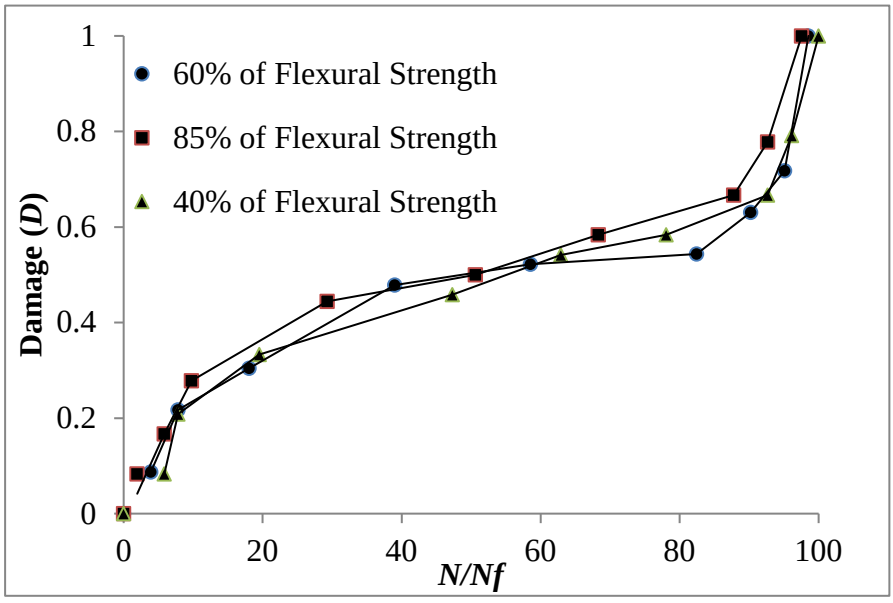

Figure 8-20. Damage accumulation in GFRP composites during fatigue life in sea water.

Comparing Figure 8-19 and Figure 8-20 with the stiffness degradation curves (Figure 8-17 and Figure 8-18) show that the evolution and development of damage state (*D*) for all samples is independent of displacement/strain conditions (in the given range of displacement). Stiffness degradation and damage (*D*) are strictly correlated and both qualitatively and quantitatively express the progressive fatigue damage.

Figure 8-17 to Figure 8-20 show that damage in composite occurs in three stages; early, intermediate and ending stage. During the early stage, the fatigue failure occurs by transverse cracks followed by longitudinal inter-laminar cracks. Transverse matrix cracks generally start from the edge of the sample, presumably due to the effects of micro damage during sample cutting. As the cyclic load continues, the crack density rises and this is followed by crack connection and interfacial de-bonding between fibres and resin (Figure 8-21). De-bonding between transversely oriented fibres and the matrix occurs as these transverse resin cracks spread. A quick decline of modulus during this stage is largely caused by crack propagation and accumulation in several stress concentration spots.

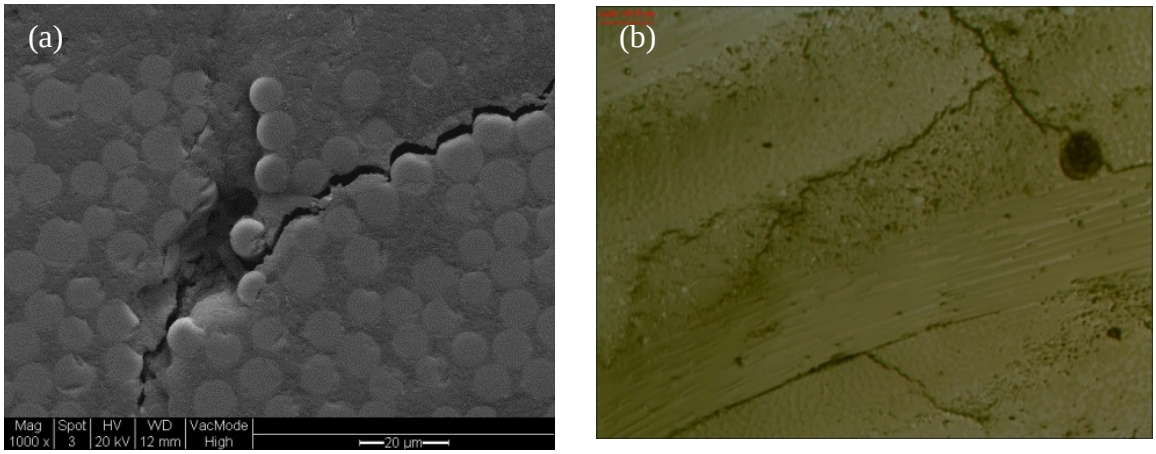

Figure 8-21. (a) Scanning electron micrograph showing interfacial de-bonding between fibres and matrix. The micrograph is taken from the edge of specimen, (b) Reflected light micrograph showing inter-laminar cracks with delamination

In the intermediate stage of fatigue life, the main damage mechanism is delamination between adjacent plies and shear failure. Typical delamination failure patterns are shown in Figure 8-22 and Figure 8-23(a). Generally, failure modes such as interfacial de-bonding between fibres and matrix and delamination are associated with the difference of interlayer stresses which originate from differences in the load magnitude among layers along the thickness direction of

the laminated composite specimens. Due to this difference, inter-laminar cracks propagate into the epoxy resin and contiguous fibres. This leads to interfacial de-bonding between the fibres and the matrix and crack growth in the fibres. When the strain level changes from low cycles (high strain) to high cycles (low strain), microstructural observation show that the number of inter-laminar cracks and resin cracks increases proportionally.

In the final stage of the fatigue life, when the cyclic load reaches the residual strength of the composite, all failure mechanisms are activated and specimen failure occurs with the evidence of fibre breakage. Fibre failure occurs in two modes; tensile and compressive (Figure 8-24).

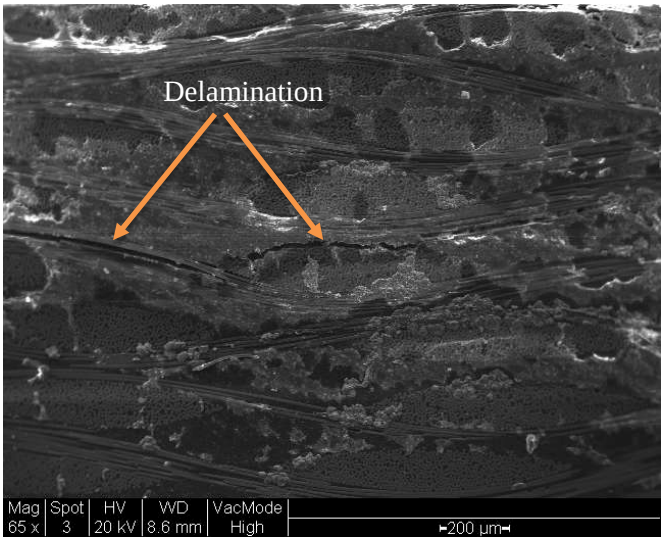

Figure 8-22. Scanning electron micrograph showing delamination failure mode (arrowed).

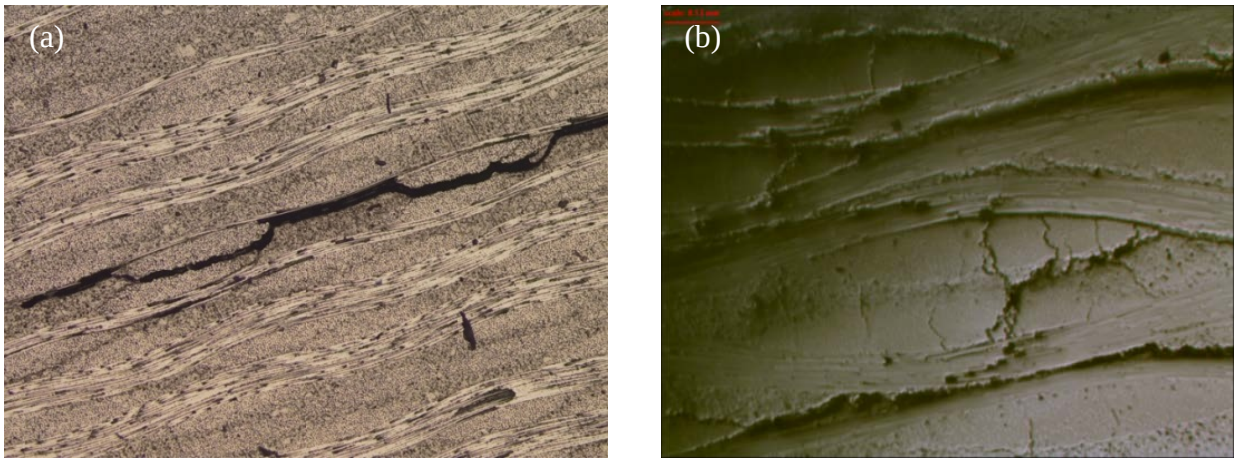

Figure 8-23. Reflected light micrograph of typical (a) delamination pattern (b) resin micro-cracking and inter-laminar cracks connected with delamination. The micrograph was taken from the edge of two test specimens near mid span after fatigue failure in sea water condition.

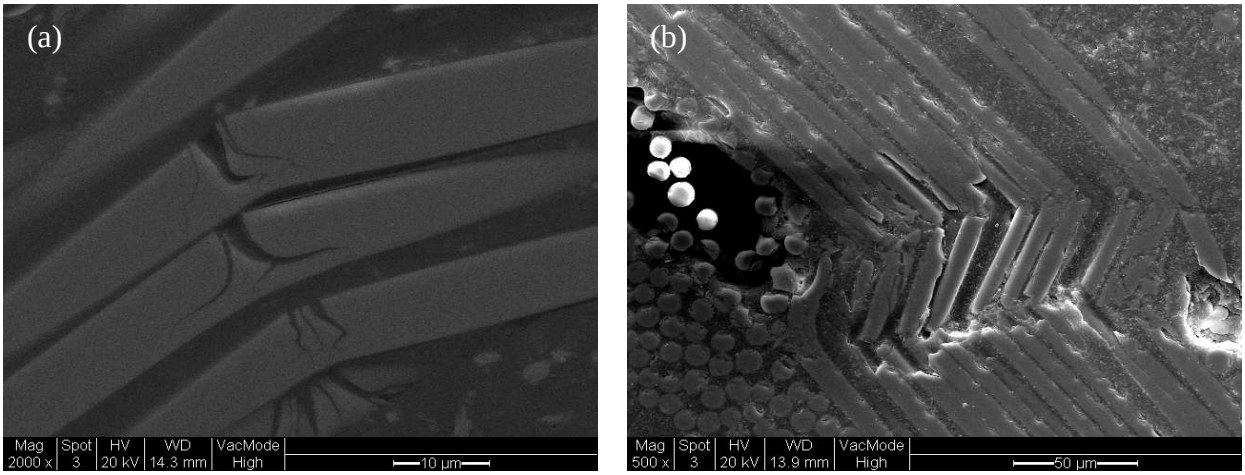

Figure 8-24. Scanning electron micrograph showing fibre breakage as a result of fatigue, (a) tensile failure of fibre in the bottom (tension) side of GFRP specimen, (b) fibre buckling/kicking in the upper (compression) side.

The corresponding graphs of damage accumulation with respect to the fatigue life for the GFRP composite studied here under bending fatigue loads were illustrated in Figure 8-19 and Figure 8-20. This description of damage mechanisms is well documented by other investigators (Naik, 2003).

Microscopic observation of the samples fatigued in air and sea water revealed that for those specimens tested in air many resin cracks were created prior to failure, while only a few resin cracks were found in the specimens tested in sea water. This indicates that complete failure follows quickly after crack formation in sea water. This is due to the fact that sea water diffuses into the network of resin cracks influencing the stiffness of fibre/resin interface region, consequently the crack propagation rate can be accelerated and the overall fatigue life decreases. This description of resin cracking effects in environmental behaviour of FRP composites has been confirmed by other authors (Carswell and Roberts, 1980; Hofer *et al.*, 1987).

8.3.5. Evaluation of Residual Fatigue Life

Due to the stochastic aspect of the fatigue process in FRP composite materials, scattering in the failure data can be witnessed for strain-life curves. This means that conservative criteria need to be employed for designing composite structures and in some cases inspection is required for verification of the component damage state. As it was shown, stiffness degradation is strictly related to the damage state of the composite test coupon and both of them can be

adopted as a potential damage variable. This consideration means that a method can be proposed to predict the residual fatigue life of GFRP components during normal operation.

As a representative example in Figure 8-25, drawing a line that fits the second stage evolution for stiffness degradation, it is possible to identify two points on this line.

S_{10}^{lin} : intercept of line with vertical axis on modulus decay diagram.

S_{90}^{lin}: The point of line corresponding to 90% of consumed fatigue life on modulus decay diagram.

Thus the following expression can be defined;

$$\Delta S_{\%} = \frac{S_{10}^{lin} - S_{90}^{lin}}{S_{10}^{lin}}$$

8-3

The quantity (ΔS) is considered as an index of irreversible composite degradation. By measuring this quantity for all displacement levels in the fatigue tests, it was found that the modulus decay rate of the fatigued samples in sea water is higher than that in the air.

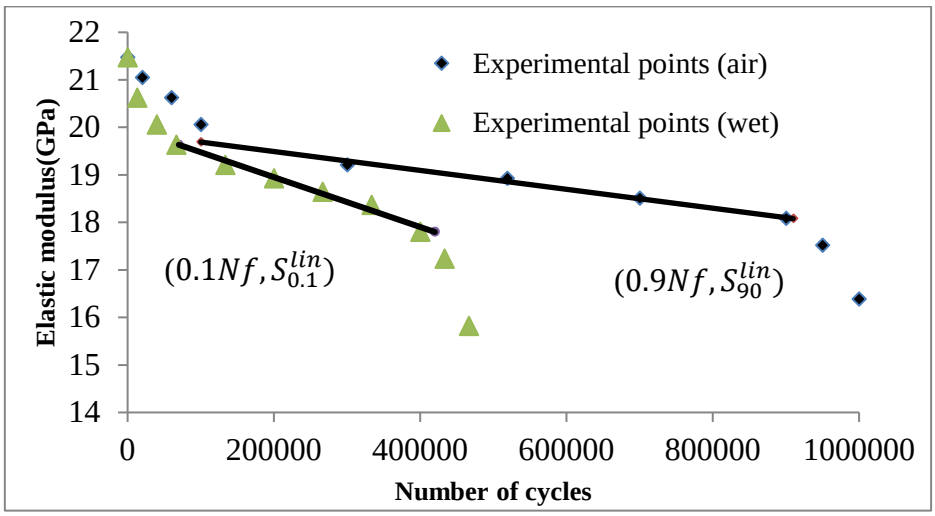

Figure 8-25. Elastic modulus evolution and line fitting the second stage (40% of Flexural strength)

Although the approach works well on the composite tested in the study, the calculation needs to be confirmed by performing fatigue tests on other types of FRP composites. If it is repeatable

on other types of composites it would be possible to find out when an element will reach a critical condition by monitoring stiffness degradation.

8.4. Influence of Sea Water on the Glass Fibre Surface

The controlling effect of the fibre/matrix interface regions on the environmentally affected fatigue performance of fibre reinforced composites has been investigated by a number of workers (Fried, 1967; Hofer Jr *et al.*, 1976; Hofer *et al.*, 1977; Watanabe and Tsai, 1979; Hofer *et al.*, 1987; Shih and Ebert, 1987). The destruction of the fibre/matrix interface region by corrosive fluid leakage, facilitates matrix crack propagation because fibres no longer sustain their reinforcing roles (i.e. no stress transfer to the matrix). The degradation process is aided by the fact that the failure strain of the matrix (epoxy resin) is diminished upon conditioning in sea water. The SEM examination of the failed surfaces revealed that, for specimens tested in air, more matrix were attached to the fibre surface. This relatively rough surface of fibres can be seen in Figure 8-26 and Figure 8-27 while “smoother” fibre surfaces with much less matrix adhering are observed on samples failed in environmentally affected fatigue (Figure 8-28 and Figure 8-29). This dissimilarity on the fibre surface points out about the destructive effect of fluid ingress on the bond between the fibres and the matrix. The same behaviour of degraded fibre surfaces due to the environment has been also reported previously (Watanabe and Tsai, 1979; Sekine *et al.*, 1988).

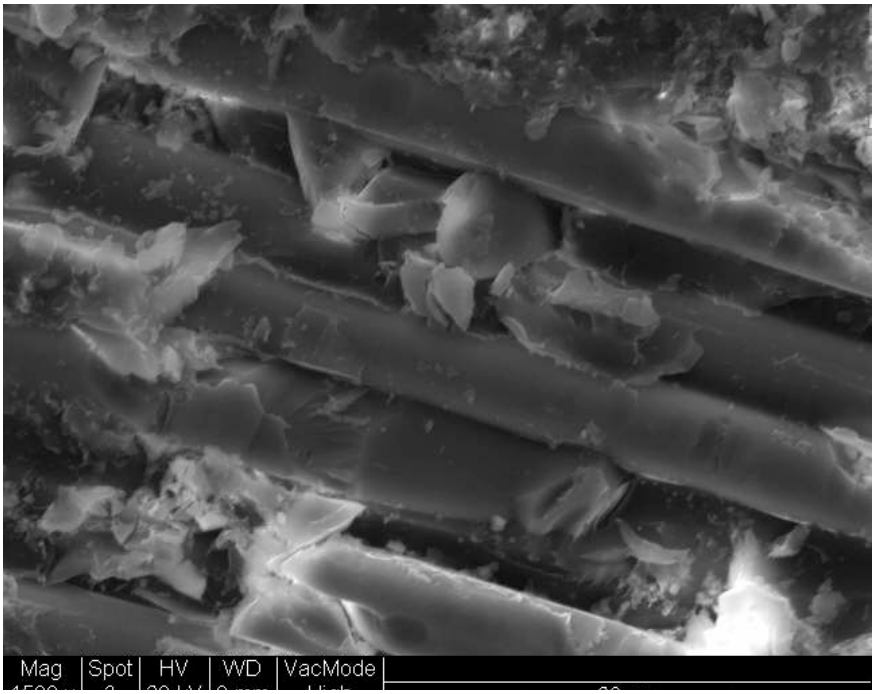

Figure 8-26. SEM micrograph showing the fibre surface of a sample failed by cyclic testing in air.

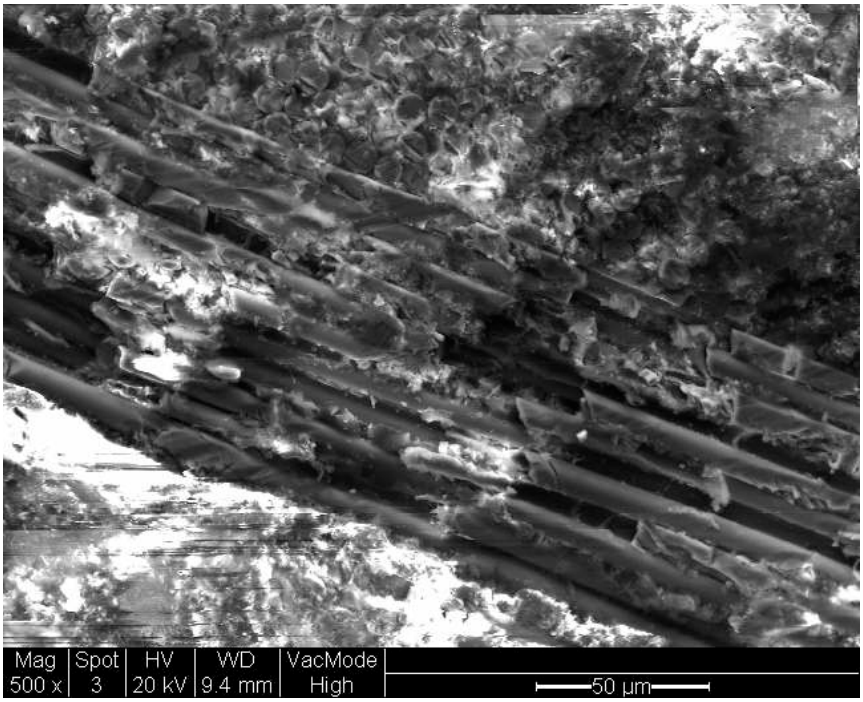

Figure 8-27. SEM micrograph showing delamination in a specimen failed by cyclic testing in air.

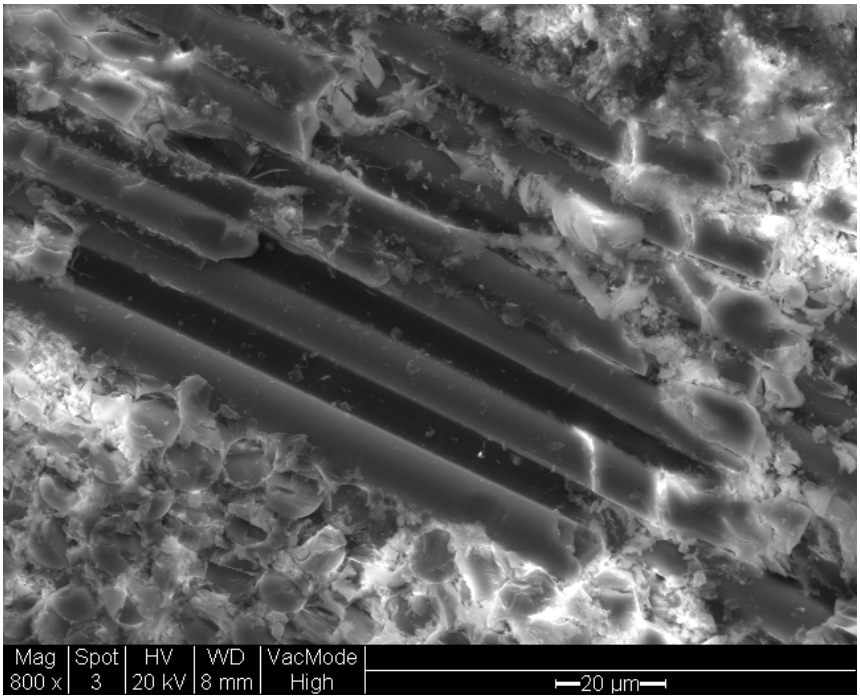

Figure 8-28. SEM micrograph showing the fibre surface of a sample failed by cyclic testing in sea water.

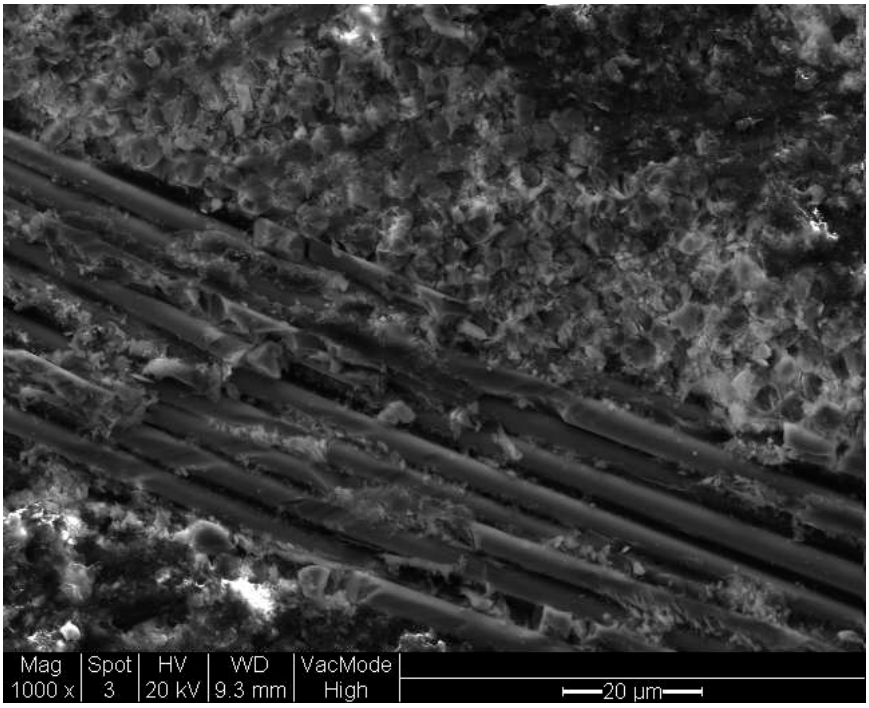

Figure 8-29. SEM micrograph showing delamination in a sample failed by cyclic loading in sea water.

The process of environmentally affected fatigue involves the combined degradation of interfaces and matrix cracking. Due to the crack initiation and propagation in the matrix, access of sea water to the fibre surface occurs, which speeds up the deterioration process in the interphase region. This process subjects the glass fibres to corrosion at an accelerated rate. Although from the fatigue data, fibre strength decay cannot be proven, microscopic investigations of the failed specimens can establish a strong indication of fibre strength deterioration during cyclic testing (Liao *et al.*, 1999a).

8.5. Effect of Sea Water on Fibre/Matrix Interface Region

EDX spectroscopy was used for elemental analysis of the fracture surface of specimens tested in both high and low cycle fatigue. The regions of the fracture surface where EDX analysis was performed are those containing matrix cracks, longitudinal and transverse micro-cracks, inter-laminar cracks, delamination, and fibre breakage areas.

8.5.1. Chemical Characterization with EDX Analysis

In order to evaluate the environmentally affected fatigue failure mechanisms of GFRP composite samples, SEM/EDX analysis was conducted on the glass fibre surface of GFRP test coupons fatigue loaded in both air and sea water. Figure 8-30 to Figure 8-32 show the EDX spectra obtained from the fatigue surface of samples tested in air. Figure 8-33 to Figure 8-35 show the EDX spectra obtained from the fatigue surface of samples tested in seawater. Comparing elemental analysis from these spectra with EDX spectra in dry conditions shows the effect of sea water. As a results, fibre degradation due to the effect of sea water penetration into the composite is considered as a controlling factor in the environmentally affected fatigue performance of GFRP composite. The main causes of the glass fibre degradation are either corrosive species or the mechanisms of ionic exchange between metallic cations and hydrogen ions from the attacking environment.

1. Corrosive species such as chlorine;

EDX spectra in Figure 8-33 to Figure 8-35, reveals the elements of chlorine (arrowed in these Figures) from the sea water environment. Once the fatigue test is done on GFRP composite samples in sea water condition, sea water diffuses into the network of resin cracks and causes the fibre degradation. The presence of chlorine ions at the glass fibre surface can cause a gradual reduction in mechanical properties.

2. Mechanisms of stress-corrosion by ionic exchange

Comparing the EDX spectra of the sea water fatigue loaded GFRP samples (Figure 8-33 to Figure 8-35) with the EDX spectra of air fatigue loaded samples (Figure 8-30 to Figure 8-32) reveals elements of Potassium and Sodium indicating the possibility of glass fibre degradation. When the fatigue test is conducted in sea water condition, sea water can penetrate into the network of resin cracks and comes into direct contact with E-glass fibres (and/or de-bonded fibres), as a results, a mechanism of ionic exchange happens between the metallic cations at the glass fibre surface and the hydrogen ions in the sea water solution. This results in the separation of sodium, potassium from the outer layer of the fibre. Fibre degradation in sea water is related to the separation of sodium and potassium ions from the fibre surface causing the development of surface micro pits, which act as stress raisers. These pits may act as the nucleation sites for micro-cracks. The possible actions of sea water exposure are briefly summarized below:

- Ion exchange between the metallic cations (e.g. Na+ ions) at the surface of glass fibre and the H+ ions in the sea water solution

$$\mathbf{— Si —O —X + H2O \rightarrow — Si —O —H + OH\text{-}X}$$

(X = sodium, potassium, and similar reactions for divalent ions: calcium, magnesium, aluminum…)

- Development of surface micro-pits and micro-cracks (i.e. stress concentration sites).
- Dissolving and decomposing of the glass fibre surface.
- Perpetual strength and stiffness decay (even after desiccation).

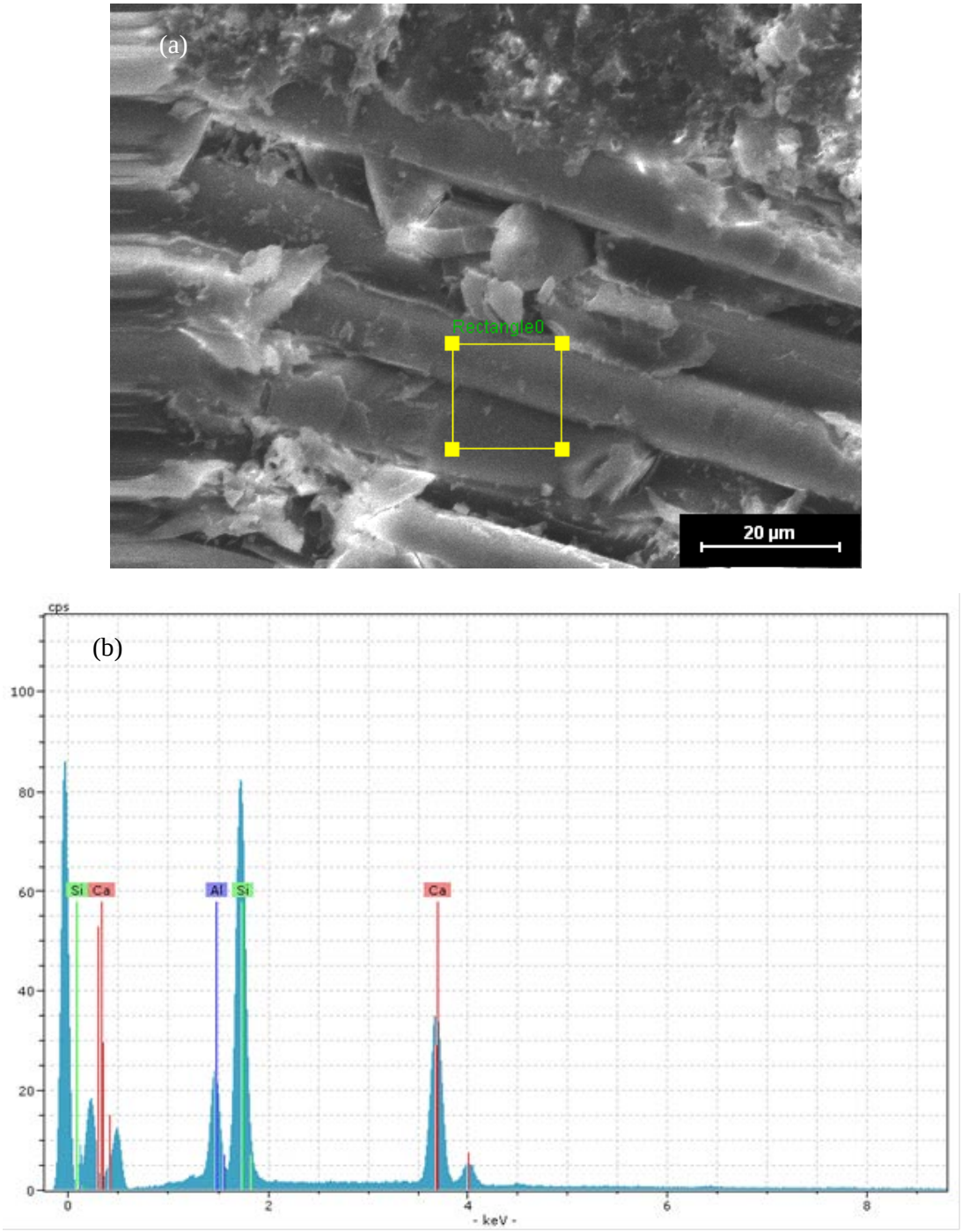

Figure 8-30. GFRP composite specimen fatigued in air.(a) SEM image showing the location for EDX analysis; (b) EDX spectrum.

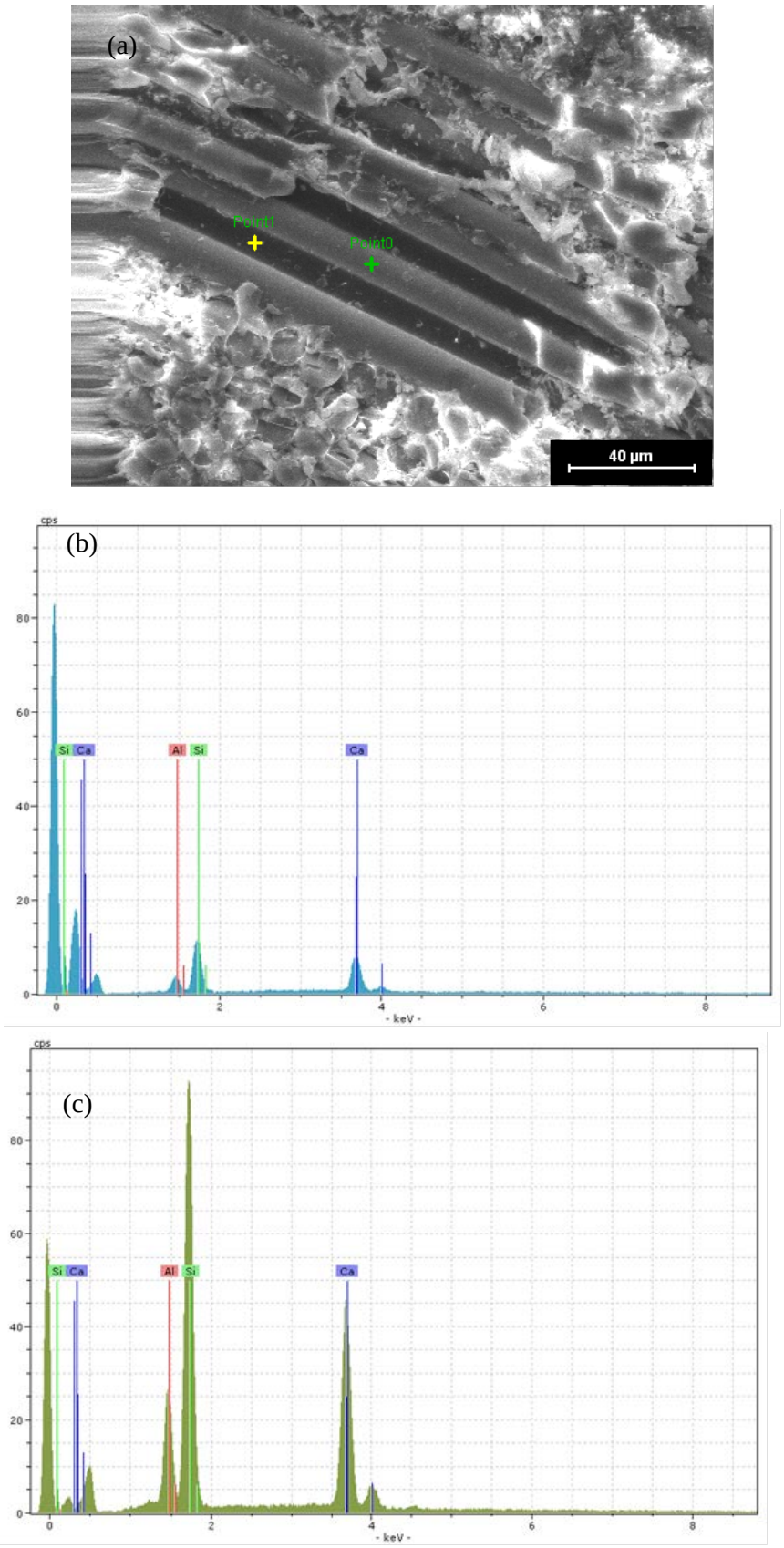

Figure 8-31. GFRP composite specimen fatigued in air. (a) SEM image showing the location for EDX analysis; (b) EDX spectrum at point 0 (fibre surface); (c) EDX spectrum at point 1 (between fibres).

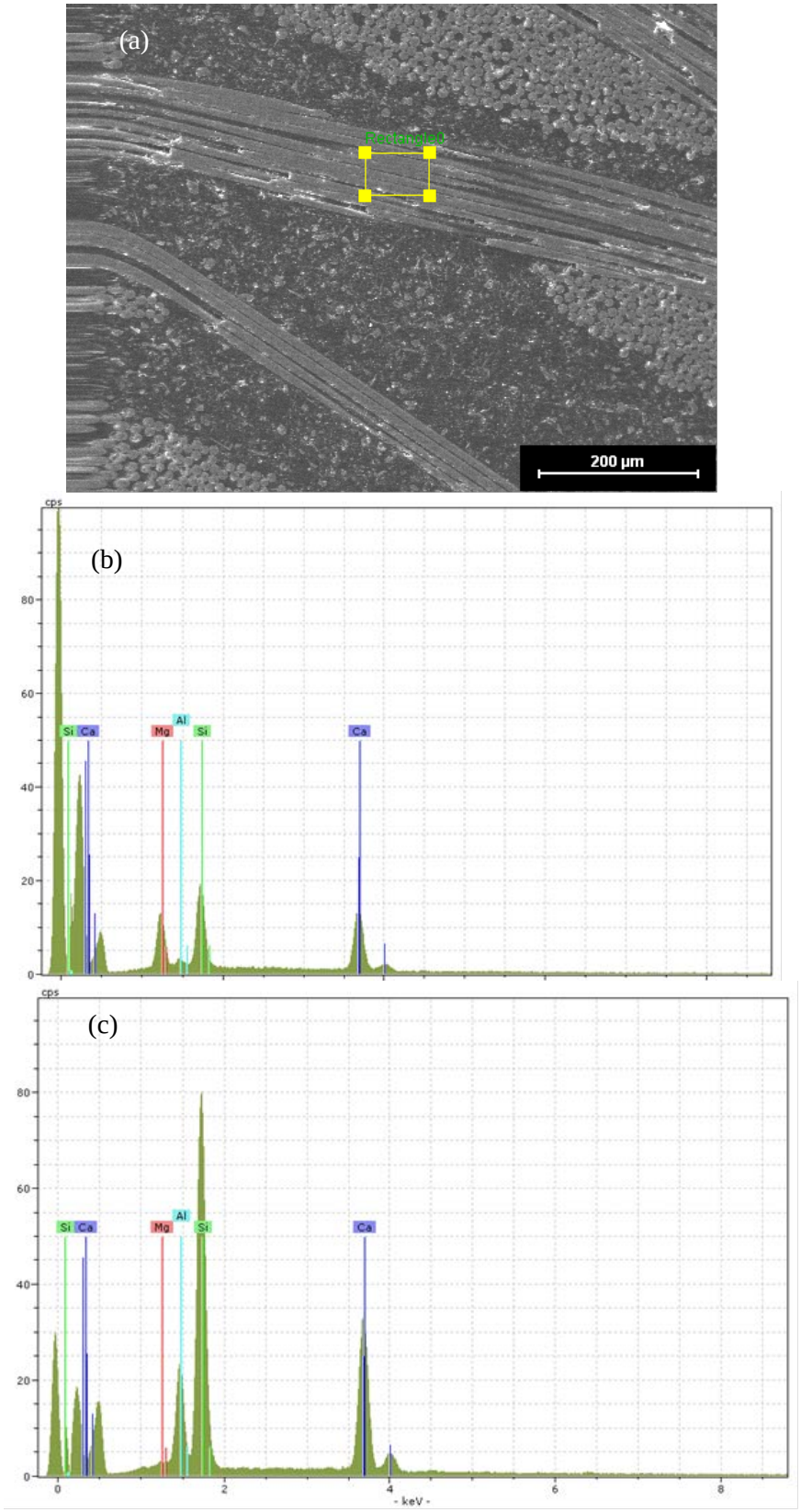

Figure 8-32. GFRP composite specimen fatigued in air. (a) SEM image showing the locations for EDX analysis; (b) EDX spectrum from the surface of a bundle of fibres; (c) EDX spectrum from the surface of the matrix.

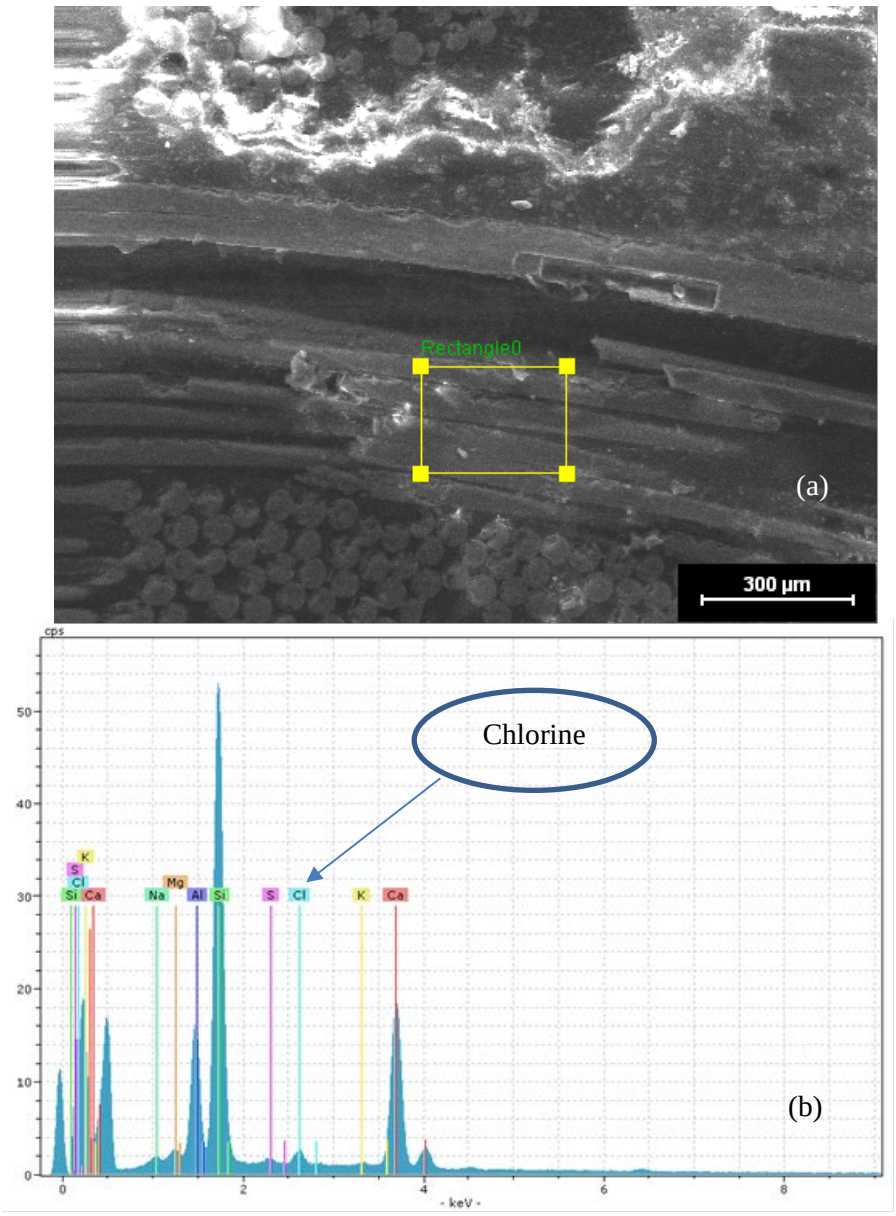

Figure 8-33. GFRP composite sample fatigued in seawater. (a) SEM image showing the location for EDX analysis; (b) EDX spectrum showing elements (chlorine, sodium) not present in the samples tested in air.

.

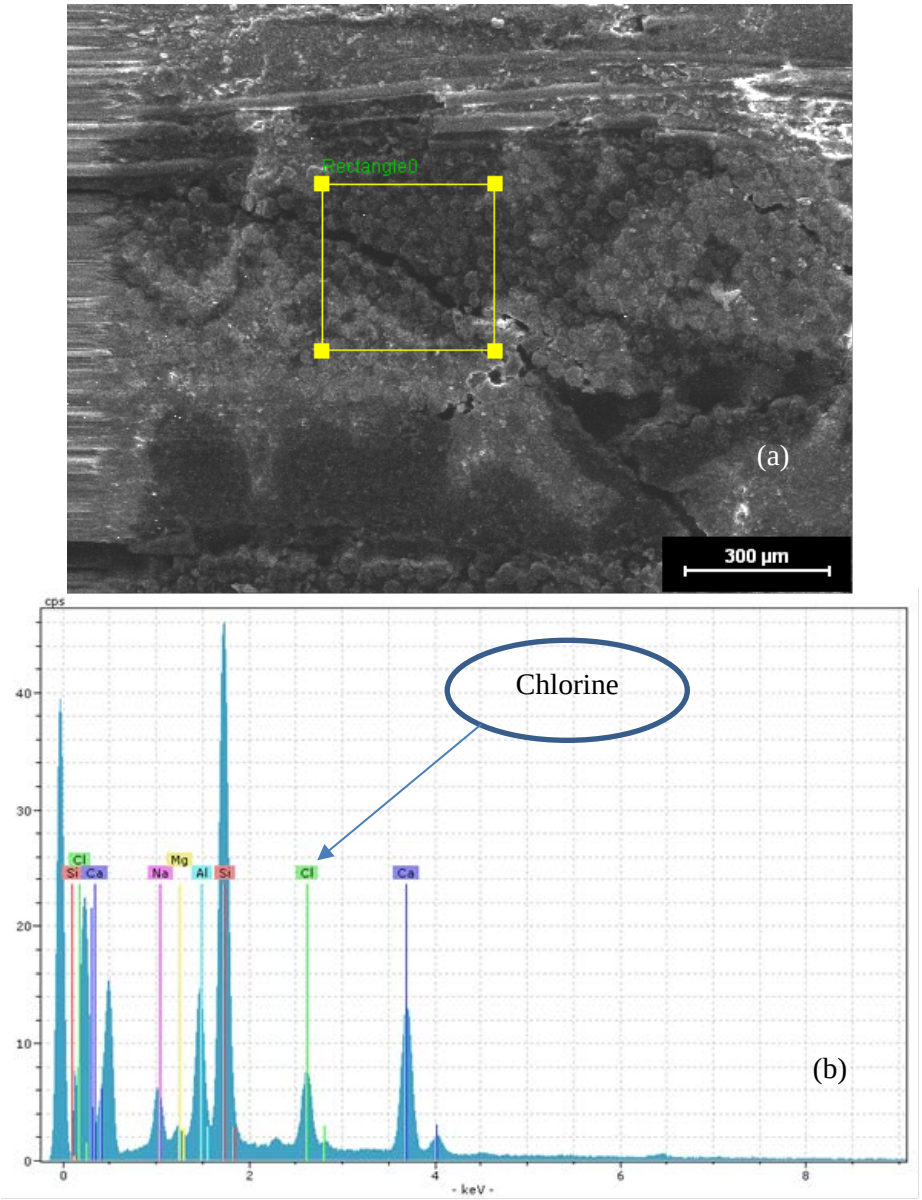

Figure 8-34. GFRP composite specimen fatigued in seawater: (a) SEM image showing a region near inter-laminar cracks and the area for EDX analysis; (b) EDX spectrum.

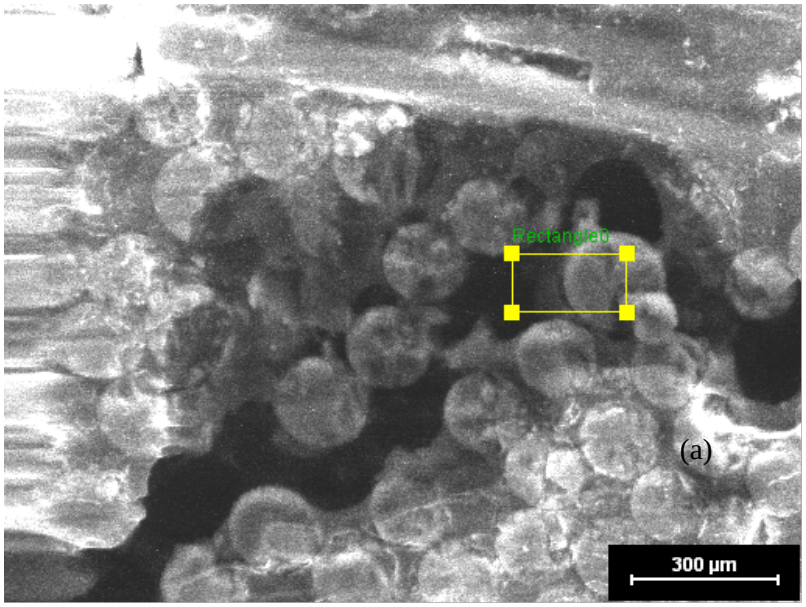

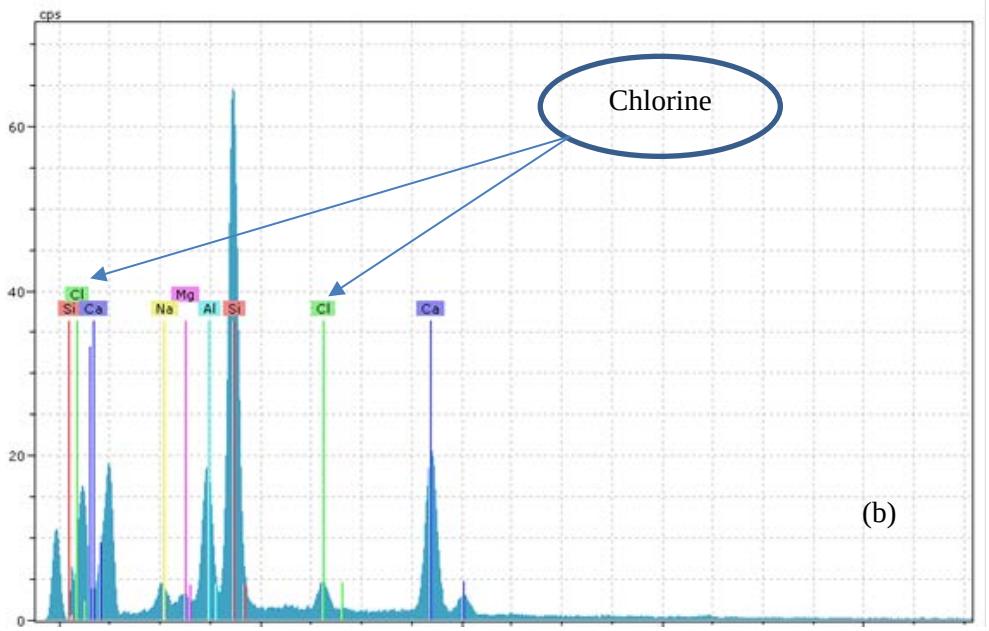

Figure 8-35. GFRP composite specimen fatigued in seawater: (a) SEM image showing an area near the de-bonded region and the location for EDX analysis; (b) EDX spectrum obtained.

8.6. Summary

In order to provide fatigue information for FE model of composite blade, a large number of coupons were subjected to the fatigue test. To approximate the blade performance and to replicate the associated stresses and failure modes on composite tidal turbine blades, a fatigue rig with a three point bending configuration was designed and manufactured. This was done in order to produce power law equation fitting fatigue data points required for the FE analysis of the blade. During the fatigue testing in both air and sea water, DIC technique was also employed to map the strain distribution. This was done in order to determine the development of elastic modulus related with damage.

In addition, damage development analysis was conducted to determine failure mechanisms in GFRP composite under 3PB fatigue tests. Environmentally affected fatigue failure modes were examined. This was done in order to assess the blade failure once the blade is subjected to the fatigue loads. Failure analysis techniques such as SEM/EDX, reflected light microscopy were used and the major failure mechanisms such as delamination, de-bonding between fibres and resin, resin cracking, fibre degradation, fibre breakage and fibre/matrix interface degradation were evaluated.

The 2D DIC technique was also suitably used to calculate full field strain maps of a sample during a cyclic mechanical test. The implemented method used for strain measurement allows information on inhomogeneity that evolves and progresses during static mechanical tests to be obtained. Especially when it was applied to fatigue tests on the GFRP composite material, DIC could be used for the determination of the development of the main materials parameter connected with damage: the elastic modulus, (E). The stiffness loss index gives evidence about the localized damage and about the process of deterioration of the composite properties. The outcomes revealed in this project showed that stiffness variation (E) and damage (D) are closely connected and interrelated, emphasizing the potential use of stiffness loss in the study of composite fatigue.

In addition, the DIC strain maps during fatigue testing of GFRP composite in both a sea water and an air environment clearly show the effect of sea water on the damage mechanisms i.e. fatigue loaded specimens in air condition fail on the tension side while for samples tested in a sea water environment the failure modes are both tension and compression.

This chapter has reported the effect of sea water on the fatigue behaviour of a GFRP composite and provides data for the life prediction approach. Chapter 10 uses this and also information from previous chapters to inform an FE model of an operational blade design in order to predict its life. Table 8-1 lists the mechanical and fatigue properties of GFRP used for an FE model of the blade.

Table 8-1. Material properties used for FE model of the blade

Mechanical Property		Method of Measurement
E_1 (GPa)	21.6	Experimental, chapter 6, section 6.2.1, Table 6-2
E_2(GPa)	21.6	*Experimental*, chapter 6, section 6.2.1, Table 6-2
E_3 (GPa)	3.5	ANSYS data base (Release, 2012)
ν_{12}	0.25	Experimental, chapter 6, section 6.2.1, Table 6-2
ν_{13}	0.33	ANSYS data base (Release, 2012)
ν_{23}	0.33	ANSYS data base (Release, 2012)
G_{12}(GPa)	3.52	Experimental, chapter 7, section 7.4, Table 7-3
G_{23}(GPa)	2.2	Experimental, chapter 7, section 7.4, Table 7-3
G_{13}(GPa)	2.2	Experimental, chapter 7, section 7.4, Table 7-3
Fatigue Life	Air $\varepsilon = 3.4207\ (logN^{-0.846})$ Sea water $\varepsilon = 3.2603\ (logN^{-0.88})$	Experimental, chapter8, section 8.2.1, Figure 8-4

Chapter 9

X-Ray Micro-Computed Tomography

9. X-Ray Micro-Computed Tomography

In this chapter it is shown how a non-destructive technique (X-ray 3D micro-computed tomography) was used to obtain information about the geometry and dimension of defects and the microstructure of FRP composites. Therefore useful information about fibre orientation which is required for FE analysis was obtained by this method. Additionally, using this non-destructive technique fatigue failure modes including matrix cracking can be investigated and the geometry and dimensions of internal defects such as cracks and delamination can be characterized.

The main advantage of this characterization technique is that, instead of consecutive sectioning, grinding and polishing FRP composites for microstructural analysis and evaluating failure modes, this technique can be used to obtain all information non-destructively. Therefore, with respect to the main objective of this project which is to understand the performance limiting issues of FRP materials, this methodology can make a positive contribution to our confidence in the use of these materials in tidal turbine applications. In the following sections, more details about the method and the results obtained are discussed.

9.1. Applying X-Ray Micro-Computed Tomography for GFRP Composite

Glass fibre reinforced polymer composites with several types of damage were investigated. Several examples which show the abilities of the μ-CT system are presented. These include E-glass/epoxy with matrix cracking, delamination and fibre breakage caused by 3PB fatigue in air and sea water. The CT scanning and reconstruction factors for an untested sample, air fatigued samples and sea water fatigued samples are summarized in Table 9-1.

Table 9-1. CT scan parameters.

Samples		Untested	Fatigued in air	Fatigued in sea water
Field of View		2008 x 2048 x 2008 slices at voxel size below (0.4x) 1976 x 2032 x 1991 slices at voxel size below (4x)	2000 x 2048 x 2008 slices at voxel size below (0.4x) 1956 x 2032 x 1986 slices at voxel size below (4x)	2004 x 2048 x 2008 slices at voxel size below 2004 x 2048 x 2008 slices at voxel size below
Voxel size		19.62 µm and 1.95 µm	19.62 µm and 1.95 µm	19.63 µm for 0.4x scan 1.95 µm for 4x scan
Objective		0.4x and 4x	0.4x and 4x	0.4x and 4x
X-ray parameters	**Filter**	LE2	LE2	LE2
	Exposure time	3.5 seconds per projection for 0.4x 20s per projection for 4x	3.5 seconds per projection (0.4x) 20 seconds per projection (4x)	3.5 seconds per projection 20s per projection (4x)
	Number of projection	3201 and 2501	3201 and 2501	3201 & 2501
	Reconstruction	center shift & beam hardening correction applied	center shift & beam hardening correction applied	center shift & beam hardening correction applied

9.2. Fabric Investigation

This specimen is made up of E-glass multidirectional fibres in an epoxy matrix. Each tow is about 750 µm wide by 100µm high, and contains 560 filaments. In the recreated cross-sections, the fibre material appears white and the matrix material appears red. 3D models were created from these sections for the glass fibre tows and the epoxy matrix, based on their grayscale image densities. The examination of the samples was carried out at the minimum scanning resolution of 5µm. Although the average fibre diameter is between 10 and 15 µm, individual fibres are not discernable even using the minimum resolution, because the space between the fibres is less than 5 µm, making it difficult to distinguish individual fibres. Figure 9-1 shows the 3D-reconstruction of a part of a sample.

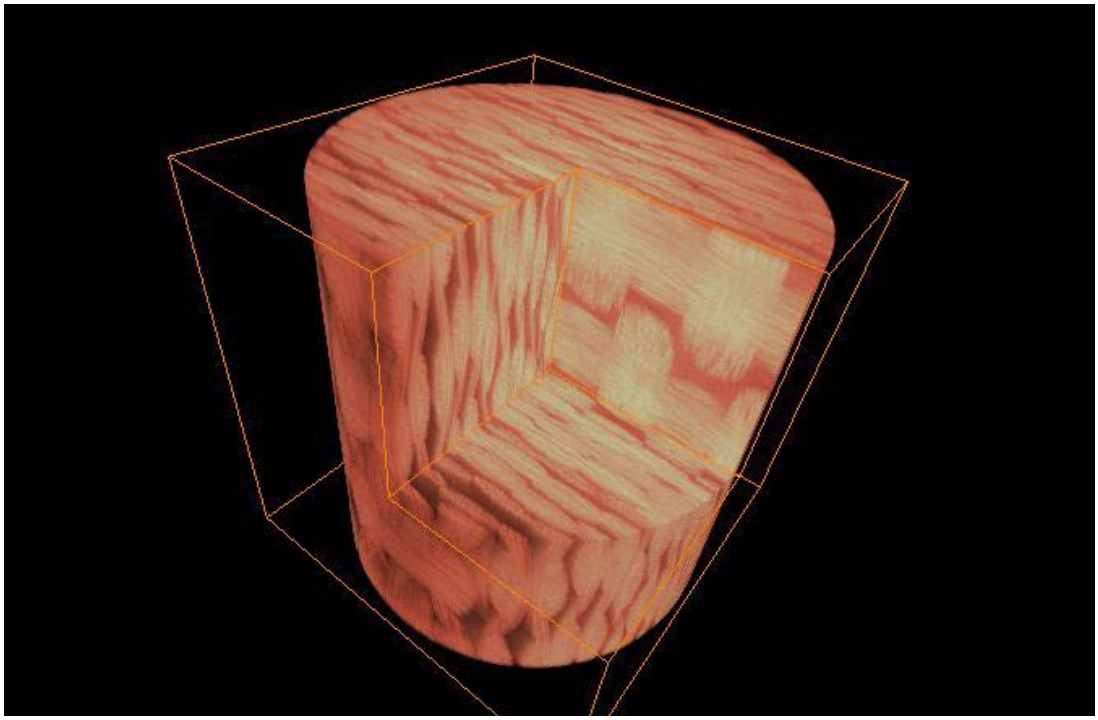

Figure 9-1. 3D volumetric models of E-glass biaxial fibre packages.

9.3. View of Individual Fabric Layers

In the next step the orientation of the fabric layers is pictured. Figure 9-2 displays a slice in the x-z plane. The individual tows and their joining are evident. The warp yarn is perpendicularly oriented and the weft yarn is horizontally oriented.

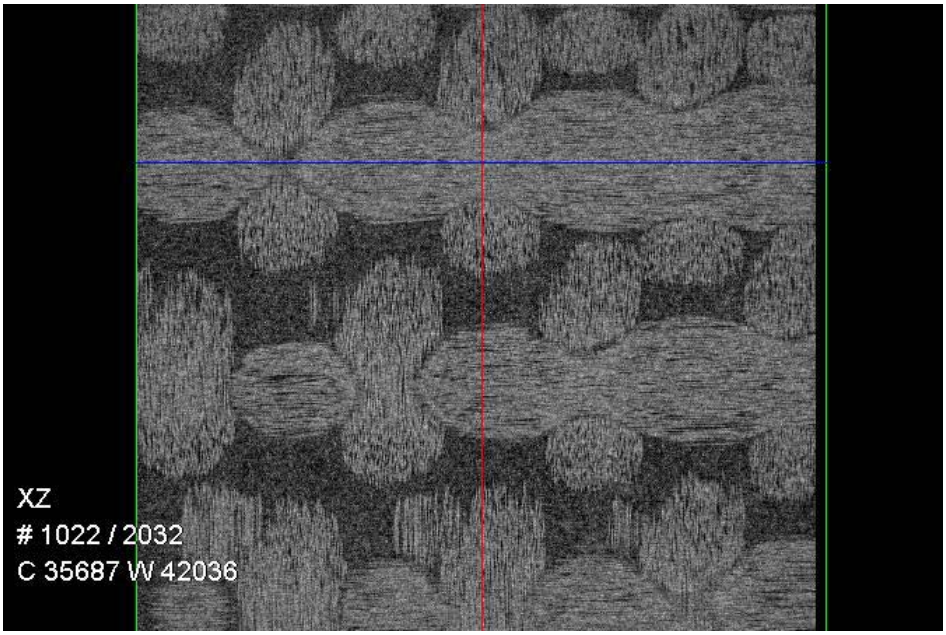

Figure 9-2. X-Ray Tomography image showing fabric layers (x-z plane).

9.4. Sectional View

The sectional view in Figure 9-3 and Figure 9-4 show the configuration of different fibre bundles in the x-z and y-z planes. The section of a perpendicular cut bundle is a flat ellipse. The parallel cut yarn has the shape of a sine wave. At the connection between the warp and weft yarn, compaction of the bundles can be observed.

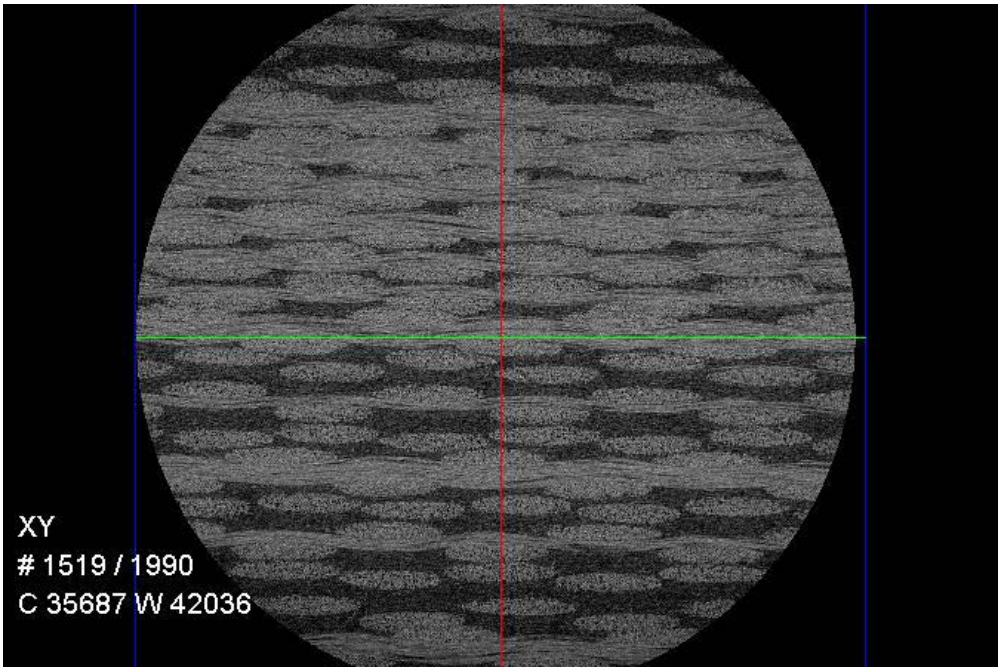

Figure 9-3. X-Ray Tomography image showing cross sectional view (x-y plane).

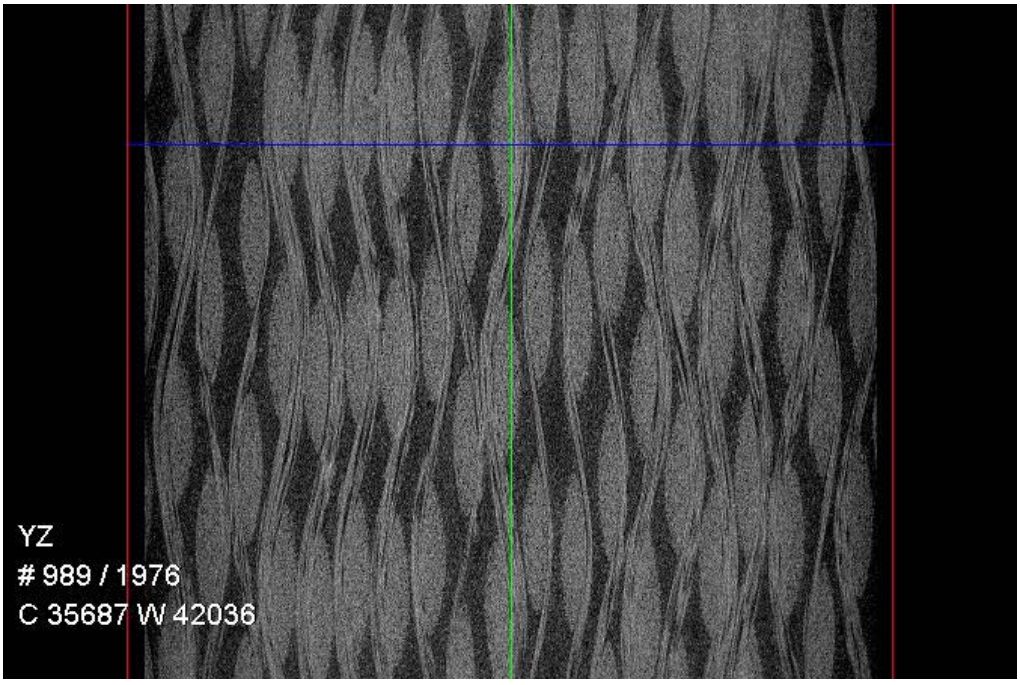

Figure 9-4. X-Ray Tomography image showing cross sectional view (y-z plane).

It is clear that position of the fibre tows is variable as there are some regions with a high glass density and others which are matrix rich. The space between adjacent plies is also variable. These factors contribute to the overall material variability.

9.5. Fatigue Damage Analysis

The evolution of fatigue damage in 0°/90° oriented glass fibre-reinforced epoxy was previously investigated, and delamination through the thickness of the specimen was detected. Characterization of delamination geometry needed slicing of consecutive sections and cuts through the sample and preparation of each section for optical and/or electron microscopy.

In this section, specimens were examined using µ-CT. Figure 9-5 and Figure 9-6 show a slice (19.6 µm voxels) revealing delamination. The location was chosen in the central region of the fatigued specimen where macroscopic failure was observed. The delamination is detected based on the difference in X-ray absorption between the glass/epoxy material and air.

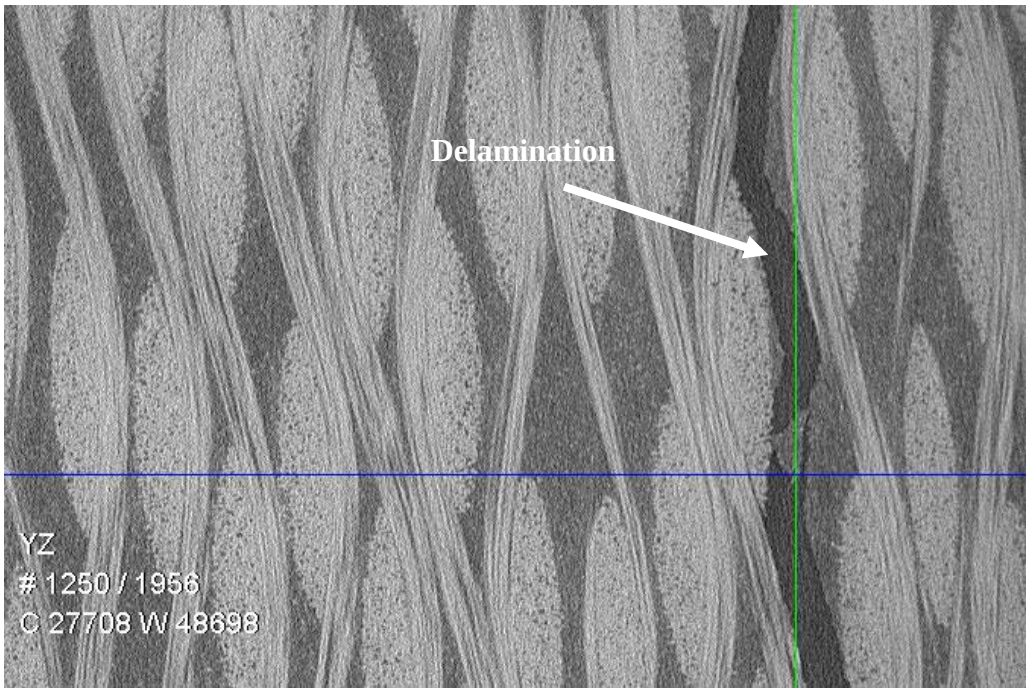

Figure 9-5. Micro-CT recreated cross-section of specimen in y-z plane showing delamination.

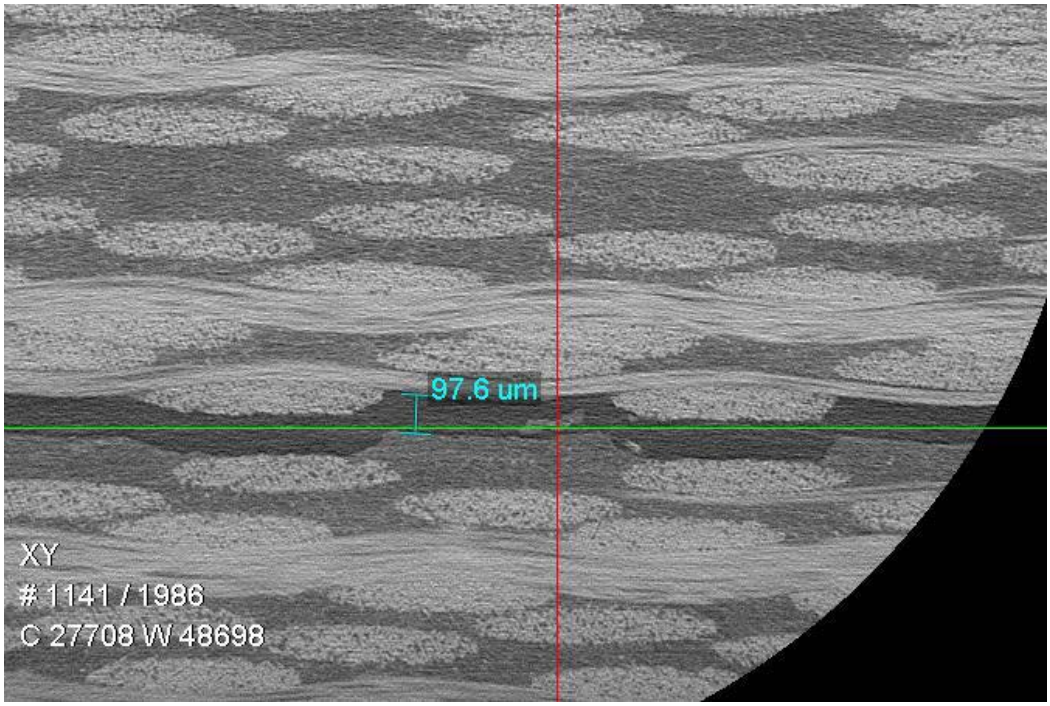

Figure 9-6. Micro-CT recreated cross-section of specimen in x-y plane showing delamination.

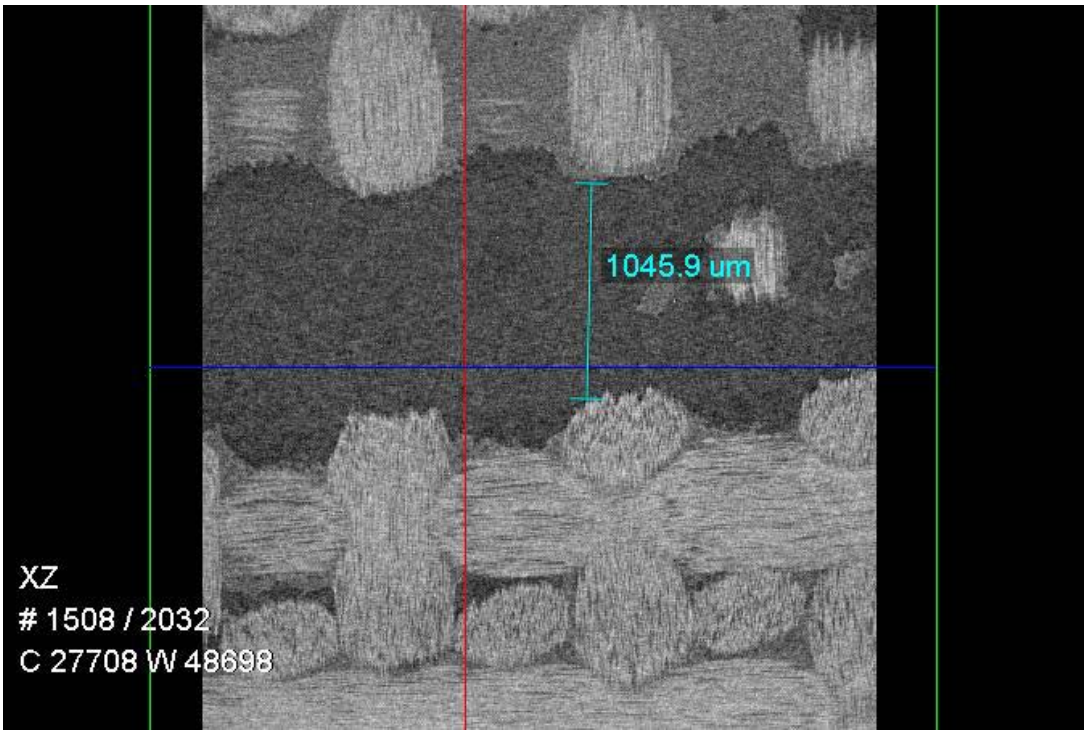

Figure 9-7. Micro-CT recreated cross-section of specimen in x-z plane showing delamination

A volumetric reconstruction can be generated for the fibre packages and matrix, with some tow layers detected in a stacked structure. The results show the ability to resolve delamination

within the epoxy resin and fibre bundles, and to measure the delamination size (Figure 9-7). The 3D geometry of the delamination is revealed in the volumetric reconstruction in Figure 9-8. The µ- CT results then offer an approach to characterize and quantify the delamination area, without the need for continuous sectioning of the specimen.

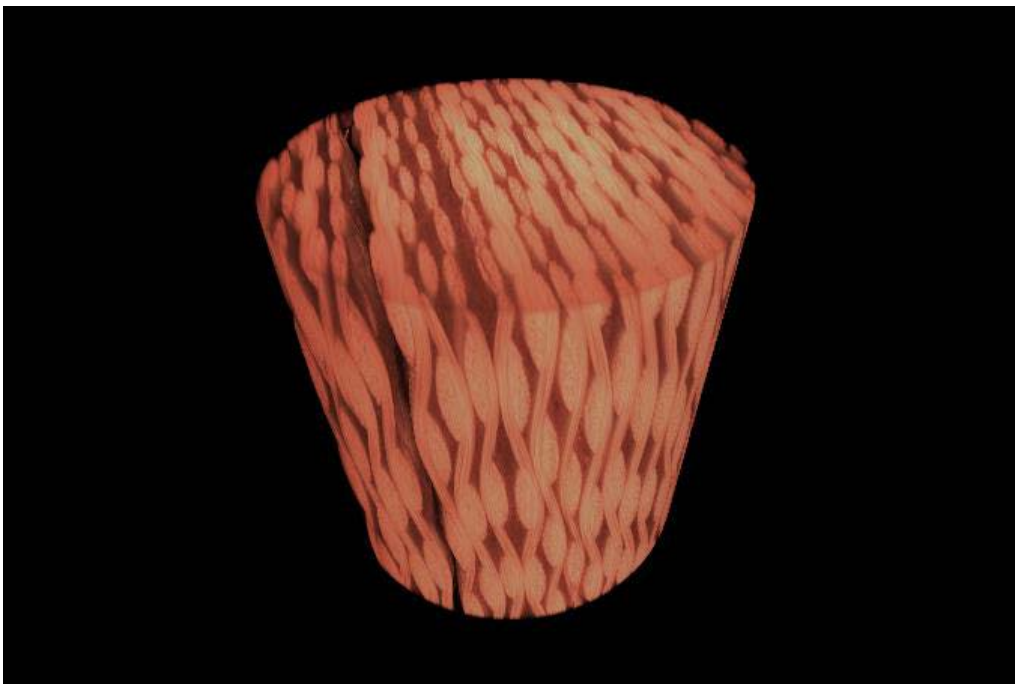

Figure 9-8. Volumetric reconstruction of the delamination in the µ-CT sample

9.6. Delamination and Fibre Breakage

An example of failure in samples tested in air is shown in Figure 9-9. The sample was a woven GFRP with a laminate thickness of 5 mm. The presence of delamination and fibre breakage was verified by SEM in (8.3.2 and 8.3.4). This damage is revealed in the 3D model recreated using µ-CT data, and is shown in Figure 9-9 and Figure 9-10.

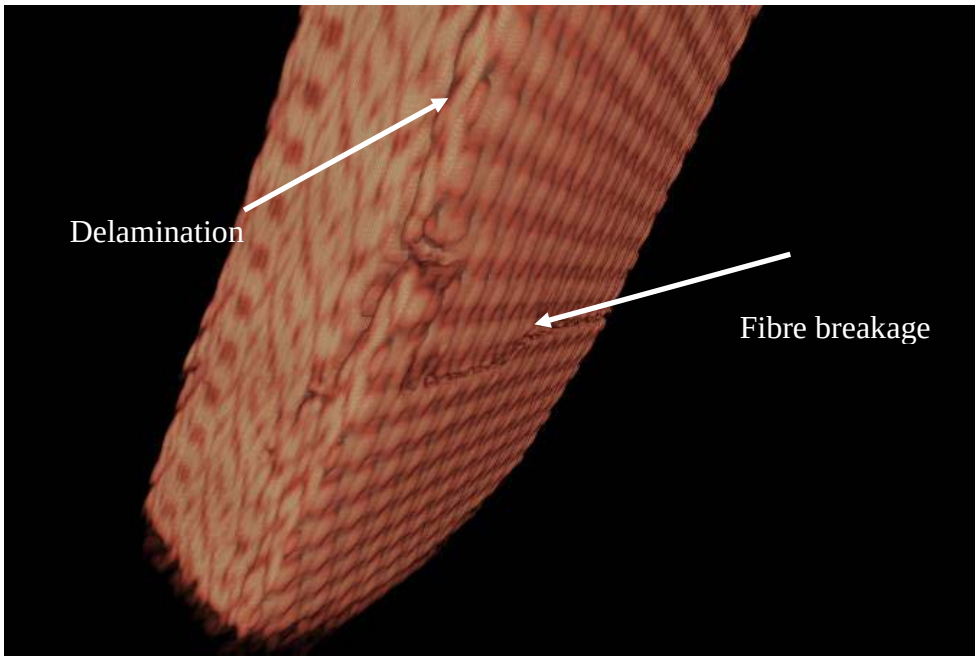

Figure 9-9. Failure damage around central area of a sample tested in air. The reconstructed volume reveals delamination and fibre breakage.

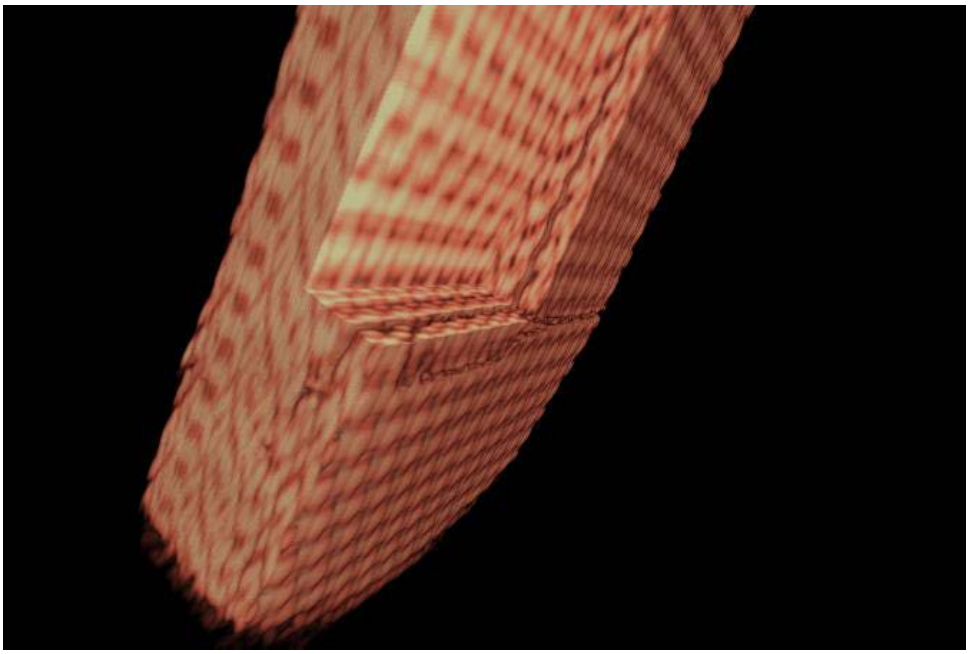

Figure 9-10. Failure damage around central area of a sample tested in air. The reconstructed volume reveals delamination and fibre breakage.

The delaminated and damaged area looks darker in the image (Figure 9-11 and Figure 9-12). This obviously corresponds to the damage geometry seen at the surface by optical and electron microscopy in (8.3.2).

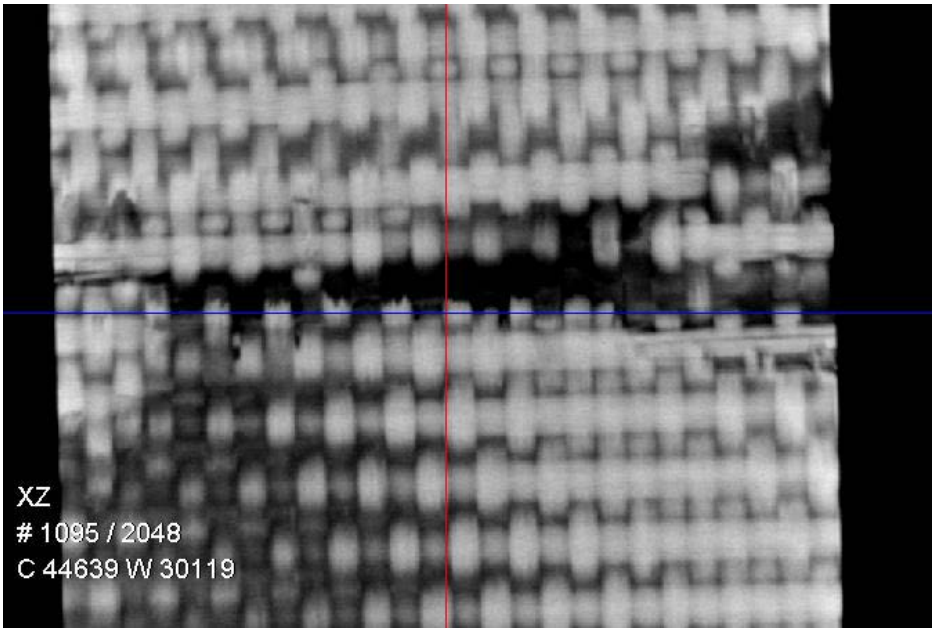

Figure 9-11. Micro-CT reconstructed cross-section (x-z plane).

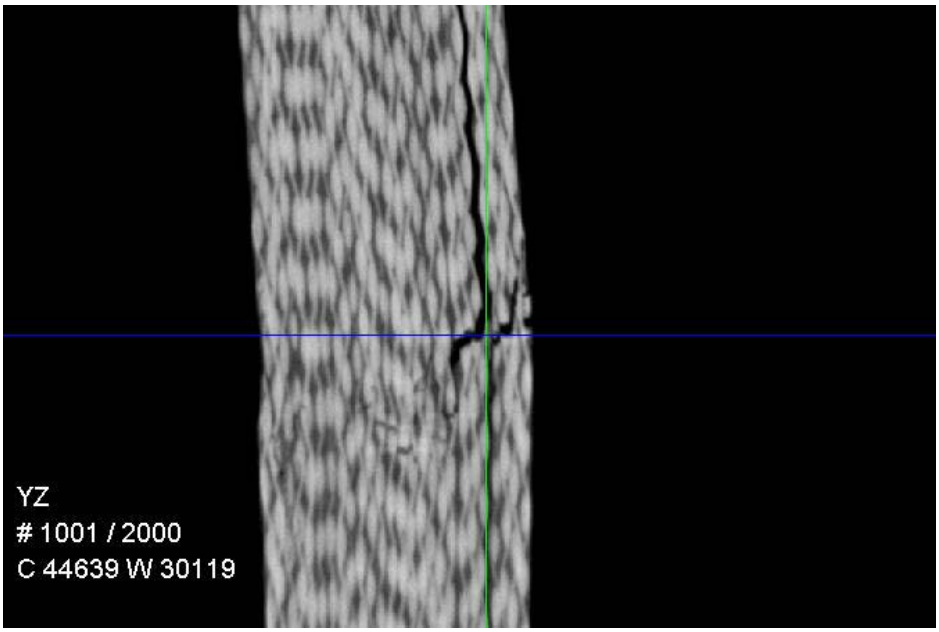

Figure 9-12. Micro-CT reconstructed cross-section (x-z plane).

9.7. Summary

The results from X-ray tomography show that μ-CT is a suitable technique to inspect the fibre bundle arrangement. The distinction between E-glass fibres, epoxy resin and air is satisfactory, thus allowing a perfect visualization of the bunch of fibres. The structural design of fabric is very well characterized. The sinusoidal shape of the longitudinal bunch of fibres and the oval-shaped cross-sectional area of the perpendicular bunch of fibres are distinguishable. However the technique does not have the resolution to measure individual fibres largely because these are too close together.

In addition, X-ray micro-tomography can assist in quantifying of the interior geometry of defects and discontinuities such as delamination, in GFRP laminates. A series of tests to evaluate the ability to identify delamination indicated that the critical experimental parameter is the magnification. It was possible to qualify the three dimensional structure of inner damage and fibre breakage.

Chapter 10

Finite Element Analysis of Turbine Blade

10. Finite Element Analysis of Turbine Blade

With reference to the methodology of fatigue life prediction (Figure 3-1), this chapter addresses the final objective of this project, the fatigue life prediction of a tidal turbine blade. Initially, the mechanical properties obtained through a series of mechanical tests including tension, shear and fatigue with the aid of the DIC method are used to generate input data for the FE analysis of blade. Furthermore the loading history predicted by hydrodynamic analysis in chapter 5, is used as input data for the boundary conditions in ANSYS modelling of the blade. By running the ANSYS simulation of the blade critical elements where the strain is maximum are detected and by performing the ACP in ANSYS environment, the Tsai-Hill failure criterion is used to predict failure. Stress analysis is also done through the thickness direction of the blade skin and therefore the magnitude of stresses/strains induced in individual plies are predicted. This is of special interest, since failure can be predicted in the through-thickness direction of the blade skin. Finally ANSYS n Code Design Life based on experimentally-generated strain-life curve is used to predict the fatigue life of the composite blade.

Fatigue failure in tidal turbine composite blades is due to the cyclic strains and/or stresses brought on by the variation in tidal current velocity. In this section, a methodology is developed for fatigue life prediction of composite blades, therefore the maximum cyclic strains on the blade are calculated with respect to the cyclic tidal current velocities. In this methodology, strain-life approach is employed in combination with Finite Element analysis to conduct analytical fatigue life assessment. Finally, given the material properties obtained from experiments, fatigue damage of the component is calculated based on Rain-Flow counting analysis and Miner's rule. In the following sections, FE analysis of blade for fatigue life prediction is discussed in more detail.

10.1. FE Analysis

In order to perform stress and failure (Tsai-Hill) analysis on the FE model of the blade, mechanical properties obtained by performing tension and shear tests on GFRP were introduced into the FE model of the blade (Table 10-1). Subsequently, the radial force distribution obtained from hydrodynamic analysis (chapter 5, section 5.1) was applied on the FE model of the blade. By applying forces calculated using the hydrodynamic model for two cases (normal and extreme tidal current velocities), the mechanical response of the blade is evaluated. The results of these analyses are summarized in Table 10-2.

Table 10-1. Mechanical properties for woven glass fibre reinforced epoxy resin laminates

Type of mechanical testing	Material characteristics for a biaxial woven fabric composite	Woven GFRP (0°/90°)
Tension	Longitudinal elastic modulus E_x(GPa)	21.6
	In-plane transverse modulus E_y(GPa)	21.6
	Major Poisson's ratio ν_{xy}	0.25
	Longitudinal ultimate tensile strength (MPa)	320
	In-plane transverse ultimate tensile strength (MPa)	320
Shear	In-plane shear modulus (GPa)	3.52
	In-plane ultimate shear strength (MPa)	80
	Inter-laminar shear modulus (GPa)	2.1
	Inter-laminar shear strength (MPa)	40

Table 10-2. Static analysis of FE model of blade structure

Load case	Tidal current velocity (m/s)	Max longitudinal Stress (hot spot) (MPa)	Max longitudinal Strain (hot spot) (%)
normal	2.5	180	0.79
extreme	3	255	1.13

10.2. Structural Performance of GFRP Composite Blade (ACP)

In this study, the interest has been focused on a composite blade simulation which is based on the knowledge of the mechanical data achieved from experiment. The tangential and axial distribution of loads were determined from a hydrodynamic model and were used as an input data for the FE model of the blade in ANSYS. The mechanical properties from mechanical tests (i.e. tensile, shear and fatigue tests) were used as an input data for ANSYS Composite Pre-post. The blade was considered as a cantilever beam and the root of the blade was fixed in all directions. The strain and stress distributions on the GFRP composite blade are shown in

Figure 10-1, showing critical zones on the surface of the blade. Higher stress/strain concentration near the root area of the blade indicates that these are the critical zones where fatigue failure may initiate. Maximum normal stresses/strains are found in the skin of the composite blade near the root area which forms the main structural load-bearing member of the blade. These high stresses are due to the large flap-wise bending moment (Figure 5-4) caused by the thrust force.

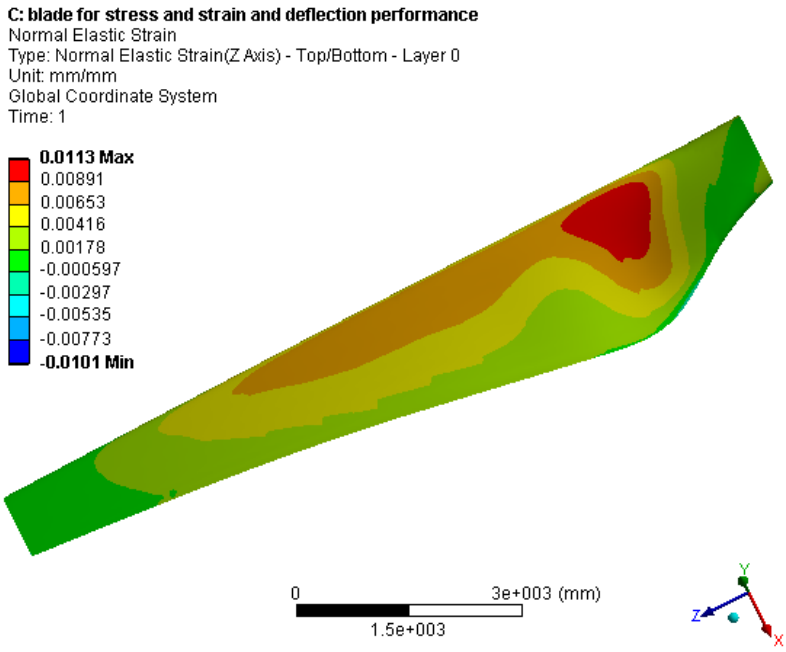

Figure 10-1. Contours of strain distribution in FE model of blade operating at 3 m/s tidal current velocity.

In order to predict the critical regions of the blade where failure is most likely to occur, the Tsai-Hill criterion was used. Figure 10-2 shows the Tsai-Hill factor for the GFRP composite blade. It is clear that the surface of blade is more susceptible to failure, therefore the first indication of failure is predicted to occur in the skin of blade near the root area.

In the tensile and shear tests of the GFRP composite it was found that the main failure modes are interfacial de-bonding, fibre pull-out and delamination. The main failure modes due to 3PB test are tensile and transverse resin cracking, delamination, fibre breakages and resin-fibre interfacial de-bonding. In the case of the 3PB test, resin cracks and delamination can be found on the surface of the damaged specimen where tensile stresses are developed, and the fibre breakage was observed on both sides where tensile and compressive stresses are created. Resin-fibre interfacial de-bonding was frequently observed in the middle of the cross-sectional area of the test coupons where shear stresses are developed. Given the magnitude of stresses and strains induced in each layer of the composite blade due to the tidal current velocities and comparing this magnitude with the mechanical properties of the composite, similar failure modes can be predicted.

Based on the Tsai-Hill failure criterion, critical zones on the blade surface are detected (Figure 10-2). The normal and shear stress variations with respect to the thickness of the blade were explored in these zones.

Figure 10-3 to Figure 10-5 show the variations of Tsai-Hill factor and stress/strain with respect to the skin thickness of the composite blade. These values are calculated in individual plies. The contours were built using ANSYS Composite Pre-Post software.

By comparing the magnitude of normal and shear strains/stresses predicted by ANSYS on the blade with the normal and shear strains in individual plies predicted in the 3PB simulation (chapter 6) and the experimental values obtained using DIC method (chapter 7, sections 7.2, 7.3 and 7.4), it can be deduced that, the potential failure modes in the shell structure of the blade at plies located near the top surface of blade will be delamination and fibre breakage.

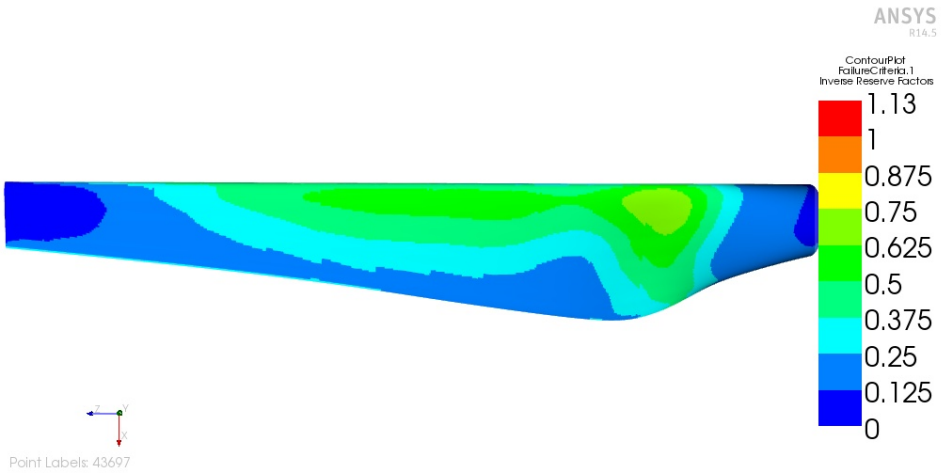

Figure 10-2. Contours of Tsai-Hill failure criterion on FE model of blade at 3 m/s water velocity, showing critical zone (hot spot) where failure is predicted.

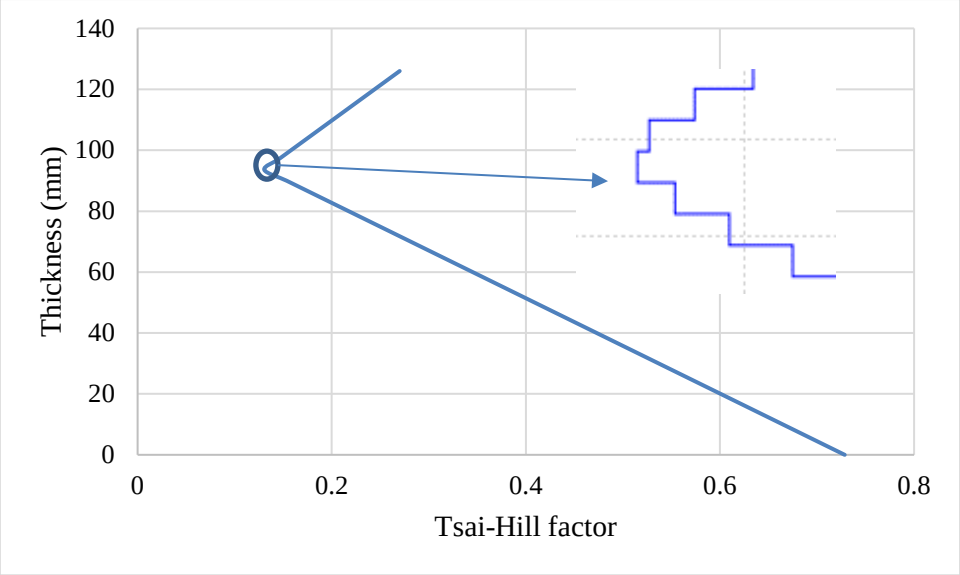

Figure 10-3. Tsai-Hill failure factor, Variations through the thickness direction of the blade skin at the hot spot on turbine blade at the velocity of 3 m/s.

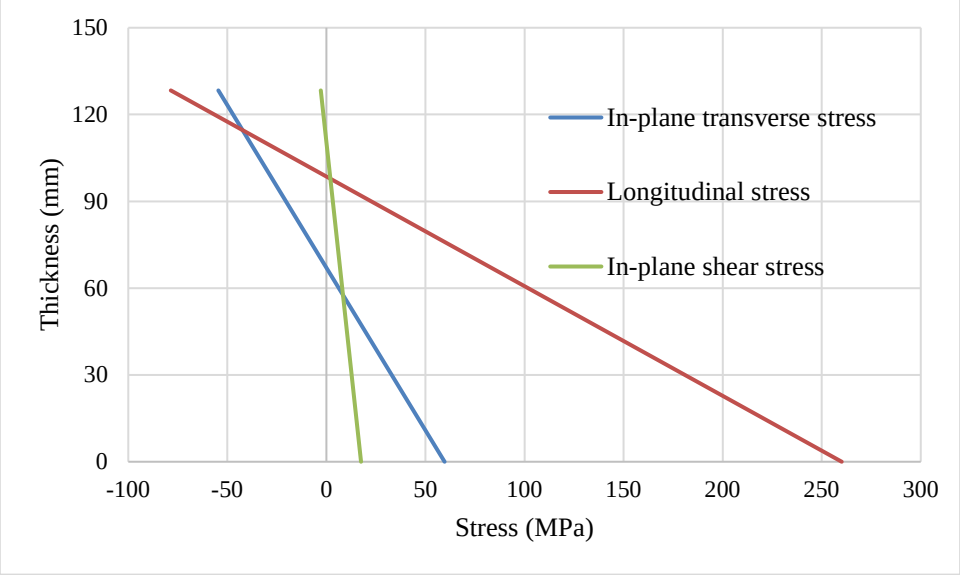

Figure 10-4. Stress distribution through the thickness direction of the blade skin at the hot spot on turbine blade.

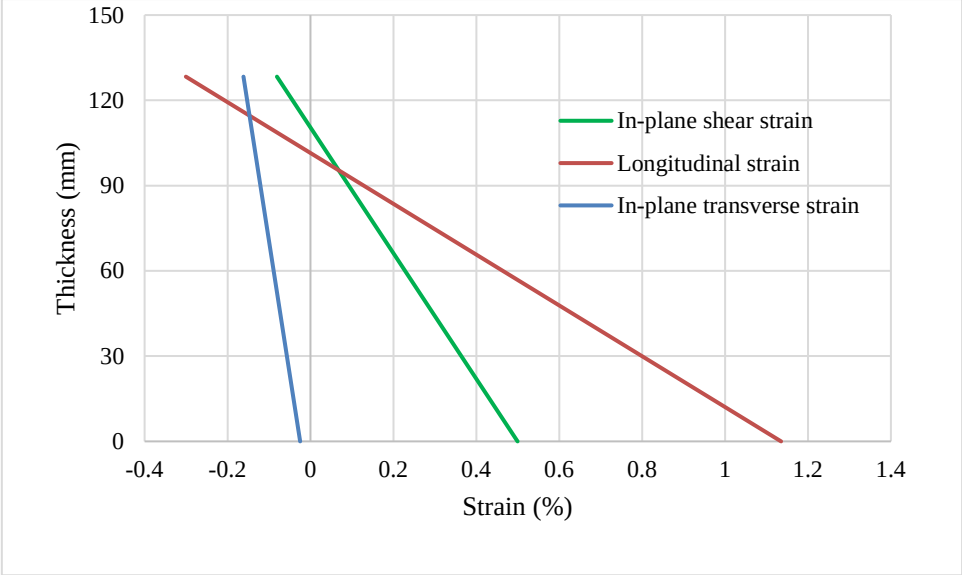

Figure 10-5. Strain distribution through the thickness direction of the blade skin at the hot spot on turbine blade.

10.3. Fatigue Life Prediction Using ANSYS n Code Design Life

For fatigue life prediction using n Code Design Life module in ANSYS, experimentally generated S-N curves and fatigue loads are used as input data. Initially, a time-series of velocity of tidal current is transformed to time-series of the load. The assumption is that the 7 days period of tidal current velocity pattern (Figure 5-5) is repeated for the entire year. Therefore, the blade experiences a time-series of axial (thrust) and tangential loads during a year similar to the pattern of tidal current velocity. These cyclic hydrodynamic loads acting on the blade are the main source of fatigue. Figure 10-6 shows the fatigue life contour on the blade when these cyclic hydrodynamic forces are imposed on the FE model of the blade.

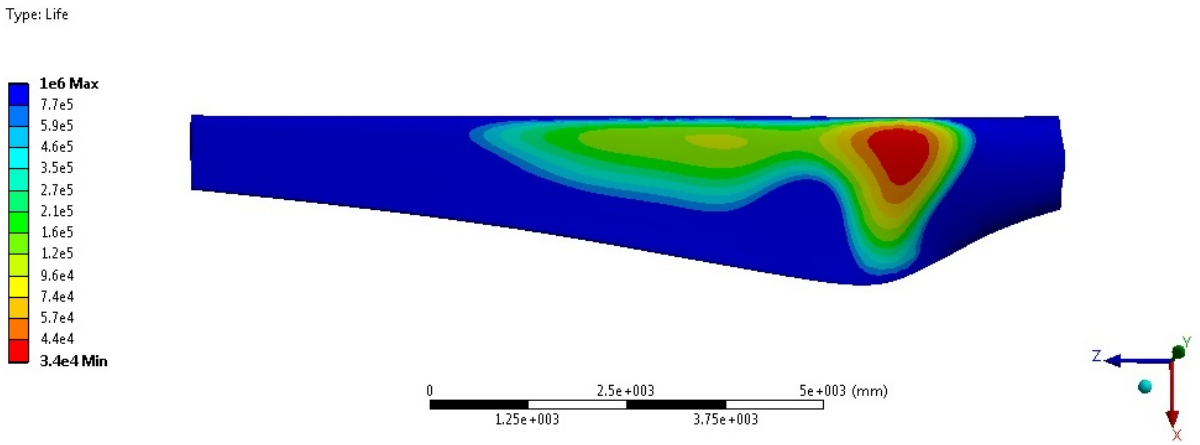

Figure 10-6. Contours of fatigue life of blade (hours).

From Figure 10-6, the minimum fatigue life for the composite blades is predicted to be about 35000 hours (about 4 years).

The effect of the thickness variation of the composite blade skin on the critical element on the blade is illustrated in Figure 10-7. As it can be seen in this Figure, a small decrease in maximum thickness has a substantial effect on minimum fatigue life of the blade. For instance reducing the maximum thickness by 15%, the minimum fatigue life of blade decreases by 75%.

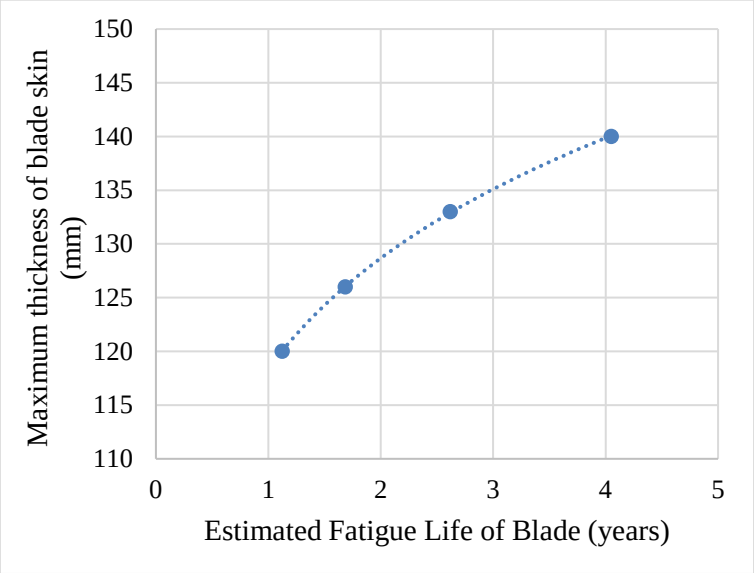

Figure 10-7. Effect of thickness (laminate of blade skin) on FE predicted fatigue life of tidal turbine blade in a tidal zone with 3 m/s maximum velocity and about 20% neap/spring variation.

Table 10-3 shows the effect of three structural designs (Figure 10-8) on mechanical and fatigue behaviour of GFRP composite blade. It is clear that shear webs can improve the bending properties by 10-15%. However due to the effect of strain concentration factor mentioned above (Figure 10-7), the effect of shear webs on fatigue life is significant.

The fatigue life of composite blade in air increases by 2.5 times indicating the effect of sea water on fatigue properties of GFRP composite blade. This is due to the difference between the slope of strain-life diagram of fatigue test results when samples are subjected to sea water and air environments (Figure 8-4). As it was mentioned in section 8.2.1, at the strain level below 1.3% (a regime of stress and environment dependence) a substantial difference in fatigue data points can be observed for the specimens tested in air and sea water. Fatigue failure analysis results which were discussed in sections 8.3, 8.4 and 8.5, have shown the degradation effect of

sea water on GFRP and therefore the difference observed in FE predicted fatigue life of composite blade in air and sea water is in agreement with experimental data.

Table 10-3. Mechanical and fatigue performance of GFRP composite blade design detailed in Figure 10-8.

Structural designs	Max bending strain (%)	Max bending stress (MPa)	Predicted fatigue life (years)	
			sea water	air
Blade without shear webs	1.23	285	2	5
Blade with shear webs	1.13	255	4	10
Blade with spar caps	1.02	230	7	14

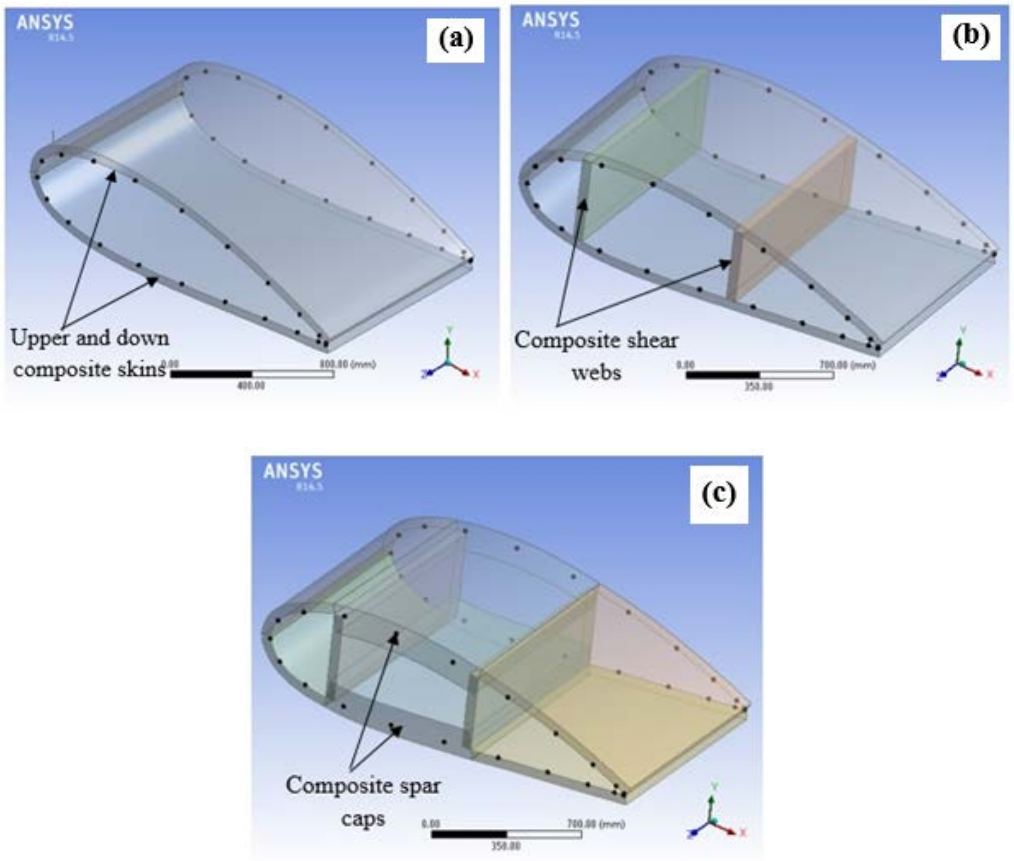

Figure 10-8. Simplified hydrofoil shapes used for FE analysis of the blade. (a), hollow blade showing empty space between the skins, (b) blade with two shear webs inserted between top and bottom skin (located at 15% and 50% of chord length back from the leading edge, (c) blade with spar caps

10.4. Fatigue Life Prediction of Critical Element on the Blade Using FE Analysis

In this section a method is introduced to assess the fatigue damage of highly stressed components such as tidal turbine blades. The method focuses on the maximum strain (i.e. critical elements/nodes on the FE model of blade where the strain magnitude in maximum) caused by bending loads which are predominantly due to the fluctuation of thrust load. In this method, the strain-life approach (Wannenburg *et al.*, 2009) is employed in combination with Finite Element and Hydrodynamic analysis to conduct analytical fatigue life assessment. Finally, fatigue damage of component is calculated based on the Miner's rule. A MATLAB code (Appendix 6) was developed based on this method for fatigue life prediction.

When the number of elements is in the thousands and the load histories are large, it becomes useful to reduce the size of the problem by selecting only the most critical elements with the maximum stresses/strains. In this work, this was done by applying loading-time history on FE model of blade to determine the critical element/node with high strain magnitude. Therefore the top critical fatigue element (hot spot) where the index of Tsai-Hill failure criterion is relatively high (Figure 10-2) was detected. As a result, a time-series strain at this hot spot is generated (Figure 10-9). The Figure shows the cyclic strains brought on by the fluctuation in hydrodynamic loads.

In the next step, the calculated strain-time histories (cyclic strains) are cycle counted using a rain flow counting analysis. This yields a spectrum of strain ranges and associated number of counted cycles. Then, the power law equation between strains (ε_{max}) and fatigue life (N), is used to provide the number of cycles to failure for maximum strain levels in Figure 10-9.

$$\boldsymbol{\varepsilon_{max}} = \boldsymbol{K}(\boldsymbol{N})^{-\boldsymbol{A}} \qquad \text{10-1}$$

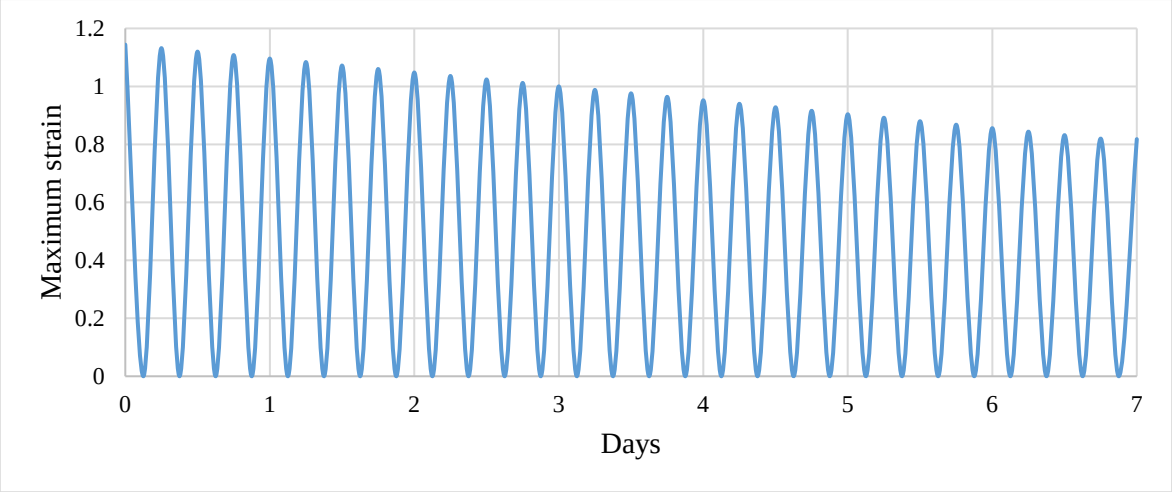

Figure 10-9. Cyclic strains (time series strain) at critical element (hot spot) due to the variations in inflow velocity during 7 days period.

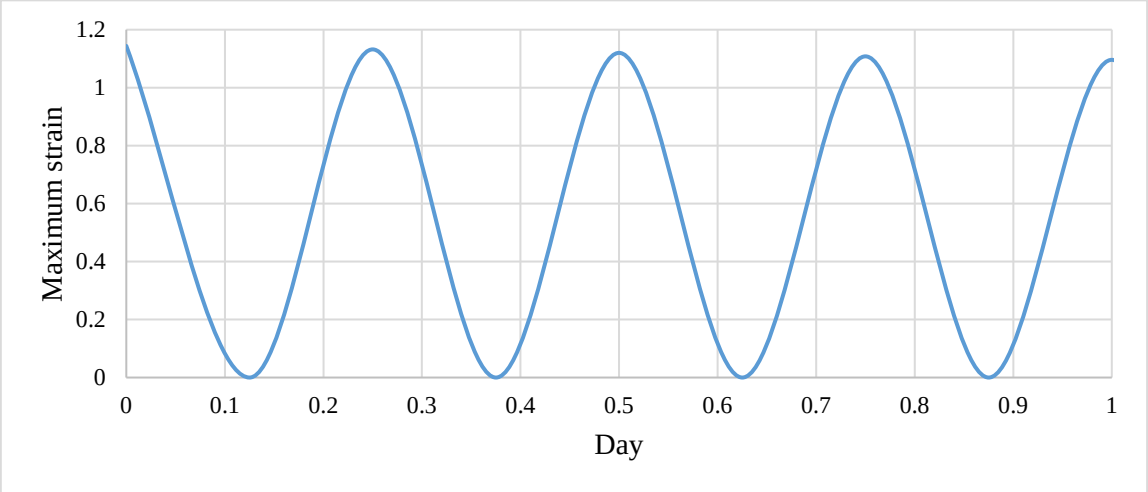

Figure 10-10. Cyclic strains (time series strain) at critical element (hot spot) due to the variations in inflow velocity during one day.

Finally damage fraction is summed to calculate the 7 days damage and therefore the fatigue life of turbine blade using damage accumulation theory of Miner (Wilkins, 1956) is estimated.

$$\text{Damage}_{(7\ days)}=\sum_{i=1}^{N_t}\left(\frac{n_i}{N_i}\right) \qquad 10\text{-}2$$

where

N_t is the number of tidal movements during the 7 days period. N_i and n_i are the number of cycles to failure at a given strain and the number of counted cycles at that strain during each tide. From above equation, damage is calculated for 7 days period. By assuming that the water

velocity spectrum repeats during each year with the same pattern, damage for one year can be obtained from:

$$Damage_{\ (1\ year)} = \text{Damage}_{(7\ days)} \times \left(\frac{365.25}{7}\right)$$

10-3

From the amount of damage for one year, life can be calculated as:

$$Life = \frac{1}{Damage_{\ (1\ year)}}$$

10-4

It must be noted that the predicted fatigue life by above method is valid for critical element/node or hot spot. In general the above method should be implemented to calculate fatigue life at other potential critical elements, however the minimum fatigue life of blade is obtained at hot spot of blade.

10.5. Summary

In this study, the interest has been focused on FE analysis of composite blade which is based on the mechanical properties of composite materials obtained from experimental tests. By defining the boundary conditions and mode of loading to the FE model of the blade, the maximum stress/strain in the composite blade and the possibility of the blade failure with respect to the operating conditions of turbine are investigated. For two normal and extreme tidal current velocities (i.e. 2.5 and 3 m/s), maximum stress/strain and Tsai-Hill failure index was predicted at the hot spot (critical zone) of the composite blade. ACP module, contributed to predict the stress/strain distribution through the thickness direction of composite laminated blade skin, as a results, the magnitude of stresses/strains induced in individual plies through the thickness direction on the blade skin were predicted.

Minimum fatigue life of the composite blade at the hot spot was estimated based on the strain-life approach. This was done by defining the power law equation fitting the fatigue data points on the S-N curve which was generated via fatigue testing. A rain flow analysis was also performed on the cyclic strains that the blade experiences and finally Miner damage rule was used to assess the damage of composite blade. Alternatively ANSYS n Code Design Life was used to map the contour of fatigue life and therefore the fatigue life was calculated for all elements (nodes) of FE model of the blade.

Chapter 11

Conclusions

11. Conclusions

The main aim of the present work was to estimate the fatigue lifetime of a low cost composite tidal turbine blade on the basis of FE analysis (chapter 10, sections 10.3 and 10.4). This was done by generating data in the form of S-N curves (chapter 8, section 8.2.1) to evaluate the environmentally affected fatigue properties of woven composites. As a result, controlling factors and limiting issues regarding the performance of the GFRP composite were identified and confidence was obtained in the use of GFRP materials in tidal turbine applications. This was obtained initially by determining failure mechanism in GFRP material subjected to mechanical loading (chapter 6, sections 6.1 and 6.2 and chapter 7) and then by obtaining and characterizing the mechanical properties of the GFRP material (chapter 6, Table 6-1 to Table 6-3) and (chapter 7, Table 7-3). Failure analysis techniques were used to identify failure modes and to observe damage development during the fatigue test of GFRP composite materials (chapter 8, sections 8.3, 8.4, 8.5). Mechanical properties have been determined based on the DIC and FEM methods for full field strain measurements (Chapters 6 and 7).

In this study, a methodology (chapter 3, Figure 3-1) for stress analysis and fatigue life prediction of composite tidal turbine blades was developed by using mechanical and bending fatigue properties of GFRP material measured in sea water (Table 8-1) . The methodology is based on a combination of (a) a hydrodynamic model based on stream tube approach to estimate the distributions of fluid forces (tangential and axial) on the blade (chapter 5); (b) a FE structural model for stress and fatigue analysis (chapter 10) and (c) cyclic and quasi static mechanical tests at the laboratory scale in both sea water and air environments to generate realistic mechanical data for FE modelling (chapter 8, section 8.2) based on orthotropic composite. As indicated in chapter 3, Figure 3-1, this is obtained through different steps as below. Specific objectives detailed in (chapter 1, section 1.2) are met with the following steps as well:

1. Mechanical properties and stress-strain response of GFRP (chapter 3, 6 and 7).

In order to provide mechanical properties for FE analysis of GFRP composite turbine blade, initially a series of test programs was defined. This includes performing a range of quasi-static mechanical tests including tensile, shear and 3PB tests (Figure 3-7, Figure 3-9, Figure 3-11) in conjunction with a full field strain measurement technique via DIC system (section 3.4), in order to assess and obtain the on and off axis mechanical properties of the GFRP material

(Figure 6-6 and Figure 6-7 and Figure 7-18 and Figure 7-19). Therefore stress-strain curves in each of these mechanical tests were built on the basis of DIC strain measurements (Figure 6-13 and Figure 6-14 from chapter 6 and Figure 7-5, Figure 7-12 to Figure 7-17 from chapter 7). In addition DIC strain localization maps contribute to the analysis of damage development during the composite sample deformation in each of mechanical test.

2. Fatigue testing and Strain-Life curve (chapter 3 and chapter 8)

In order to provide fatigue properties (i.e. Strain-Life diagrams) for FE fatigue life prediction of composite blade, a large number of coupons were subjected to a 3PB fatigue test. Since composite turbine blades are in direct contact with sea water, a fatigue rig was designed capable of applying cyclic loads while the samples are in direct contact with sea water (section 3.8.2, Figure 3-21 to Figure 3-24 from). The main objective of fatigue testing was to produce strain-life data (Figure 8-4) for the FE analysis of the blade. Therefore the blade performance can be evaluated using real mechanical properties of the composite which are obtained by the experimental techniques.

Using the fatigue rig, a large number of coupons were tested under a 3PB fatigue load configuration in both sea water and air. The DIC technique was also employed to map the strain distribution (Figure 8-11 to Figure 8-14 from) during the fatigue test and to determine the elastic modulus evolution associated with fatigue damage (Figure 8-17 to Figure 8-20). Modulus decay gives clear evidence about damage localization and gradual deterioration of mechanical properties of composites during their fatigue history. Specific characteristic parameters (ΔS and D) are proposed for damage evaluation which are a function of modulus decay parameter (sections 8.3.4 and 8.3.5)

3. Microscopic and Damage development analysis (chapter 6, 8 and 9).

Failure analysis was performed to identify failure modes in woven GFRP composite under tension (Figure 6-2 to Figure 6-4 and Figure 6-9 to Figure 6-12) and bending tests (Figure 6-19). Most importantly, environmentally affected fatigue failure mechanisms were evaluated (sections 8.3, 8.4 and 8.5). This was done in order to predict the failure of composite tidal turbine blade once the blade is subjected to static and cyclic loads in sea water conditions. A range of characterization techniques including DIC, SEM, and reflected light microscopy were used and the main failure modes including delamination, inter-facial de-bonding between fibres and matrix, matrix cracking, fibre degradation, fibre breakage (Figure 8-21 to Figure 8-24) and

fibre/matrix degradation (Figure 8-26 to Figure 8-29) as a result of sea water penetration in the matrix were investigated. EDX analysis was also used to reveal information about the degraded fibre-matrix interface region (section 8.5.1, Figure 8-30 and Figure 8-35) and finally the X-ray 3D micro-computed tomography technique was used to identify and measure the geometry and dimensions of internal defects such as delamination (chapter 9). Therefore performance limiting issues for the composite blade were clearly understood meaning that using composite materials resistant to above failure modes can improve the fatigue performance of the blade.

In addition, damage development analysis of composite under environmentally affected fatigue loads was investigated using stiffness degradation criterion (sections 8.3.3, 8.3.4 and 8.3.5). The conclusion was that delamination plays an important role in limiting the fatigue life of composite structures and components. Therefore confidence was acquired in the use of GFRP composite in tidal turbine blades, meaning that reducing the rate of delamination can increase the blade life. Therefore, using a laminated composite resistant to delamination can significantly improve the fatigue life of composite blades.

4. Hydrodynamic model (chapter 5).

In this step, a hydrodynamic model based on stream tube approach was used in order to determine the hydrodynamic loads (section 5.1, Figure 5-2) acting on the FE model of the blade. The loading history (section 5.2) on the blade is the most important input for FE structural analysis of turbine blade.

5. FE modelling of the blade (chapter 4 and 10).

In the next stage, a typical turbine blade was modelled using different modules in ANSYS environment. One of the main advantages offered by ANSYS was the use of the ACP module in order to define fibre orientation and lay-up of composite in order to create FE model of the blade (section 4.3.3). Many design criteria including lay-up of the woven composite, orthotropic properties of the composite obtained through the experiments (Table 4-2) and composite ply drops (Figure 4-7) were taken into account. This has made a positive contribution for fatigue life estimation of composite blade since stress and/or strain analysis on critical elements on the blade can be conducted in order to predict the magnitude of stress/strain between layers. Also using ACP, the Tsai-Hill failure criterion was used in order to predict failure in FE model of the composite blade (Figure 10-2). ACP enabled the estimation of stress magnitude between layers (Figure 10-4).

6. Fatigue life prediction by FE analysis (chapter 10).

In the final stage, by incorporating mechanical properties obtained through experiments (i.e. tension, shear and 3PB fatigue test in sea water condition) with FE model of turbine blade, structural analysis was performed for stress and fatigue analysis of the blade. Initially critical elements/hot spots on blade in terms of maximum strain were detected and then ANSYS n Code Design Life module was employed to predict the fatigue life (section 10.3, Figure 10-6). The fatigue life of a woven GFRP composite blade was estimated to be about between 4-5 years. This means that if replacing tidal turbine blades every 5 years is economically viable, the low cost GFRP composite can be a good candidate for tidal turbine systems.

This study delivers a methodology for fatigue life estimation of GFRP composite tidal turbine blades based on experimental measurements. Three point bending fatigue and quasi-static standard testing of a low cost candidate (woven GFRP) materials was conducted to enable application of the methodology for predicting the life of tidal turbine blades. Some important conclusions and contribution from this investigation are discussed as follows;

- ✓ Fatigue life of tidal turbine composite blade is sensitive to the magnitude of stress or strain distributed on blade surface. This is because of the slope in the strain-life diagrams for GFRP composites, consequently a small increase in stress or strain on the blade causes a significant drop in minimum blade fatigue life (Figure 10-7).
- ✓ The flexural fatigue properties were determined for the woven laminates by means of 3PB fatigue test rig with a strain ratio of R=0.1 at strain levels of 30-90% of the maximum static strain (section 8.2). The laminates exhibited a decreasing failure stress with an increasing number of load cycles. The decrease was similar to those previously reported in the literature for fibre reinforced materials with a maximum load reduction of about 40% for 10^6 load cycles. The failure generally initiated on the compression side and a damage zone developed near the contact. SEM examination of the specimens identified some of the mechanisms involved in failure to be tensile matrix failure, inter-laminar cracking, delamination, interfacial fibre-matrix de-bonding, crazing, shear cracks and tensile/compression glass fibre breakage in response to fibre tension and fibre buckling.
- ✓ To discuss the fatigue failure modes of the GFRP composites under flexural loads, microstructural analysis via scanning electron and light microscopes was performed near the failed zones. It was found that resin cracking, delamination, fibre breakage as

well as resin-fibre interface de-bonding are the main visible failure mechanisms of GFRP under flexural loading.

- ✓ Considering damage accumulation in GFRP composites during the fatigue test, approximately 80-90% of the fatigue life is taken by stage 2 associated with the delamination failure mode (section 8.3.3 and 8.3.4), consequently for composite tidal turbine blades, reducing the delamination rate plays an important role for increasing the fatigue life of the blade.
- ✓ Low cycle fatigue of GFRP composites is a stress-dependent and environment-independent regime. This is due to the overlapping of fatigue data points for samples tested in air and sea water environment as there is insufficient time for fibre corrosion reactions to be significant, However high cycle fatigue can be classified as a stress-dependent and environment-dependent regime. This is because of considerable difference between fatigue data points of wet and dry conditions due to the effect of water penetration in matrix micro-cracks and fibre corrosion (section 8.2.1).
- ✓ Due to the lower measured slope of the strain-life curves of C-GFRP than GFRP, it is predicted that the fatigue life of GFRP blade is more vulnerable to the magnitude of normal and shear stresses induced on the blade than the C-GFRP blade. Thus the use of a few carbon fibres in the main loading direction on the tension side may be a cost-effective method to increase blade life (section 8.2.3).
- ✓ Microscopic inspection of the fatigue-loaded samples gives indication of a degraded fibre/matrix interface area for samples exposed to sea water environment with premature failure, therefore it is concluded that the degradation of fibre/matrix interface is a controlling factor in the environmental performance of the GFRP composite (section 8.4 and 8.5).
- ✓ Near the root area on the composite blade is the critical zone where potential fatigue failure modes such as delamination and fibre breakage might initiate (Figure 10-2).

11.1. Hydrodynamic and FE validation

1. The results of hydrodynamic modelling of tidal turbine blade have been compared and validated with those work from literature (Kennedy *et al.*, 2012; Grogan *et al.*, 2013). In terms of hydrodynamic model, using the same chord length and twist angle distribution of the blades (i.e. two blade profile with 3.5 and 12 meter length) in the hydrodynamic model in this project (MATLAB code detailed in appendix 3 and 4),

resulted the same axial and tangential force distribution detailed in the literature (appendix 7). This shows that the hydrodynamic model used in this study is validated.

2. Results of FE analysis of composite tidal turbine blades are validated based on the information from the literature. Using the same blade profile and geometry (twist angle and chord length distribution) detailed in (Kennedy *et al.*, 2012; Grogan *et al.*, 2013 and applying the same material and lay-up configuration, resulted in similar structural performance of the blade (appendix 7). This shows that the boundary condition and element type of SHELL are suitably defined for FE model of composite tidal turbine blades.

Chapter 12

Future work

12. Future Work

In this chapter, some suggestions in the context of future work regarding the assessment of FRP composites for wind/tidal turbine blades are discussed. This is considered from different points of view including type of material, design, experimental techniques (mechanical and fatigue tests), failure analysis techniques and FE analysis, However composite blade performance still needs to be evaluated to determine the validity of the analysis. In the following sections these ideas are discussed.

12.1. Experimental Techniques

12.1.1. Effect of Environment

Corrosion-fatigue behaviour of CFRP, GFRP and KFRP composites need to be investigated. In order to characterize the effect of corrosion, fatigue tests should be done on composites in distilled water and then by adding artificial salt in distilled water (to the tank of fatigue rig), the effects of salt on composite can then be assessed. This can be done by making comparison between fatigue failure mechanisms of composites in different amounts of salt. If applicable such test can determine which types of salt have a greater impact on the fatigue life of composites.

12.1.2. Mechanical Tests

Aside from the bending fatigue behaviour of a composite, in-plane shear, inter-laminar shear and tension-compression fatigue behaviour of a composite needs to be evaluated. Durability of composite wind/tidal turbine blades depends on all components of stresses/strains. In fact cyclic behaviour of all components of stress and/or strain (longitudinal, transverse, in-plane and inter-laminar shear) on FE model of blade should be assessed. This will provide an accurate methodology for fatigue life prediction of composite wind/tidal turbine blades.

The inter-laminar bending behaviour of composite is of special interest near the connecting area of the blade root. Performing inter-laminar shear and in-plane shear fatigue tests in order to predict fatigue failure of composite materials due to the in-plane and inter-laminar shear stresses can make substantial contribution for fatigue damage assessment of composite wind/tidal turbine blades.

In addition, performing tension-compression or tension-tension fatigue tests in order to predict fatigue failure of composites due to the tension and compression stresses can increase our

understanding about fatigue life of composite blades. Since tensile tests take place under conditions of uniform stress.

12.1.3. Effect of Size and Fibre Orientation

The size effect (thickness, width and span to thickness ratio) needs to be assessed in terms of fatigue tests on each composite (GFRP, CFRP and KFRP) to see the effect of these parameters. The defect concentration and manufacturing variability this reveals would be important to set appropriate safety factor in design.

The effect of fibre orientation on all types of fatigue testing (In-plane, Inter-laminar shear and tension-compression) also needs to be evaluated. This is necessary since in the designing and manufacturing processes of composite wind/tidal turbine blades, shear webs with $\pm 45°$ fibre orientation can increase the shear strength of composite blades. In addition, placing some composite plies with $\pm 45°$ fibre orientation at the blade surface might reduce the magnitude of shear stresses in critical areas. This has been demonstrated on static stress analysis but the effect on fatigue is less well documented.

12.2. Experiments on a Small Scale Blade

Most work in this thesis has been done on test coupons. Performing bending fatigue test on small scale blade using fatigue test rig which has been designed for this project is necessary for validation of the fatigue failure approach. Fatigue test on small scale blades can be carried out by applying cyclic loads at the tip of the blade and then using the DIC technique to determine strain distribution at critical zones on the blade surface is then possible. It should be noted that the critical zones on the blade surface were initially identified by applying static load on a small scale blade and the DIC system was successfully employed to measure the strain maps. In a fatigue test of the small blade the focus can be made on strain mapping during the cyclic loading. Using several small scale blades, a full S-N curve for composite characterization of the fatigue behaviour can be constructed. In the meantime, the small scale blade which was modelled in ANSYS workbench can be used in ANSYS n code Design Life, therefore FE modelling of blade and fatigue life prediction can be validated using experimental fatigue test results on small scale blade.

12.3. Effect of Ply-Drop on Test Coupons

It is important to evaluate the effect of ply drops in FE simulation and mechanical/fatigue testing of coupons to assess the performance of the as-manufactured composite. Using the DIC

technique the effect of ply drops on strain distribution can be observed. This should be done by performing static mechanical and fatigue tests on composite samples with ply drops in the sample configuration. Applying static and cyclic 3PB on samples with such ply drops can increase our understanding about what happens near the ply drops in terms of stress/strain concentration and failure mechanisms. In addition, mechanical tests on samples with ply drops can be simulated in ANSYS Composite Pre-post and ANSYS n Code Design Life, therefore, the effect of processing on stress/strain concentration can be modelled.

12.4. Predicting the Rate of Crack Growth Based on FE and X-ray CT Methods

In this study it was shown how CT scan technique can be used to detect failure modes including delamination, micro-cracks in composite structures and materials. Using X-ray 3D tomography the geometry and dimensions of crack can be measured and characterized. A test sample could be fatigued and regular CT scan undertaken to follow damage evolution. This could be done ex situ (i.e. in a normal fatigue rig) or in situ (in a special loading rig in the CT scan). Using information about the geometry of delamination or cracks, an FE model can be constructed to simulate the effect of crack propagation and therefore the rate of crack growth can be estimated.

12.5. Failure analysis of degraded fibres

Although in this project SEM/EDX analysis gives a clear evidence of degraded glass fibres, more investigation on degraded fibres and glass fibre/matrix interface is required. During the fatigue testing of composite in sea water, DIC maps contributed to reveal localized strain giving evidence of sea water diffusion into the network of resin cracks. In this process, entrapped sea water can degrade both fibres and fibre/matrix interface by a mechanisms of ionic exchange which was discussed in this project. Electron microscopy showed this degraded fibres. To verify this, Nano-indentation technique could be useful. By applying indenter on individual glass fibres and comparing the stiffness of glass fibres for samples subjected to cyclic loads in both air and sea water, reduced properties of glass fibres (fibre strength decay) due to sea water penetration can be established. It must be noted that the micro-hardness testing technique was unable to measure the stiffness of glass fibres as the diameter of indenter is bigger than the diameter of glass fibres. Nano-indentation technique also can be used to establish fibre/matrix degradation which is usually observed in a form of interfacial de-bonding between fibres and matrix in fractography.

12.6. Validation of Hydrodynamic Loads

The results of hydrodynamic models could be validated using a small scale blade. The resultant load distribution can be evaluated on small scale blade using flume. In this case there is no need to provide a blade made up of real composite materials, tests can be done on single blade made up of different materials that are easier to manufacture (e.g. Aluminium).

12.7. ANSYS n Code Design Life

More research and studies should be carried out using ANSYS n Code Design life for durability or fatigue analysis of load bearing components like wind/tidal turbine blades with different geometry. Because ANSYS n Code Design Life is integrated within the ANSYS Workbench environment, it provides results and materials data from simulations within the framework directly to Design Life. Design Life durability results such as fatigue life or damage can be parameterized and included in design optimization studies. This means that various parameters in n Code design Life of composites such as weight, thickness of blade skin, fibre volume fraction, fibre orientations and types of fibres and matrix can be optimized.

In addition to offering stress-life and strain-life approaches, virtual strain gauges can be positioned on the finite element model and strain or stress time series extracted for direct correlation to help validate models. This time series could also be used for crack growth analysis, employing linear elastic fracture mechanics to predict how a crack will grow after initiation.

12.8. Materials

12.8.1. KFRP

Apart from carbon and glass fibre composites, another option for turbine blade application is a Kevlar fibre composite, in particular the non-woven configuration of KFRP [0,±45,90]. One of the big advantages of this composite is that, it has additional fibres in 45 orientation and therefore makes the composite more uniform mechanically. In this project from mechanical tests on glass fibre composite, it was found that in 45 direction, the lowest mechanical properties (tension and bending and bending fatigue properties) were obtained. Therefore using KFRP with [0,±45,90] can significantly improve the blade performance in regions where a single loading direction is not dominant. Therefore from this point of view, a testing programme including wide range of mechanical tests and corrosion-fatigue tests on composites

with various fibre orientations could be useful. Finally, comparison can be made not only between different types of fibres but also on composites with different fibre orientation (composites with unidirectional, woven, non-woven and [0,±45,90]). There is very little published corrosion-fatigue data in Kevlar composites.

12.8.2. Sandwich Composites

Performing a wide range of static mechanical and fatigue tests on sandwich composite materials. These can be a cheap composites with chopped strand mat-glass in the matrix of polyester resin in the core with the GFRP skins and therefore high bending stiffness using this type of composite can be obtained. In terms of mechanical and corrosion-fatigue testing, comparison can be made between this type of composite and other types. There is little or no reported corrosion-fatigue data of sandwich composites in sea water.

13. Appendix 1

Raw data of tension and 3PB tests for GFRP at (0°/90°) fibre orientation

1. Tension test

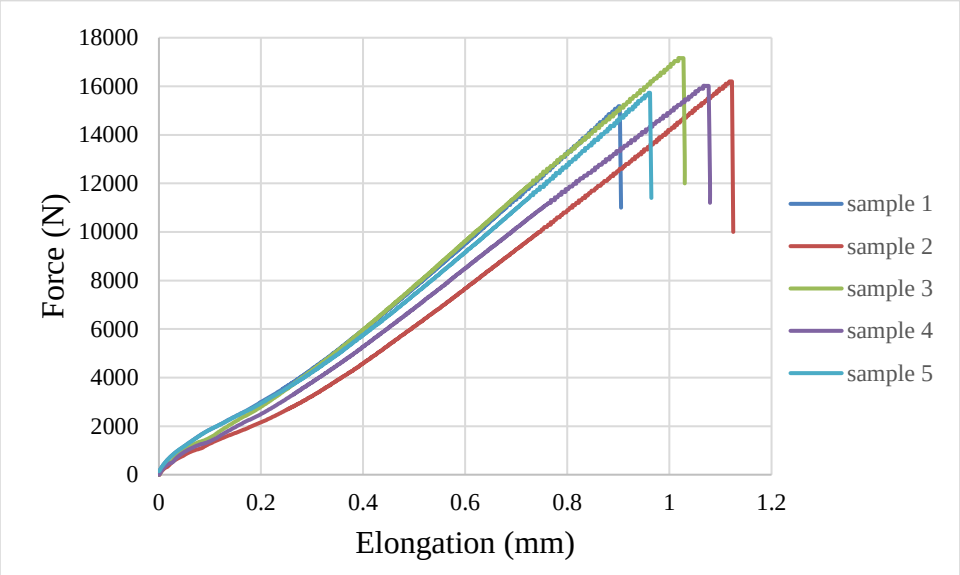

2. 3PB test

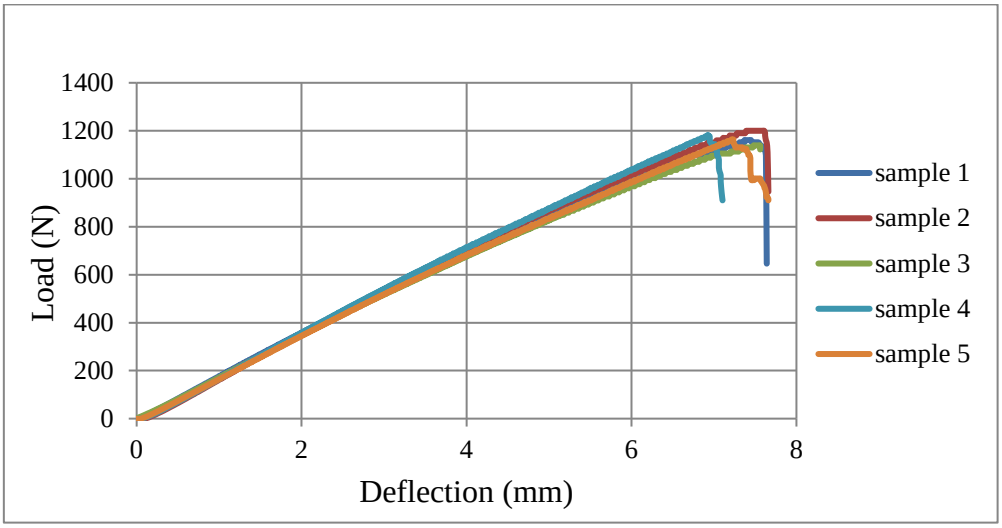

14. Appendix 2

G10 Product Data Sheet

Attwater & Sons Ltd

Custom Composites Ltd

Attwater & Sons Ltd +44 (0)1772 258245
Email: info@attwater.com
www.attwater.com

Date Generated: 04.05.18

Material Details

Grade:	G10. (Type: Glass Based Laminates - SRBG)
Description:	Epoxy Glass. Commercial epoxy grade
Comments:	General purpose Epoxy glass laminate. Temperature class B (130 deg C), with good mechanical and electrical properties at moderate cost. See also B46.
Specifications:	BSEN60893-3-2-EPGC201 (Which supersedes BS3953 EP3). The closest NEMA equivalent to this specification is NEMA G10.
Body Colour:	Green
Cover Colour:	Green
Standard Finish:	Satin/Glossy
Size:	1220 x 1220 Thickness Range: 0.4 - 100.0 †

Typical Applications

- Transformer Spacers
- Terminal Boards and Tag Strips
- Slot Wedges
- Precision Machined Parts
- Pipeline Insulation
- Phase Barriers
- Insulating Bushes Spacers Sleeves
- High Voltage Insulation
- Electromagnetic Coil Insulation
- Cryogenic Resistance Components
- Chemical Resistance Components

General Properties

Property	Unit of measure	Typical Value
Density	g/cm3	2
Water Absorption	mg	8

† The test method is used solely to control and monitor consistency of production. Under no conditions should the results be considered in relation to fire hazards under actual conditions of use.

Electrical Properties

Property	Unit of measure	Typical Value
IR (Dry)	G Ω	17000
Electric Strength (Flat Rapid)	MV/m	15
Breakdown Voltage (Edge Step by Step)	kV	80
Relative Permittivity @ 1 MHz	-	5.2
Dissipation Factor @ 1 MHz	-	0.025
Tracking Index	V	210

Mechanical Properties

Property	Unit of measure	Typical Value
Flexural Strength	MPa	482
Tensile Strength	MPa	320
Impact (Notched CHARPY)	kJ/m2	65

Thermal Properties

Property	Unit of measure	Typical Value
Thermal Rating Continuous	°C	120
Thermal Rating Intermittent	°C	130

Notes

- Datasheet Issue No. 2

Source: http://www.attwater.com/products/g10/

15. Appendix 3

```
%BEM - Tidal turbine Stream Tube Model
clear
clc
%% Inputs
%Number of Blades
NoB=3;
%free stream velocity of the fluid
Vs=[2.5]    % (speed in m/s)
%Fluid Density (kg/m^3)
Ro=1025;
%Blade length (m). 0 degree twist angle
BL= 11;
Z= 0.33 ; fraction of axial velocity remaining at the downstream exit of
the streamtube
% Sectional Data
SD=importdata('SectionalData.txt');
ro=SD(:,1)*.001;    %Radius (Original)  (m)
Co=SD(:,2)*.001;    %Chord Length (Original)  (m)
%Element data
NoE=45;    %Number of Elements
L=BL/NoE;    %Length of each element
r0=.5;    %Radial position of circular section (Root joint)  (m)
%NACA 4415 airfoil data
NACA4415=importdata('NACA4415.txt');
Alpha=NACA4415(:,1);    %Angles of attack (Original)
Clo=NACA4415(:,2);    %Lift Coefficient (Original)
Cdo=NACA4415(:,3);    %Drag Coefficient (Original)
%% Loop over spectrum speeds (Load calculations)
for j=1:length(Vs)
% Stream Speed (m/s)
SS=Vs(j);
w=4.82*SS/11.5; angular velocity of blade, tip speed ratio=4.82
%Rotor sspeed in rad/sec using Tip seed ratio
%Loop ver elements
for i=1:NoE
    r(i)=r0+(i-1)*L+(L/2);
    C(i)=interp1(ro,Co,r(i));
    G(i)=(r(i)*w)/SS;  local blade speed ratio
    Vw(i)=SS*sqrt((1+(G(i)^2)+Z-(G(i)*(sqrt(1+(G(i)^2)-(Z^2))))/2); axial
velocity in stream tube at rotor disk
    Vd(i)=Vw(i)*((sqrt(1+(G(i)^2)-(Z^2))-G(i))/(1-Z)); tangential velocity
of the fluid in a stream tube at the rotor disc
    disp (Vd(i))
    Vb(i)=r(i)*w;  tangential velocity at the stream tube due to its
angular velocity
Theta(i)=atand(Vw(i)/(Vd(i)+Vb(i)));    %Element's Theta angle
Vrel(i)=sqrt(Vw(i)^2+(Vd(i)+Vb(i))^2);    %element's relative speed
A(i)=C(i)*L;    %Element's area
AoA(i)=6;   %Angle of Attack
Cl(i)=interp1(Alpha,Clo,AoA(i));
Cd(i)=interp1(Alpha,Cdo,AoA(i));
dp(i)=.5*w*r(i)*Ro*A(i)*Vrel(i)^2*((Cl(i)*sind(Theta(i)))-
(Cd(i)*cosd(Theta(i))));    %Element's power
dFth(i)=.5*Ro*A(i)*Vrel(i)^2*((Cd(i)*sind(Theta(i)))+(Cl(i)*cosd(Theta(i)))
);    %Element's Thrust
dFtan(i)=.5*Ro*A(i)*Vrel(i)^2*((Cl(i)*sind(Theta(i)))-
(Cd(i)*cosd(Theta(i))));    %Element's power
end
```

```
% plot(r,dFn,'o')
% hold on
% plot(r,dFt,'>')
Pt(j)=NoB*sum(dp);   %Power
% Ft=NoB*sum(dFt);    %Tangential force
% Fn=NoB*sum(dFn);    %Normal force
Fth(:,j)=dFth';    %Normal force
Ftan(:,j)=dFtan';    %Tangential force
end
disp('Power in "kW" =')
disp(Pt*.001)
disp('Thrust Force in "N" =')
disp(Fth)
disp('Tangential Force in "N" =')
disp(Ftan)
disp('Note: in Ft and Fn, number of rows equals to number of elements')
disp('and number of columns equals to number of speeds in the spectrum')
```

16. Appendix 4

```
%BEM - Tidal turbine BEMT model
clear
clc
hold on
%% Inputs
%Number of Blades
NoB=3;
%Stream spectrum
Vs= 2.5;     % (speed in m/s)
%Fluid Density (kg/m^3)
Ro=1025;
%Blade length (m). 0 degree twist angle
BL= 11;
Z= 0.33 ;
% Sectional Data
SD=importdata('SectionalData.txt');
ro=SD(:,1)*.001;    %Radius (Original)  (m)
Co=SD(:,2)*.001;    %Chord Length (Original)  (m)
%Element data
NoE=45;    %Number of Elements
L=BL/NoE;    %Length of each element
r0=.5;    %Radial position of circular section (Root joint)  (m)
%NACA 4415 airfoil data
NACA4415=importdata('NACA4415.txt');
Alpha=NACA4415(:,1);    %Angles of attack (Original)
Clo=NACA4415(:,2);    %Lift Coefficient (Original)
Cdo=NACA4415(:,3);    %Drag Coefficient (Original)
%% Loop over spectrum speeds (Load calculations)
for j=1:length(Vs)
% Stream Speed (m/s)
SS=Vs(j);
RS=10;
w=2*pi*RS/60;
for i=1:NoE
    r(i)=r0+(i-1)*L+(L/2);
    C(i)=interp1(ro,Co,r(i));
    Vw(i)=(2/3)*SS;
    Vb(i)=r(i)*w;
Theta(i)=atand(Vw(i)/(Vb(i)));    %Element's Theta angle
Vrel(i)=sqrt(Vw(i)^2+(Vb(i))^2);    %element's relative speed
A(i)=C(i)*L;    %Element's area
AoA(i)=6;   %Angle of Attack
Cl(i)=interp1(Alpha,Clo,AoA(i)); Lift coefficient
Cd(i)=interp1(Alpha,Cdo,AoA(i)); Drag coefficient
dp(i)=.5*w*r(i)*Ro*A(i)*Vrel(i)^2*(Cl(i)*sind(Theta(i))-
Cd(i)*cosd(Theta(i)));    %Element's power
dFth(i)=.5*Ro*A(i)*Vrel(i)^2*(Cd(i)*sind(Theta(i))+Cl(i)*cosd(Theta(i)));
%Element's Thrust
dFtan(i)=.5*Ro*A(i)*Vrel(i)^2*(Cl(i)*sind(Theta(i))-Cd(i)*cosd(Theta(i)));
%Element's power
end
% plot(r,dFtan,'o')
% hold on
% plot(r,dFth,'>')
Pt(j)=NoB*sum(dp);   %Power
% Fth=NoB*sum(dFth);    %Thrust force
% Ftan=NoB*sum(dFtan);    %Tangential force
```

```
Fth(:,j)=dFth';    %Thrust force
Ftan(:,j)=dFtan';    %Tangential force
end
disp('Power in "kW" =')
disp(Pt*.001)
disp('Thrust Force in "N" =')
disp(Fth)
disp('Tangential Force in "N" =')
disp(Ftan)
disp('Note: in Fth and Ftan, number of rows equals to number of elements')
disp('and number of columns equals to number of speeds in the spectrum')
plot(Vs,Pt)
```

17. Appendix 5

Validation of MATLAB code

EXCEL file verifying the MATLAB code in appendix 3 (based on input parameter detailed in Table 5-1.

r_i(m)	γ_i	U_d(m/s)	V_d(m/s)	V_b(m/s)	V_r(m/s)	δl (N)	δD (N)	F_A (N)	F_T (N)
2.00	0.87	1.74	1.08	2.18	3.70	3916.81	24.45	3.04E+03	1.60E+03
2.24	0.97	1.73	0.99	2.44	3.84	4233.56	26.43	3.49E+03	1.79E+03
2.47	1.07	1.72	0.92	2.69	4.00	4592.26	28.67	3.93E+03	1.95E+03
2.71	1.18	1.71	0.85	2.95	4.17	4903.48	30.61	4.37E+03	2.10E+03
2.95	1.28	1.71	0.79	3.21	4.35	5256.29	32.81	4.81E+03	2.20E+03
3.19	1.38	1.70	0.74	3.46	4.53	5633.45	35.17	5.25E+03	2.30E+03
3.42	1.48	1.70	0.70	3.72	4.73	6032.82	37.66	5.69E+03	2.38E+03
3.66	1.58	1.69	0.66	3.97	4.93	6452.36	40.28	6.13E+03	2.45E+03
3.90	1.69	1.69	0.62	4.23	5.13	6881.42	42.96	6.57E+03	2.48E+03
4.13	1.79	1.69	0.59	4.48	5.35	7336.11	45.79	7.01E+03	2.52E+03
4.37	1.89	1.69	0.56	4.74	5.56	7805.20	48.72	7.45E+03	2.53E+03
4.61	1.99	1.68	0.53	4.99	5.78	8286.90	51.73	7.90E+03	2.53E+03
4.84	2.1	1.68	0.51	5.25	6.00	8772.93	54.76	8.34E+03	2.53E+03
5.08	2.2	1.68	0.49	5.51	6.22	9274.94	57.90	8.78E+03	2.53E+03
5.32	2.3	1.68	0.47	5.76	6.45	9784.26	61.08	9.22E+03	2.53E+03
5.56	2.4	1.68	0.45	6.02	6.68	10299.14	64.29	9.66E+03	2.53E+03
5.79	2.5	1.68	0.43	6.27	6.91	10817.87	67.53	1.01E+04	2.53E+03
6.03	2.6	1.68	0.42	6.53	7.14	11338.75	70.78	1.05E+04	2.53E+03
6.27	2.7	1.67	0.40	6.78	7.38	11860.06	74.03	1.10E+04	2.53E+03
6.50	2.8	1.67	0.39	7.04	7.61	12380.09	77.28	1.14E+04	2.53E+03
6.74	2.9	1.67	0.37	7.29	7.85	12897.16	80.51	1.19E+04	2.53E+03
6.98	3	1.67	0.36	7.55	8.09	13409.56	83.71	1.23E+04	2.53E+03
7.21	3.1	1.67	0.35	7.80	8.32	13915.59	86.87	1.27E+04	2.53E+03
7.45	3.2	1.67	0.34	8.06	8.56	14413.56	89.97	1.32E+04	2.53E+03
7.69	3.3	1.67	0.33	8.32	8.81	14901.79	93.02	1.36E+04	2.53E+03
7.93	3.4	1.67	0.32	8.57	9.05	15378.57	96.00	1.41E+04	2.53E+03
8.16	3.5	1.67	0.31	8.83	9.29	15842.23	98.89	1.45E+04	2.53E+03
8.40	3.6	1.67	0.30	9.08	9.53	16291.06	101.69	1.50E+04	2.53E+03
8.64	3.7	1.67	0.30	9.34	9.78	16723.38	104.39	1.54E+04	2.53E+03
8.87	3.8	1.67	0.29	9.59	10.02	17137.51	106.98	1.58E+04	2.53E+03
9.11	3.9	1.67	0.28	9.85	10.27	17531.74	109.44	1.63E+04	2.53E+03
9.35	4	1.67	0.27	10.10	10.51	17904.41	111.77	1.67E+04	2.53E+03
9.58	4.1	1.67	0.27	10.36	10.76	18253.82	113.95	1.72E+04	2.53E+03
9.82	4.25	1.67	0.26	10.61	11.00	18568.16	115.91	1.76E+04	2.53E+03
10.06	4.35	1.67	0.25	10.87	11.25	18866.50	117.77	1.80E+04	2.53E+03
10.30	4.45	1.67	0.25	11.13	11.49	19136.49	119.46	1.85E+04	2.53E+03
10.53	4.55	1.67	0.24	11.38	11.74	19376.46	120.96	1.89E+04	2.53E+03
10.77	4.65	1.67	0.24	11.64	11.99	19584.72	122.26	1.94E+04	2.53E+03
11.00	4.75	1.67	0.23	11.89	12.24	19759.58	123.35	1.98E+04	2.53E+03

r_i= Distance from the blade root
γ_i = Local blade speed ratio
U_d= Axial water velocity at the rotor disc
V_d= Tangential velocity of the fluid at the rotor disc
V_b= Tangential velocity of the blade due to its angular velocity
V_r= relative resultant velocity
δL= Lift force at each blade section
δD= Drag force at each blade section
F_A= Axial force at each blade section
F_T= Tangential force at each blade section

18. Appendix 6

```
%Damage calculator
clear
clc
%% Input Data
% Strain data
Strain=importdata('StrainData.txt');
% Load data
Load=importdata('LoadData.txt');
% Critical Element ID
CEID=input('Critical Element ID=');
%% Damage Calculations
NLP=10;   %Number of load points/directions
ELData=Strain(:,CEID);
for i=1:NLP
   Sig(i)= Load(:,i);
end
%Combination
E11Sig=0;
for i=1:NLP
E11Sig=E11Sig+(Sig(i))*ELData(i)*100; %E11Sig : Strain signal (without
filteration of non-turning points)
end
% plot(E11Sig)
rf = rainflow(E11Sig);
AmpS=rf(1,:);   %Amplitude strains
MeanS=rf(2,:);   %Mean strains
Cnt=rf(3,:);   %Frequency
% Histogram
[m,mx,my] = rfmatrix(rf,5,5);
bar3(m)
set(gca,'XTickLabel', mx')
set(gca,'YTickLabel', my')
xlabel('Amplitude Strain (%)')
ylabel('Mean Strain (%)')
zlabel('Frequancy')
% Damage Calculations
Damage=sum((Cnt)./(((2*AmpS/2.7901).^(-(1/0.109)))));   %S-N curve with
R=0.1 and Damage in 7 days
OneYearDamage=Damage*(365.25/7);   % 1 year damage
disp(' ')
disp('Miners Damage in 1 year=')
disp(OneYearDamage)
Life=1/OneYearDamage;   %Life in Years
disp(' ')
disp('Life in years')
disp(Life)
```

19. Appendix 7

1. **Title of paper:** A preliminary design methodology for fatigue life prediction of polymer composites for tidal turbine blades (Kennedy *et al.*, 2012)

- Chord length and pitch angle distribution detailed in above paper:

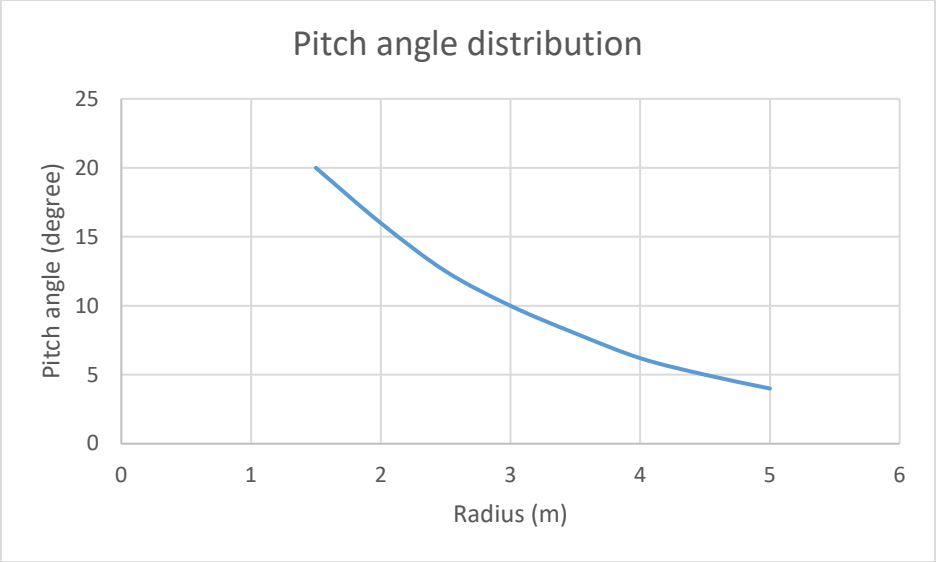

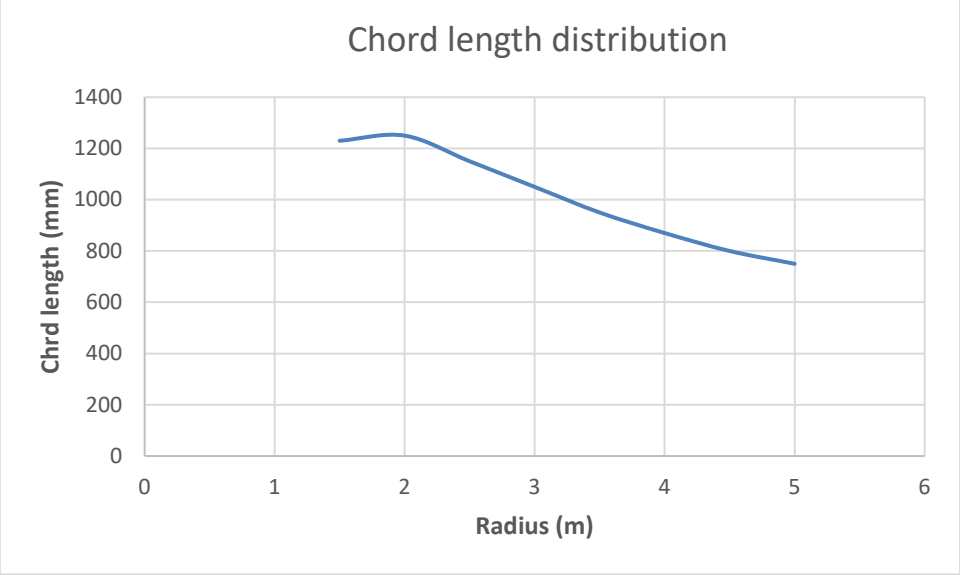

- Design of blade in ANSYS

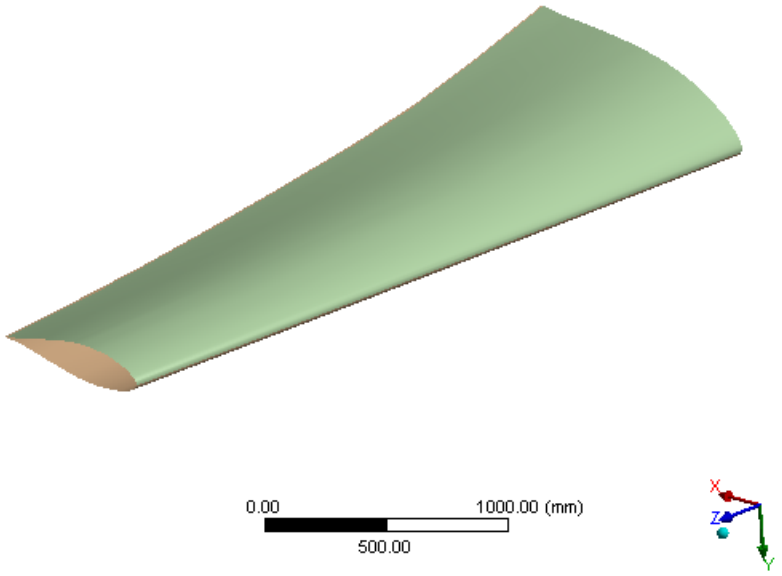

- Parameters for base case hydrodynamic model :

Parameter	value
Peak water velocity range during 7 days	**2.6-4.1 (m/s)**
Number of blades	**3**
RPM	**16**
Water density	**1025 kg/m^3**
Water viscosity	**0.0013155 Pas**
Lift to drag ratio	**70**
Lift coefficient	**1**
Blade length	**3.5 m**
Angle of attack (degrees)	**7**
Z (the fraction of axial velocity remaining at the downstream exit of the stream tube) assuming that the water in each of these stream tubes has slowed down to 1/3 of its initial velocity at the exit of stream tube.	**0.333**
Number of stream tube/blade elements	**45**

- Materials properties and lay up configuration used for ANSYS model of blade and parameters used on 3.5 meter blade (Keneddy paper) to extract the same tip deflection

Table 1. Material properties.

Inputs		Single unidirectional ply properties		QI laminate $[(45\backslash135\backslash90\backslash0)_2]_s$	
Panel A: Epoxy/E-glass					
V_f	50%	E_1	38 GPa	E_x, E_y	19.3 GPa
E_f	72.4 GPa	E_2	11.5 GPa	G_{xy}	7.2 GPa
ν_f	0.22	G_{12}	3.5 GPa	ν_{xy}	0.330
E_m	3.5 GPa	ν_{12}	0.285		
ν_m	0.35				
Panel B: Vinyl ester/E-glass					
V_f	50%	E_1	37.9 GPa	E_x, E_y	19.1 GPa
E_f	72.4 GPa	E_2	11.3 GPa	G_{xy}	7.2 GPa
ν_f	0.22	G_{12}	3.4 GPa	ν_{xy}	0.330
E_m	3.4 GPa	ν_{12}	0.285		
ν_m	0.35				

QI: quasi-isotropic.

- Reproducing the same forces and flap-wise bending moment

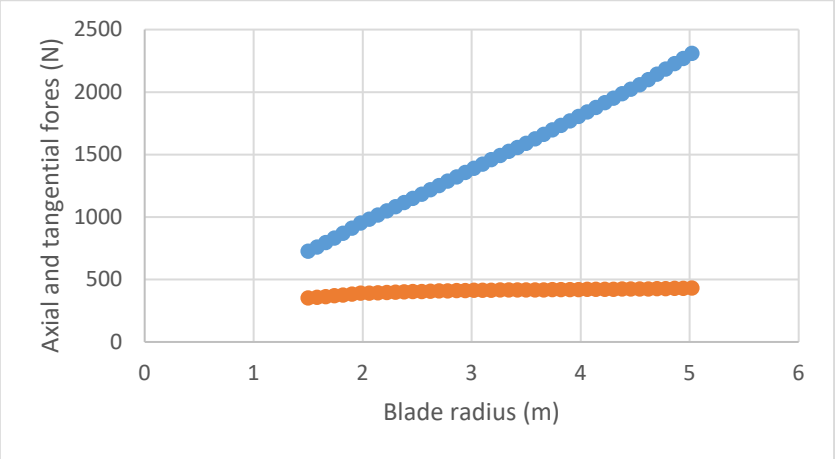

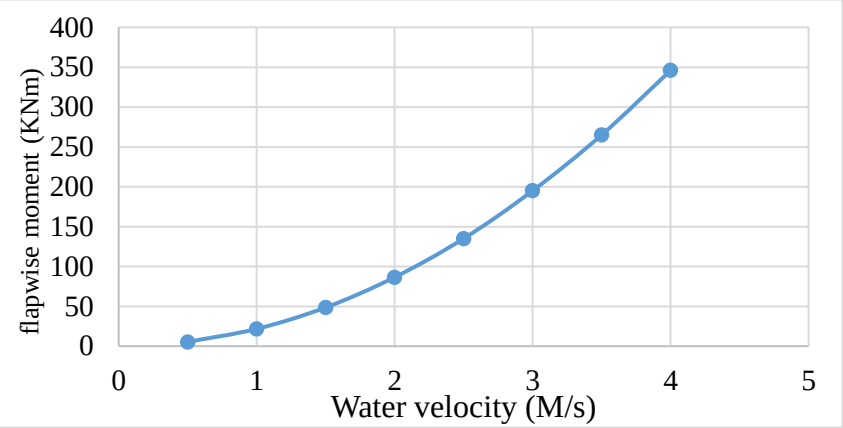

- Applying boundary conditions on FE model of the blade

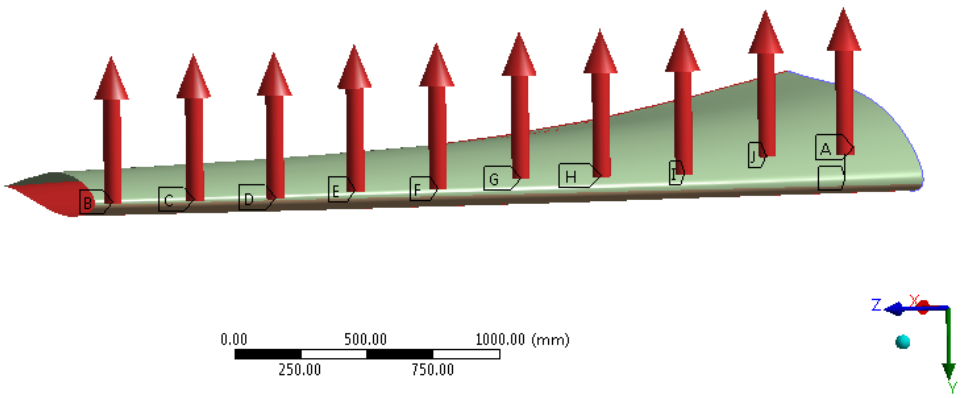

- Predicting the same FE results as detailed in the paper (tip deflection)

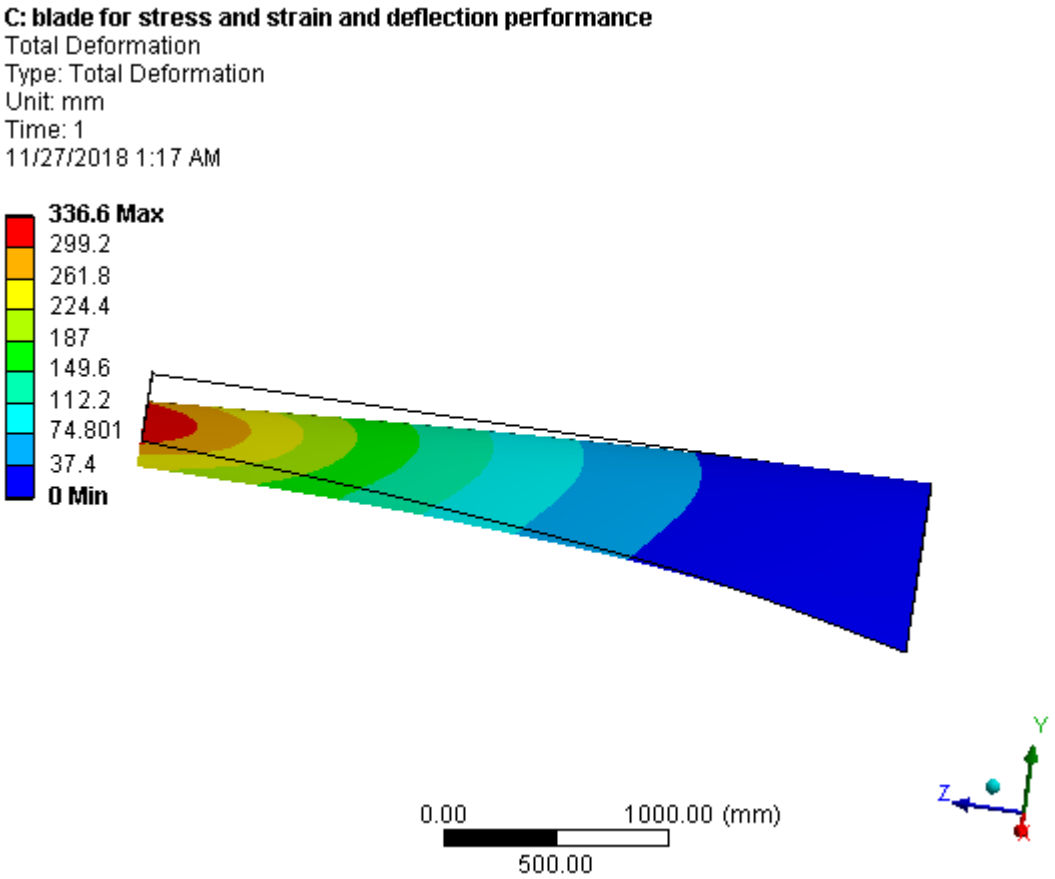

Title of paper: Design of composite tidal turbine blades (Grogan *et al.*, 2013)

- Twist angle and chord length distribution detailed in above paper

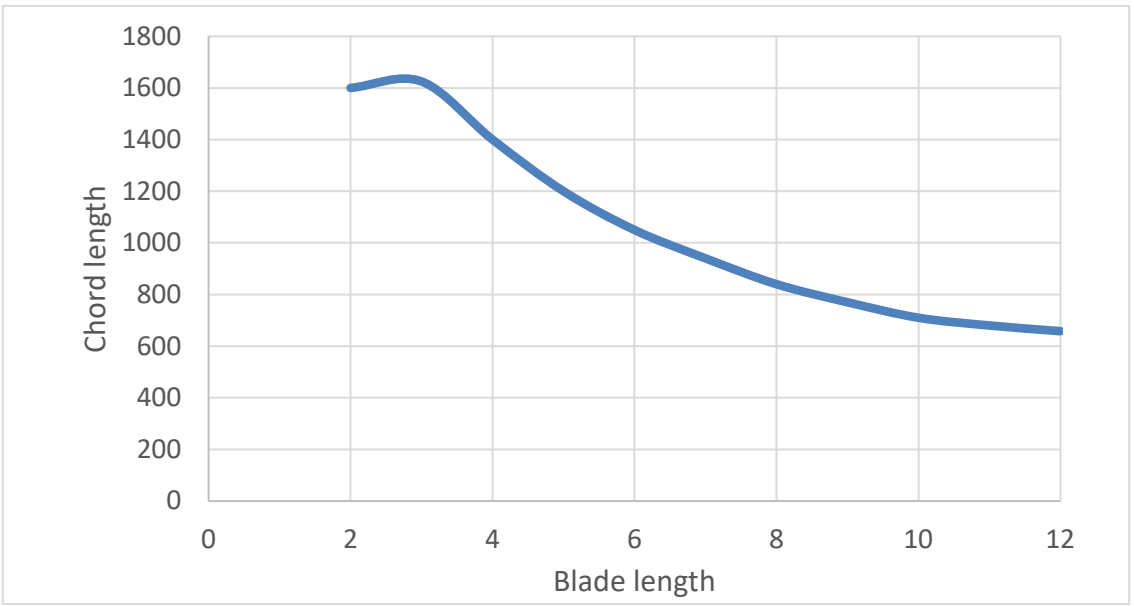

- Blade design in ANSYS

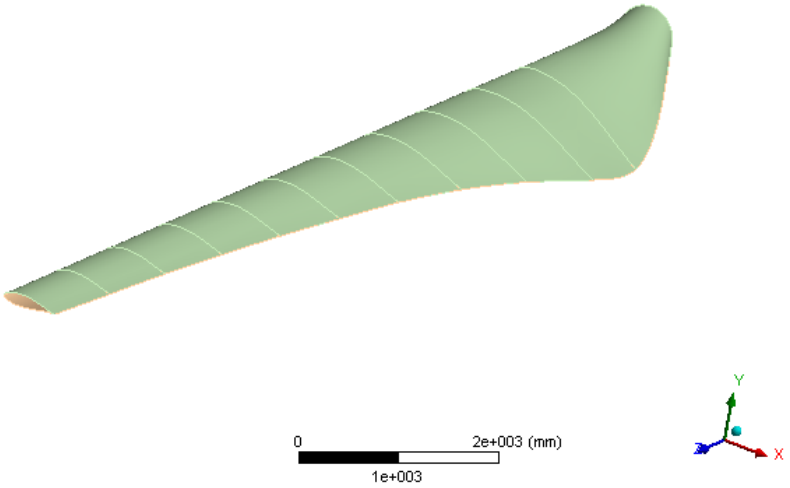

- Parameters for stream tube mode under normal operating conditions

Parameter	value
Peak water velocity range during 7 days	**2.4-4.1 (m/s)**
Number of blades	**3**
RPM	**10**
Water density	**1025 kg/m^3**
Water viscosity	**0.0013155 Pas**
Lift to drag ratio	**70**
Lift coefficient	**1.15**
Blade length	**12 m**
Riso A1	
Angle of attack (degrees)	**6**
Material	**CFRP**
Number of stream tube/blade elements	**45**

- The same force distribution and flap-wise bending moment was predicted

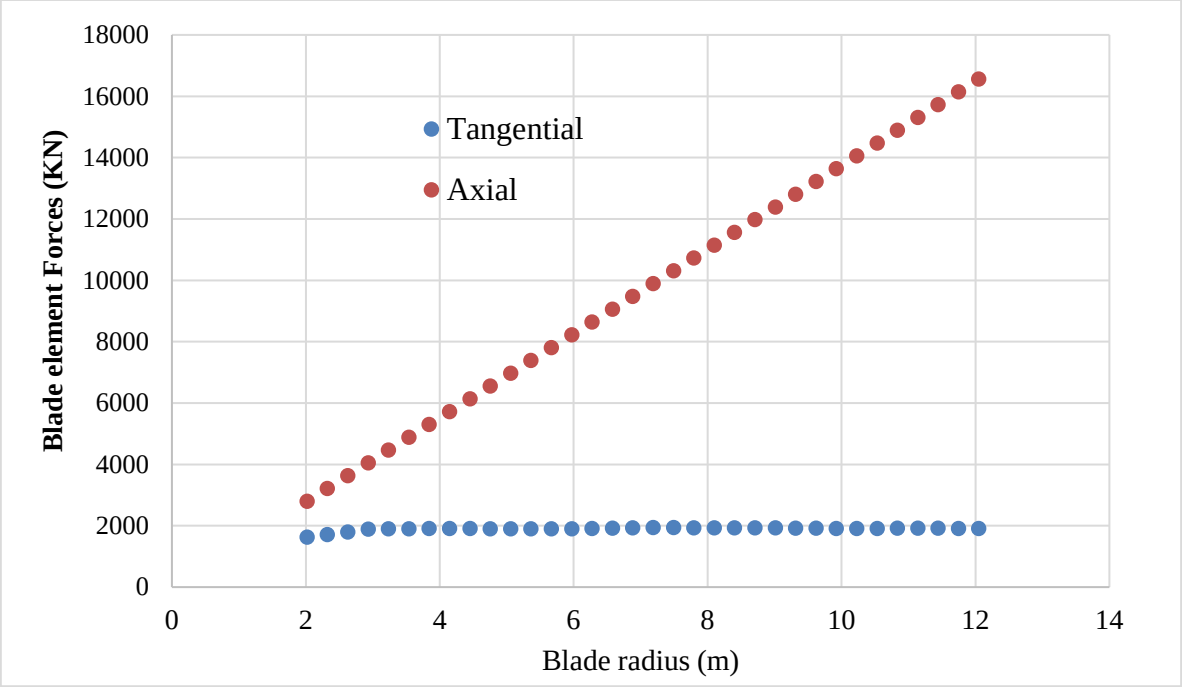

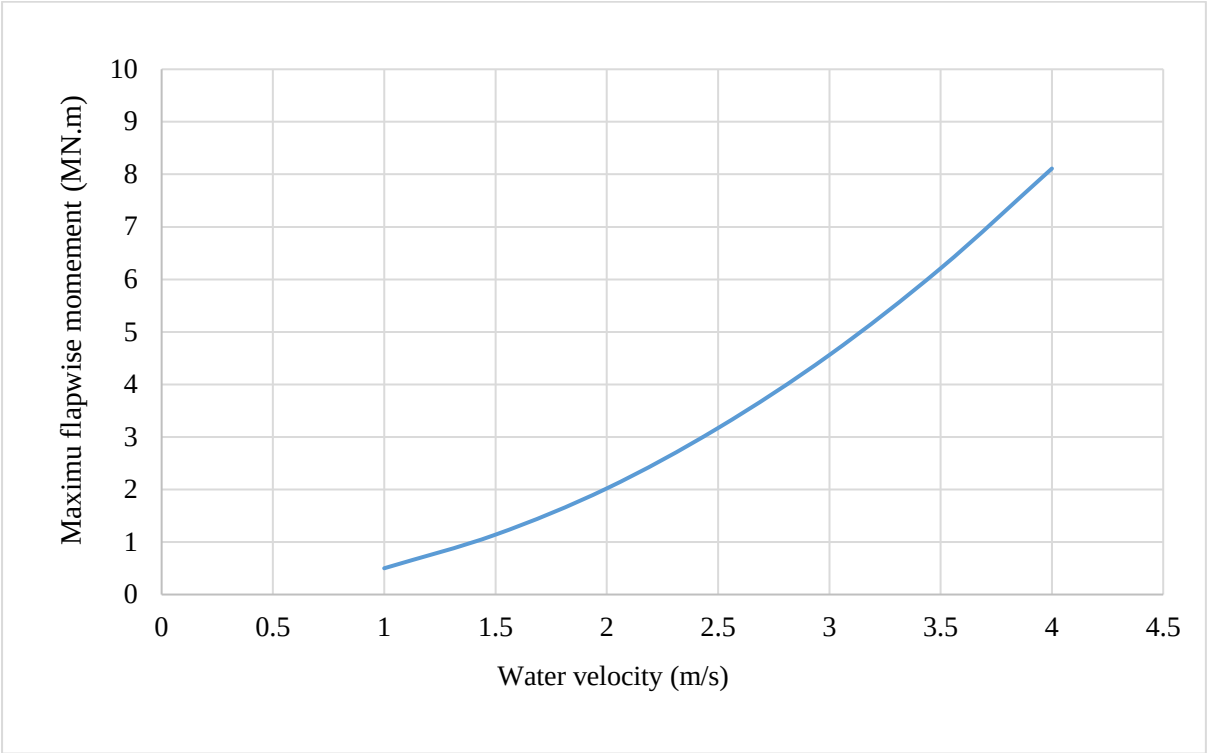

- Materials properties and lay up configuration used for ANSYS model of blade and parameters used on 12 meter blade to extract the same tip deflection

Material	E_1 (GPa)	E_2 (GPa)	G_{12} (GPa)	ν_{12}	Density (kgm^{-3})
UD CFRP	142.0	10.3	7.2	0.27	1580
DB GFRP	22.0	22.0	2.7	0.30	1850
Gelcoat	1×10^{-8}	1×10^{-8}	1×10^{-9}	0.30	1830
Corecell	0.044	0.044	0.020	0.30	65

- Predicting the same FE results as detailed in the paper (tip deflection)

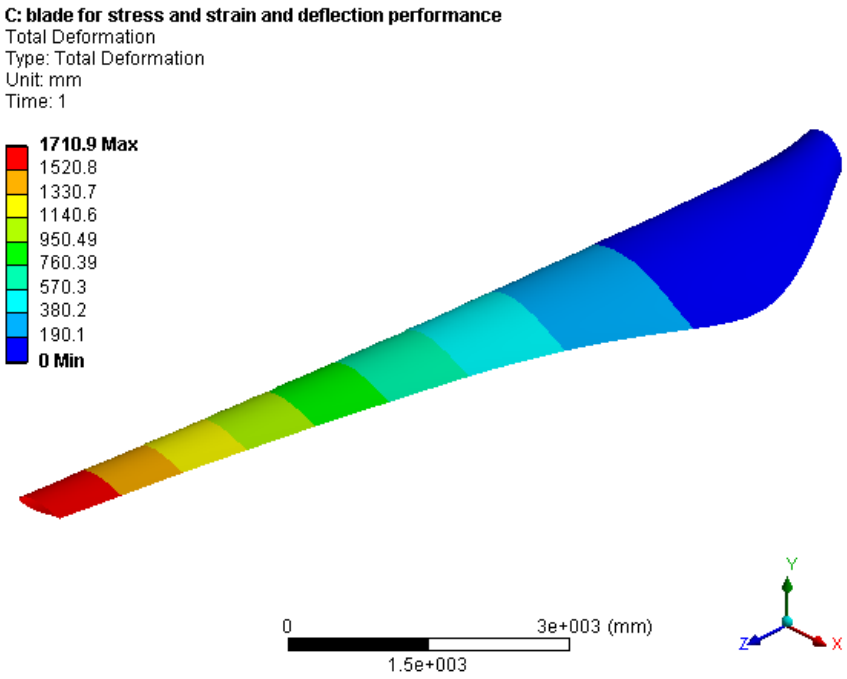

2. Comparison between hydrodynamic forces on the blade in this thesis (NACA4415, 2MW power output) and the blade in literature (Riso-A1, 1.5MW power output)

- Chord length and twist angle distribution

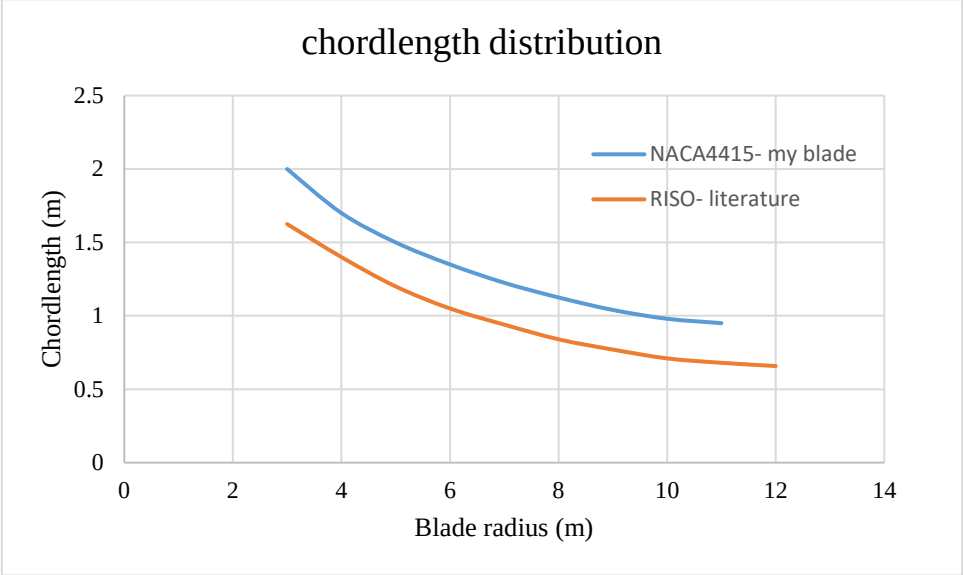

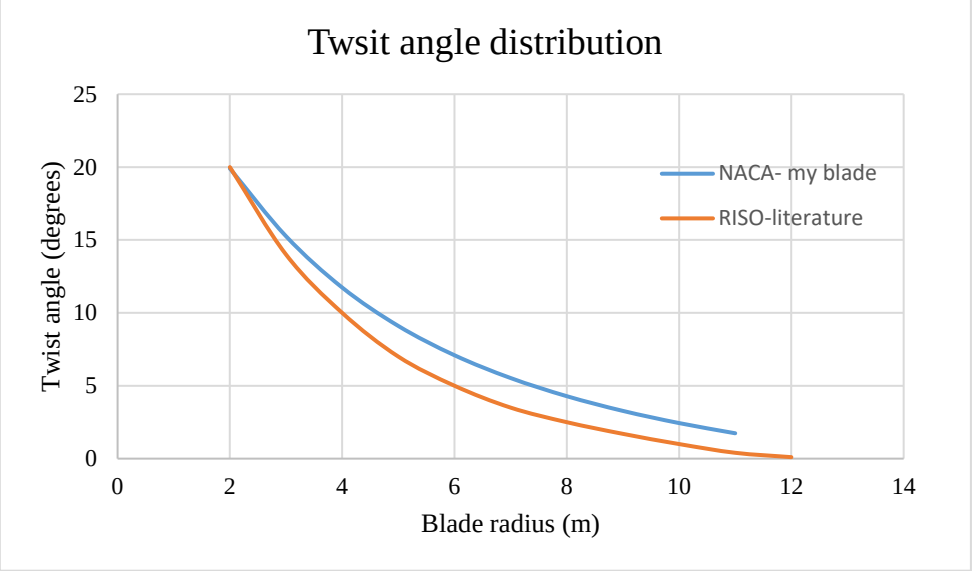

- Comparison between hydrodynamic loading:

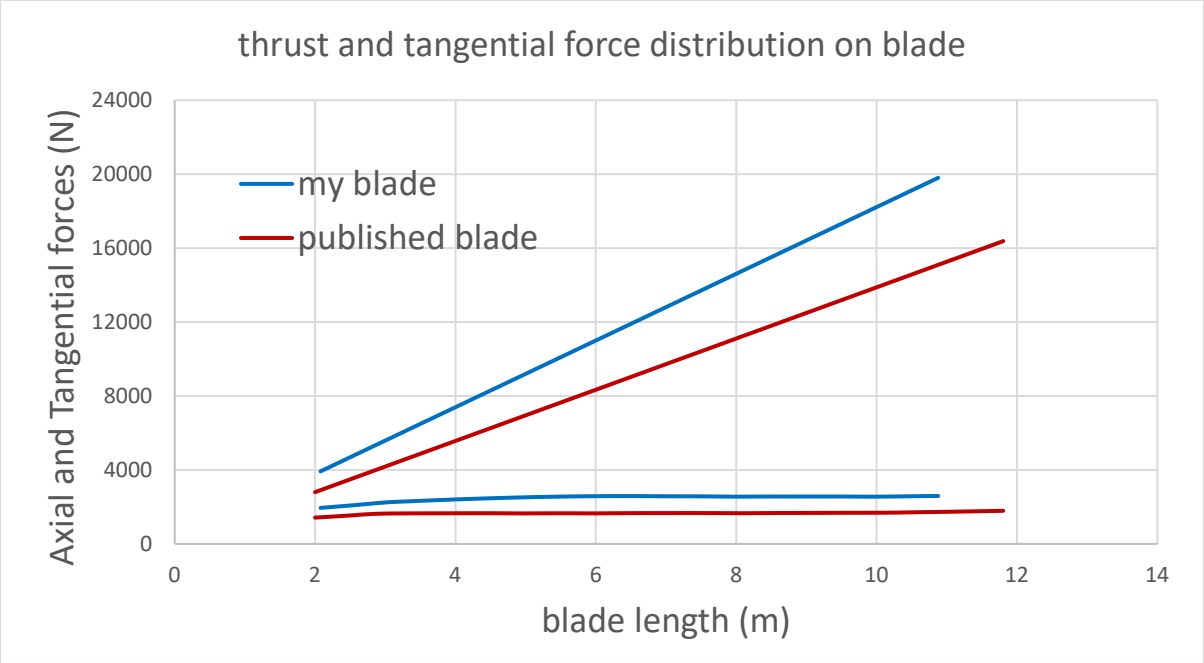

References

Abdel-Magid, B., Ziaee, S., Gass, K. and Schneider, M. (2005) 'The combined effects of load, moisture and temperature on the properties of E-glass/epoxy composites', *Composite Structures*, 71(3), pp. 320-326.

Agarwal, B.D., Broutman, L.J. and Chandrashekhara, K. (2006) *Analysis and performance of fibre composites*. John Wiley & Sons.

Ahmed, K.S. and Vijayarangan, S. (2008) 'Tensile, flexural and interlaminar shear properties of woven jute and jute-glass fabric reinforced polyester composites', *Journal of materials processing technology*, 207(1-3), pp. 330-335.

Alam, S., Habib, F., Irfan, M., Iqbal, W. and Khalid, K. (2010) 'Effect of orientation of glass fibre on mechanical properties of GRP composites', *J. Chem. Soc. Pak*, 32(3), p. 265.

Alawsi, G., Aldajah, S. and Rahmaan, S.A. (2009) 'Impact of humidity on the durability of E-glass/polymer composites', *Materials & Design*, 30(7), pp. 2506-2512.

Alias, M.N. and Brown, R. (1993) 'Corrosion behaviour of carbon fibre composites in the marine environment', *Corrosion science*, 35(1), pp. 395-402.

Allen, D.H. (2012) *Introduction to the mechanics of deformable solids: Bars and beams*. Springer Science & Business Media.

Altabey, W.A. and Noori, M. 'An Extensive Overview of Lamb Wave Technique for Detecting Fatigue Damage in Composite Structures'.

am E Grami, M., Moilanen, M.J. and Rosenow, M.W.K. (1995) *Proceedings of the Tenth International Conference on Composite Materials: Microstructure, degradation, and design*. Woodhead Publishing.

ANSYS, I. *Element Reference* (Version Release 15.0) [Computer program].

ANSYS, Inc.Element Reference (Version Release 11.00) [Computer program].

Apicella, A., Migliaresi, C., Nicodemo, L., Nicolais, L., Iaccarino, L. and Roccotelli, S. (1982) 'Water sorption and mechanical properties of a glass-reinforced polyester resin', *Composites*, 13(4), pp. 406-410.

Araj, K.J., Fisher, T.A. and Kronenburg, J.C. (1991) *Assessment of research needs for wind turbine rotor materials technology*. National Research Council, Washington, DC (United States).

Arnold, J.C. (1996) 'Environmental stress crack initiation in glassy polymers', *Trends in polymer science*, 4(12), pp. 403-408.

Asp, L.E., Berglund, L.A. and Gudmundson, P. (1995) 'Effects of a composite-like stress state on the fracture of epoxies', *Composites science and technology*, 53(1), pp. 27-37.

'Attwater and Sons Ltd', *Available from http://www.attwater.com/*.

Azzi, V.D. and Tsai, S.W. (1965) 'Anisotropic strength of composites', *Experimental mechanics*, 5(9), pp. 283-288.

Bahaj, A.S. (2011) 'Generating electricity from the oceans', *Renewable and Sustainable Energy Reviews*, 15(7), pp. 3399-3416.

Bakir, B. and Hashem, H. 'Effect of Fibre Orientation for Fibre Glass Reinforced Composite Material on Mechanical Properties'.

Bathias, C. (1991) 'Fracture and fatigue of high performance composite materials: mechanisms and prediction', *Engineering fracture mechanics*, 40(4), pp. 757-783.

Bay, B.K., Smith, T.S., Fyhrie, D.P. and Saad, M. (1999) 'Digital volume correlation: three-dimensional strain mapping using X-ray tomography', *Experimental mechanics*, 39(3), pp. 217-226.

Beaumont, P.W.R. and Harris, B. (1971) *Int. Conf. Carbon Fibres, Their Composites and Appl., Plast. Inst., London, Paper*.

Beckwith, S.W. (2007) 'Resin Infusion Technology—Part 3: A Detailed Overview of RTM and VIP Infusion Processing Technologies', *SAMPE J*, 43(4).

Benham, P.P., Crawford, R.J. and Armstrong, C.G. (1996) *Mechanics of engineering materials*. Longman Harlow.

Bernasconi, A., Davoli, P., Basile, A. and Filippi, A. (2007) 'Effect of fibre orientation on the fatigue behaviour of a short glass fibre reinforced polyamide-6', *International Journal of Fatigue*, 29(2), pp. 199-208.

Bhatnagar, N., Ramakrishnan, N., Naik, N.K. and Komanduri, R. (1995) 'On the machining of fibre reinforced plastic (FRP) composite laminates', *International journal of machine tools and manufacture*, 35(5), pp. 701-716.

Boisseau, A., Davies, P. and Thiebaud, F. (2012) 'Sea water ageing of composites for ocean energy conversion systems: influence of glass fibre type on static behaviour', *Applied Composite Materials*, 19(3-4), pp. 459-473.

Boisseau, A., Davies, P. and Thiebaud, F. (2013) 'Fatigue behaviour of glass fibre reinforced composites for ocean energy conversion systems', *Applied Composite Materials*, 20(2), pp. 145-155.

Boller, K.H. (1964) 'Fatigue characteristics of RP laminates subjected to axial loading', *Modern Plastics*, 41(10), pp. 145-150.

Bonniau, P. and Bunsell, A.R. (1981) 'Water absorption by glass fibre reinforced epoxy resin', in *Composite structures*. Springer, pp. 92-105.

Bradley, W.L., Chiou, P.L. and Grant, T.S. (1995) 'The effect of seawater on polymeric composite materials', *NIST special publication*, (887), pp. 193-202.

Briançon, C., Sigety, P. and G'Sell, C. (1996) 'In situ study of matrix strain in carbon/resin composite materials', *Composites science and technology*, 56(7), pp. 835-840.

Brynk, T., Molak, R.M., Janiszewska, M. and Pakiela, Z. (2012) 'Digital Image Correlation measurements as a tool of composites deformation description', *Computational Materials Science*, 64, pp. 157-161.

BSOL (2006) *Glass fibre reinforced plastics-Tensile test*. BSI.

BSOL (2011) *Fibre-reinforced plastic composites. Determination of flexural properties*. BSI.

Bullock, R.E. (1974) 'Strength ratios of composite materials in flexure and in tension', *Journal of Composite Materials*, 8(2), pp. 200-206.

Bureau, M.N. and Denault, J. (2000) 'Fatigue behaviour of continuous glass fibre composites: effect of the matrix nature', *Polymer composites*, 21(4), pp. 636-644.

Burrell, P., McCabe, T. and de la Rosa, R. (1986) *Proc. 41st Ann. Tech. Conf. Reinforced Plastic/Composite Inst., Society of the Plastics Industry, Paper*.

Canal, L.P., González, C., Molina-Aldareguía, J.M., Segurado, J. and Llorca, J. (2012) 'Application of digital image correlation at the microscale in fibre-reinforced composites', *Composites Part A: Applied Science and Manufacturing*, 43(10), pp. 1630-1638.

Canino, M.M. (2016) *Finite element modeling and fatigue analysis of composite turbine blades under random ocean current and turbulence*. Florida Atlantic University.

Caprino, G. and D'Amore, A. (1998) 'Flexural fatigue behaviour of random continuous-fibre-reinforced thermoplastic composites', *Composites Science and Technology*, 58(6), pp. 957-965.

Carswell, W.S. and Roberts, R.C. (1980) 'Environmental fatigue stress failure mechanism for glass fibre mat reinforced polyester', *Composites*, 11(2), pp. 95-99.

Cauich-Cupul, J.I., Pérez-Pacheco, E., Valadez-González, A. and Herrera-Franco, P.J. (2011) 'Effect of moisture absorption on the micromechanical behaviour of carbon fibre/epoxy matrix composites', *Journal of materials science*, 46(20), pp. 6664-6672.

'CES EduPack 2017', *Remote Application Service of Newcastle University, Available from https://ras-gateway.ncl.ac.uk/Citrix/RASWeb/*.

Charles, R.J. (1958a) 'Static fatigue of glass. I', *Journal of Applied Physics*, 29(11), pp. 1549-1553.

Charles, R.J. (1958b) 'Static fatigue of glass. II', *Journal of Applied Physics*, 29(11), pp. 1554-1560.

Christensen, R.M. (2012) *Mechanics of composite materials*. Courier Corporation.

Christensen, R.M. and Rinde, J.A. (1979) 'Transverse tensile characteristics of fibre composites with flexible resins: Theory and test results', *Polymer Engineering & Science*, 19(7), pp. 506-511.

Chu, T.C., Ranson, W.F. and Sutton, M.A. (1985) 'Applications of digital-image-correlation techniques to experimental mechanics', *Experimental mechanics*, 25(3), pp. 232-244.

Clocksin, W.F., da Fonseca, J.Q., Withers, P.J. and Torr, P.H.S. (2002) *International Symposium on Optical Science and Technology*. International Society for Optics and Photonics.

Crupi, V., Guglielmino, E., Risitano, G. and Tavilla, F. (2013) *CONVEGNO IGF XXII ROMA 2013*.

Curry, J.M., Ohnson, E.R. and Tarnes, J.H. (1992) 'Effect of dropped plies on the strength of graphite-epoxy laminates', *AIAA journal*, 30(2), pp. 449-456.

Curtis, P.T. (1980) 'Residual strains and the effects of moisture in fibre reinforced plastics', *RAE Technical Report 80045*.

Curtis, P.T. (1984) 'The effect of edge stresses on the failure of (0, 45, 90) CFRP laminates', *Journal of materials science*, 19(1), pp. 167-182.

Curtis, P.T. (1987) *ICCM*.

Curtis, P.T. (1989) 'The fatigue behaviour of fibrous composite materials', *The Journal of Strain Analysis for Engineering Design*, 24(4), pp. 235-244.

Curtis, P.T. and Dorey, G. (1986) 'Fatigue of composite materials', *Fatigue of Engineering Materials and Structures.*, 2, pp. 297-306.

Curtis, P.T. and Moore, B.B. (1983) 'The effects of environmental exposure on the fatigue behaviour of CFRP laminates', *Composites*, 14(3), pp. 294-300.

Daniel, I.M., Ishai, O., Daniel, I.M. and Daniel, I. (1994) *Engineering mechanics of composite materials*. Oxford university press New York.

Davalos, J.F., Qiao, P., Wang, J., Salim, H.A. and Schlussel, J. (2002) 'Shear moduli of structural composites from torsion tests', *Journal of composite materials*, 36(10), pp. 1151-1173.

Davies, P., Germain, G., Gaurier, B., Boisseau, A. and Perreux, D. (2013a) 'Evaluation of the durability of composite tidal turbine blades', *Philosophical Transactions of the Royal Society of London A: Mathematical, Physical and Engineering Sciences*, 371(1985), p. 20120187.

Davies, P., Germain, G., Gaurier, B., Boisseau, A. and Perreux, D. (2013b) 'Evaluation of the durability of composite tidal turbine blades', *Philosophical Transactions of the Royal Society A: Mathematical, Physical and Engineering Sciences*, 371(1985), p. 20120187.

Davis, J.W., McCarthy, J.A. and Schurb, J.N. (1964) 'The fatigue resistance of reinforced plastics', *Materials in Design Engineering*, 60(7), pp. 87-91.

De Buhan, P. and Taliercio, A. (1991) 'A homogenization approach to the yield strength of composite materials', *European journal of mechanics. A. Solids*, 10(2), pp. 129-154.

Demchik, R.P., Mandell, J.F. and McGarry, F.J. (1973) *Marine Environment Effects on Fatigue Crack Propagation in GRP Laminates for Hull Construction*.

Dew-Hughes, D. and Way, J.L. (1973) 'Fatigue of fibre—reinforced plastics: a review', *Composites*, 4(4), pp. 167-173.

Dharan, C.K.H. (1975) 'Fatigue failure mechanisms in a unidirectionally reinforced composite material', *ASTM special technical publication*, (569), pp. 171-188.

Digimat, A. (2011) 'Software for the Linear and Nonlinear Multi-Scale Modeling of Heterogeneous Materials; e-Xstream Engineering: Louvain-la-Neuve'. Belgium.

DNV, G. (2015) *Rotor blades for wind turbines*. Standard DNVGL-ST-0376.

Doremus, R.H. (1974) 'Static Fatigue in Glass', in *Recent Advances in Science and Technology of Materials*. Springer, pp. 203-206.

Dowling, N.E. (2012) *Mechanical behaviour of materials: engineering methods for deformation, fracture, and fatigue*. Pearson.

Draycott, S., Sutherland, D., Steynor, J., Sellar, B. and Venugopal, V. (2017) 'Re-Creating Waves in Large Currents for Tidal Energy Applications', *Energies*, 10(11), p. 1838.

Drela, M. and Youngren, H. (2008) 'Xfoil subsonic airfoil development system', *Software Package, available online at http://web. mit. edu/drela/Public/web/xfoil [retrieved Feb. 2011]*.

Echaabi, J., Trochu, F. and Gauvin, R. (1996) 'Review of failure criteria of fibrous composite materials', *Polymer Composites*, 17(6), pp. 786-798.

Egerton, R. (2006) *Physical principles of electron microscopy: an introduction to TEM, SEM, and AEM*. Springer Science & Business Media.

Ellyin, F. and El-Kadi, H. (1990) 'A fatigue failure criterion for fibre reinforced composite laminae', *Composite Structures*, 15(1), pp. 61-74.

Ellyin, F. and Rohrbacher, C. (2003) 'The influence of aqueous environment, temperature and cyclic loading on glass-fibre/epoxy composite laminates', *Journal of reinforced plastics and composites*, 22(7), pp. 615-636.

Fagan, E.M., Kennedy, C.R., Leen, S.B. and Goggins, J. (2016) 'Damage mechanics based design methodology for tidal current turbine composite blades', *Renewable Energy*, 97, pp. 358-372.

Faudot, C. and Dahlhaug, O.G. (2012) 'Prediction of wave loads on tidal turbine blades', *Energy Procedia*, 20, pp. 116-133.

Favre, J.P. and Vidal, G. (1983) 'In-plane and interlaminar shear fatigue characterization of unidirectional GFRP and CFRP, including moisture effects', *ONERA, TP*, (1983), p. 10.

Forrest, P.G. (2013) *Fatigue of metals*. Elsevier.

Fraenkel, P.L. (2006) 'Tidal current energy technologies', *Ibis*, 148(s1), pp. 145-151.

Franz, H.E. (1990) 'Microfractography of fibre reinforced composite materials', *Microstructural and Microanalytical Characterization in Material Development and Quality Control*, pp. 221-232.

Fried, N. (1967) 'Degradation of composite materials: the effect of water on glass-reinforced plastics', *Mechanics of Composite Materials. Pergamon Press, Pensylvania*.

Ganesan, R. and Liu, D.Y. (2008) 'Progressive failure and post-buckling response of tapered composite plates under uni-axial compression', *Composite Structures*, 82(2), pp. 159-176.

Ganesh, V.K. and Naik, N.K. (1996) 'Failure Behaviour of Plain Weave Fabric Laminates under On-Axis Umnaxial Tensile Loading: III—Effect of Fabric Geometry', *Journal of composite materials*, 30(16), pp. 1823-1856.

Garcia, D., Orteu, J.J. and Penazzi, L. (2002) 'A combined temporal tracking and stereo-correlation technique for accurate measurement of 3D displacements: application to sheet metal forming', *Journal of Materials Processing Technology*, 125, pp. 736-742.

Garg, A.C. and Paliwal, V. (1982) 'Effect of water on the fracture behaviour of glass fibre reinforced polyesters', *Fibre Science and Technology*, 17(1), pp. 63-69.

Garg, A.C. and Pawar, S.K. (1982) 'Environmental effect on fracture behaviour of glass fibre reinforced polyester', *Fibre Science and Technology*, 17(2), pp. 133-139.

Garnich, M.R. and Akula, V.M.K. (2009) 'Review of degradation models for progressive failure analysis of fibre reinforced polymer composites', *Applied Mechanics Reviews*, 62(1), p. 010801.

Gellert, E.P. and Turley, D.M. (1999) 'Seawater immersion ageing of glass-fibre reinforced polymer laminates for marine applications', *Composites Part A: Applied Science and Manufacturing*, 30(11), pp. 1259-1265.

Giachetti, A. (2000) 'Matching techniques to compute image motion', *Image and Vision Computing*, 18(3), pp. 247-260.

Giancane, S., Panella, F.W. and Dattoma, V. (2010a) 'Characterization of fatigue damage in long fibre epoxy composite laminates', *International Journal of Fatigue*, 32(1), pp. 46-53.

Giancane, S., Panella, F.W., Nobile, R. and Dattoma, V. (2010b) 'Fatigue damage evolution of fibre reinforced composites with digital image correlation analysis', *Procedia Engineering*, 2(1), pp. 1307-1315.

Gilchrist, M.D., Svensson, S. and Shishoo, R. (1998) 'Fracture and fatigue performance of textile commingled yarn composites', *Journal of materials science*, 33(16), pp. 4049-4058.

Godara, A. and Raabe, D. (2007) 'Influence of fibre orientation on global mechanical behaviour and mesoscale strain localization in a short glass-fibre-reinforced epoxy polymer composite during tensile deformation investigated using digital image correlation', *Composites Science and technology*, 67(11), pp. 2417-2427.

Grédiac, M. and Hild, F. (2012) *Full-field measurements and identification in solid mechanics*. John Wiley & Sons.

Greene, E. (1999) *Marine composites*. Eric Greene Associates.

Grogan, D.M., Leen, S.B., Kennedy, C. and Brádaigh, C.Ó. (2013) 'Design of composite tidal turbine blades', *Renewable Energy*, 57, pp. 151-162.

Guedes, R.M. and de Moura, M.F. (2012) 'Matrix-Controlled Failure Modes of Polymeric Composites', *Wiley Encyclopedia of Composites*.

Hahn, H.T. (1979) *Composite materials: testing and design (Fifth Conference)*. ASTM International.

Hahn, H.T. and Chiao, T.T. (1980) 'Long-term behaviour of composite materials', *Advances in composite materials*, pp. 584-596.

Hameed, M.S., Afaq, S.K. and Shahid, F. (2015) 'Finite Element Analysis of a Composite VAWT Blade', *Ocean Engineering*, 109, pp. 669-676.

Harper, C.A. (2000) *Modern Plastics Handbook: handbook*. McGraw-Hill Professional.

Harper, P.W. and Hallett, S.R. (2015) 'Advanced numerical modelling techniques for the structural design of composite tidal turbine blades', *Ocean Engineering*, 96, pp. 272-283.

Harris, B. (1977) 'Fatigue and accumulation of damage in reinforced plastics', *Composites*, 8(4), pp. 214-220.

Harris, B. (2003) *Fatigue in composites: science and technology of the fatigue response of fibre-reinforced plastics*. Woodhead Publishing.

Hashin, Z. (1980) 'Failure criteria for unidirectional fibre composites', *Journal of applied mechanics*, 47(2), pp. 329-334.

Hashin, Z. and Rotem, A. (1973) 'A fatigue failure criterion for fibre reinforced materials', *Journal of composite materials*, 7(4), pp. 448-464.

Hayes, B.S. and Gammon, L.M. (2010) *Optical Microscopy of Fibre-Reinforced Composites*. ASM international.

He, J., Chiang, M.Y.M., Hunston, D.L. and Han, C.C. (2002) 'Application of the V-notch shear test for unidirectional hybrid composites', *Journal of composite materials*, 36(23), pp. 2653-2666.

He, Y., Makeev, A. and Shonkwiler, B. (2012) 'Characterization of nonlinear shear properties for composite materials using digital image correlation and finite element analysis', *Composites Science and Technology*, 73, pp. 64-71.

Helm, J.D., McNeill, S.R. and Sutton, M.A. (1996) 'Improved three-dimensional image correlation for surface displacement measurement', *Optical Engineering*, 35(7), pp. 1911-1920.

Hermann, T.M., Mamarthupatti, D. and Locke, J.E. (2005) 'Postbuckling analysis of a wind turbine blade substructure', *Journal of solar energy engineering*, 127(4), pp. 544-552.

Hertzberg, R.W., Vinci, R.P. and Hertzberg, J.L. (1996) *Deformation and fracture mechanics of engineering materials*. Wiley New York.

Highsmith, R., Crossman, W., O'Brien, W., Eisenmann, C., Margolis, B., Sendeckyj, M., Porter, R., Ratwani, K., Badaliance, D. and Fong, M. (1982) 'Damage in Composite Materials: Basic Mechanisms, Accumulation, Tolerance, and Characterization', in *Damage in Composite Materials: Basic Mechanisms, Accumulation, Tolerance, and Characterization*. ASTM International.

Hild, F., Domergue, J.-M., Leckie, F.A. and Evans, A.G. (1994) 'Tensile and flexural ultimate strength of fibre-reinforced ceramic-matrix composites', *International Journal of Solids and Structures*, 31(7), pp. 1035-1045.

Hill, R. (1998) *The mathematical theory of plasticity*. Oxford university press.

Hinton, M.J., Kaddour, A.S. and Soden, P.D. (2004) *Failure criteria in fibre reinforced polymer composites: the world-wide failure exercise*. Elsevier.

Hofer Jr, K.E., Benett, L.C. and Stander, M. (1976) *Proceeding of the 31st Annual Technical Conference of SPI, Washington (DC).*

Hofer, K.E., Bennett, L.C. and Stander, M. (1977) 'Effects of moisture and fatigue on the residual mechanical properties of S-glass/graphite/epoxy hybrid composites', *ASTM STP*, 636, pp. 103-122.

Hofer, K.E., Skaper, G.N., Bennett, L.C. and Rao, N. (1987) 'Effect of moisture on fatigue and residual strength losses for various composites', *Journal of reinforced plastics and composites*, 6(1), pp. 53-65.

Hojo, M., Matsuda, S., Tanaka, M., Ochiai, S. and Murakami, A. (2006) 'Mode I delamination fatigue properties of interlayer-toughened CF/epoxy laminates', *Composites Science and Technology*, 66(5), pp. 665-675.

Hull, D. (1981) *An introduction to composite materials*. Cambridge Soli State Science Series.

Hwang, W. and Han, K.S. (1986) 'Fatigue of composites—fatigue modulus concept and life prediction', *Journal of Composite Materials*, 20(2), pp. 154-165.

Icardi, U., Locatto, S. and Longo, A. (2007) 'Assessment of recent theories for predicting failure of composite laminates', *Applied Mechanics Reviews*, 60(2), pp. 76-86.

Ingram, G. (2005) 'Wind turbine blade analysis using the blade element momentum method version 1.0', *School of Engineering, Durham University, UK*.

Iso, B.S. (2003) '13003. Fibre-reinforced plastics–determination of fatigue properties under cyclic loading conditions', *British Standards International*.

Jalali Mosallam, S.J. (1998) 'A new test method for measuring the longitudinal and shear moduli of fibre-reinforced composites'.

Joneja, S.K. (1984) 'Influence of matrix ductility on transverse fatigue and fracture toughness of glass reinforced composites', *SAMPE Q.*, 15(4), pp. 31-38.

Jones, C.J., Dickson, R.F., Adam, T., Reiter, H. and Harris, B. (1984a) 'ENVIRONMENTAL FATIGUE BEHAVIOUR OF REINFORCED PLASTICS', *Proceedings of The Royal Society of London, Series A: Mathematical and Physical Sciences*, 396(1811), pp. 315-338.

Jones, C.J., Dickson, R.F., Adam, T., Reiter, H. and Harris, B. (1984b) 'The environmental fatigue behaviour of reinforced plastics', *Proceedings of the Royal Society of London. A. Mathematical and Physical Sciences*, 396(1811), pp. 315-338.

Jones, F.R. (2003) 'The effects of aggressive environments on long-term behaviour', *Fatigue in composites. Cambridge: Woodhead Publishing Limited*, pp. 117-46.

Jones, F.R. and Rock, J.W. (1983) 'On the mechanism of stress corrosion of E-glass fibres', *Journal of materials science letters*, 2(8), pp. 415-418.

Jones, F.R., Rock, J.W. and Wheatley, A.R. (1983) 'Stress corrosion cracking and its implications for the long-term durability of E-glass fibre composites', *Composites*, 14(3), pp. 262-269.

Kammers, A. and Daly, S. (2011) 'Experimental investigation of deformation mechanisms present in ultrafine-grained metals', in *MEMS and Nanotechnology, Volume 4*. Springer, pp. 105-110.

Kang, J., Jain, M., Wilkinson, D.S. and Embury, J.D. (2005) 'Microscopic strain mapping using scanning electron microscopy topography image correlation at large strain', *The Journal of Strain Analysis for Engineering Design*, 40(6), pp. 559-570.

Karbhari, V.M. and Zhang, S. (2003) 'E-glass/vinylester composites in aqueous environments–I: experimental results', *Applied Composite Materials*, 10(1), pp. 19-48.

Kassapoglou, C. (2010) 'Fatigue of composite materials under spectrum loading', *Composites Part A: Applied Science and Manufacturing*, 41(5), pp. 663-669.

Kennedy, C.R., Leen, S.B. and Brádaigh, C.M.Ó. (2012) 'A preliminary design methodology for fatigue life prediction of polymer composites for tidal turbine blades', *Proceedings of the Institution of Mechanical Engineers, Part L: Journal of Materials Design and Applications*, p. 1464420712443330.

Kennedy, C.R., Leen, S.B. and Brádaigh, C.r.M.O. (2011) *ASME 2011 30th International Conference on Ocean, Offshore and Arctic Engineering*. American Society of Mechanical Engineers.

Kensche, C.W. (2006) 'Fatigue of composites for wind turbines', *International Journal of Fatigue*, 28(10), pp. 1363-1374.

KH, B. (1970) 'Some fatigue characteristics of glass reinforced composite laminates ', *ASME Paper*.

Khan, M.J., Bhuyan, G., Iqbal, M.T. and Quaicoe, J.E. (2009) 'Hydrokinetic energy conversion systems and assessment of horizontal and vertical axis turbines for river and tidal applications: A technology status review', *Applied Energy*, 86(10), pp. 1823-1835.

Khashaba, U.A. (2004) 'In-plane shear properties of cross-ply composite laminates with different off-axis angles', *Composite structures*, 65(2), pp. 167-177.

Kies, J.A. (1962) *Maximum strains in the resin of fibreglass composites*. DTIC Document.

Komai, K., Minoshima, K. and Shiroshita, S. (1991) 'Hygrothermal degradation and fracture process of advanced fibre-reinforced plastics', *Materials Science and Engineering: A*, 143(1), pp. 155-166.

Kong, C., Kim, T., Han, D. and Sugiyama, Y. (2006) 'Investigation of fatigue life for a medium scale composite wind turbine blade', *International journal of Fatigue*, 28(10), pp. 1382-1388.

Konur, O. and Matthews, F.L. (1989) 'Effect of the properties of the constituents on the fatigue performance of composites: a review', *Composites*, 20(4), pp. 317-328.

Kootsookos, A. and Mouritz, A.P. (2004) 'Seawater durability of glass-and carbon-polymer composites', *Composites Science and Technology*, 64(10), pp. 1503-1511.

Kotsikos, G., Evans, J.T., Gibson, A.G. and Hale, J.M. (2000) 'Environmentally enhanced fatigue damage in glass fibre reinforced composites characterised by acoustic emission', *Composites Part A: Applied Science and Manufacturing*, 31(9), pp. 969-977.

Kumosa, M., Odegard, G., Armentrout, D., Kumosa, L., Searles, K. and Sutter, J.K. (2002) 'Comparison of the±45° tensile and losipescu shear tests for woven fabric composite materials', *Journal of composites technology & research*, 24(1), pp. 3-16.

Kuo, W.-S. and Pon, B.-J. (1997) 'Elastic moduli and damage evolution of three-axis woven fabric composites', *Journal of materials science*, 32(20), pp. 5445-5455.

Laurin, F., Charrier, J.S., Lévêque, D., Maire, J.F., Mavel, A. and Nunez, P. (2012) 'Determination of the properties of composite materials thanks to digital image correlation measurements', *Procedia IUTAM*, 4, pp. 106-115.

Lee, H.G., Kang, M.G. and Park, J. (2015) 'Fatigue failure of a composite wind turbine blade at its root end', *Composite Structures*, 133, pp. 878-885.

Lee, Y.-J., Jhan, Y.-T. and Chung, C.-H. (2012) 'Fluid–structure interaction of FRP wind turbine blades under aerodynamic effect', *Composites Part B: Engineering*, 43(5), pp. 2180-2191.

Liao, K., Schultheisz, C.R. and Hunston, D.L. (1999a) 'Effects of environmental aging on the properties of pultruded GFRP', *Composites Part B: Engineering*, 30(5), pp. 485-493.

Liao, K., Schultheisz, C.R. and Hunston, D.L. (1999b) 'Long-term environmental fatigue of pultruded glass-fibre-reinforced composites under flexural loading', *International journal of fatigue*, 21(5), pp. 485-495.

Lind, D.J. and Richards, J. (1984) 'Method of manufacturing composite materials'. Google Patents.

Lorenzo, L. and Hahn, H.T. (1986) 'Fatigue failure mechanisms in unidirectional composites', *Composite Materials: Fatigue and Fracture*, pp. 210-232.

Luo, P.F., Chao, Y.J., Sutton, M.A. and Peters Iii, W.H. (1993) 'Accurate measurement of three-dimensional deformations in deformable and rigid bodies using computer vision', *Experimental Mechanics*, 33(2), pp. 123-132.

Maalej, M. and Li, V.C. (1994) 'Flexural/tensile-strength ratio in engineered cementitious composites', *Journal of Materials in Civil Engineering*, 6(4), pp. 513-528.

Makeev, A. (2013) 'Interlaminar shear fatigue behaviour of glass/epoxy and carbon/epoxy composites', *Composites Science and Technology*, 80, pp. 93-100.

Mandell, J.F., Huang, D.D. and McGarry, F.J. (1980) 'Tensile fatigue performance of glass fibre dominated composites'.

Mao, H. and Mahadevan, S. (2002) 'Fatigue damage modelling of composite materials', *Composite Structures*, 58(4), pp. 405-410.

Martin, J.R. and Gardner, R.J. (1981) 'Effect of long term humid aging on plastics', *Polymer Engineering & Science*, 21(9), pp. 557-565.

Martin, R. (2008) *Ageing of composites*. Elsevier.

Matthews, F.L., Davies, G., Hitchings, D. and Soutis, C. (2000a) *Finite element modelling of composite materials and structures*. Elsevier.

Matthews, F.L., Davies, G.A.O., Hitchings, D. and Soutis, C. (2000b) '5 - Composites and finite element analysis', in *Finite Element Modelling of Composite Materials and Structures*. Woodhead Publishing, pp. 71-93.

Metcalfe, A.G. and Schmitz, G.K. (1972) 'MECHANISM OF STRESS-CORROSION IN E GLASS FILAMENTS', *Glass Technology*, 13(1), pp. 5-&.

Miller, A.G. and Wingert, A.L. (1979) 'Fracture surface characterization of commercial graphite/epoxy systems', *Nondestructive Evaluation and Flaw Criticality for Composite Materials*, pp. 223-273.

Milne, I., Sharma, R., Flay, R. and Bickerton, S. (2010) *Proceedings of the 3rd International Conference on Ocean Energy, Bilbao, Spain*.

Miyano, Y. and Nakada, M. (2006) *Long term durability and damage tolerance of innovative marine composites*. Technical report, Material systems laboratory,(2006), Japan.

Miyano, Y., Nakada, M. and Sekine, N. (2005) 'Accelerated testing for long-term durability of FRP laminates for marine use', *Journal of composite materials*, 39(1), pp. 5-20.

Mortazavian, S. and Fatemi, A. (2015) 'Effects of fibre orientation and anisotropy on tensile strength and elastic modulus of short fibre reinforced polymer composites', *Composites Part B: Engineering*, 72, pp. 116-129.

Morton, J., Ho, H., Tsai, M.Y. and Farley, G.L. (1992) 'An evaluation of the Iosipescu specimen for composite materials shear property measurement', *Journal of Composite Materials*, 26(5), pp. 708-750.

Mukherjee, A. and Varughese, B. (2001) 'Design guidelines for ply drop-off in laminated composite structures', *Composites Part B: Engineering*, 32(2), pp. 153-164.

Mukhopadhyay, M. (2005) *Mechanics of composite materials and structures*. Universities press.

Myers, T.J., Kytömaa, H.K. and Smith, T.R. (2007) 'Environmental stress-corrosion cracking of fibreglass: Lessons learned from failures in the chemical industry', *Journal of hazardous materials*, 142(3), pp. 695-704.

NACA Airfoil Generator. Available at: http://airfoiltools.com/airfoil/naca4digit.

Naik, N.K. (2003) 'Woven-fibre thermoset composites', *Fatigue in Composites: Science and Technology of the Fatigue Response of Fibre-Reinforced Plastics*, p. 296.

Naik, N.K. and Ganesh, V.K. (1996) 'Failure behaviour of plain weave fabric laminates under on-axis uniaxial tensile loading: I—analytical predictions', *Journal of Composite Materials*, 30(16), pp. 1779-1822.

Naik, N.K. and Shembekar, P.S. (1992) 'Elastic behaviour of woven fabric composites: I—Lamina analysis', *Journal of composite materials*, 26(15), pp. 2196-2225.

Nettles, A.T. (1994) 'Basic mechanics of laminated composite plates'.

Nevalainen, T.M. (2016) *The effect of unsteady sea conditions on tidal stream turbine loads and durability*. University of Strathclyde.

Newaz, G.M. (1985) 'Influence of matrix material on flexural fatigue performance of unidirectional composites', *Composites Science and Technology*, 24(3), pp. 199-214.

Nicholls-Lee, R.F. (2011) *Adaptive composite blades for horizontal axis tidal turbines*. University of Southampton.

Odegard, G. and Kumosa, M. (1999) 'Elasto-plastic analysis of the Iosipescu shear test', *Journal of composite materials*, 33(21), pp. 1981-2001.

Owen, M.J. (1974) 'Fatigue of carbon-fibre-reinforced plastics', *Fracture and fatigue.(A 75-24879 10-24) New York, Academic Press, Inc., 1974*, pp. 341-369.

Owen, M.J. and Griffiths, J.R. (1978) 'Evaluation of biaxial stress failure surfaces for a glass fabric reinforced polyester resin under static and fatigue loading', *Journal of Materials Science*, 13(7), pp. 1521-1537.

Owen, M.J. and Howe, R.J. (1972) 'The accumulation of damage in a glass-reinforced plastic under tensile and fatigue loading', *Journal of Physics D: Applied Physics*, 5(9), p. 1637.

Pagano, N.J. and Pipes, R.B. (1971) 'The influence of stacking sequence on laminate strength', *Journal of Composite Materials*, 5(1), pp. 50-57.

Papanicolaou, G.C., Zaoutsos, S.P. and Kontou, E.A. (2004) 'Fibre orientation dependence of continuous carbon/epoxy composites nonlinear viscoelastic behaviour', *Composites science and technology*, 64(16), pp. 2535-2545.

Pelc, R. and Fujita, R.M. (2002) 'Renewable energy from the ocean', *Marine Policy*, 26(6), pp. 471-479.

Peters, W.H. and Ranson, W.F. (1982) 'Digital imaging techniques in experimental stress analysis', *Optical engineering*, 21(3), pp. 213427-213427-.

Press, W.H. (2003) 'C++ numerical algorithms', *Publishing House of Electronics Industry, Beijing*.

Price, J.N. and Hull, D. (1983) 'Propagation of stress corrosion cracks in aligned glass fibre composite materials', *Journal of Materials Science*, 18(9), pp. 2798-2810.

Pritchard, G. and Taneja, N. (1973) 'Water damage in polyester/glass laminates. Part II: Microscopic evidence', *Composites*, 4(5), pp. 199-202.

Purslow, D. (1981) 'Some fundamental aspects of composites fractography', *Composites*, 12(4), pp. 241-247.

Qin, L., Zhang, Z., Li, X., Yang, X., Feng, Z., Wang, Y., Miao, H., He, L. and Gong, X. (2012) 'Full-field analysis of shear test on 3D orthogonal woven C/C composites', *Composites Part A: Applied Science and Manufacturing*, 43(2), pp. 310-316.

Quaresimin, M., Susmel, L. and Talreja, R. (2010) 'Fatigue behaviour and life assessment of composite laminates under multiaxial loadings', *International Journal of Fatigue*, 32(1), pp. 2-16.

Rastogi, P.K. (2003) *Photomechanics*. Springer Science & Business Media.

Reddy, J.N. (2004) *Mechanics of laminated composite plates and shells: theory and analysis*. CRC press.

Rege, S.K. and Lakkad, S.C. (1983) 'Effect of salt water on mechanical properties of fibre reinforced plastics', *Fibre Science and Technology*, 19(4), pp. 317-324.

Reifsnider, K. (1980) 'Fatigue behaviour of composite materials', *International Journal of Fracture*, 16(6), pp. 563-583.

Reifsnider, K.L. (1990) 'Damage and damage mechanics', *Fatigue of composite materials*, 4, pp. 11-75.

Reifsnider, K.L. (2012) *Fatigue of composite materials*. Elsevier.

Reifsnider, K.L. and Gao, Z. (1991) 'A micromechanics model for composites under fatigue loading', *International journal of fatigue*, 13(2), pp. 149-156.

Reifsnider, K.L. and Jamison, R. (1982) 'Fracture of fatigue-loaded composite laminates', *International Journal of Fatigue*, 4(4), pp. 187-197.

Release, A. (2012) '14.5, ANSYS Inc', *Canonsburg, USA*.

Renaud, C. and Greenwood, M. (2005) *Proceedings of 9 EFUC Meeting, Wroclaw, Poland*.

Romanenkov, I.G. (1967) 'Dependence of the Mechanical Properties of GRPs on their water Absorption', *Soviet Plastics*, 2, pp. 74-75.

Rosenfeld, M.S. and Gause, L.W. (1981) 'Compression fatigue behaviour of graphite-epoxy in the presence of stress raisers', in *Fatigue of fibrous composite materials*. American Society for Testing and Materials, pp. 174-196.

Sachtleber, M., Zhao, Z. and Raabe, D. (2002) 'Experimental investigation of plastic grain interaction', *Materials Science and Engineering: A*, 336(1), pp. 81-87.

Sauer, J. and Richardson, G. (1980) 'Fatigue of polymers', *International journal of fracture*, 16(6), pp. 499-532.

Schaff, J.R. and Davidson, B.D. (1997) 'Life prediction methodology for composite structures. Part I—Constant amplitude and two-stress level fatigue', *Journal of composite materials*, 31(2), pp. 128-157.

Schmitz, G.K. and Metcalfe, A.G. (1966) 'Stress corrosion of E-glass fibres', *Industrial & Engineering Chemistry Product Research and Development*, 5(1), pp. 1-8.

Scholte, H. (1994a) 'Fatigue characteristics', *Composite Materials in Maritime Structures Volume 2 (Practical Considerations)*, pp. 178-196.

Scholte, H.G. (1994b) 'Fatigue characteristics', *Composite Materials in Maritime Structures Volume 2 (Practical Considerations)*, pp. 178-196.

Sekine, H., Shimomura, K. and Hamana, N. (1988) 'Strength deterioration and degradation mechanism of glass chopped reinforced plastics in water environment', *JSME international journal. Ser. 1, Solid mechanics, strength of materials*, 31(3), pp. 619-626.

Shenoi, R.A. and Wellicome, J.F. (1993) *Composite Materials in Maritime Structures: Volume 1, Fundamental Aspects*. Cambridge University Press.

Shih, G.C. and Ebert, L.J. (1987) 'The effect of the fibre/matrix interface on the flexural fatigue performance of unidirectional fibreglass composites', *Composites science and technology*, 28(2), pp. 137-161.

Shokrieh, M.M. and Lessard, L.B. (1997) 'Multiaxial fatigue behaviour of unidirectional plies based on uniaxial fatigue experiments—II. Experimental evaluation', *International journal of fatigue*, 19(3), pp. 209-217.

Shokrieh, M.M. and Rafiee, R. (2006) 'Simulation of fatigue failure in a full composite wind turbine blade', *Composite Structures*, 74(3), pp. 332-342.

Slepetz, J.M., Zagaeski, T.F. and Novello, R.F. (1978) *In-Plane Shear Test for Composite Materials*. DTIC Document.

Smith, C.S. (1990) *Design of marine structures in composite materials*. Elsevier London.

Smith, T.S., Bay, B.K. and Rashid, M.M. (2002) 'Digital volume correlation including rotational degrees of freedom during minimization', *Experimental Mechanics*, 42(3), pp. 272-278.

Solutions, C. (2009) 'Vic-2D', *Reference Manual*.

Soni, S.R. (1983) 'A comparative study of failure envelopes in composite laminates', *Journal of Reinforced Plastics and Composites*, 2(1), pp. 34-42.

Spera, D.A. (1994) *Wind turbine technology: fundamental concepts of wind turbine engineering*. ASME press New York.

Springer, G.S. (1988) 'Environmental effects on composite materials. Volume 3'.

Standard, A. (2005) 'D5379/D5379M, 2005,"', *Standard Test Method for Shear Properties of Composite Materials by the V-Notched Beam Method." West Conshohoncken, PA*.

Standard, A. (2010) 'Standard test method for short-beam strength of polymer matrix composite materials and their laminates', *Annual book of ASTM standards*, pp. 71-78.

Steeves, C.A. and Fleck, N.A. (2005) 'Compressive strength of composite laminates with terminated internal plies', *Composites Part A: applied science and manufacturing*, 36(6), pp. 798-805.

Stephens, R.I., Fatemi, A., Stephens, R.R. and Fuchs, H.O. (2000) *Metal fatigue in engineering*. John Wiley & Sons.

Stinchcomb, W.W. and Reifsnider, K.L. (1979) 'Fatigue damage mechanisms in composite materials: a review', *Fatigue mechanisms*, pp. 762-787.

Stock, S.R. (1999) 'X-ray microtomography of materials', *International Materials Reviews*, 44(4), pp. 141-164.

Stronge, M. 'UK Weather Portal available from http://www.stronge.org.uk/marine/tides/'.

Sturgeon, J.B. (1977) 'Fatigue of multi-directional carbon fibre-reinforced plastics', *Composites*, 8(4), pp. 221-226.

Sun, W., Guan, Z., Li, Z., Zhang, M. and Huang, Y. (2017) 'Compressive failure analysis of unidirectional carbon/epoxy composite based on micro-mechanical models', *Chinese Journal of Aeronautics*, 30(6), pp. 1907-1918.

Sun, Z., Lyons, J.S. and McNeill, S.R. (1997) 'Measuring microscopic deformations with digital image correlation', *Optics and Lasers in Engineering*, 27(4), pp. 409-428.

Suri, C. and Perreux, D. (1995) 'The effects of mechanical damage in a glass fibre/epoxy composite on the absorption rate', *Composites Engineering*, 5(4), pp. 415-424.

Sutton, M.A., McNeill, S.R., Helm, J.D. and Chao, Y.J. (2000) 'Advances in two-dimensional and three-dimensional computer vision', in *Photomechanics*. Springer, pp. 323-372.

Sutton, M.A., Mingqi, C., Peters, W.H., Chao, Y.J. and McNeill, S.R. (1986) 'Application of an optimized digital correlation method to planar deformation analysis', *Image and Vision Computing*, 4(3), pp. 143-150.

Sutton, M.A., Orteu, J.J. and Schreier, H. (2009) *Image correlation for shape, motion and deformation measurements: basic concepts, theory and applications*. Springer Science & Business Media.

Talreja, R. (1980) 'STIFFNESS BASED FATIGUE DAMAGE CHARACTERISATION OF FIBROUS COMPOSITES', *Economic Computation and Economic Cybernetics Studies and Research*, 2, pp. 1732-1739.

Talreja, R. (1981a) *Proceedings of the Royal Society of London A: Mathematical, Physical and Engineering Sciences*. The Royal Society.

Talreja, R. (1981b) 'Fatigue of composite materials: damage mechanisms and fatigue-life diagrams', *Proceedings of the Royal Society of London. A. Mathematical and Physical Sciences*, 378(1775), pp. 461-475.

Talreja, R. (1987) *Fatigue of composite materials*. Technomic.

Talreja, R. (2008a) 'Damage and fatigue in composites–a personal account', *Composites Science and Technology*, 68(13), pp. 2585-2591.

Talreja, R. (2008b) 'Damage and fatigue in composites – A personal account', *Composites Science and Technology*, 68(13), pp. 2585-2591.

Talreja, R. (2015) 'Manufacturing defects in composites and their effects on performance', in *Polymer Composites in the Aerospace Industry*. Elsevier, pp. 99-113.

Tang, R., Guo, Y.-J. and Weitsman, Y.J. (2004) 'An appropriate stiffness degradation parameter to monitor fatigue damage evolution in composites', *International journal of fatigue*, 26(4), pp. 421-427.

Tanimoto, T. and Amijima, S. (1975) 'Progressive nature of fatigue damage of glass fibre reinforced plastics', *Journal of Composite Materials*, 9(4), pp. 380-390.

Thom, H. (1998) 'A review of the biaxial strength of fibre-reinforced plastics', *Composites Part A: Applied Science and Manufacturing*, 29(8), pp. 869-886.

Thompson, A.W. (July 1957) 'Reinforced Plastics'.

Thomsen, O.T., Mortensen, F. and Frostig, Y. (2000) 'Interface failure at ply drops in CFRP/sandwich panels', *Journal of composite materials*, 34(2), pp. 135-157.

Tong, J. (2002) 'Characteristics of fatigue crack growth in GFRP laminates', *International journal of fatigue*, 24(2), pp. 291-297.

Tong, W. (2005) 'An evaluation of digital image correlation criteria for strain mapping applications', *Strain*, 41(4), pp. 167-175.

Tsai, S.W. and Wu, E.M. (1971) 'A general theory of strength for anisotropic materials', *Journal of composite materials*, 5(1), pp. 58-80.

Van Briel, J. and Van Leuven, J. (1985) *Wind Energy Conversion 1984: Proceedings of the Sixth BWEA Wind Energy Conference University of Reading, 28-30 March 1984*.

Van Grieken, R. and Markowicz, A. (2001) *Handbook of X-ray Spectrometry*. CRC Press.

Van Paepegem, W. and Degrieck, J. (2002) 'A new coupled approach of residual stiffness and strength for fatigue of fibre-reinforced composites', *International Journal of Fatigue*, 24(7), pp. 747-762.

Varughese, B. and Mukherjee, A. (1997) 'A ply drop-off element for analysis of tapered laminated composites', *Composite structures*, 39(1), pp. 123-144.

Vauthier, E., Chateauminois, A. and Bailliez, T. (1995) *Tenth International Conference on Composite Materials. VI. Microstructure, Degradation, and Design*.

Walkington, I. and Burrows, R. (2009) 'Modelling tidal stream power potential', *Applied Ocean Research*, 31(4), pp. 239-245.

Walrath, D.E. and Adams, D.F. (1983) 'The losipescu shear test as applied to composite materials', *Experimental Mechanics*, 23(1), pp. 105-110.

Wannenburg, J., Heyns, P.S. and Raath, A.D. (2009) 'Application of a fatigue equivalent static load methodology for the numerical durability assessment of heavy vehicle structures', *International Journal of Fatigue*, 31(10), pp. 1541-1549.

Watanabe, M. and Tsai, T.W. (1979) *Composite Materials: Testing and Design (Fifth Conference), ASTM STP*.

Watt, I.M. (1997) *The principles and practice of electron microscopy*. Cambridge University Press.

Weitsman, Y. (1991) 'Moisture in composites: sorption and damage'. Elsevier Science Publishers BV, pp. 385-429.

Whitney, J.M. and Knight, M. (1980) 'The relationship between tensile strength and flexure strength in fibre-reinforced composites', *Experimental Mechanics*, 20(6), pp. 211-216.

Whitworth, H.A. (1997) 'A stiffness degradation model for composite laminates under fatigue loading', *Composite structures*, 40(2), pp. 95-101.

Wicaksono, S. (2009) *Fracture of laminated panels in tension*.

Wicaksono, S. and Chai, G.B. (2013) 'A review of advances in fatigue and life prediction of fibre-reinforced composites', *Proceedings of the Institution of Mechanical Engineers, Part L: Journal of Materials Design and Applications*, 227(3), pp. 179-195.

Wilkins, E. (1956) *Colloquium on Fatigue/Colloque de Fatigue/Kolloquium über Ermüdungsfestigkeit*. Springer.

Wilklns, D.J. (1982) 'APRELIMINARY DAMAGE TOLERANCEMETHODOLOGY FOR COMPOSTTE STRUCTURES', *Failure Analysis and Mechanisms of Failure, of Fibrous Composite Structures*, p. 67.

Wisnom, M.R. (1992) 'The relationship between tensile and flexural strength of unidirectional composites', *Journal of Composite Materials*, 26(8), pp. 1173-1180.

Wright, D.C. (1996) *Environmental stress cracking of plastics*. iSmithers Rapra Publishing.

Zhang, D., Luo, M. and Arola, D.D. (2006) 'Displacement/strain measurements using an optical microscope and digital image correlation', *Optical Engineering*, 45(3), pp. 033605-033605-9.

Zhuang, H. (1995) 'The influence of surface properties on carbon fibre/epoxy matrix interfacial adhesion'.